UNIVERSITY OF CAMERINO

School of Advanced Studies

Doctorate Course in Chemical and Pharmaceutical Sciences and Biotechnology

PhD Thesis

SYNTHESIS OF METAL-ORGANIC FRAMEWORKS CONTAINING HETEROCYCLIC LINKERS FOR APPLICATIONS IN CO_2 STORAGE/UTILIZATION AND LUMINESCENT SENSING

Cycle XXXV

Scientific Sector CHIM/03

PhD Candidate

Giorgio Mercuri

Supervisor

Prof. Claudio Pettinari

Co-Supervisor

Dr. Andrea Rossin

2019/2020-2022/2023

Abstract

Metal-organic frameworks (MOFs) are hybrid organic/inorganic 3D coordination polymers with open structures deriving from the self-assembly of polytopic linkers and metal ions or metal-based clusters. In more recent years, MOFs have emerged as promising alternative to all-inorganic materials (e.g. activated carbons and zeolites) in industrially and technologically relevant applications requiring porous compounds, such as gas adsorption or separation, heterogeneous catalysis and luminescence sensing. The tailored design of polydentate linkers (carboxylates, azolates) for MOFs construction is of fundamental importance to prepare well-performing materials for a target application. At present, a wide plethora of organic spacers has been prepared for this task. In many cases, the building units exploited are rigid aromatic six-membered fully carbocyclic rings (isolated or conjugated: benzene, 4,4'-biphenyl, terphenyl, naphthalene, anthracene, pyrene) decorated with carboxylate groups as coordinating units to metal centers. The introduction of heteroatoms or tailored functional groups within the linkers skeleton is generally beneficial to improve the MOF performance in a given process like gas adsorption/separation/transformation. One important example belonging to this category is that of carbon dioxide. The steadily increasing atmospheric concentration of carbon dioxide and the consequences of this phenomenon in terms of Earth's global warming (the so-called greenhouse effect), ocean acidification, melting of polar ices and rising sea level are of primary concern for the scientific community. Carbon capture and storage (CCS) is a modern approach to solve this problem. CCS technologies based on CO_2 adsorption by nano-porous adsorbents have become popular. MOFs have gained great attention in this context. The extraordinary versatility in MOFs design is the main reason for their applicative success. MOFs hold unique advantages, including control of their pore size and shape, high specific surface area, and the possibility to include proper functional groups on their linkers' skeleton. An alternative approach to reduce CO_2 concentration in the atmosphere and to mitigate its environmental effects moves from a radically new viewpoint, the so-called Carbon Capture and Utilization (CCU), where CO_2 is no longer regarded as a simple waste but as a renewable resource to be harvested and recycled into C-containing products and feedstocks of added value. CCU sees CO_2 as a safe and inexpensive C_1 building block to yield expedient organic compounds. In a combined [CCS + CCU] perspective, MOFs represent excellent heterogeneous catalysts, showing great potentiality in terms of CO_2 adsorption and its subsequent chemical conversion into useful chemicals (carbonates, methanol,

methane). MOFs may have high CO_2 adsorption, thus enhancing the local concentration of CO_2 inside their pores and improving the catalytic efficiency. The introduction of basic heteroatoms in the MOF skeleton or the presence of basic functional groups further increases the concentration of CO_2 at the catalytically active sites because of the enhanced interaction with acidic CO_2. Indeed, various literature works have proved that MOFs built with heterocyclic linkers show a better CO_2 uptake (in terms of mmol/g CO_2 adsorbed) and a higher thermodynamic affinity (isosteric adsorption enthalpy, Q_{st}) if compared with those made of fully carbocyclic rings. Another important applicative context from an environmental point of view is that of pollutants sensing in wastewaters. Pollutants as the so-called "contaminants of emerging concern" (CECs, *i.e.* a class of chemical and biological compounds such as pharmaceutical and personal care products that have been recognized as potentially harmful to human health and the environment) or cyanide anions (present in water sources as result of industrial processes and mining activity) are two classes of pollutants that can be particularly hazardous both to humans and the environment. Ideally, pollutants detection requires rapid, simple, cheap, sensitive and selective detection methods. Chemical sensors, *i.e.* analytical tools that provide information about the chemical composition of the environment in which they are introduced, are based on a variety of transduction mechanisms (e.g. optic, electronic, optoelectronic). Luminescent materials release energy in the form of electromagnetic radiation in the visible region in response to external stimuli. Recently, luminescent materials have gained the stage as chemical sensors, as luminescence is among the most desirable transduction mechanisms for its relative easiness of use, technical simplicity and broad adaptability. As chemical sensors, luminescent MOFs possess a number of advantages over other luminescent materials. Analyte adsorption within MOF pores allows for its pre-concentration, increasing sensor sensitivity. Selectivity in MOFs can be achieved by tuning pore dimension and/or by proper functionalization of the linkers. Fluorescent linkers typically bear π-conjugated electrons which can give emission upon irradiation. Linkers made of heterocyclic rings are particularly suitable for this application, since the presence of a heteroatom enhances the luminescent response.

Table of Contents

List of abbreviations

3,3'-H_2L – 3,3'-diamino-4-4'-bipyrazole

3,5-H_2L – 3,5-diamino-4-4'-bipyrazole

Ad – Adeninate

BET – Brunauer-Emmett-Teller

bio-MOF-1 – $[Zn_8(ad)4(BPDC)_6O]\cdot 2Me_2NH_2 8DMF 11H_2O$

BJH – Barret-Joyner-Halenda

BPP – 1,3-bis(4-pyridyl)propane

Br-H_2BDC – 2-bromo-1,4-benzenedicarboxylate

CCS – Carbon Capture and Sequestration

CCU – Carbon Capture and Utilization

CCUS – Carbon Capture Utilization and Storage

CECs – Contaminants of Emerging Concerns

DCF – Diclofenac sodium

DFT – Density Functional Theory

DH – Dollimore and Heal

DMA – N,N'-dimethylacetamide

DMF – Dimethylformamide

DMSO – Dimethylsulfoxide

DoE – U.S. Department of Energy

DSC – Differential Scanning Calorimetry

DTG – Derivative Thermogravimetry

ESI-MS – Electrospray Ionization – Mass Spectrometry

Et_2SpSP – Diethyl-2,2'-Biselenophene-5,5'-dicarboxylate

FTIR – Fourier Transform Infrared

FXT – Fluoxetine

GC/MS – Gas-Chromatography/Mass Spectroscopy

GCMCS – Grand Canonical Monte Carlo simulations

GF-AAS – Grafite Furnace – Atomic Absorption Spectroscopy

H_2-2,3-PYDC – Pyridine-2,3-dicarboxylic acid

H_2BBTA – 1H,5H-benzo(1,2- d:4,5-d')bistriazole

H_2BDC – 1,4-benzenedicarboxylic acid

H_2BPDC – Biphenyl-4,4’-dicarboxylic acid

H_2BPZ – 4,4’-bipyrazole

H_2BPZNH$_2$ – 3-amino-4,4’-bipyrazole

H_2BPZNO$_2$ – 3-nitro-4,4’-bypirazole

H_2Me$_2$BPDC – 2,2'-dimethylbiphenyl-4,4'-dicarboxylic acid

H_2Me$_2$-TPDC – 2',5'-dimethy-terphenyl-4,4''-dicarboxylate

H_2NDC – Naphthalene-2,6-dicarboxylic acid

H_2PhPh – Biphenyl-4,4’-dicarboxylic acid

H_2SpSp – 2,2’-biselenophene-5,5’-dicarboxylic acid

H_2TpTp – 2,2’-bithiophene-5,5’-dicarboxylic acid

H_2TzPh – 5-Carboxy-3-(4-carboxybenzyl)thiazolium Bromide

H_2TzTz – 2,2’-bithiazole-5,5’-dicarboxylic acid

H_3BBC – 1,3,5-tris(4’-carboxy[1,1’-biphenyl]-4-yl)benzene

H_3BIDC – 1H-benzimidazole-5,6-dicarboxylic acid

H_3BTB – 1,3,5-tris(4-carboxyphenyl)benzene

H_3BTC – 1,3,5-benzenetricarboxylic acid

H_3BTE – 1,3,5-triscarboxyphenylethynylbenzene

H_3PTC – Pyridine-2,4,6-tricarboxylic acid

H_4DOT – 2,5-dihydroxyterephtalic acid

H_4TBAPy – 1,3,6,8-tetrakis(*p*-benzoic acid)pyrene

HATZ – 5-aminotetrazole

HKUST – Hong Kong University of Science and Technology

HOMO – Highest Occupied Molecular Orbital

HSAB – Hard-Soft Acid-Base

IAST – Ideal Adsorption Solution Theory

IBR – Ibuprofen

IR-MOFs – Isoreticular Metal-Organic Frameworks

IUPAC – International Union of Pure and Applied Chemistry

LAG – Liquid-Assisted Grinding

LEDs – Light Emitting Diodes

LMCT – Ligand – Metal Charge Transfer

LOD – Limit Of Detection

LUMO – Lowest Unoccupied Molecular Orbital

MAF-25X – $Mn(II)_2Cl_2(bbta)$

MAF-25X-ox – $Mn(II)Mn(III)(OH)Cl_2(BBTA)$

MeCN – Acetonitrile

MIXMOFs – Mixed – linkers MOFs

MLCT – Metal – Ligand Charge Transfer

MM-MOF-74 – Mixed-metal-MOF-74; $M_2(DOT)$

MOF-1 – $Co(BTC)(Py)_2$

MOF-177 – $Zn_4O(BTB)_2$

MOF-177 – $Zn_4O(BTB)_2$

MOF-180 – $Zn_4O(BTE)_2$

MOF-2 – $Zn(BDC)(H_2O)$

MOF-200 – $Zn_4O(BBC)_2$

MOF-5 – $Zn_4O(BDC)_3$

MOF-74 – $M_2(DOT)$

MOF-808 – $[Zr_6O_4(\mu_3\text{-}OH)_4(OH)_6(H_2O)_6(BTC)_2]\cdot nH_2O$

MOFs – Metal – Organic Frameworks

MSD – Mean – Square displacement

MTV-MOFs – Multivariate Metal-Organic Frameworks

MW – Micro – Wave

NH_2- H_2BDC – 2-amino-1,4-benzenedicarboxylate

NIR – Near – Infrared

NLDFT – Non – Local Density Functional Theory

NMR – Nuclear Magnetic Resonance

NU – Northwestern University

NU-1000 – $Zr_6(\mu_3\text{-}O)_8(OH)_8(TBAPy)_2$

OX – Oxalate

PCN-700 – Porous Coordination Network-700; $Zr_6O_4(OH)_8(Me_2\text{-}BPDC)_4$

PCN-701 – Porous Coordination Network-701; $Zr_6O_4(OH)_6(H_2O)_2(Me_2\text{-}BPDC)_4(BDC)$

PCN-702 – Porous Coordination Network-702; $Zr_6O_4(OH)_7(H_2O)_3(Me_2\text{-}BPDC)_4(Me_2\text{-}TPDC)_{0.5}$

PCN-703 – Porous Coordination Network-703; $Zr_6O_4(OH)_5(H_2O)(Me_2\text{-}BPDC)_4(BDC)(Me_2\text{-}TPDC)_{0.5}$

PCP – Personal Care Product

PIC – γ-Picoline

PSA – Pressure Swing Adsorption

PSD – Pore Size Distribution

PSM – Post – Synthetic Modification

PXRD – Powder X-Ray Diffraction

Py – Pyridine

Q_{st} – Isosteric heat of adsorption

SALE – Solvent – Assisted Linker Exchange

SALI – Solvent – Assisted Ligand Incorporation

SBUs – Secondary Building Units

SCN – Thiocyanate

SDWA – Safe – Drinking Water Act

SLI – Sequential Linker Installation

SMZ – Sulfamethoxazole

TGA – Thermo – Gravimetric Analysis

TOF – Turnover Frequency

TSA – Temperature Swing Adsorption

UiO – University of Oslo

UiO-66 – $Zr_6O_4(OH)_4(BDC)_6$

UiO-67 – $Zr_6O_4(OH)_4(PhPh)_6$

UiO-67-TpTp – $[Zr_6O_4(OH)_4(PhPh)_5(TpTp)]$

UiO-67TzTz – $[Zr_6O_4(OH)_4(PhPh)_5(TzTz)]$

UMCM-1 – University of Michigan Crystalline Material -1; $Zn_4O(BDC)(BTB)_{4/3}$

UV – Ultraviolet

VSA – Vacuum Swing Adsorption

VT-PXRD – Variable – Temperature Powder X-Ray Diffraction

XPS – X-Ray Photoelectron Spectroscopy

XRF – X-Ray Fluorescence

ΔH_{ads} – Isosteric enthalpy of adsorption

ΔH_{des} – Isosteric enthalpy of desorption

$\lambda_{max,em}$ – Maximum λ of emission

Background: the rise of Metal-Organic Frameworks

This thesis is based on the synthesis and applications of Metal-Organic Frameworks (MOFs), a relatively new class of compounds that has witnessed an extraordinary boost in the last 30 years, mostly due to their incredible properties and multiple fields of application. MOFs have marked the birth of a completely new field of chemistry called "reticular chemistry".

In this first part, I would like to retrace the story behind the birth and the development of reticular chemistry, a path full of challenges but also full of scientific innovations.

The best way to start this "journey back in history" is to explain what reticular chemistry is. According to Professor Omar M. Yaghi (one of the most relevant experts in this field), *"Reticular chemistry is concerned with linking molecular building blocks (molecules and clusters) through strong bonds to form crystalline extended structures in a designed manner"*[1]. In this simple definition the three milestones of the field are summarized: (I) the structure of the framework is controlled by the geometry of the molecular building blocks; (II) the formation of strong bonds enhance the (chemical, thermal and architectural) framework stability and (III) the structure should be crystalline to ensure the possibility to characterize it by diffraction techniques[2]. With reticular chemistry, chemists tried to push the limits of organic synthesis creating infinite 2D and 3D structures and going beyond molecules (0D) and polymers (1D). From this viewpoint, the ordered and regular combination of inorganic metal ions or clusters and organic polytopic linkers generates the so-called Metal-Organic Frameworks. MOFs are a class of 3D crystalline materials that possess many interesting properties like high stability, ultra-high surface area and permanent porosity.

Even if MOFs chemistry has a relatively recent origin, the basis of this new field dates back to centuries ago. In fact, reticular chemistry stems from coordination chemistry. The first example of coordination compound reported is the "Prussian blue" a pigment firstly synthesized by chance in Germany in the eighteenth century[3]. At that time however, due to the fortuitous discovery, nothing was known about its structure or chemical composition and, for this reason, any hypothesis about its behavior was based only on a physical observation (its deep blue color). A step forward was made with the work of Alfred Werner whose experiments led to the understanding of the connectivity and geometry of complexes[4].

Werner's work provided new and useful information about molecular structures, inspiring the work of other chemists to extend the coordination chemistry from the molecular level (0D) to structures with higher dimensionality (2D and 3D).

A few years later (1897), Karl A. Hofmann published a new crystalline material of formula $[Ni(CN)_2(NH_3)](C_6H_6)]$ (the Hofmann clathrate) by diffusion of benzene into an ammonia solution of $Ni(CN)_2$ [5]. After the resolution of the crystal structure made by Herbert M. Powell in 1952 [Figure 1], it was found that the Hofmann clathrate was an extended coordination compound with a 2D structure in which the Ni^{2+} ions were linked by CN^- anions[6]. The cavities between the 2D layers were able to trap the solvent molecules (benzene) as guest species. However, structural collapse was observed upon removal of these molecules. This behavior witnesses the importance of the guest molecules for the formation of the material.

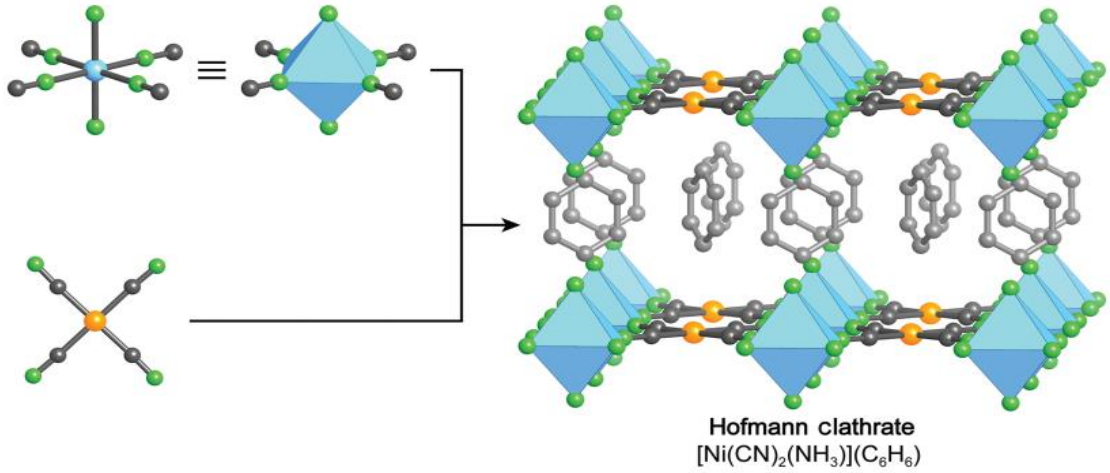

Figure 1: Representation of the crystal structure of the first Hofmann clathrate as determined in 1952 . Color code: Ni – blue and orange, C – grey, N – green. [1]

After the structural elucidation of the Hofmann clathrate, the interest around extended coordination compounds grew really fast, leading to the synthesis of a lot of new Hofmann clathrate-type compounds.

It is over the following years that chemists started to insert organic linkers between the layers of the coordination compounds and, consequently, to link directly metal ions through polydentate organic linkers giving rise to coordination networks (or polymers)[7]. These networks were classified using the geometric principles established by Alexander Wells that consider the nets only on the basis of the nodes and the links without considering the chemical information[8]. The linkage between metal centers and organic linkers leads to the formation of frameworks

containing open space. However, the presence of this open space could generate the so-called "interpenetration", in which another framework is mechanically stuck inside the first framework open space[9]. Moreover, these coordination networks are kept together by non-covalent weak metal-linker interactions, resulting in a low chemical and architectural stability. To overcome this aspect, in 1995 Omar M. Yaghi first used charged chelating linkers for the synthesis of coordination polymers. The use of these linkers provides two major advantages: (I) the stronger metal-linker bond enhances the thermal and chemical stability; (II) the charge of the linker can balance the charge of the metal center avoiding the formation of ionic networks and the need of counter-ions inside the pores. Yaghi and coworkers reported the first solvothermal synthesis of a cobalt(III) compound using benzene tricarboxylate (H_3BTC) as tritopic linker and pyridine (Py) as solvent to synthesize the 2D layered structure $Co(BTC)(Py)_2$, known to history as MOF-1[10] [Figure 2]. As expected, this compound has great stability and it is formed by alternating layers of pyridine and Co-BTC that remain unaltered even after pyridine removal (*i.e.*, the structure does not collapse).

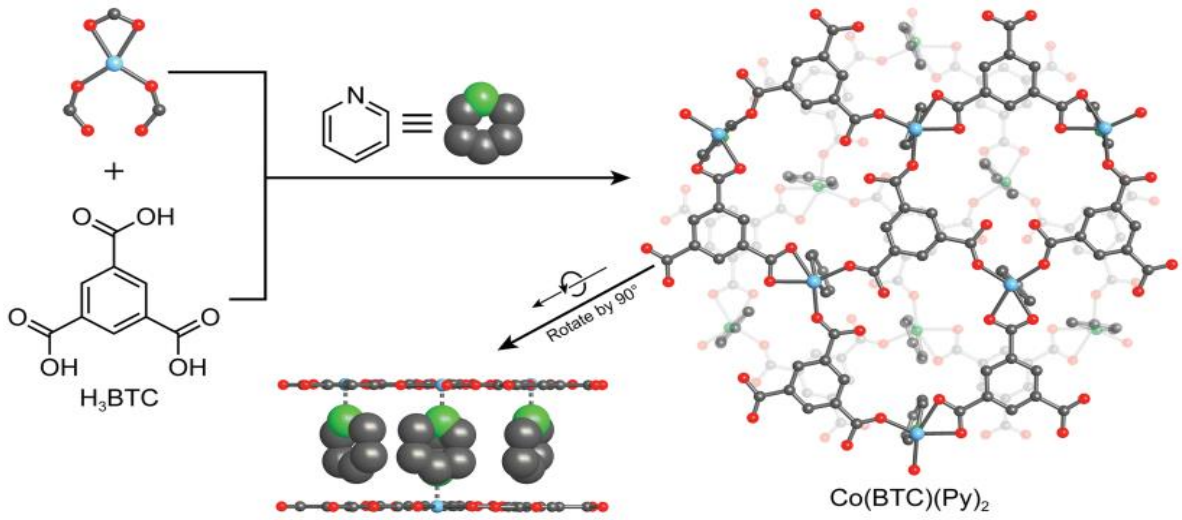

Figure 2: The 2D layered structure of MOF-1 [$Co(BTC)(Py)_2$]. Color code: Co – blue, C – grey, N – green, O – red. [1]

This state of affair continues until 1998 when the single metal ion nodes were replaced by polynuclear clusters named Secondary Building Units (SBUs) in order to further increase the network stability. These clusters lock the metal ions in fixed positions, providing rigidity and directionality to the whole structure. SBUs are usually formed *in situ* under specific reaction conditions. The concept of using SBUs was first realized by Yaghi and coworkers with MOF-2. This compound was synthesized by a vapor diffusion of a trimethylamine/toluene mixture into a

solution of $Zn(NO_3)_2 \cdot 6H_2O$ and 1,4-Benzenedicarboxylic acid (H_2BDC) in dimethylformamide (DMF)/toluene to afford a 2D crystal structure of minimal formula $Zn(BDC)(H_2O)$[11]. MOF-2 has a layered structure of "paddle wheel" $Zn_2(RCOO)_4$ SBUs connected by ditopic BDC linkers to form layers with a square grid topology [Figure 3].

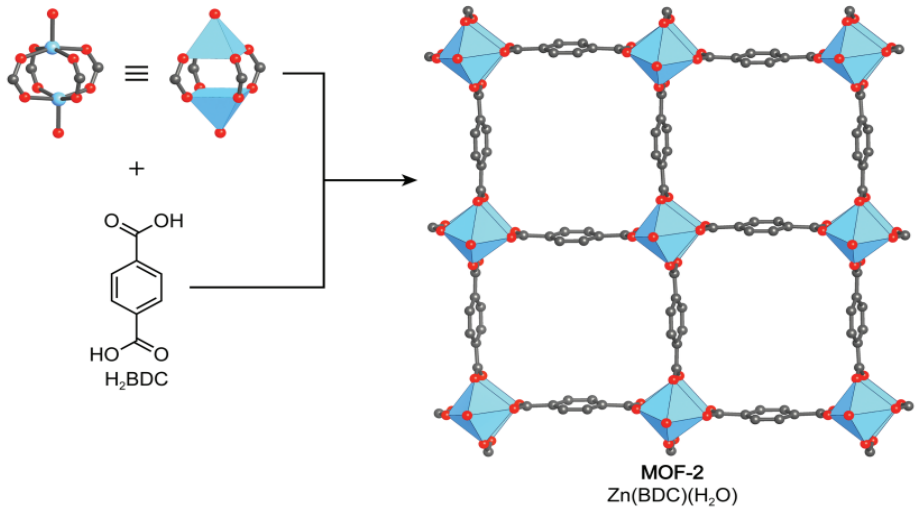

Figure 3: Crystal structure of MOF-2 [$Zn(BDC)(H_2O)$]. The ditopic paddle wheel SBUs are connected by BDC linkers. Color code: Cu – blue, C – grey, N – green, O – red. [1]

With MOF-2 it was reached an important turning point for the chemistry of MOFs: the high stability imparted by the paddlewheel SBUs allowed for a complete DMF removal from the pores without causing a structural collapse. Then, the nitrogen adsorption isotherm recorded at 77K showed the proof of the material permanent porosity. Moreover, the "new use" of SBUs with different geometry and connectivity allows for the formation of a variety of different MOFs structures. The latter aspect (*i.e.* the possibility to design new stable and permanently porous structures) was precisely what generated chemist's interest around the development of MOFs chemistry.

Starting from these geometrical considerations, in 1999 Yaghi and coworkers tried to first synthesize a MOF with a three-dimensional structure. The key idea at the base was to use a particular zinc cluster as SBU for the synthesis of this new MOF. The choice fell on zinc acetate, a tetra-nuclear cluster that possesses six acetates coordinated to a central $[Zn_4O]^{6+}$ core in an octahedral coordination geometry (the acetates are bridging adjacent Zn ions along the tetrahedron edges). The synthesis of $Zn_4O(CH_3COO)_6$ was well known at that time and foresee the addition of a small amount of hydrogen peroxide to an acetic acid solution of a zinc salt[12]. Starting from this point, Yaghi and coworkers decided to add some hydrogen peroxide to the

same procedure used for the synthesis of MOF-2. In this way, they wanted to favor the formation of the octahedral SBUs instead of the $Zn_2(RCOO)_4$ paddle wheels. However, even using this approach the only product obtained was MOF-2. Interestingly, it was a student who noticed that after the reaction some small cube-shaped crystals were formed on the meniscus of the solvent. The X-ray analysis of these crystals showed a different structure from that of MOF-2: four tetrahedral [Zn_4O] units linked together by bridging BDC linkers to form a 3D primitive cubic (pcu) framework [Figure 4]. This new compound named MOF-5[13] showed some incredible properties: not only high thermal and architectural stability (no structural collapse even after the complete removal of guest molecules, the biggest worry for this kind of large open structure), but also presence of large pores of 8.0 Å with no walls (wide open structure where solvent molecules can move easily) and an unprecedented surface area of 2900 m^2/g, a way higher with respect to all the other zeolites or porous materials known at that time.

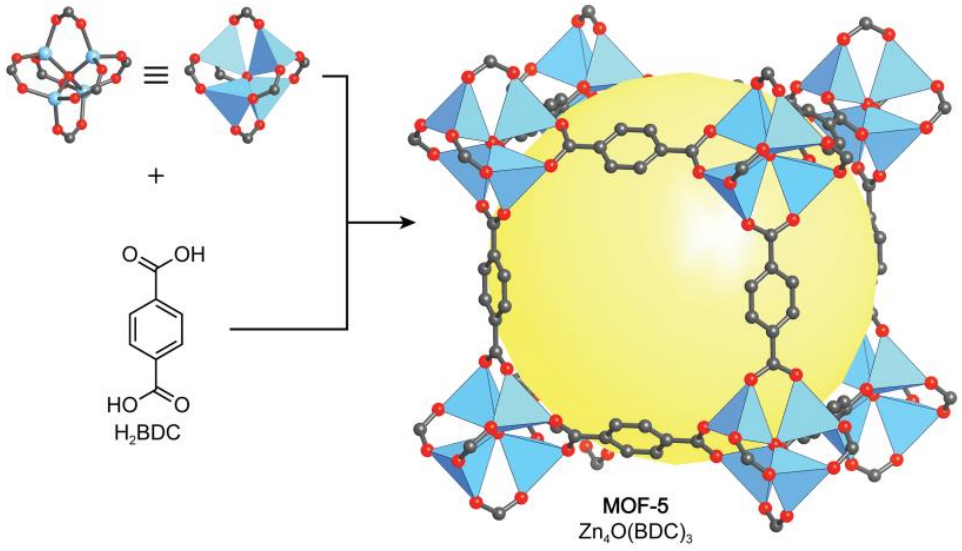

Figure 4: Crystal structure of MOF-5 [$Zn_4O(BDC)_3$]. The yellow sphere represents the largest sphere that can be inserted inside the pores of the structure. Color code: Zn – blue, C – grey, O – red. [1]

MOF-5 established itself as a milestone in the field of reticular chemistry, boosting MOF research all over the following decades and to date.

In this short paragraph I wanted to highlight the steps through which MOFs have been established during recent years, from the first simple 2D structures to the huge number of complex 3D structures of nowadays. The rapid evolution in this field is also witnessed by the changes in the definition used to describe MOFs. At first, in fact, the term “Metal-Organic framework” was coined to describe the overall composition of the structure (presence of metal

ions and organic linkers) and its character (a framework, precisely)[14]. Since then, the definition began to be expanded to take into consideration also the other aspects that are characteristics for MOFs like, for example, properties and structural attributes. Nowadays, the recognized IUPAC definition for MOF is *"A coordination network*[1] *with organic ligands containing potential voids*[15]*".*

[1] A coordination compound extending, through repeating coordination entities, in one dimension, but with cross-links between two or more individual chains, or a coordination compound extending through repeating coordination entities in two or three dimensions.

Chapter 1

INTRODUCTION

In the previous paragraph, I reported the historical steps that have led to the discovery and spread of MOFs. Within this chapter, it is time to go deeper inside the chemistry of this class of materials and understand why they are attracting increasing attention in the last decades.

1.1. Metal-Organic Frameworks

MOFs, as already said, are made of metal ions or clusters (SBUs) linked together by organic linkers to form a three-dimensional framework that possess a permanent porosity[16]. The metallic nodes usually consist of polyatomic groups (for example the aforementioned $[Zn_4O]^{6+}$ tetrahedron) that enhance stability. The linkers are organic polyanions, so the overall framework is neutral, and the interstitial space can be empty because there are no counter-ions inside. The whole structure is characterized by strong covalent bonds high in energy, for this reason MOFs possess an excellent chemical and thermal stability[17]. Moreover, these bonds guarantee a stable architecture of the framework which does not collapse after the removal of the solvent trapped inside.
MOFs can be constructed starting from a huge number of linkers and combinations with different metallic nodes, synthesizing a virtually infinite number of new structures [Figure 5]. Furthermore, linkers can be prepared with a tailor-made approach adding specific functionalities useful for a certain application [see chapter 3 – MOFs applications].

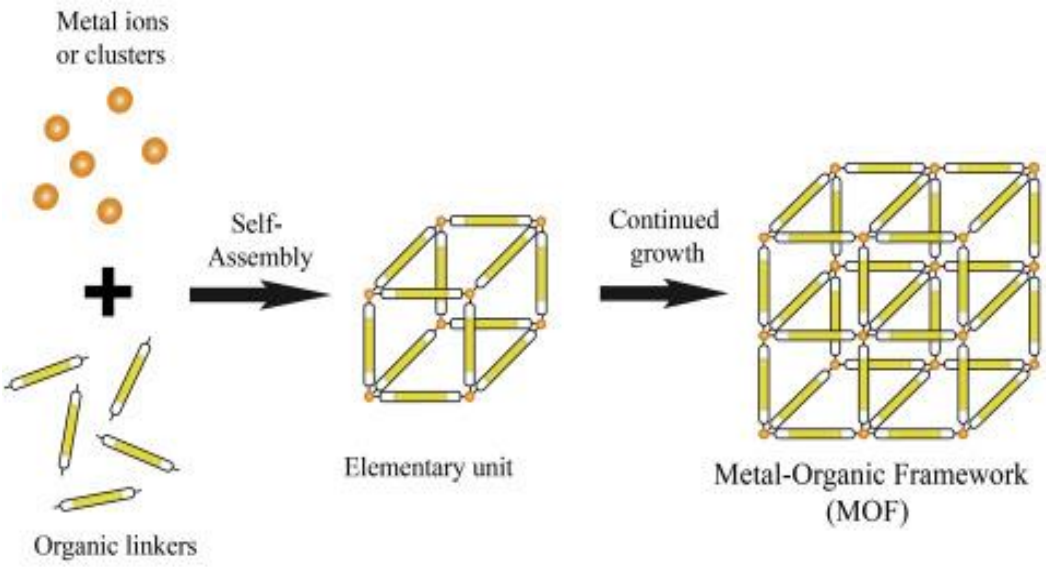

Figure 5: schematic representation of MOFs assembly.

One of the most important properties of MOFs is the surface area, which is strictly related to the linkers length. MOFs usually have ultra-high surface areas (even more than 7000 m^2/g)[18], exceeding those of other porous materials as activated carbons and zeolites and making them suitable to take up voluminous amounts of gases such as carbon dioxide, methane and hydrogen[19]. To enhance MOFs surface area, it is necessary to use longer linkers. However, the large space inside the framework may result in an interpenetration[2] of the structure that reduces the free space available [Figure 6]. The best way to prevent interpenetration is to synthesize a MOF whose topology would require the second framework to assume a different topology[20].

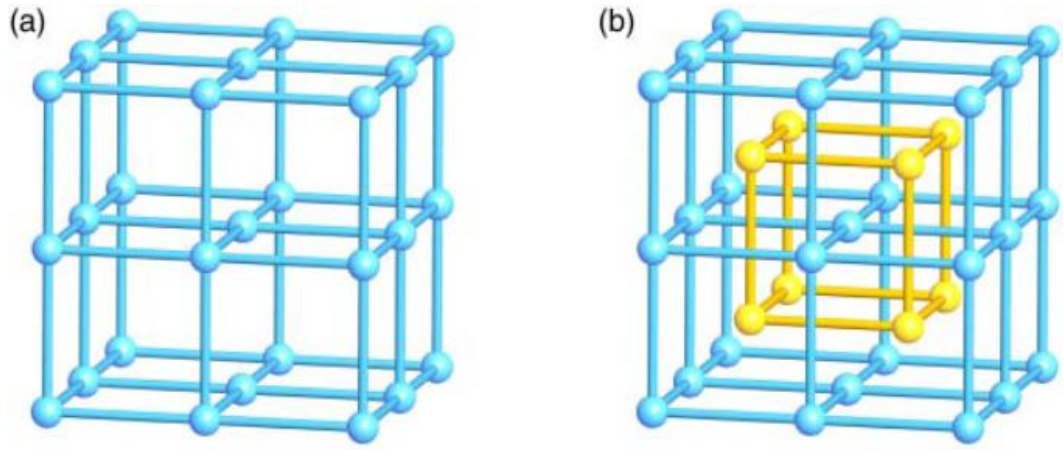

Figure 6:examples of a normal cubic framework (a) and an interpenetrated cubic framework (b).[1]

Isoreticular expansion (i.e. changing the linker length but keeping the same network topology) gives birth to the so-called *isoreticular-MOFs* (IRMOFs) [Figure 7]. IRMOFs are featured by larger pore apertures when built using a longer linker, allowing the inclusion of larger molecules (like proteins) inside the framework. In addition, it is possible to use the same linker but chemically modified to include different functionalities making functionally distinctive structures with the same topology[21].

[2] Phenomenon by which two or more frameworks intertwine together.

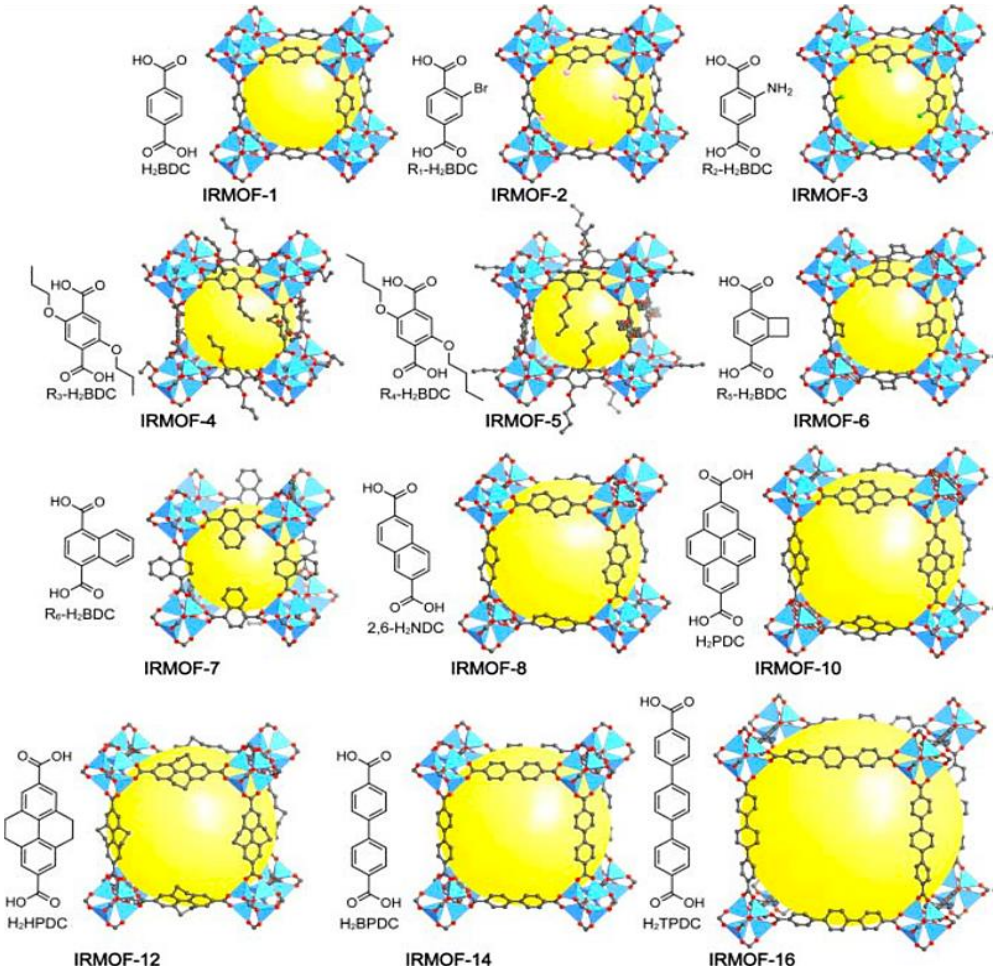

Figure 7: Isoreticular series based on MOF-5 (IRMOF-1). In the picture are shown the linkers used and, on their right, the corresponding obtained framework. Color code: Zn – blue, O – red, C – grey. [1]

Another distinctive trait of MOFs chemistry is that it is possible to synthesize structures where more than two kinds of "building units" (SBUs and linkers) are present together in the same framework. When more than one SBU is present we referred to it as *"complexity within frameworks"* because the crystallographic position of every unit is well defined. If the SBUs are generated by different metals, the resulting structure is called "Mixed-metal MOF" [see paragraph 1.1.2 – Mixed-metal MOFs]. The other case is when more than one linker (which individually would form different MOFs but with the same topology) are combined in the same framework. In this case, what is formed is a MOF with the same parent structure but that contains all the different linkers. These MOFs are called "Multivariate MOFs" (MTV-MOFs) or "Mixed-linker MOFs" and it is referred to as "*heterogeneity in frameworks*" because it is unknown the spatial arrangement of the different linkers [see paragraph 1.1.3 – Mixed-linker MOFs].

The use of more than one metal ion or linker or even the use of differently functionalized linkers to synthesize a new MOF it is not always possible *"a priori",* due to the susceptibility of these

building blocks to the changes in reaction parameters (geometry of SBUs and nature of the linkers, to mention a few). Fortunately, it is possible to modify the MOF framework structure also after its synthesis. This method is called "Post-Synthetic Modification" (PSM) and allows for the functionalization of the as-synthesized MOF while its fundamental properties (porosity, crystallinity and structure) remain unaltered [see paragraph 1.1.4 – Post-synthetic modification]. All these characteristics give to MOFs the aforementioned extraordinary properties like porosity, high surface area, the possibility to include on the linkers' skeleton suitable functional groups and chemical and thermal stability. For this reason, MOFs are widely exploited for a number of practical applications like gas storage and separation[22], catalysis[23], carbon capture and reutilization[24], luminescence[25], chemical sensing[26], drug delivery[27] and many others [see chapter 3 – MOFs applications]

1.1.2. Mixed-Metal MOFs

The term "mixed-metal" is referred to MOFs that contain in their framework at least two different metal ions in their nodes. This kind of compounds can be prepared both through direct synthesis and PSM.

The first case implies the use of multiple metal salts for the synthesis. To have a controlled synthesis, however, it is important that the metal cations have a similar reactivity otherwise a single-metal MOF can be obtained. Considered this, usually the direct synthetic strategy results in a homogeneous dispersion of the different cations that are randomly distributed over the structure. In one of his works, Omar M. Yaghi demonstrated that it is possible to incorporate up to ten metals in the same structure[28]. This result was obtained through a solvothermal synthesis of a varying amount of Mg, Ca, Sr, Ba, Mn, Fe, Co, Ni, Zn and Cd metal salts with the linker 2,5-dihydroxyterephtalic acid (H_4DOT). The resulting structure is the same as that of MOF-74 (a M(II) MOF with H_4DOT linker) but with different metal nodes (mixed-metal-MOF-74; MM-MOF-74) [Figure 8]. The final molar ratio of the metal ions is influenced by some parameters like the coordination number (Ca, Sr and Ba are less present because they tend to have coordination number 8 instead of 6), the solubility of the metal salts and the reactivity of the cations.

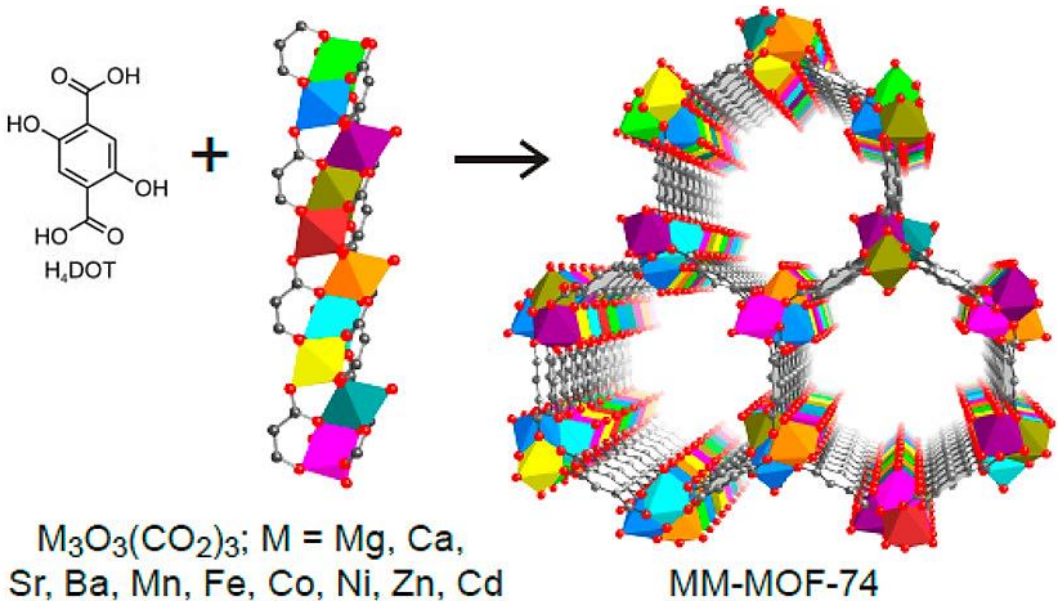

Figure 8: Organic linker, SBUs and crystal structures of MM-MOF-74 with ten different metals represented by different colors: Mg - light green, Ca - yellow, Sr - cyan, Ba - light brown, Mn - violet, Fe - red, Co - purple, Ni - water green, Zn - blue and Cd - orange. [28]

Another synthetic approach to obtain mixed-metal MOFs is the post-synthetic modification. In this process, usually, the MOF is soaked in a metal ion solution at a certain temperature for some days. The amount of metal ions replaced in the framework depends on the time and the concentration of the metal in the solution. The PSM method, unlike the direct synthesis, allows to incorporate metal ions that could not be employed in the synthesis of a "pure-phase" MOF. Some metals, for example V^{2+} and Ti^{3+}, are actually incompatible with the usual synthetic conditions. The method used to exchange metal ions is called *"post-synthetic ion metathesis"* [29].

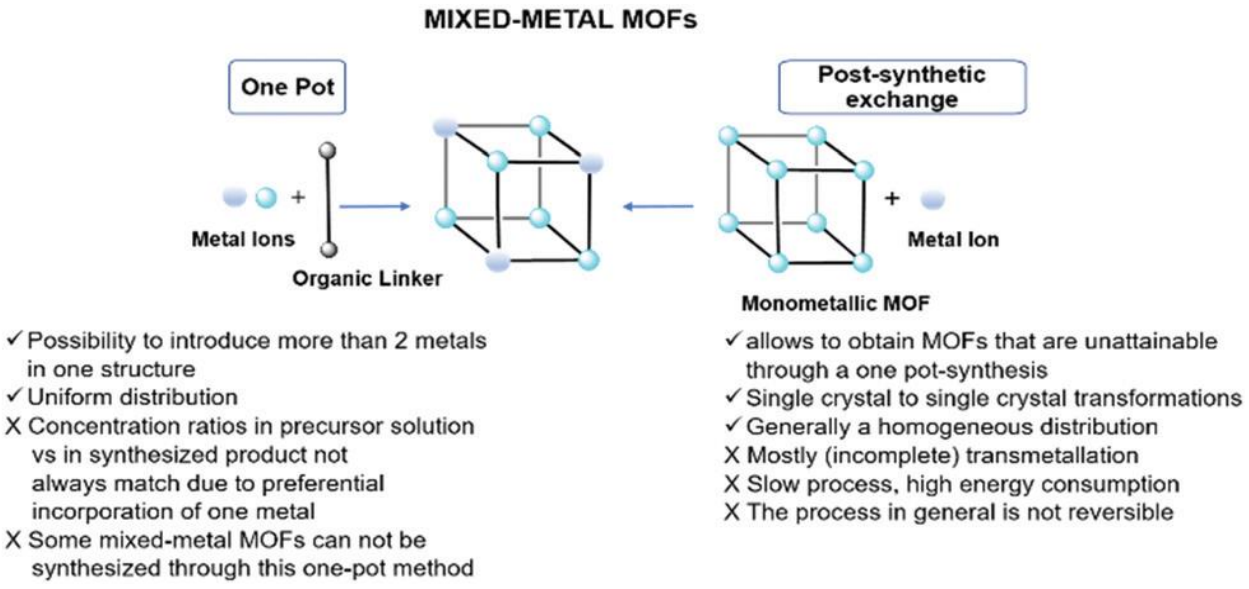

Figure 9: Schematic representation of the different methods to obtain mixed-metal MOFs with pros and cons.

As for the resulting structure, the metal ions can be distributed inside the SBUs in two distinct ways: (I) every SBU is composed only by a single metal forming domains (typical of metals with significant differences in radius and electronegativity) or (II) the different metals are mixed and present inside the same SBU (typical of metals with same radius and electronegativity).

The presence of more metal ions inside the framework can be useful for particular applications because they can enhance some properties of the MOF. In catalysis, the presence of more than one active site can help in the activation of the reactants (synergistic catalysis)[30]. In gas sorption and storage, the presence of another metal ion can improve the affinity and the selectivity toward a certain gas[31]. In luminescence applications, mixed-metal MOFs (in particular with lanthanides) show properties that exceed that of the homometallic counterparts making them potential candidates for smart materials[32].

1.1.3. Mixed-Linker MOFs

As for the mixed-metal MOFs, we call "mixed-linker" those MOFs that possess more than one linker type in the framework. Even in this case, the synthesis can be made through a direct approach by mixing the different linkers in the reaction solvent or by PSM exchanging the linker in an already formed structure with another one.

The linkers can have either similar metrics and linking geometry (isostructural approach) or different linking geometries (heterostructural approach).

The latter is the case of UMCM-1 (University of Michigan Crystalline Material-1) a Zn MOF synthesized from the ditopic H_2BDC linker and the trigonal tritopic 1,3,5-Tris(4-carboxyphenyl)benzene (H_3BTB) linker [Figure 10]. These linkers alone can react, under almost the same conditions, with zinc to form MOF-5 and MOF-177 ($Zn_4O(BTB)_2$) respectively, two MOFs that possess different topology. However, if they are mixed together, the resulting structure is UMCM-1 where the octahedral [$Zn_4O(RCOO)_6$] SBUs are connected with four BTB and two BDC linkers[33].

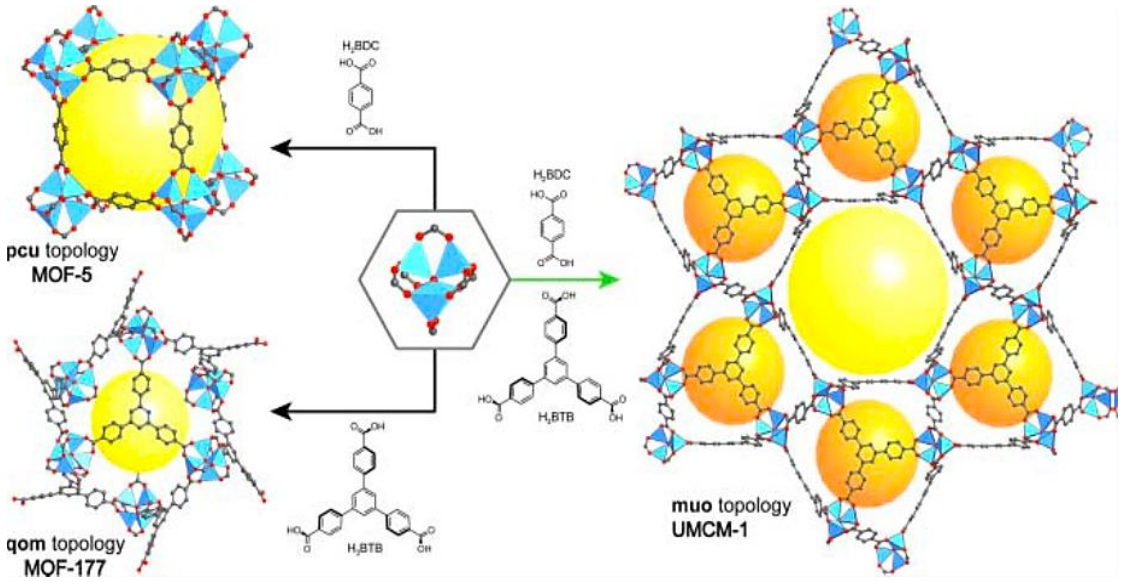

Figure 10: crystalline structure of the two "single-linker" MOF-5 (H_2BDC) and MOF-177 (H_3BTB) and of the "mixed-linker" MOF UMCM-1. Color code: Zn – blue, C – grey, O – red. [1]

The isostructural approach instead makes use of interchangeable linkers and produces MTV-MOFs. In this case, all the linkers alone would form different MOFs with the same topology. Mixing the linkers together provides a framework with the same topology as the parent MOFs but containing all the different linkers within the same solid phase. Usually, linkers with the same backbone but different functional groups are used in this synthesis. Since the linkers usually have no topological preference in the position occupied in the crystal structure, the result is a spatially undefined linkers arrangement. The first example of multivariate-MOF reported is the MTV-MOF-5 in which a number of functionalized X-H_2BDC-derivative linkers (X= H, NH_2, Br, Cl_2, NO_2, $(CH_3)_2$, C_4H_4, $(OC_3H_5)_2$, and $(OC_7H_7)_2$) were used to synthesize new MOF-5-type structures[34]. One of the structures shows up to eight different linkers in the same framework. The resulting material is isostructural to MOF-5 and keep both crystallinity and microporosity [Figure 11]. The arrangement of the linkers can follow a random distribution, a clustering of functionalities or an alternating pattern. The distribution depends on the chemical nature of the linkers: some favor the formation of clusters (-CH_3), others a random arrangement (-NO_2).

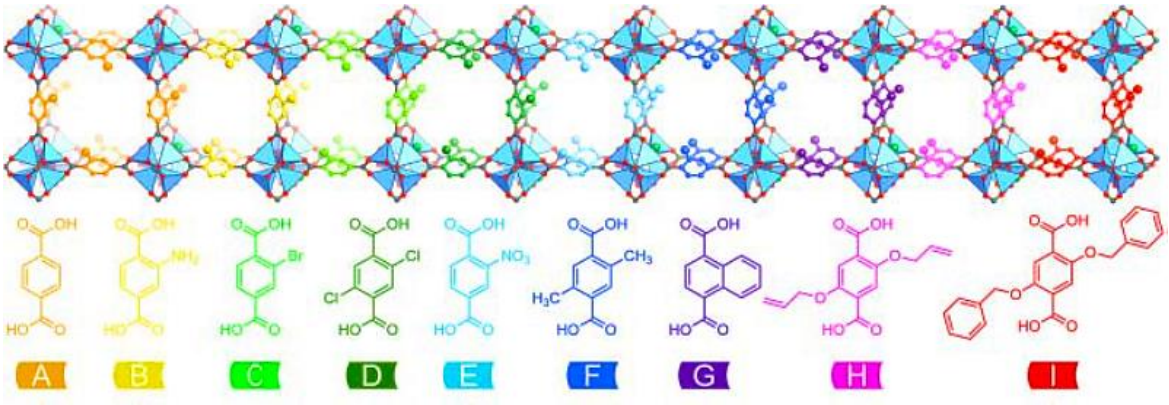

Figure 11: linkers structures and combinations to prepare MTV-MOF-5 with up to eight different H_2BDC derivatives. [34]

Another class of mixed-linker MOFs is the "pillared-layer" MOFs in which a second linker (the pillar) is inserted as support of a 2D organic layer to form a 3D structure [Figure 12]. Usually, the pillars are O-donor or N-donor linkers (as 4,4'-bipyridine) while the organic layer is composed by SBUs linked together by carboxylate linkers[35]. The variation of the pillar size (or the use of a functionalized pillar) tunes the framework properties (mainly the pore size).

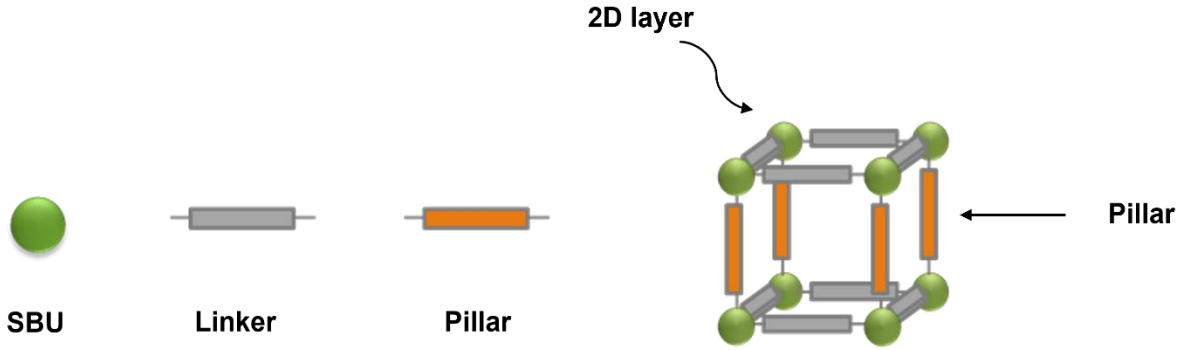

Figure 12: Schematic representation of a pillared-MOF structure.

The inclusion of more than one chemically distinct linker in the framework may impart new physical and chemical properties that go beyond the sum of those of the single components (synergistic effect). For example, the MTV-MOF-5 materials show better gas sorption properties with respect to the parent MOF-5, due to the presence of a larger number of chemically different adsorption sites inside the framework pores [36].

1.1.4. Post-Synthetic Modification

The isoreticular principle allows to synthesize MOFs using linkers that can be functionalized before the synthesis. However, the pre-synthetic functionalization of MOFs is a method that suffers from some limitations that make it difficult to be generally applicable. In fact, the formation of a MOF is influenced by the reaction parameters such as the composition of SBUs, the geometry and the chemical nature of the linker, so the functionalities present on the linker do not have to interfere with the formation of the MOF. To overcome this limitation, it is possible to use a process called "post-synthetic modification" (PSM)[3] that permits the functionalization of an already synthesized MOF while retaining the crystallinity, the structure and the porosity of the parent MOF. With PSM it is possible to exchange or add framework constituents in a controlled manner, either linkers or metal ions. In this way, it is achievable to synthesize structures inaccessible through direct synthesis[37].

In a previous section [see paragraph 1.1.2. – Mixed-metal MOFs], I have already talked about the post-synthetic method to prepare MOFs with different metals in the SBUs, so I will not spend more time on it.

Another PSM approach is to exchange the linkers that constitute the framework of a particular MOF. This is a good method to prepare mixed-linker MOFs. To do that, it is possible to use a technique called "Solvent-Assisted Linker Exchange" (SALE) [38]. SALE involves the soaking of the MOF in a concentrated solution of a different multitopic linker at a certain temperature and for a long time. Even the most robust MOFs undergo linker exchange, because the energy difference between the two structures containing the similar linkers is small enough to be overcome[39]. The main advantage in using this technique is that the parent and daughter material have the same topology, a feature that is not always possible to achieve with a *"de novo"* synthesis of a new MOF made with the new linker. For this reason, SALE it is often used to tune porosity and aperture size of MOFs[40]. An example of SALE application is represented by the work of Kim and coworkers[41] that performed a linker exchange on a UiO-66-based MOF (UiO = University of Oslo). UiO-66 is a zirconium(IV)-based MOF built with terephthalic acid (H_2BDC) with minimal formula $Zr_6O_4(OH)_4(BDC)_6$. In this work, they synthesize a UiO-66 mixed linker derivative starting from 2-amino-1,4-benzenedicarboxylate (NH_2-H_2BDC) and 2-bromo-1,4-benzenedicarboxylate (Br-H_2BDC) linkers. Both linkers give a UiO-66-type MOF (UiO-66-NH_2 and UiO-66-Br respectively)

[3] This principle is not new in chemistry, but it was already used for zeolites and mesoporous silica.

with the same topology as the parent MOF. After soaking UiO-66-Br for five days at different temperatures in an aqueous solution of NH_2-H_2BDC, a partial amino-/bromo-terephthalate exchange occurs producing the mixed-linker UiO-66-(Br)(NH_2) [Figure 13]. The extent of replacement was demonstrated to be temperature-dependent and goes from 9% at room temperature up to 76% at 85° C. Interestingly, in an opposite situation *i.e*. the replacement of NH_2-H_2BDC linkers in UiO-66-NH_2 by Br-H_2BDC results in a lower degree of exchange in the same conditions. This behavior can be explained by a combination of factors including solubility, donor ability and steric hindrance.

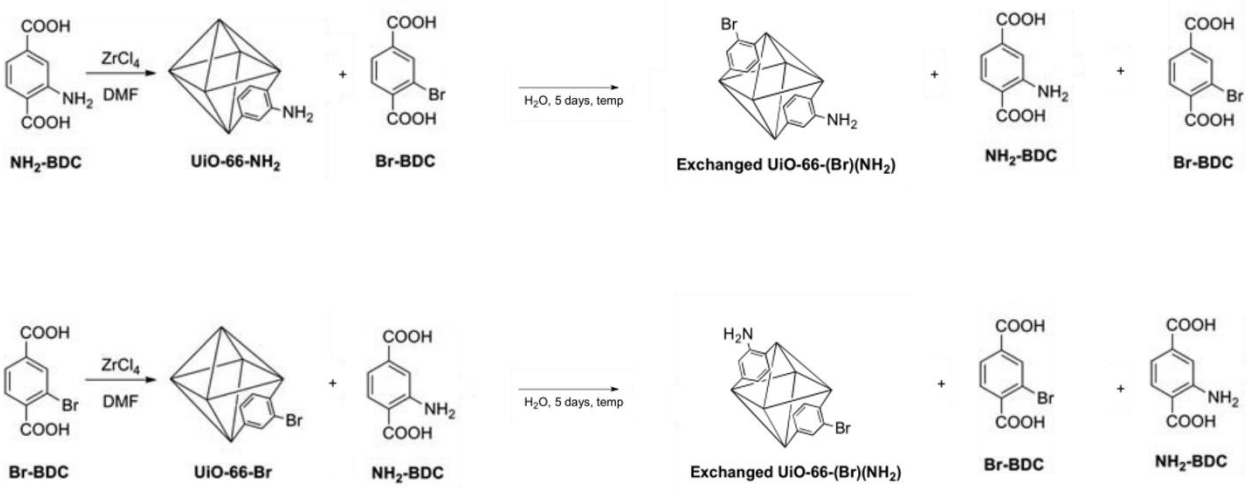

Figure 13: Linker exchange obtained using SALE technique. The uncomplete exchange arranges for the presence of both linkers in solution after the reaction. [41]

Another PSM technique is the "Solvent-Assisted Ligand Incorporation" (SALI) which involves the replacement of non-structural inorganic ligands with functional organic ligands. With this technique, the terminal -OH and -OH_2 groups that are present on the SBUs are (partially) replaced by a new charged ligand. Even in this case, the reaction foresees the soaking of the MOF in a solution of the ligand at an elevated temperature for a certain time. However, the reaction conditions are usually milder than those of the direct synthesis of a MOF, so it is possible to incorporate even "fragile" functionalities[42]. The main advantage of this technique is the possibility to include lots of different functionalities inside the framework, enhancing properties like gas adsorption or catalytic activity. The linkers can also be further modified using organic reactions even after inclusion[43]. An example of the application of SALI technique is given by Farha and coworkers who performed different ligand incorporations in the NU-1000 (NU= Northwestern University) MOF[44]. NU-1000 is a zirconium(IV)-based MOF made with

1,3,6,8-tetrakis(*p*-benzoic acid)pyrene (H_4TBAPy) with minimal formula [$Zr_6(\mu_3\text{-}O)_4(OH)_8(H_2O)_4(TBAPy)_2$]. Four -OH groups and four aquo ligands on the octahedral [Zr_6] SBUs equatorial region may undergo condensation reactions with extra carboxylic acids (with concomitant water elimination). In this work, they attached different perfluoro-alkane carboxylates of various chain lengths (1 to 9) to the nodes of NU-1000. To incorporate the ligands, NU-1000 was soaked in a 0.1 M DMF solution of the various ligands at 60°C for 24h. The number of ligands that can be incorporated is approximately 4 (lower for longer chains ligands) per [Zr_6] node (quantified by ^{1}H-NMR and ^{19}F-NMR signal integration of the digested sample) and it is not higher for longer times and higher temperatures [Figure 14]. As expected, the presence of bulky ligands inside the pores reduces the surface area of the MOFs with respect to NU-1000. However, measurements on CO_2 capture capacity reveal that the functionalized-MOFs adsorb higher CO_2 quantities because of the high C-F bonds polarity that improves the materials thermodynamic affinity for CO_2.

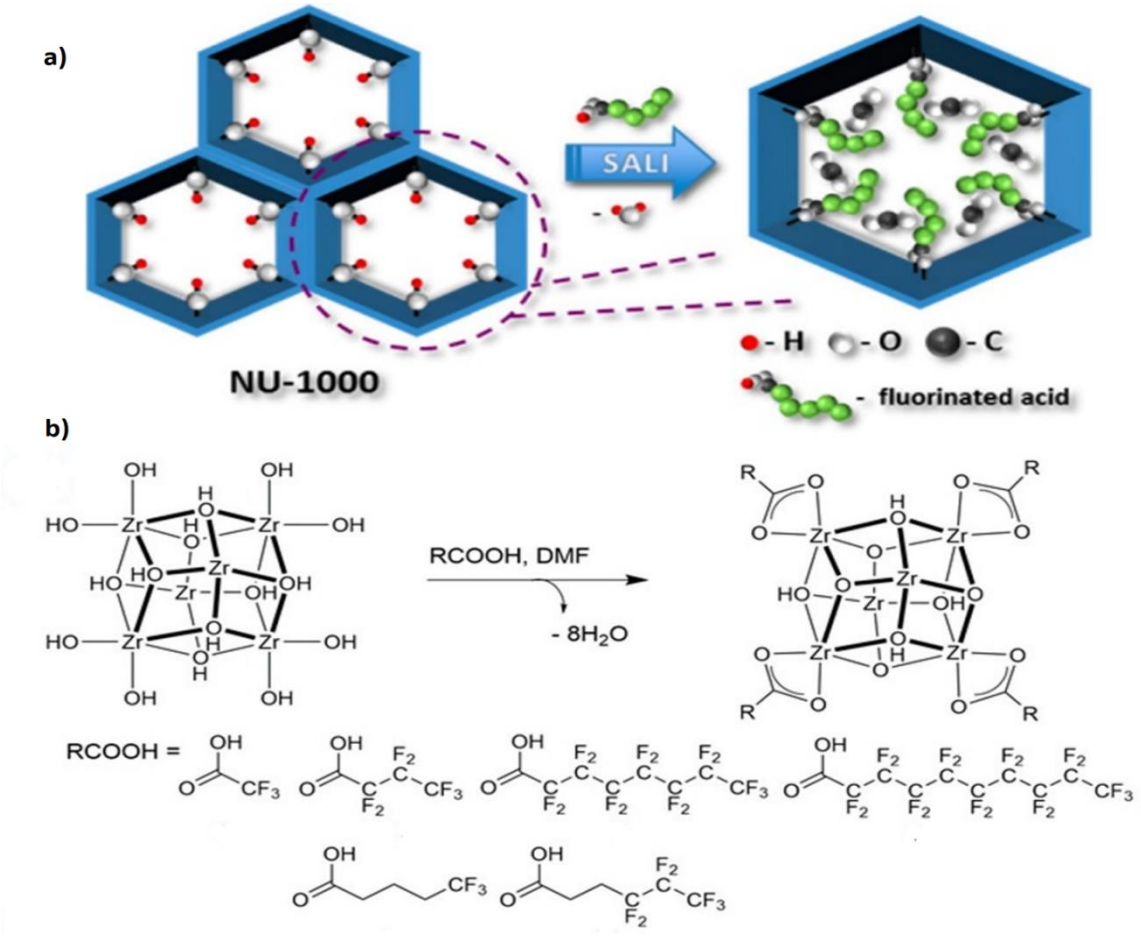

Figure 14: Schematic representation of SALI technique (a) and its application on NU-1000 SBU (b). [44]

The last PSM technique is the "Sequential Linker Installation" (SLI) that is used to transform MOF topology from the original to another one that is not accessible through direct synthesis. As for SALI, this technique involves the replacement of terminal -OH and -OH_2 groups with a ditopic linker that connects two different SBUs. This method is useful to synthesize MTV-MOFs with functionalities that are precisely positioned. An example of SLI is provided by the Porous Coordination Network-700 (PCN-700), a zirconium MOF and 2,2'-dimethylbiphenyl-4,4'-dicarboxylic acid (H_2Me_2BPDC) with formula $[Zr_6O_4(OH)_8(H_2O)_4(Me_2\text{-}BPDC)_4]$. The space between two adjacent Zr SBUs in the equatorial and in the axial plane form two different "pockets" suitable for the insertion of linear ditopic linkers. Two different linkers, H_2BDC and 2',5'-dimethy-terphenyl-4,4''-dicarboxylate (H_2Me_2-TPDC), were used based on their lengths (6.9 Å and 15.2 Å respectively). For the SLI approach, crystals of PCN-700 were exposed first to a DMF solution of H_2BDC and then to a DMF solution of H_2Me_2-TPDC at 75°C for 24h. The resulting compound, named PCN-703, it is characterized by the presence of all the three linkers for an overall composition that is $[Zr_6O_4(OH)_5(H_2O)(Me_2\text{-}BPDC)_4(BDC)(Me_2\text{-}TPDC)_{0.5}]$[45]. Interestingly, the sequence of the installation is crucial for the final reaction: if the H_2Me_2-TPDC linker is installed first (PCN-702), the remaining pockets will be stretched to a dimension bigger than H_2BDC making impossible its incorporation. In the other case, after the introduction of H_2BDC (PCN-701), the stretching of the pocket is low enough to permit to incorporate some H_2Me_2-TPDC linkers (but after every inclusion, other pockets will be stretched too much to permit any other linker installation).[Figure 15].

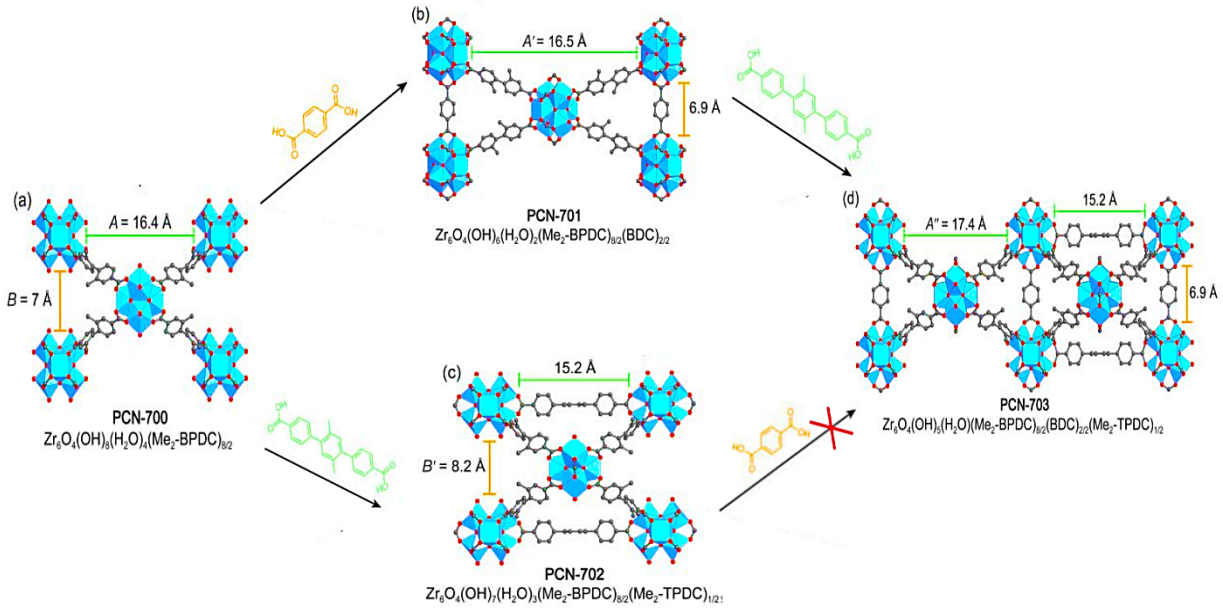

Figure 15: SLI in PCN-700 (a) obtained replacing the terminal -OH and -OH_2 ligands with the H_2BDC (PCN-701, (b)) and H_2Me_2-TPDC (PCN-702, (c)) linkers. PCN-701 can be further modified installing H_2Me_2-TPDC linkers in the pocket to obtain PCN-703 (d), whereas installation of H_2BDC linkers in PCN-702 is not possible. Color code: Zr – blue, C – grey, O – red. [1]

To evaluate the PSM outcome, it is possible to use a number of analytical methods. The most powerful is for sure the single-crystal X-ray diffraction that allows for the structural determination and the quantification of the functionalities. The reduction of the surface area indicates the presence of bulkier groups inside the structure that reduce the accessible pore volume. On the contrary, an increment of the surface area could be synonymous of the presence of longer linkers. The elemental analysis can be performed only on well-activated samples, otherwise the result may not be precise enough to determine the right chemical formula. The insertion of different metals can be traced by UV-Visible spectroscopy, while the formation of new bonds (not originally present in the MOF) can be confirmed by infrared spectroscopy. Also Nuclear Magnetic Resonance (NMR) can be used for this purpose. In this case, the sample is digested under acidic or basic conditions and then analyzed through NMR spectroscopy and peak integration.

1.2. Porosity of MOFs

One of the most important characteristics of MOFs is their high and permanent porosity that makes them useful in various applications as gas storage and separation, catalysis and sensing.
The porosity of a material is defined as the ratio between the volume of the pores and the total volume occupied by the solid. This concept was first introduced in 1896 for zeolites and experimentally proven in the middle of 1900s[46]. In coordination compounds, porosity was observed for the first time in some Werner-type complexes with formula β-$[M(PIC)_4(SCN)_2]$ (M= Ni^{2+}, Co^{2+} and PIC = γ-picoline; SCN = thiocyanate)[47]. These compounds possess empty voids inside the structure that are capable of reversible gas uptake. However, the structure is based on weak non-covalent interactions; thus, after every uptake and release cycle the porosity decreases[48]. It was Yaghi with MOF-2, which is characterized by a high mechanical and architectural stability, to report the first metal-organic extended solid with a proven permanent porosity[11]. To do that, he used a procedure already employed to prove permanent porosity in zeolites: the measure of a nitrogen adsorption/desorption isotherm at low pressure and temperature. Based on the requirements of the International Union of Pure and Applied Chemistry (IUPAC), to evaluate the permanent porosity of a compound it is necessary to measure at least three or more points of the nitrogen adsorption isotherm carried out at the N_2 boiling point (T= 77 K). Always according to IUPAC, porous materials can be divided into three different

classes on the basis of their pore size: (I) "microporous" if the pore diameters are smaller than 2nm, (II) "mesoporous" if the pore size is between 2 nm and 50 nm and (III) "macroporous" when the pores are larger than 50 nm[49] [Figure 16].

Figure 16: Classification of pores according to IUPAC. [1]

1.2.1. Gas Adsorption Measurements

Originally, the term "adsorption" was used in relation to the condensation of a gas on a flat surface differently from the "absorption" i.e. the entry of the gas in the bulk of a solid. However, in the case of porous materials, it is always referred to as adsorption or simply "sorption". Regardless the physical mechanism involved, the term sorption describes both the adsorption and the desorption (or negative adsorption) of a gas[50].

The adsorption of guest molecules onto the solid surface of a material plays an essential role for the definition of their properties. The interaction between the solid (the adsorbent) and the gas (the adsorbate) can be of physical nature (we referred to it as physisorption) or of chemical nature (chemisorption). Physisorption is an exothermic process characterized by weak interactions (Van der Waals forces) between adsorbent and adsorbate. For this reason, physisorbed molecules do not suffer of particular changes in their structure and are capable of forming more layers at high relative pressures. On the contrary, chemisorption is characterized by strong interactions (chemical bonds) between adsorbent and adsorbate. Therefore, the adsorbate molecules are strongly bound to the surface where further reactions (as dissociation) can take place. Consequently, chemisorbed molecules are confined in a monolayer.

In most MOFs, gas adsorption is actually a physisorption. The data are presented as "quantity of gas adsorbed" vs "relative pressure" at a constant temperature and the result is a plot called "physisorption isotherm" (or simply "isotherm"). The data can be reported both as volumetric (g/cm^3) and gravimetric (wt.%) uptake. IUPAC has defined six distinct isotherm types named from type I to type VI [Figure 17][51]. The isotherm shape is based on the nature of the adsorbent that can be microporous (type I), mesoporous (type IV and V) or macroporous (type II, III and VI)

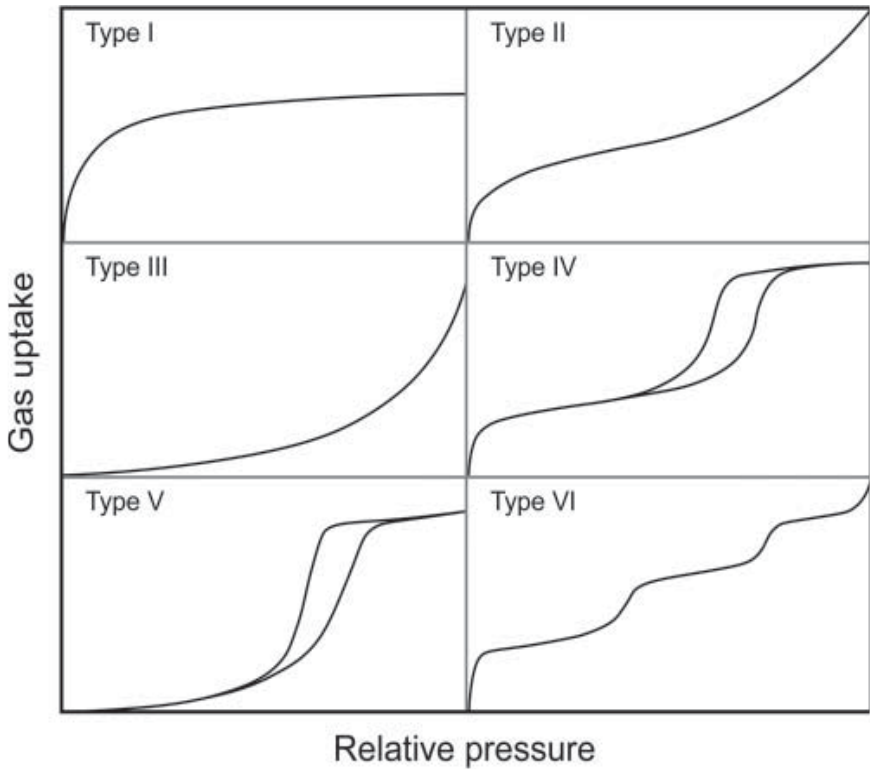

Figure 17: IUPAC classification of adsorption isotherms for microporous (type I), mesoporous (type IV and V) and macroporous (type II, III and VI) materials. [1]

In some cases, the desorption process does not proceed in the exact reverse pathway of the adsorption and a hysteresis (upper branch in Figure 17) is present. Usually, materials with pore width larger than 4 nm (isotherms of type IV and V) show hysteresis in the desorption branch[52]. The hysteresis loop shape is correlated to the material texture (pore geometry and size distribution). Typically, four diverse types of hysteresis can be found in porous materials [Figure 18]. IUPAC named them as follows: (I) H1 well-defined cylindrical pores or agglomerates of uniform spheres, (II) H2 ink-bottles pores, (III) H3 is associated with wide slit pores and (IV) H4 is relative to narrow-slit pores.

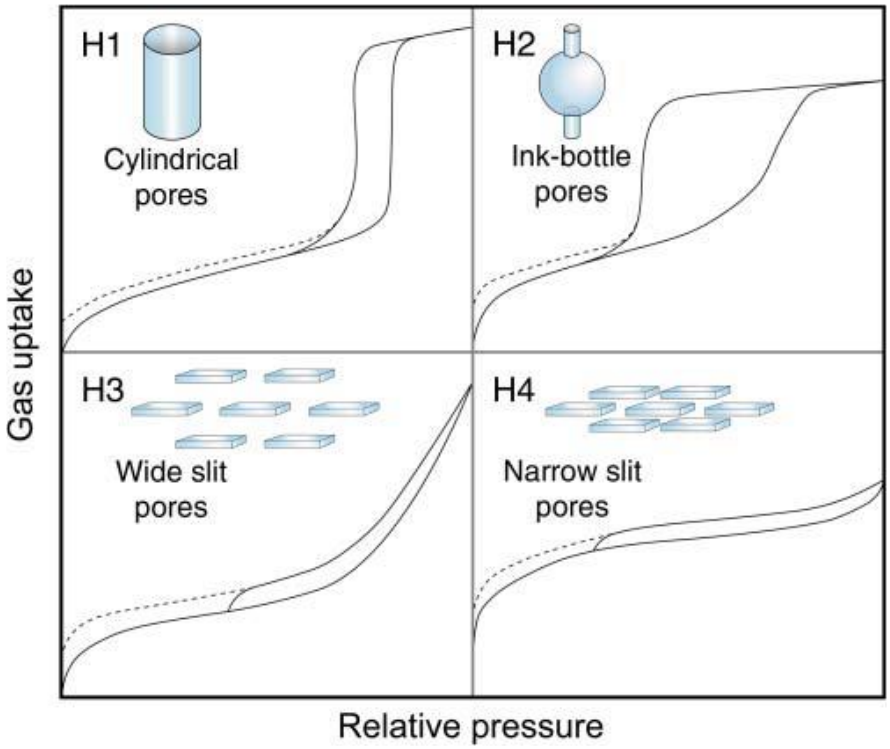

Figure 18: IUPAC classification of hysteresis loop according to the textural properties.[1]

Gas adsorption in a material is correlated to the pore type and to the gas pressure. For low-pressure values, only a little quantity of gas is adsorbed in the inner and in the outer surface of the adsorbent. Increasing the pressure, a monolayer of the gas is formed and the micropores are completely filled (corresponding to a plateau in the isotherm). As the pressure increases more, a multilayer adsorption takes place and also the mesopores are filled (corresponding to the steep ascent in the isotherm). Finally, if the appropriate pressure is reached, it is possible to fill also the macropores (corresponding to the last ascent in the isotherm) [Figure 19]. At lower pressures, the gas uptake is governed mainly by the surface area because the adsorbate molecules cover with a monolayer all the surface of the material, while the rest of the pores do not contribute to the adsorption.

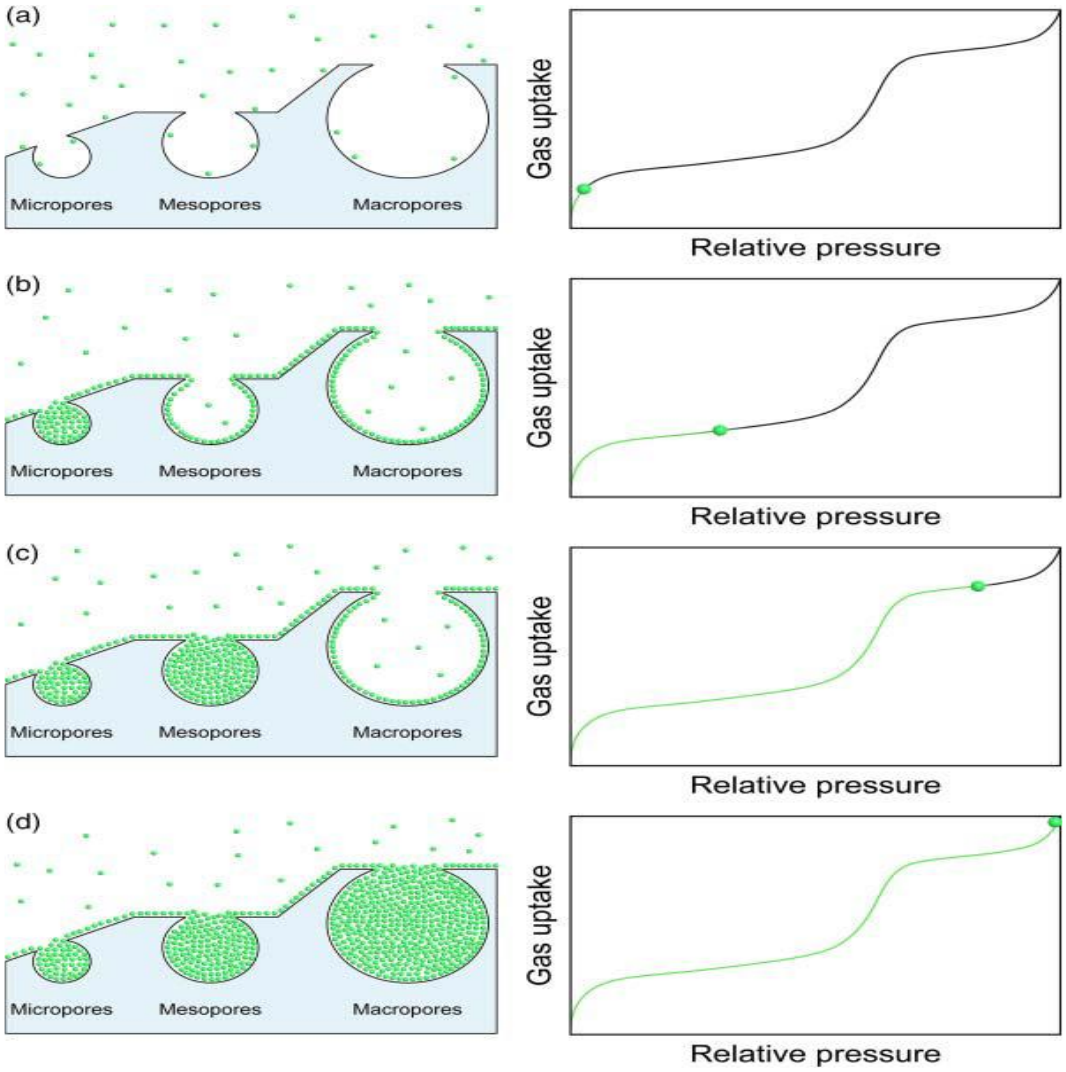

Figure 19: Adsorption process for a material containing micro-, meso-, and macropores and comparison with the isotherm plot. In the low-pressure region, the adsorption is mainly governed by the surface area (a). At slightly higher pressures, micropore filling is observed (b). A further increase in pressure affords the filling of the mesopores (c). Ultimately, when pressures close to the bulk saturation pressure are reached, also macropores are filled. [1]

To describe the adsorption phenomena in MOFs, two different models are commonly used: the Langmuir model and Brunauer-Emmett-Teller (BET) model. The key idea at the basis of the Langmuir model is to consider a plane surface with only one kind of adsorption sites where each adsorption site can hold only one adsorbate molecule[53]. Langmuir equation can be written as:

$$\theta = \frac{bp}{1+bp} \quad \text{where} \quad bp = Ke^{\frac{-E_A}{RT}}$$

Where θ is the number of occupied sites, b is the adsorption coefficient, K is the ratio between the adsorption (α) and desorption (β) coefficients, E_A is the activation energy, R is the gas constant and T is the temperature.

This model can be applied to describe gas adsorption in MOFs only if some assumptions are made: (I) the whole surface has the same adsorption energy for the adsorbate (all adsorption sites are equivalents), (II) the isotherm should presents a linear region at low pressures and a plateau when θ is equal to 1, (III) the ability of adsorption of a given site is independent from the filling of the neighboring sites and (IV) it is assumed that the adsorption can forms only a monolayer of the adsorbate[54]. All these considerations indicate that the Langmuir model can be applied for chemisorption, but not really for physisorption systems. However, many MOFs show a type I isotherm that is like that expected from Langmuir model, for this reason this model is often used to calculate the surface area of the porous materials. Nevertheless, the particular shape of the isotherm is associated to the filling of the micropores rather than to a monolayer adsorption, so the surface area calculated using this model is usually overestimated. The equation used to calculate the surface area (S_t) is:

$$S_t = N_m A_x = \frac{W_n \bar{\mathrm{N}} A_x}{\bar{\mathrm{M}}}$$

Where N_m is the number of adsorbate molecules present in a complete monolayer, A_x is their cross-section area, $\bar{M}$ is the molecular weight of the adsorbate and $\bar{N}$ is the Avogadro number.
On the contrary, the BET model represents an extension of the Langmuir model to multilayer adsorption. In fact, this is based on the observation that if the relative pressure (p/p_0) is higher than a certain value, physisorption is not limited to a monolayer[55]. BET equation can be applied for all the type of isotherms but, in the case of type I isotherms (the most common for MOFs), it is more complicated. In fact, it is difficult to differentiate between multilayer adsorption, monolayer adsorption and micropores filling[56]. In this case, it is better to use the term "estimated BET area" when we refer to the calculation of the surface area. The equation for BET model is:

$$\frac{p}{n(p_0 - p)} = \frac{1}{n_m c} + \frac{c - 1}{n_m c} * \frac{p}{p_0}$$

Where p is the pressure, p_0 is the saturation pressure of the adsorbate at the analysis temperature, n is the total amount of gas adsorbed at the corresponding p/p_0, n_m is the gas adsorbed by the monolayer coverage and c is a constant (BET constant) related to the energy of adsorption of the first layer.

The analysis of the experimental isotherm data using BET method is made by plotting $p/n(p_0-p)$ versus p/p_0. The resulting "BET plot" is a straight line. As a matter of fact, BET model is applicable only in the pressure region in which it is possible to obtain a straight line (usually at extremely low relative pressures). BET method is nowadays the most used one to determine MOFs surface area. In fact, despite some limitations, recent theoretical calculations showed that BET model provides surface area values that are well-acceptable[57].

Since the gas adsorption in MOFs is typically a physisorption process and therefore involves weak interactions, both the Langmuir and BET models can be used to evaluate the gas adsorption and the surface area (with the already reported limitations) [Figure 20].

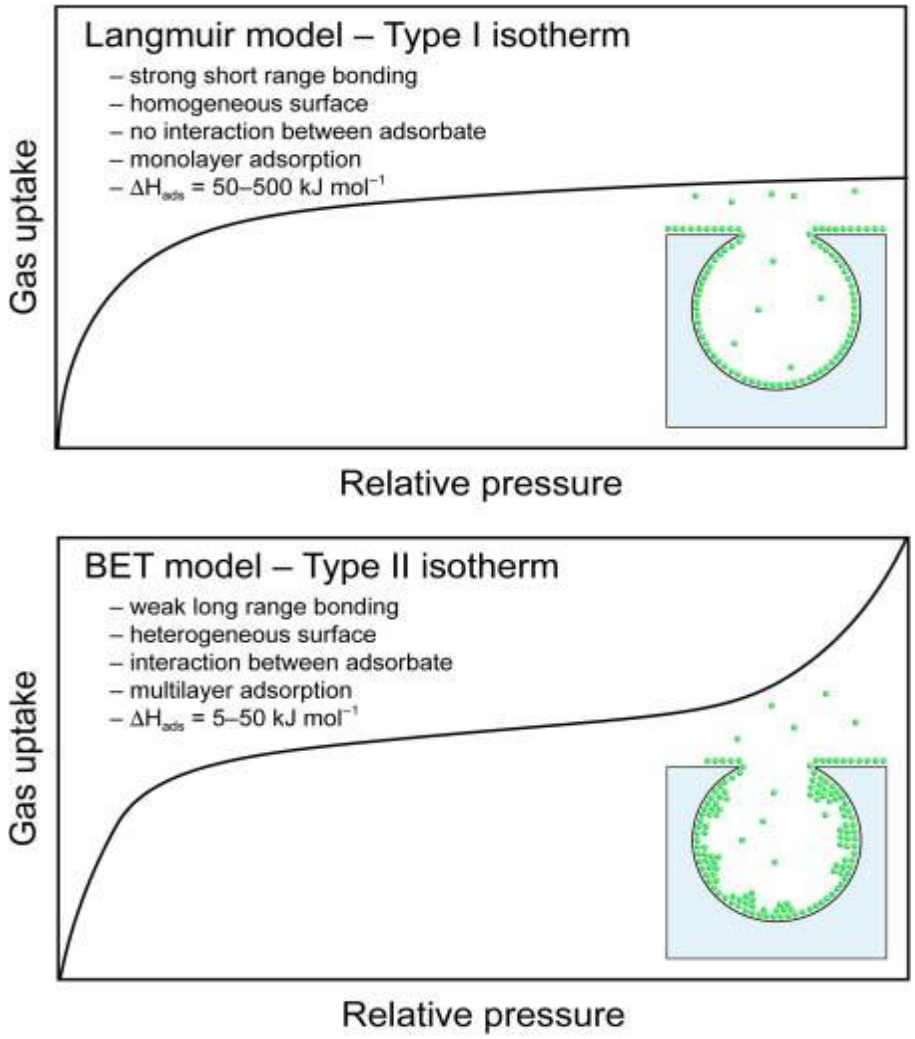

Figure 20: Comparison between Langmuir and BET models for adsorption. [1]

1.2.2. Isosteric Enthalpy of Adsorption

As already said, physisorption is an exothermic process, so it is associated with a release of heat when a gas molecule is adsorbed on MOFs surface. The amount of heat released when a molecule of the adsorbate binds to the surface is called "isosteric enthalpy of adsorption" (ΔH_{ads}) and its value (measured as kJ/mol) depends on the strength of the interaction between adsorbent and adsorbate[58]. In the literature, the expression "isosteric heat of adsorption" (Q_{st}) is often found to describe the same concept. However, the use of the latter is discouraged because it does not correspond to a change of the thermodynamic state properly. Nevertheless, since Q_{st} is a positive quantity and (for adsorption process) ΔH_{ads} has to be negative, it applies that ΔH_{ads} = -Qst. In the case of physisorption, where there are no activation barriers to overcome, the enthalpy of adsorption is negative during the adsorption process and positive for desorption process (ΔH_{des}) and their absolute values are the same (ΔH_{ads}= -ΔH_{des}). The situation is more complicated when considering chemisorption, because of the presence of activation energies and large interaction potentials. Since the enthalpy of adsorption is a measure of the energy required to adsorb a certain amount of gas on an adsorbent, the higher its value (*i.e*. more negative), the higher the adsorbent's thermodynamic affinity for that specific gas.

ΔH_{ads} can be estimated either theoretically (adsorption isotherms construction using molecular dynamics: Grand Canonical Monte Carlo (GCMC) methods)[59] or experimentally. In the latter case, the approach can be both direct and indirect. The direct approach involves the use of a complex and costly calorimetric-volumetric system to measure the heat released during the adsorption process[60]. The indirect approach is usually the most common and makes use of at least two isotherms measured at different temperatures to derive the value of ΔH_{ads}. Since the isosteric heat of adsorption is temperature-dependent, it is recommended to measure the isotherms within a narrow temperature range (25-30 K) in order to avoid big errors in the estimation. For two temperatures, the following simplified Clausius-Clapeyron equation can be applied:

$$\Delta H_{ads} = -Q_{st} = R\left(\frac{\partial \ln p}{\partial \frac{1}{T}}\right)_n = R\left(\frac{\ln(p_2) - \ln(p_1)}{\frac{1}{T_2} - \frac{1}{T_1}}\right)_n$$

Where R is the gas constant (8.314 J K^{-1} mol^{-1}) and p_2, p_1, T_2 and T_1 are respectively the pressures and the temperatures at which both isotherms correspond to the same amount of gas adsorbed (n)[61].

Since the value of ΔH_{ads} is a measure of the affinity of the gas with the adsorbent, its experimental or theoretical evaluation could give important information not only on the ability of the MOF to adsorb a particular gas but also on its ability to separate different species from a gaseous mixture. In fact, in order to separate two (or more) species from a gaseous mixture it is necessary that their ΔH_{ads} are very different, so that one species is preferentially adsorbed over the other.

1.2.3. Pore Volume and Pore Size Distribution

Another important parameter for the determination of MOFs porosity is the pore volume. The total pore volume is usually derived from the gas uptake at a relative pressure that is close to unity (e.g. p/p^0 = 0.95 – 0.99) and assuming that the pores are filled with the adsorbate condensed in liquid state. The pore volume can be determined computationally (for example, using GCMC simulations)[62] or experimentally from the nitrogen adsorption isotherm[63].

Related to the pore volume is pore size distribution (PSD) *i.e*. the distance between two opposite pore walls. This value can be calculated from the full adsorption isotherm, distributing the total pore volume into the different pore widths. Since pores can have different geometries, these must be considered when interpreting the pore size distribution.

There are various methods that can be used to evaluate the pore size distribution: the Barret-Joyner-Halenda (BJH)[64], the Dollimore and Heal (DH)[65] and the Grand Canonical Monte Carlo simulation[66]. However, the most versatile and reliable method is the Density Functional Theory (DFT)[67]. This method is based on the theorem of Hohenberg and Kohn according to which the ground state energy of a system depends on its electron density.

1.3. Surface Area of MOFs

As already said in the previous paragraphs, both Langmuir and BET models can be applied to calculate the surface area of MOFs starting from the nitrogen adsorption isotherm measured at T = 77 K. MOFs usually possess extremely high surface areas, especially useful in gas adsorption-based applications. Since the accessible surface area determines the gas uptake in the low-

pressure region (the most relevant for practical applications), it is independent from the pore size. In fact, there is no direct correlation between surface area and pore size, *i.e.* an increase in pore dimensions does not always correspond to the same increase (or to any increase) in the surface area. Actually, very large pores can result in a "dead volume" where there is no interaction between the pore surface and the adsorbate. Another disadvantage of large pores is that the gravimetric gas uptake increases with the pore size until a theoretical limit is reached, while the volumetric uptake increases until reaching of a critical pore size and decreases in the case of a further expansion.

To design MOFs with ultra-high surface area, the storage space per weight of the material needs to be increased. To do that, the first step is to identify and to maximize the number of the adsorption sites of the MOF. Usually, the majority of adsorption sites are found in the proximity of the SBUs because they are polar in nature, and they trigger stronger interactions with the adsorbate. Other adsorption sites can be found close to the organic linkers, in particular at the edges and on the faces of aryl units[68]. Even if these binding sites are weaker, they play a fundamental role in gas uptake mostly because it is possible to maximize their number through a judicious choice of shape and metrics of the linker [Figure 21]. For example, linkers like H_2BDC with only one benzene ring, lowers the number of adsorption sites. On the contrary, linkers as H_3BTB provide the maximum number of edges and faces increasing the number of adsorption sites[20].

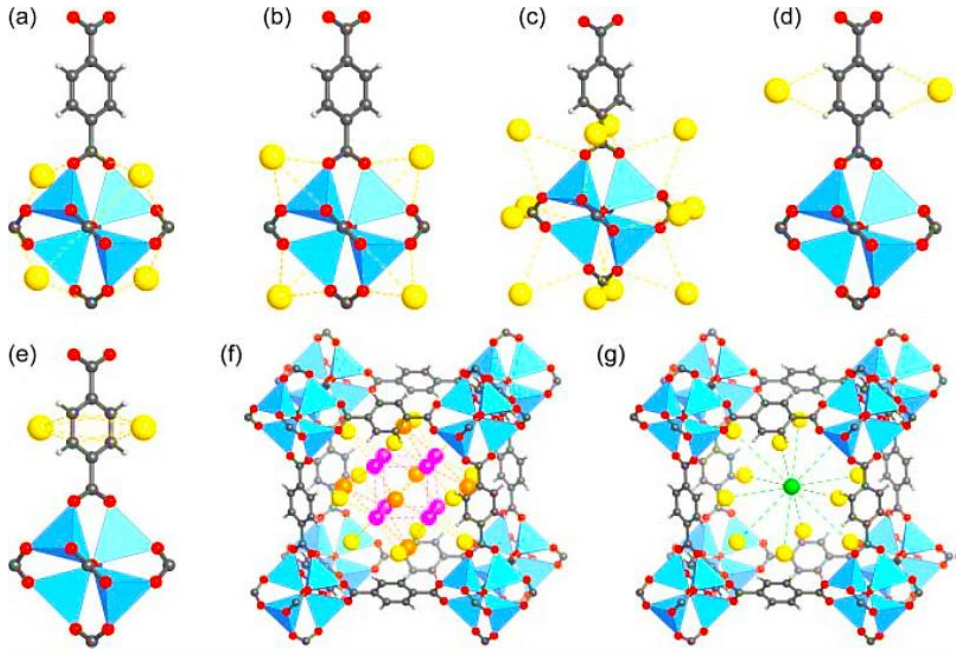

Figure 21: Adsorption sites of argon (yellow spheres) present in MOF-5. Gas molecules are preferentially adsorbed near the SBUs (a-c). The edges and the faces of organic linkers provide additional adsorption sites (d-e). The pores are large enough to permit the formation of a second layer represented by oranges and violet spheres (f). An additional adsorption site is present in the center of the pore (green sphere) (g). color code: Zn – blue, C – grey, O – red. [1]

Since a high number of faces and edges provide a higher surface area, the use of linkers like H_3BTB is more promising to synthesize MOFs with ultra-high surface area. In fact, this linker can be modified adding additional alkynyl (1,3,5-Triscarboxyphenylethynylbenzene, H_3BTE) or aryl units (1,3,5-Tris(4'-carboxy[1,1'-biphenyl]-4-yl)benzene, H_3BBC) allowing for the isoreticular framework expansion [Figure 22]. Reaction of these linkers with a zinc carboxylate cluster as ($Zn_4O(COO)_6$), leads to the obtainment of three different MOFs sharing the same topology. These MOFs are named MOF-177 ($Zn_4O(BTB)_2$), MOF-180 (($Zn_4O(BTE)_2$) and MOF-200 ($Zn_4O(BBC)_2$) and they have a surface area of 4740, 6080 and 6400 m^2/g, respectively[69].

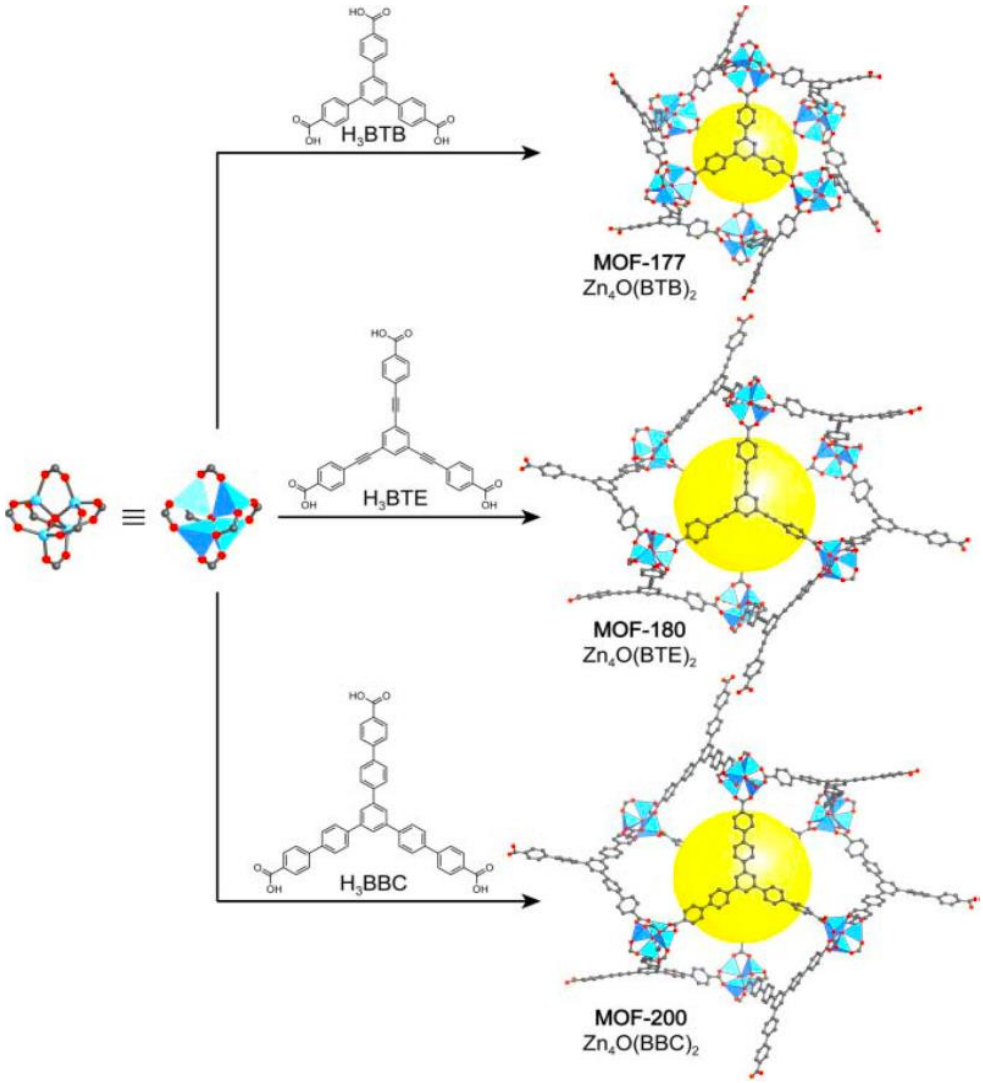

Figure 22: Isoreticular series of MOFs obtained from the expansion of H_3BTB linker. Color code: Zn – blue, C – grey, O – red. [1]

To fully exploit the high surface area and the porosity of MOFs, their channels and pores need to be emptied. In fact, as-synthesized MOFs can contain guest molecules such as solvents, unreacted linkers or modulators that are trapped inside the framework. The removal of the guest

species is possible through a process called “activation” [Figure 23]. There are lots of techniques that can be used to activate a sample, but the most exploited are the solvent exchange and the thermal activation. Solvent exchange foresees the exchange of the reaction solvent (often represented by the high-boiling DMF) with another one that is more volatile like dichloromethane, ethanol or acetone. Thermal activation makes use of elevated temperatures and high vacuum for a prolonged time to evaporate and remove the solvent from the pores. Since this method is made under harsh conditions, during the liquid-gas phase transition the solvent may generate a high surface tension and capillary forces that damage the MOF crystallinity and lead to a negligible surface area. To overcome this problem, these two activation methods are often used together: first the high boiling point solvent is exchanged with another one with a low boiling point, then the sample is activated at a medium-high temperature that prevents the network collapse/damage[70].

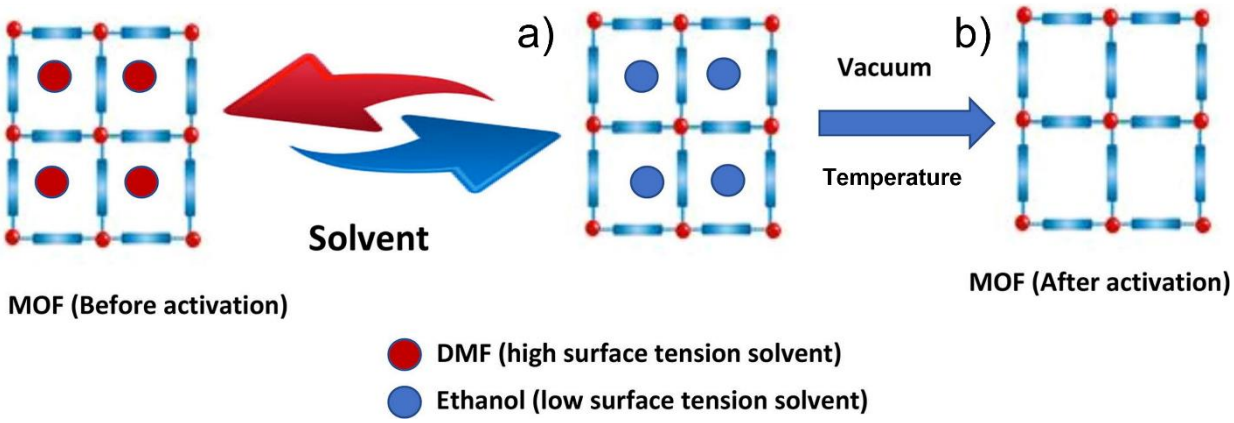

Figure 23: Schematic representation of MOFs activation. Exchange of the high-boiling reaction solvent with a low-boiling solvent (a) followed by thermal activation under vacuum (b). [70]

Chapter 2

BUILDING MOFS

Before starting the synthesis of a new MOF, there are some variables to consider. In fact, not only MOFs can be synthesized using a number of synthetic methods, but it is also necessary to consider their building units. As already said, the building units of MOFs are the organic linkers and the inorganic SBUs. The geometry of the individual building units marks out the outcome of the synthesis, opening at the possibility of *a priori* design of a MOF with a targeted structure.

2.1. Secondary Building Units

The term "Secondary Building Units" was first used in relation to zeolites chemistry to describe the structural subunits from which they are formed. The same concept in MOFs chemistry is used to describe the inorganic part that composes the framework.

The introduction of SBUs was one of the most important developments in the field of MOFs because they play a significant role in the crystallinity, porosity and stability of the framework, in the isoreticular principle and in the targeted synthesis (synthesis of a MOF with a predetermined topology)[71] [Figure 24].

SBUs are polynuclear clusters of metal ions kept together by the linkers binding groups. They are not introduced directly in the reaction, but they are formed *in situ* under specific synthetic conditions, allowing for the assembly of the overall crystalline structure. SBUs provide directionality and confer to the MOF high chemical, mechanical and architectural stability[72].

After the identification of the right conditions that lead to the self-assembly of a SBU with a specific geometry, it is possible to synthesize a framework with a predictable pore shape and metrics[73]. However, to design a MOF *"a priori"* two conditions are necessary: the chemistry of the metal ion assure the formation of a specific SBU under certain conditions (different synthetic conditions can lead to the formation of different SBUs) and the geometry of the organic linker during the synthesis remains unaltered.

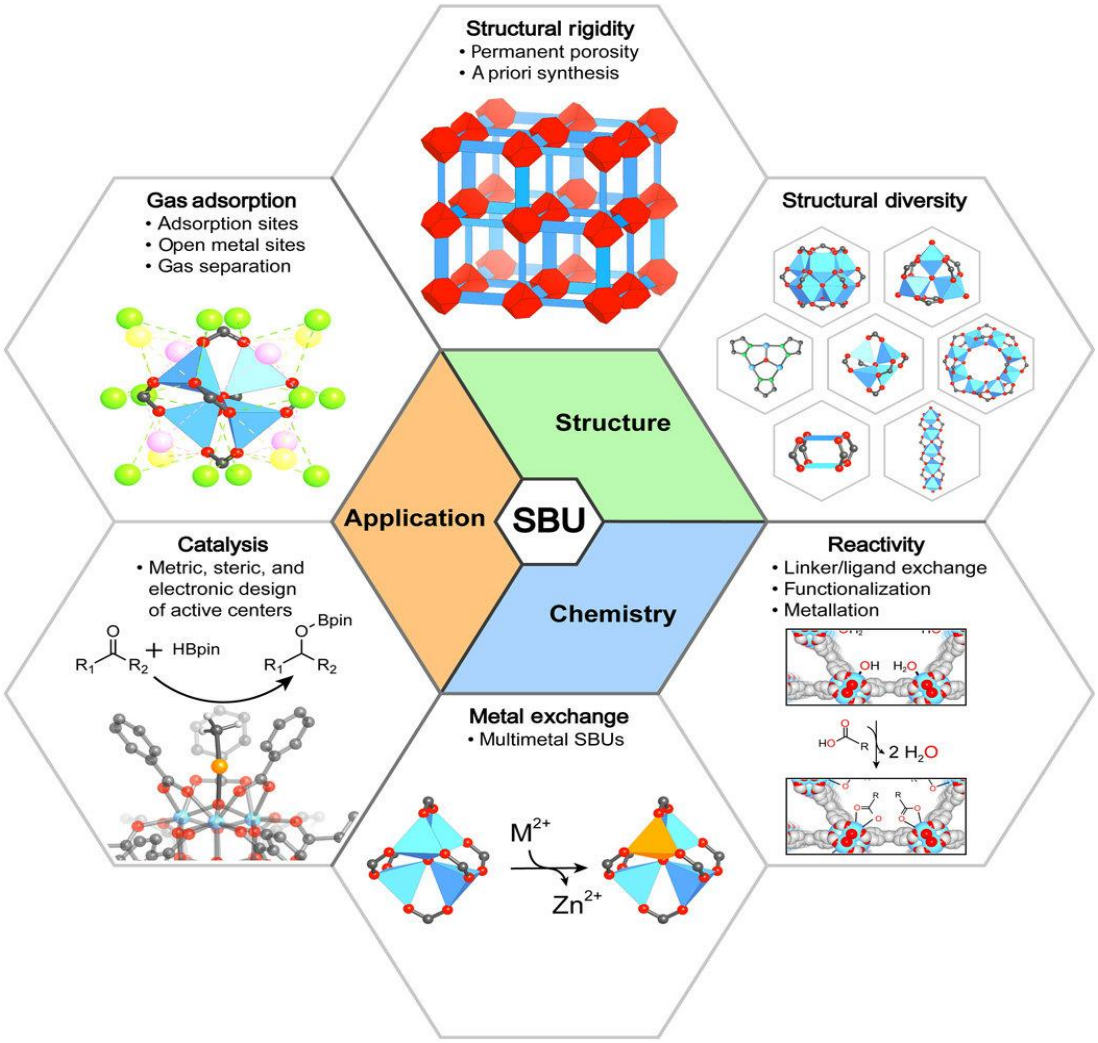

Figure 24: The impact of SBUs on the chemistry, structure and applications of MOFs. [72]

2.2. Organic Linkers

Organic linkers are fundamental in MOFs chemistry not only because they are primary constituents of the framework, but also because they play an important role in the resulting properties of the MOF itself. In fact, organic linkers can influence the gas adsorption behavior and performances, the dimension of the pores, the internal surface area, the catalytic activity and the luminescence properties. Moreover, linkers with different shapes lead to the formation of frameworks with different network topologies[4].

The organic linkers used in MOFs chemistry commonly have rigid backbones built from unsaturated hydrocarbon fragments. The linkers can be prepared in high purity and high yield

[4] Although network topology is a fundamental concept to understand the rich structural diversity of MOFs, I will not treat it in detail in this thesis because an exhaustive treatment of the subject falls outside the thesis scope.

through the standard organic reactions, and they can be modified to incorporate suitable functional groups useful to enhance specific properties.

Generally speaking, organic linkers can be viewed as built from three different fragments: (I) the "binding groups" (usually electron-donor atoms like oxygen and nitrogen) that connect the linker to the metal ions, (II) the "extending unit" that extends the linker length and separates the binding groups from each other (they can influence both geometry and connectivity) and (III) the central "core unit" that is the central part of the linker and usually defines its geometry [Figure 25].

The extending units, in turn, can be of several types: linear (no changes in geometry and connectivity of the linker but only on its length), angled (alter symmetry but not connectivity) and branched (alter both geometry and connectivity).

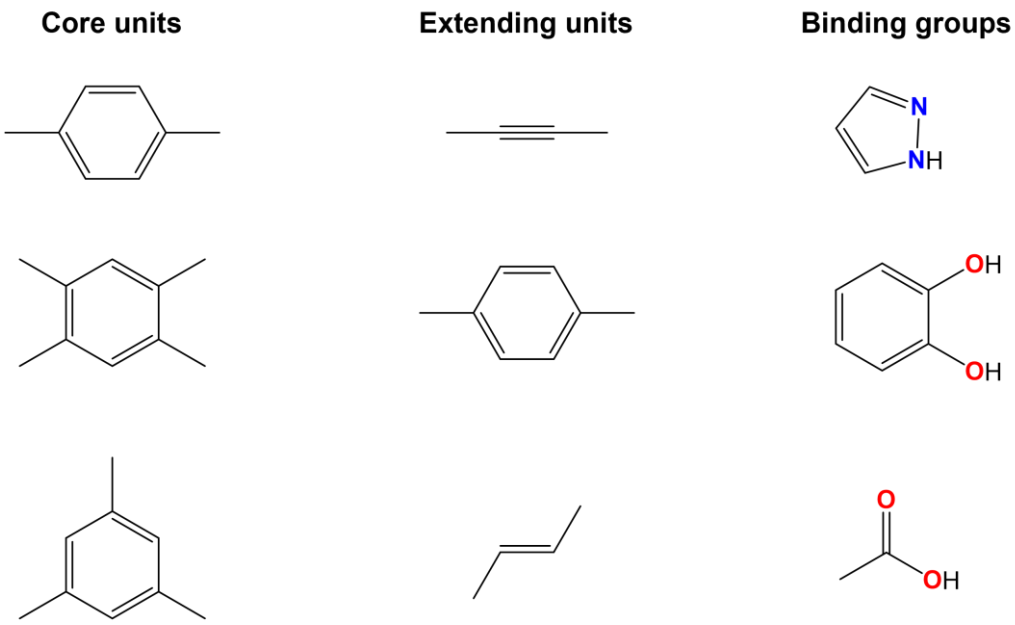

Figure 25: Examples of core units, extending units and binding groups that are possible to find in organic linkers.

The organic linkers that connect the SBUs can have more than two binding sites. The number of connections a linker can make to the nearby SBUs are called *"points of extension"* [Figure 26]. Usually, organic linkers have two (ditopic), three (tritopic), four (tetratopic), six (hexatopic), eight (octatopic) or twelve (dodecatopic) points of extension and, for a certain number of points of extension, can adopt different geometries (linear, bent, branched, asymmetric.).

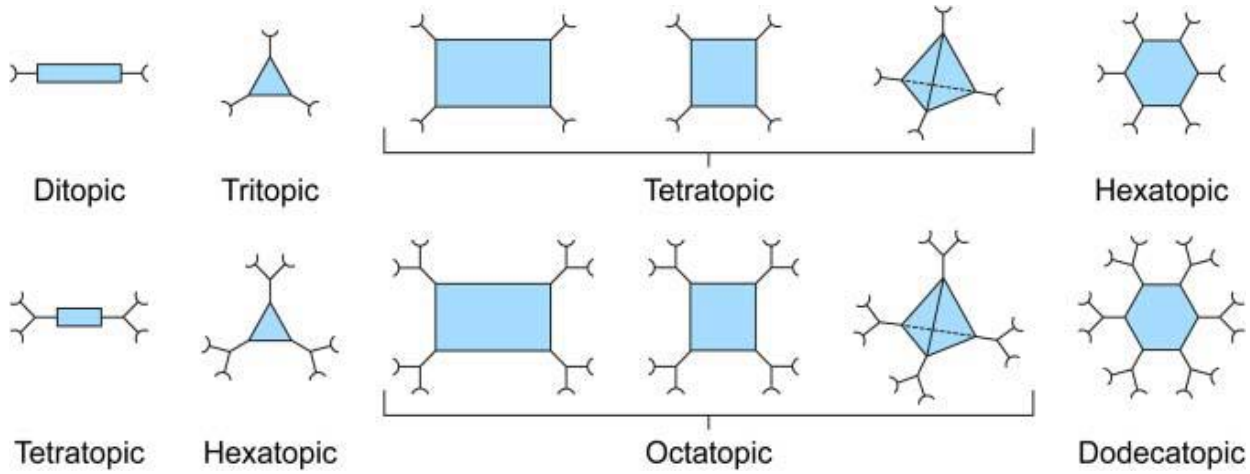

Figure 26: Representation of the basic geometries of organic linkers for the synthesis of MOFs. [1]

The metal-linker bond strength depends on different factors: the binding groups atom charge and nature, the metal ion radius and its charge. Based on Hard-Soft Acid-Base (HSAB) principle, highly charged metal ions with small ionic radius as Zr^{4+} (hard acid) tend to bind hard donor atoms like oxygen (hard base), while softer metal ions with large size and low oxidation state as Zn^{2+} (soft acid) prefer soft donor linkers like N-donors (soft bases). However, hard acids and soft bases as well as soft acids and hard basis can react together, but the result is a less stable MOF (this is the case of MOF-5 and HKUST-1). Since the M-L bond strength has an enormous influence on the stability of the framework, the choice of the metal to use is of great importance in the synthesis (also in light of the desired application).

2.2.1. O-Donor Linkers

Charged chelating linkers such as carboxylates [Figure 27] is the most frequently chosen class for the synthesis of robust MOFs. The use of carboxylate-based linkers provides some important advantages in the synthesis: the negative charge neutralizes the positive charge of metal ions with the consequent formation of a neutral framework, they favor the formation of SBUs with fixed geometry and connectivity, their chelating properties provide directionality and structural rigidity to the framework and the strong bonding with metal atoms results in high thermal, chemical and mechanical stability[74].

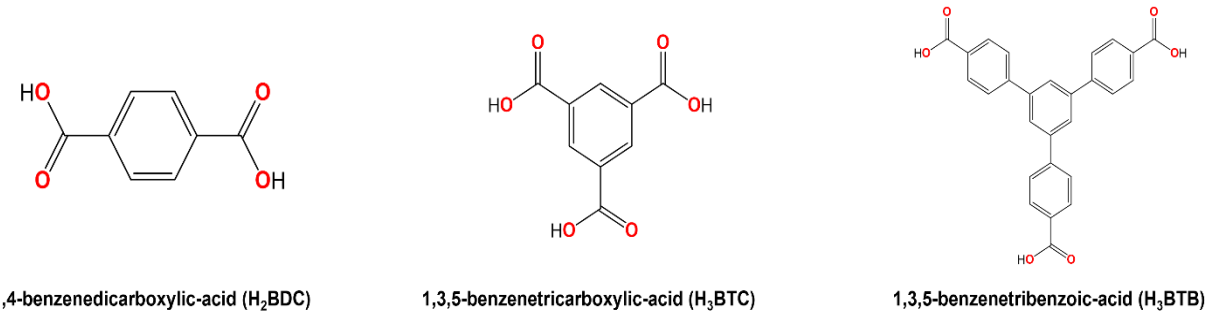

Figure 27: Examples of some O-donor linkers.

Carboxylate-based linkers can bind the metal centers in several ways [Figure 28]: monodentate or chelating (symmetric and asymmetric) if the binding groups are linked to only one metal atom, bridging (syn-syn, anti-anti, syn-anti and monoatomic) if the linker connects more than one metallic center.

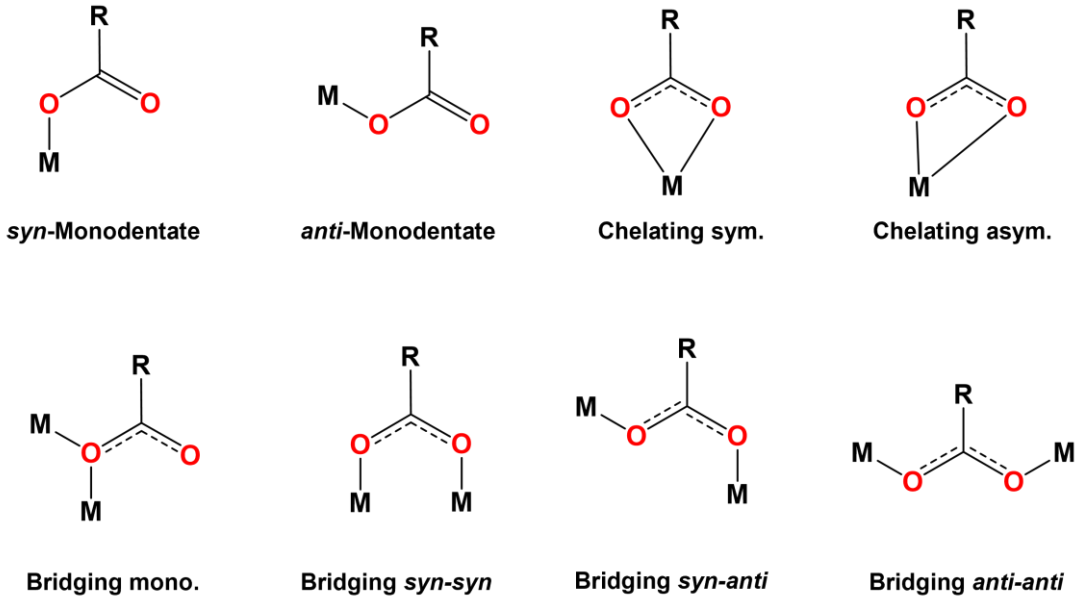

Figure 28: Different binding modes of carboxylate moieties to metals.

2.2.2. N-Donor Linkers

Another class of compounds widely used as building blocks in MOFs chemistry is that of N-donor linkers. These linkers can be divided into two distinct classes: neutral (as 4-4'-bypiridine) and charged (as 4-4'-bypirazole).

As for the neutral N-donor linkers [Figure 29], they are usually employed as co-linkers to connect 2D metal carboxylate structures to extend the bidimensional framework into the third dimension

and thus create 3D mixed-linker pillared-structures (see paragraph 1.1.3 – Mixed-metal MOFs)[75]. For this purpose, the most popular molecules are pyridine, pyrazine and their (longer) derivatives.

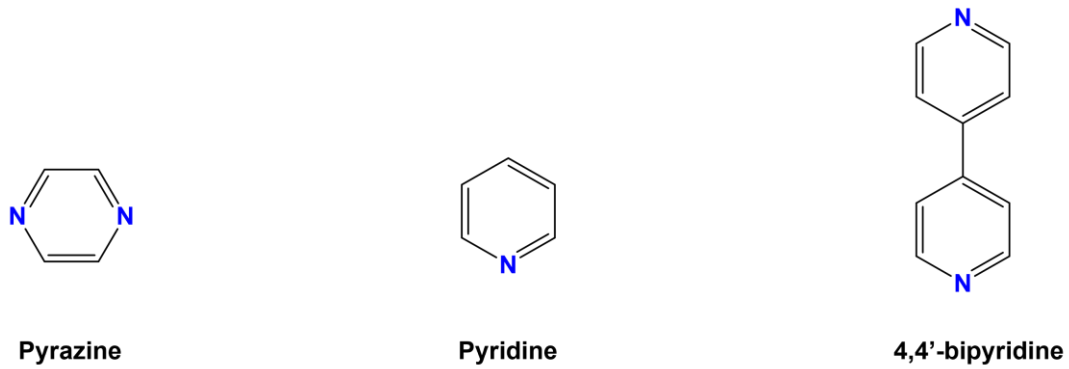

Figure 29: Examples of neutral N-donor linkers.

Azoles (five-membered aromatic N-containing heterocycles) belong to the class of charged N-donor linkers [Figure 30]. These molecules are the building blocks of many important biologically active compounds used in agriculture and medicine[76]. Although azoles are known as bases, they can still be deprotonated using another base, generating the corresponding azolate.

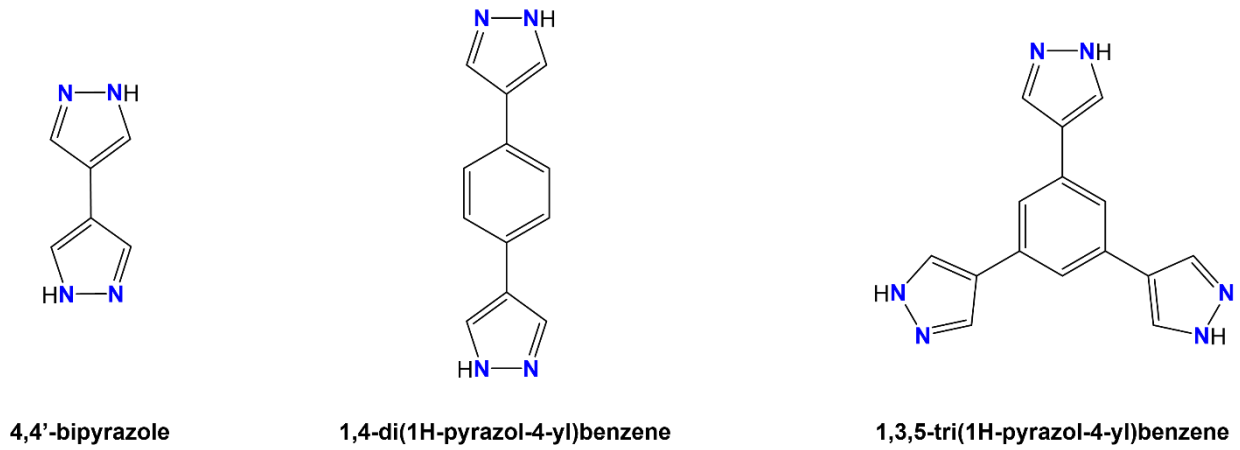

Figure 30: Examples of charged N-donor linkers.

The azolate coordinates to the metal via its sp^2 N-donor atoms. Thanks to the electron-withdrawing effect of the nitrogen, the presence of more N-atoms in the linker skeleton enhances the acidity (easier deprotonation) of the donor group. Then, deprotonation increases the donor atoms basicity and further promotes coordination to the metal ions. Usually, azolates coordinate to only one metal ion and in the same direction of their lone pair (differently to O-donor linkers that usually coordinate more than one metal). However, in the special case of

pyrazole derivatives the position of the two nitrogen atoms allows for three different coordination modes: *mono*-dentate, *exo*-bidentate and *endo*-bidentate [Figure 31]. The *mono*-dentate and *endo*-bidentate coordination modes are more often observed for pyrazolates functionalized with bulky substituents. In the case of the *exo*-bidentate coordination, the small bridging angle of *ca.* 70°C keeps the two metal centers at a rather short distance of 3.5-4.7 Å based on the ion radius[77].

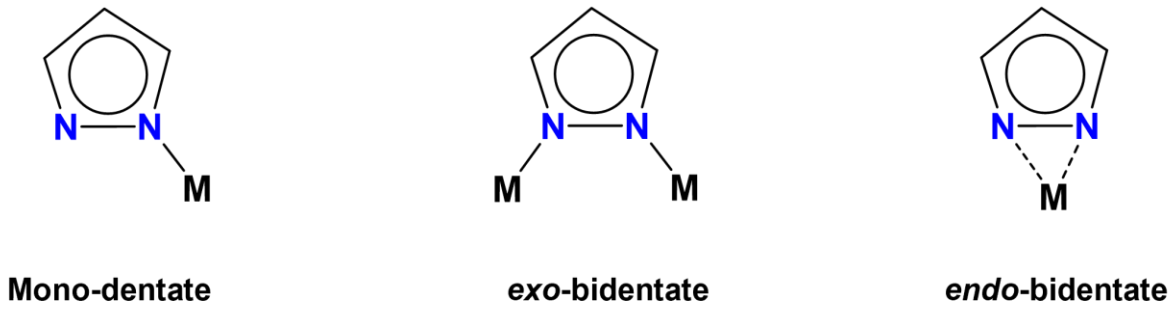

Figure 31: Common coordination modes for azolates.

Typical metal ions that react with N-donor linkers are coinage metals (Ag(I) and Cu(I)) and first row transition metals (Zn(II), Ni(II), Co(II)). The strong nature of the M-N bond (for the HSAB principle, the linkage between a soft Lewis acid and a soft Lewis base has a relatively covalent nature) provides a structure featured by high thermal, mechanical and chemical stability. Moreover, after the coordination to the metal ion the linker donor sites become coordinatively saturated (the lone pair is shared between the metal ion and the N-donor atom) and unavailable for other interactions. This imparts to the framework a hydrophobic character that is not always observed with metal carboxylates[78].

2.3. Synthesis of MOFs

After the analysis of the various linkers and SBUs that can be used for building MOFs, it is now time to analyze the various methods employed to synthesize MOFs. The synthesis of MOFs is not an easy task. In fact, there are many factors that can influence the final result: type of solvent used, reaction time and temperature, the kinetics of crystallization, the choice, the nature and the characteristics of the metal ions and of the organic linkers, the formation of a particular SBU, the pH of the solution, the solubility of the reactants and their concentration[79]. The main goal when a MOF synthesis is planned is to find the proper synthetic conditions that lead to the

formation of the framework without causing the decomposition of the organic linkers. However, the synthesis should also allow the nucleation and growth of the desired phase. It is not always possible to obtain single crystals from the synthesis (actually, it is really challenging) but all structural information can be retrieved even if the product is a crystalline powder *via* Powder X-Ray Diffraction (PXRD).

There are several synthetic techniques and strategies that can be chosen for MOFs: room temperature synthesis, solvothermal reactions, mechanochemical, sonochemical and microwave-assisted synthesis[80] [Figure 32]. PSM can also be considered a synthetic technique, but it will not be further treated in this chapter (see paragraph1.1.4 – Post-synthetic modification).

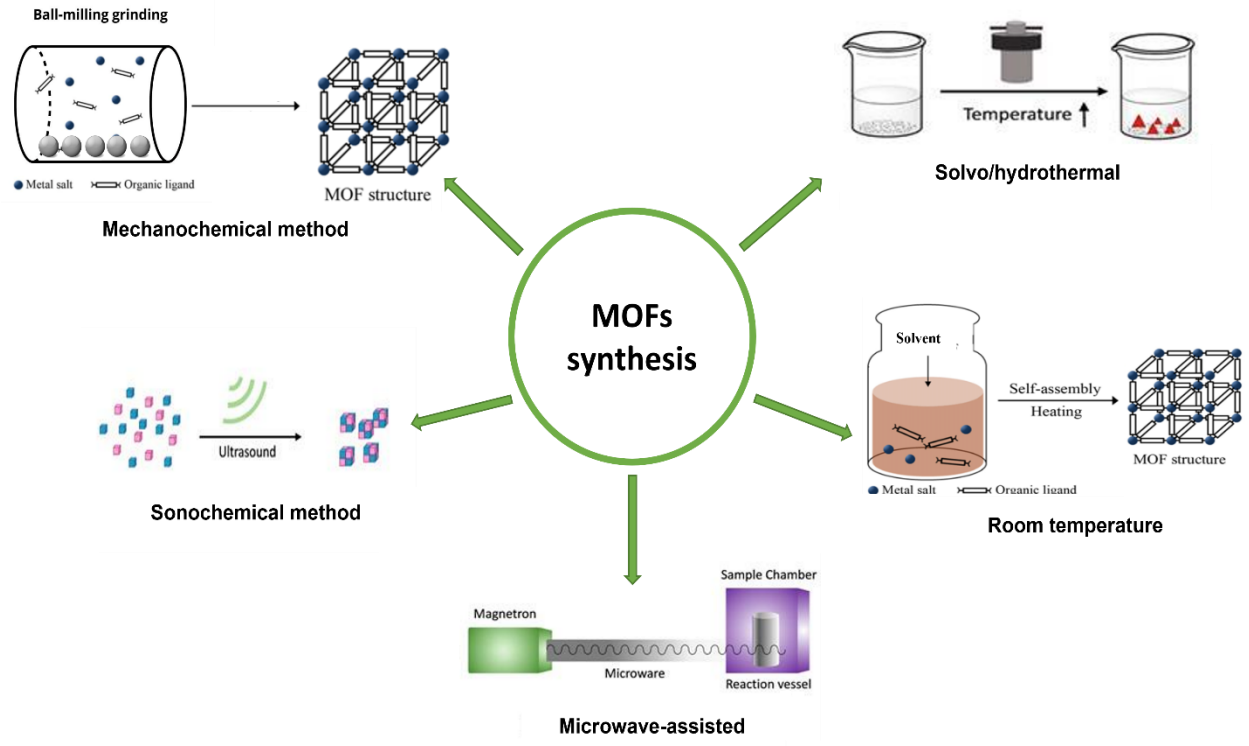

Figure 32: Some of the common methods for MOFs synthesis.

In the case of synthetic methods that make use of a solvent, both organic linker and metal salt are dissolved in that particular solvent. Then, the solutions are mixed together in the same vials and the reaction mixture is made to react following the chosen method (room temperature, microwave assisted…). The choice of the solvent plays a fundamental role because it is one of the most important parameters in MOFs synthesis[81], not only because it is incorporated inside the synthesized MOF acting as "space-filling" molecule but also because it can contribute to the synthesis through chemical reactions. For example, DMF (or other amides) decomposes at

elevated temperatures to form dimethylamine, which is a relatively strong base, and carbon monoxide. Dimethylamine can help to deprotonate the organic linker if it is not very soluble in the amide solvent. In some cases, the solvent may act as linker itself during the synthesis. For example, Biswas and coworkers have reported the synthesis of Zn MOFs using 1H,5H-benzo(1,2-d:4,5-d')bistriazole (H_2BBTA) as linker in both DMF and N,N'-dimethylacetamide (DMA)[82] [Figure 33]. In the first case, the result is a porous 3D MOF of structure $[Zn_5Cl_4(BBTA)_3]\cdot 3DMF$ where the removal of the residual DMF trapped in the network pores is straightforward. In the second case instead, the product is a 2D coordination polymer of structure $[ZnCl(BBTA)_{0.5}(DMA)]$ where DMA is coordinated to the metal ion; its removal leads to structural collapse.

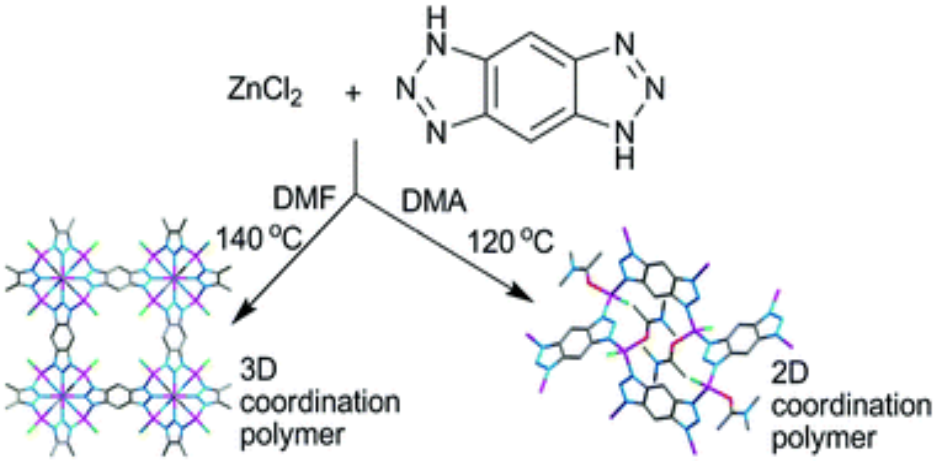

Figure 33: Example of how the use of different solvents can lead to different structures. [82]

In some cases, the synthesis of MOFs results in an amorphous rather than a crystalline product. To overcome this issue, it is possible to use the so-called "modulators". A modulator is an organic or inorganic acid that contains the same binding groups of the organic linker but with a lower denticity. These species compete with the linkers in coordination to the metal ions. However, the low denticity does not facilitate the connection between adjacent SBUs, thereby the organic linkers will eventually replace the modulators during the synthesis. The use of modulators is a good way to slow down the rate of framework formation, hence facilitating the growth of larger MOF crystals. An example of modulator is the formic acid that is a monocarboxylic acid, so its denticity is lower with respect to the organic linkers that are usually (at least) ditopic. An example in which the use of modulator is essential in the success of the synthesis is the case of the UiO-6x family. Without the use of benzoic acid (or acetic acid) as modulator, the resulting product is an aggregate of nanocrystals and not individual crystals as obtained using a fixed quantity of modulator[83].

Even if MOFs are crystalline compounds, it is not rare that the structure resulting from the synthesis is not a "perfect crystal". Any deviation from the ideally ordered crystal structure is called a "defect" and MOFs possessing defects are called "defective". Defects naturally occur and are randomly formed during synthesis. There are two types of defects that can be found in MOFs: missing-linkers (generated when an organic linker is absent from the structure, leaving coordination vacancies on two adjacent metal atoms/clusters) or missing-metal sites. The latter is very rare while the former is more common, especially when a modulator is used because it can coordinate to the metal and replace the linker[84]. Defects have an impact on the physico-chemical properties of the material and an evidence of the presence of defects are the lower density and thermal/mechanical stability with respect to the MOF without any defects[85]. Despite defects are naturally formed, they can even be introduced and controlled[86]. In some cases, the presence of defects can be beneficial in some applications such as catalysis, just to make an example. In fact, the absence of some linkers means more open metal sites that is advantageous for catalytic efficiency. Moreover, diffusion limitations are reduced, permitting to the guest species (even the big ones) to easily reach the active site and leave the environment after the reaction[87].

2.3.1. Room Temperature Synthesis

In some cases, it is possible to synthesize MOFs without the need for high temperatures or particular instruments. The room temperature synthesis is the easiest method to use and foresees the mixing of two solutions, one containing the organic linker (usually with a base useful to deprotonate the linker) and the other one containing the metal salt and let them react for a certain time [Figure 34]. Tranchemontagne report the synthesis of the famous MOF-5 (and other MOFs) using room temperature synthesis. In this work[88], a DMF solution of zinc acetate is added to a DMF solution of H_2BDC and triethylamine. After the addition, a white precipitate (MOF-5 indeed) is immediately formed. Further studies demonstrated that the use of the base is not fundamental to obtain the MOF but, in this case, the reaction time is longer.

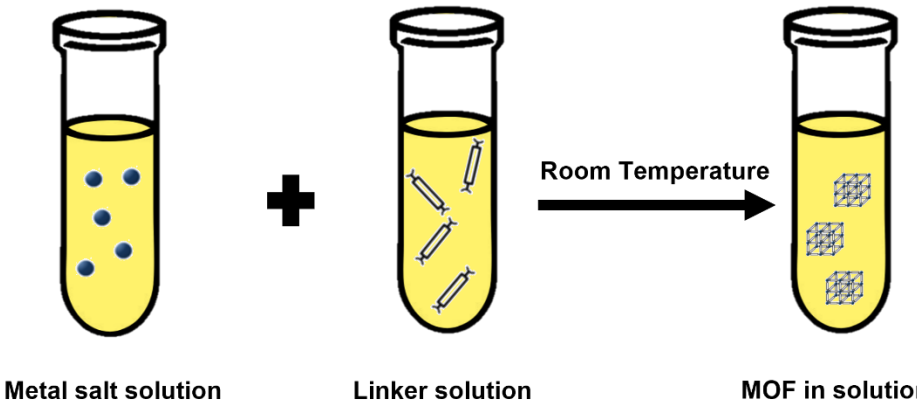

Figure 34: Schematic representation of a room temperature synthesis of a MOF.

2.3.2. Solvothermal Synthesis

The solvothermal method is also referred to as "conventional synthesis" because it is the most used synthetic method in MOFs field. In this case, the organic linker and the metal salt are dissolved in an organic solvent (typically DMF or DMA) and then put in a scintillation vial or a stainless-steel autoclave with an inner Teflon beaker and heated at elevated temperatures inside an oven [Figure 35]. The temperature must be higher than the boiling point of the solvent in order to create an "autogenous pressure" inside the reaction vessel[89]. If the solvent used for the reaction is water, we refer to it as "hydrothermal synthesis". To facilitate the solubility of both building blocks (metal salt and organic linker may not be soluble in the same solvent), it is possible to use a mixture of different solvents (for immiscible solvents the crystals grow at the contact surface)[90]. For the solvothermal synthesis, parameters that must be considered are the choice of the solvent, the temperature and the reaction time.

Another kind of solvothermal synthesis is the ionothermal synthesis. Ionothermal synthesis makes use of ionic liquids[5] as solvents. Ionic liquids have high thermal stability, nonflammability, and high solubility for organic molecules, so they are good solvents for the synthesis of MOFS. Moreover, they are formed by anions and cations that can act as counterions for MOFs frameworks, for these reasons they gained a great attention in recent years[91].

[5] Liquids that consist almost exclusively of ions. Usually are salts with melting temperatures below 100°C.

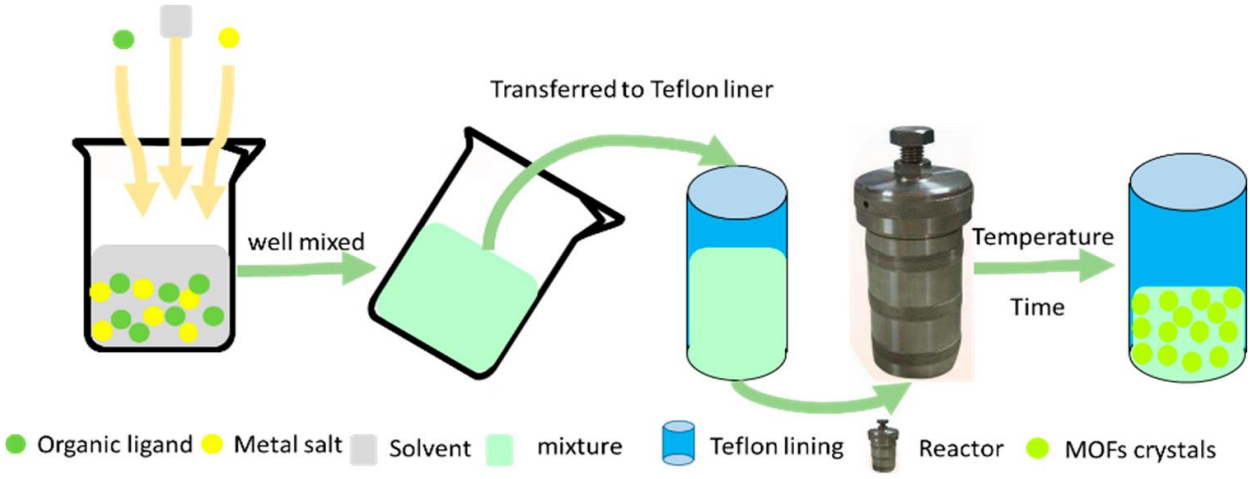

Figure 35: Schematic representation of solvothermal synthesis. [90]

2.3.3. Mechanochemical Synthesis

Mechanochemical synthesis uses mechanical forces to break intramolecular bonds and allow the chemical reaction between the precursors to form the desired product[92]. The key idea behind this method is to promote chemical reactions by milling or grinding solid starting materials reducing the particle size and locally melting the reactants [Figure 36]. In MOFs field this solid-solid reaction represents a more "environmentally friendly" alternative for the synthesis of new products. In fact, mechanochemical synthesis can be conducted without the use of organic solvents (or with a minimal amount of solvent), at room temperature and for short reaction times (normally 10-60 minutes)[93]. In some cases, it is possible to use metal oxides instead of metal salts with the advantage that the only side product formed from the reaction is water. The addition of a small quantity of organic solvent is called Liquid-Assisted Grinding (LAG) and it has some advantages: a faster reaction time (increased mobility of the reactants) and the solvent may show structure-directing properties that modify the nature of the product. The mechanochemical synthesis of MOFs can be easily scaled-up, however the biggest disadvantage is that the final product is obtained as a powder unsuitable for single crystal structural studies[94].

Parameters that can influence the synthesis are the metal salt, the nature of the solvent (if used), the reaction time and the grinding frequency (higher frequency means high kinetic energy and then much more heat generated that can causes side reactions) .

An example of mechanochemical synthesis is the work of Klimakow and coworkers[95] that used this method for the synthesis of the famous HKUST-1 (Hong Kong University of Science and

Technology) a copper MOF with the H_3BTC linker of minimal formula $Cu_3(BTC)_2$. In this work, they have mixed the linker with copper acetate in a ball mill and then grinded for 25 minutes. As result, they obtained the pure and crystalline MOF as a powder.

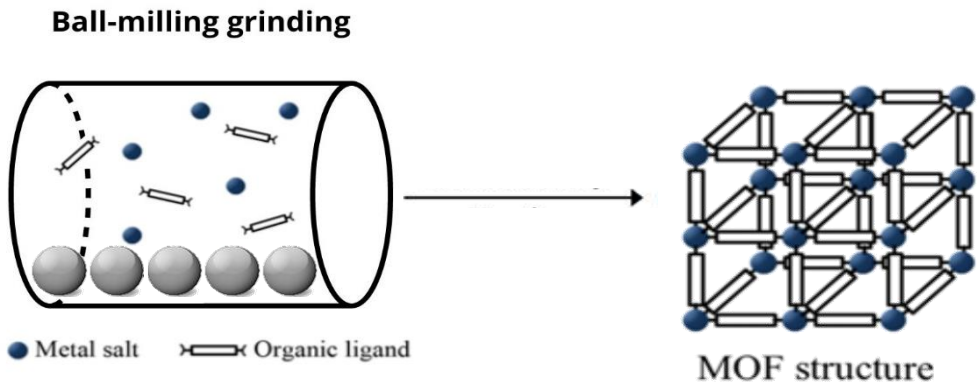

Figure 36: Schematic representation of the ball-milling method for the synthesis of MOFs.

2.3.4. Sonochemical Synthesis

Despite sonochemistry has been widely used in organic synthesis[96], sonochemical synthesis is one of the most recent techniques applied to the MOFs synthesis. Sonochemical synthesis is based on the application of high-energy ultrasound to the reaction mixture. Ultrasound is a mechanical vibration characterized by a frequency between 20 kHz and 10 MHz. The reaction does not occur due to a direct interaction between reactant molecules and the ultrasound (its wavelength is larger than the molecular dimensions) but due to the interaction between the ultrasound and the solvent. Irradiation of a solution with high-energy ultrasound creates bubbles inside the liquid. These bubbles grow until their maximum size and then collapse (this process is called "cavitation") creating local "hot spots". These hot spots are characterized by an extremely elevated temperature (up to 5000K), huge pressure (up to 1000 bar) and fast cooling rates (10^{10} K/s) that favor the chemical reactions and the crystal formation[97] [Figure 37]. Parameters that influence the reaction are the frequency and intensity of the ultrasounds (depend mostly on the equipment), the temperature and the choice of the solvent (volatile organic solvents are not a good medium because they possess a high vapor pressure that reduces the intensity of the bubbles collapse.

The advantage of sonochemical synthesis is that it is an environmentally friendly and fast method that can be used to synthesize MOFs even at ambient temperature. However, the sonochemical

method is not very exploited nowadays, and there are few examples in literature and, mostly, of already known MOFs as MOF-5[98] and HKUST-1[99].

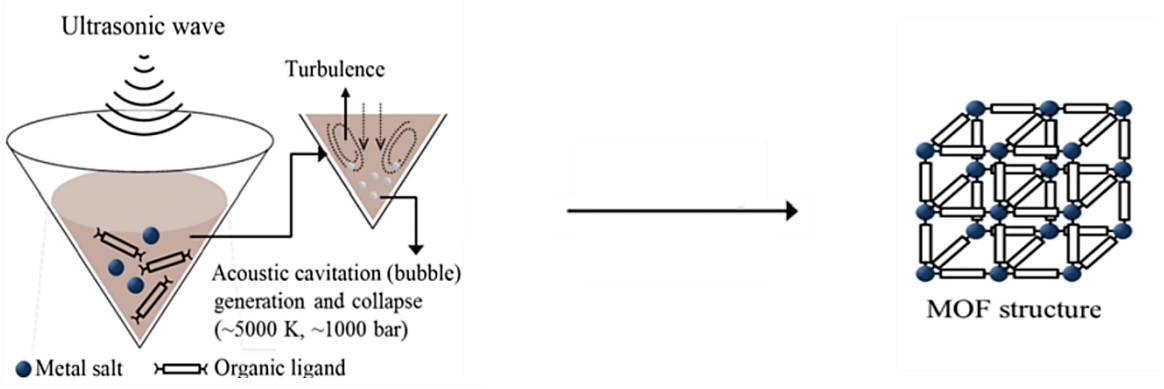

Figure 37: Schematic representation of sonochemical synthesis of MOFs. [80]

2.3.5. Microwave Assisted Synthesis

The use of microwave (MW) radiation is a well-known synthetic method in organic chemistry[100], and it has been used in MOFs chemistry only recently[101]. The method relies on the interaction between the microwaves generated from the instrument (usually a magnetron inside an oven) with the solvent molecules [Figure 38]. Many (polar) solvents possess a dielectric moment and tend to align themselves with the (alternating) electric field generated from the microwaves. Applying an appropriate frequency, the solvent molecules start to move and collide with each other generating a huge amount of heat. The MW heating is very efficient from an energetic point of view because the radiation interacts directly with the bulk material and not with the external surface of the reaction vessel. The heat generated during the synthesis is instantaneous and enough to reach temperatures higher than that of the boiling point of the solvent. The MW oven allows to monitor pressure and temperature during the reaction to have control over the reaction conditions. Due to the fast kinetics of crystal nucleation and growth, the product obtained from this kind of synthesis is a microcrystalline powder or in the form of nano-sized crystals[102]. As an advantage, however, the MW assisted method allows to greatly reduce the reaction time[103]. For example, Seo and coworkers reported the synthesis of the MOF HKUST-1 in high yield using the MW-assisted method with a reaction time of 30 minutes[104].

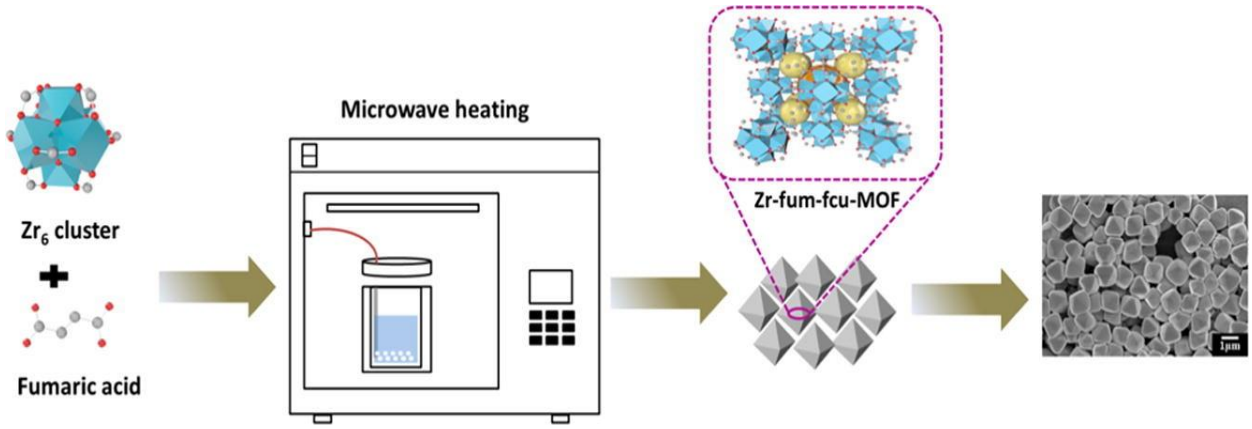

Figure 38: Schematic representation of MW-assisted synthesis of a zirconium MOF. [102]

Chapter 3

MOFS APPLICATIONS

The finely-tuned synthesis of MOFs through a careful selection of organic linkers and metal nodes allows to obtain materials with ultrahigh porosity, high surface area, and high chemical and thermal stability. The precise control over the structure, the possibility to be chemically modified after the synthesis (PSM) or to create heterogenous structures with multiple and different metals or organic linkers (MTV-MOFs) and the ability to expand their metrics keeping the same topology (IR-MOFs), are revolutionary aspects not achieved by any other porous solid in the past. Nowadays, MOFs chemistry has reached a point where all the material features (structure, functionalities, porosity, metrics and so on) can be designed *a priori* for a specific application. All these extraordinary properties make MOFs applicable in many fields of chemistry as gas storage[105] and separation[106], luminescence sensing[107], catalysis[108], drug delivery[109] and water purification[110] among the others [Figure 39].

Unfortunately, MOFs application on an industrial scale is still limited by a number of issues that are mostly related to their synthesis. In fact, the production of high quantities of MOFs is fairly expensive, both for the cost of the raw materials and for their synthetic methods that usually involve high energy consumption and the use of large quantities of toxic solvents. A particularly important step to be made is the transition towards "greener" synthetic conditions using low reaction temperatures, inexpensive precursors and non-toxic solvents like water. Another critical issue to face is the lack of information on the long-term stability of MOFs under the operating conditions.

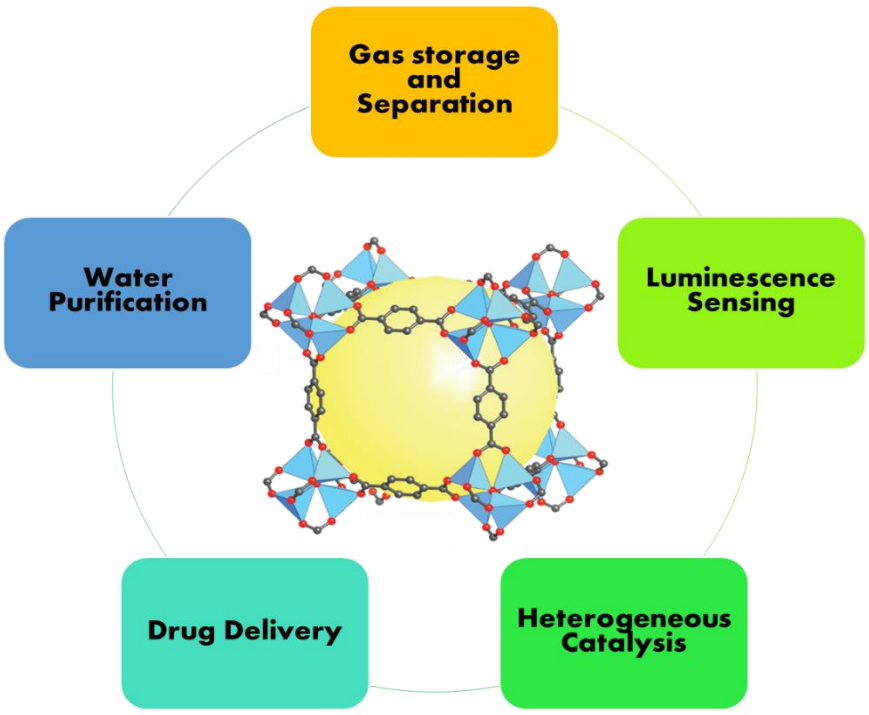

Figure 39: Some of the possible applications of MOFs.

3.1. Gas Adsorption and Storage

The extensive use of fossil fuels in the transport industry or to produce energy for industrial and domestic applications releases massive quantities of pollutants and greenhouse gases in the atmosphere. As an alternative, the use of gaseous fuels like methane and hydrogen lowers carbon emissions and reaches a higher thermal efficiency. Nonetheless, the use of this gaseous fuels presents some issues related to their storage and transportation that usually requires high energy consumption and harsh conditions. From this point of view, the high surface area, high porosity and high chemical and thermal stability of MOFs make them very promising for gas adsorption and storage [111]. Indeed, this is probably the main MOFs application studied at present. In the next sections, examples of storage in MOFs of the three most popular gases currently studied for renewable energy and environmental reasons (CO_2, H_2 and CH_4) will be briefly presented.

Gas adsorption experiments in a research laboratory context are usually conducted at low pressures (0 - 1 bar), where the adsorption capacity is only related to the surface area. The higher pressure reached in “real life” applicative contexts provides a total amount of gas adsorbed that is greater than that owed to the mere surface area. The value of gas adsorbed at high pressures is equal to the sum of the gas adsorbed on the surface of the MOF plus the bulk gas that is compressed inside the structure and does not interact with pores or with surface. Another important aspect to take into consideration is the *working capacity* of MOFs[112]. This parameter is often related to devices powered by gaseous fuels that usually requires minimum and maximum operating pressures. To understand the concept of working capacity, imagine a hydrogen engine that can operate in a range of hydrogen pressure between 5 (minimum inlet pressure) to 65 bar (maximum pressure of the tank). In this case, the working capacity is represented by the amount of gas that the MOF can deliver to the engine when the pressure is lowered from the maximum to the minimum value [Figure 40]. The desorbed gas quantity depends on the conditions that are used to trigger the release: using heat or vacuum may induce a higher gas release. However, the working capacity is always lower than the storage capacity because the quantities below 5 bar and above 65 bar must be excluded from the total uptake.

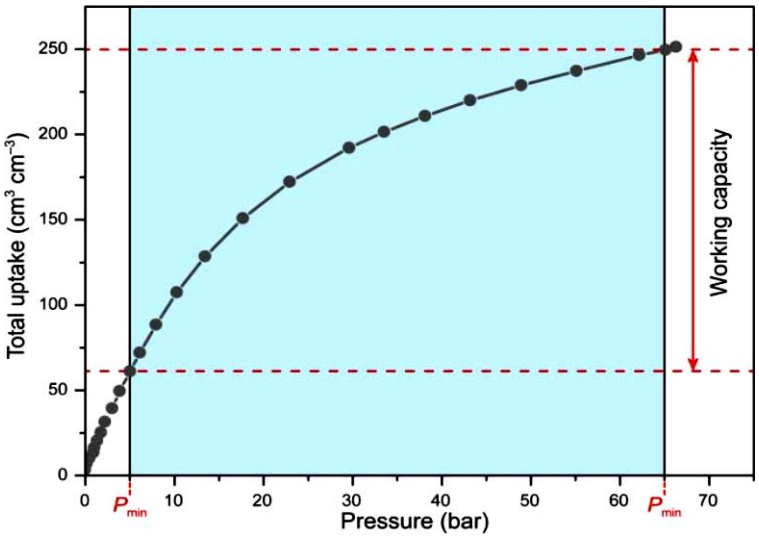

Figure 40: An example of a methane adsorption isotherm conducted between 0 and 65 bar. The working capacity is represented by the deliverable amount of gas between 5 and 65 bar (lower than the total uptake). [1]

The thermal effects produced by the charge and discharge operations can have a huge impact on the gas storage capacity. During gas adsorption (refueling), a certain amount of heat is released (equal to Q_{st}) that leads to a temperature increase if not efficiently dissipated, which in turn causes a lower total gas storage capacity. In the same way, if the heat adsorbed during the gas desorption (discharge) is not re-supplied the temperature drops and a larger amount of gas is retained (lower release).

To use MOFs in gas adsorption and storage applications, they not only need to show high adsorption capacities and fast kinetics (that are fundamental prerequisites), but they also must be stable under the operating conditions and for a long number of adsorption-desorption cycles. During the operating time, MOFs undergo thermal and mechanical stress that may cause degradation and loss in storage capacity.

3.1.1. Carbon Dioxide Capture and Storage

The ever-increasing level of carbon dioxide present in the atmosphere is one of the most relevant problems that afflict our planet. Since about 80% of the total CO_2 emissions are related to the combustion of fossil fuels[113], there is an urgent need for alternative fuels and for a transition to renewable energy sources. Since the current Worldwide energy demand cannot be covered by these alternative strategies, an alternative approach to solve the problem is to prevent the emission of CO_2 in the atmosphere. To do that, it is necessary to develop efficient carbon capture

and sequestration (CCS) technologies. The most widely used carbon capture technology is based on the adsorption of CO_2 by aqueous solutions of alkanolamine from flue gases (chemisorption with formation of carbamates). However, a large amount of energy needs to be used to remove the trapped CO_2 and to regenerate the capture medium[114]. In the optic of developing new materials for CCS applications with greater efficiency[115], MOFs have the potential to fulfill this requirement, since CO_2 adsorption in MOFs does not imply formation of new adsorbate-adsorbent chemical bonds (being a simple physisorption and not a chemisorption). As a matter of fact, the tunability of MOFs structure offers the possibility to design materials with a high affinity towards CO_2, enhancing the adsorption properties and the maximum gas uptake[116]. Actually, there are several parameters that can influence CO_2 adsorption. The presence of Lewis acidic open metal sites results in a partial positive charge that can strongly interact with the oxygen atoms of CO_2. This strong interaction is usually witnessed by a high value of Q_{st} even at low pressures and, consequently, by a high gas uptake. An example is represented by the magnesium analogue of MOF-74 (Mg-MOF-74) that shows a remarkable CO_2 uptake of 27,5 wt% at T = 298 K and at ambient pressure (1 bar)[117]. Every metal center of this MOF has an open metal site where CO_2 can bind in an end-on manner [Figure 41]. However, also water has a strong affinity for open metal sites. Thus, the total CO_2 adsorption capacity of Mg-MOF-74 can greatly decrease in the presence of water.

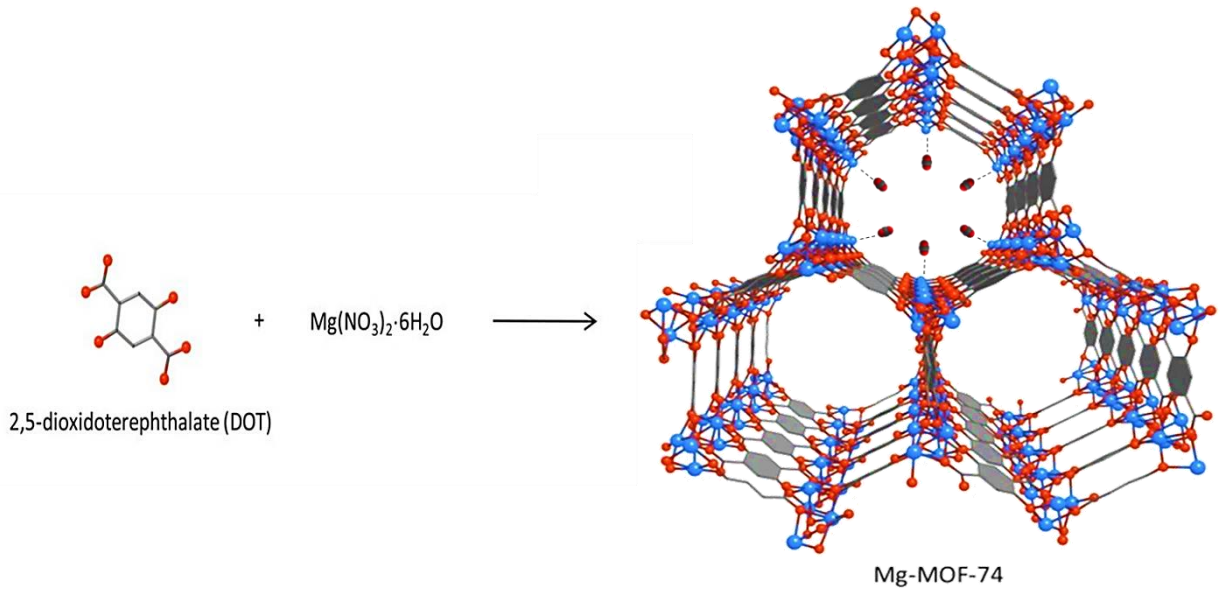

Figure 41: Schematic representation of synthesis and structure of Mg-MOF-74. In the upper pore is represented the interaction of CO_2 with the open metal sites. Color code: Mg – blue, C – grey, O – red. [117]

Even in the absence of open metal sites, SBUs can interact strongly with CO_2 due to their high polarity. Moreover, it is possible to increase the affinity for CO_2 by the introduction of hydroxyl moieties as capping ligands in the SBUs. An example is represented by MAF-X25 a manganese MOF with minimal formula $Mn(II)_2Cl_2(BBTA)$ [H_2BBTA = 1H,5H-benzo(1,2- d:4,5-d')bistriazole]. Using H_2O_2 it is possible to partially oxidize its metal centers, thus obtaining the analog called MAF-X25-ox with minimal formula $[Mn(II)Mn(III)(OH)Cl_2(BBTA)]$, with an almost 1:1 molar ratio of Mn(III)-OH and Mn(II) sites[118]. The presence of the -OH groups not only enhances CO_2 adsorption capacity up to 30% but also modifies the adsorption mechanism: in MAF-25X-ox, CO_2 is not adsorbed on the open metal sites as in MAF-25X, but it is covalently bound through reversible formation (and decomposition) of bicarbonate during the adsorption (and desorption) processes [Figure 42].

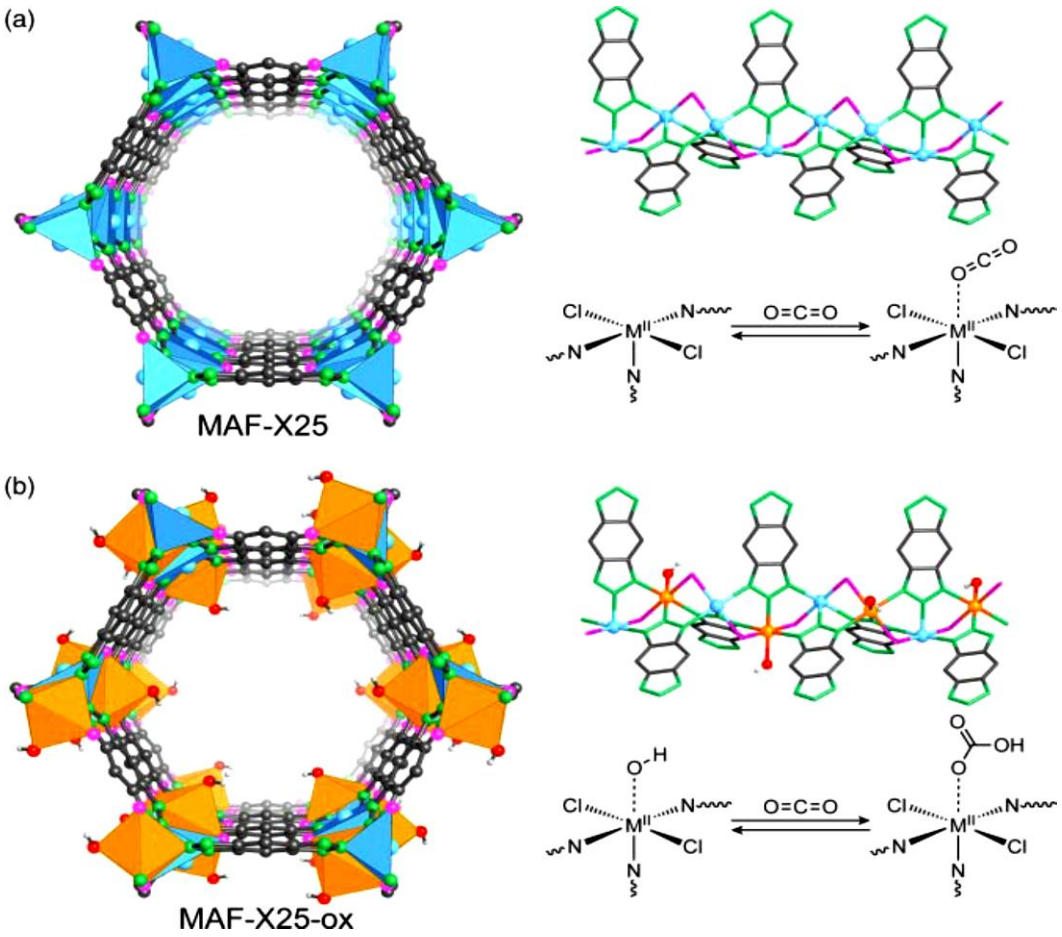

Figure 42: Adsorption mechanism of CO_2 in MAF-X25 (a) and MAF-X25-ox (b). In MAF-X25, CO_2 is adsorbed on the open metal sites. In MAF-X25-ox CO_2 is covalently bound as bicarbonate after reaction with the hydroxyl moieties. Color code: Mn(II) – blue, Mn(III) – orange, C – grey, O – red, Cl – violet, N – green. [1]

The carbon atom of the CO_2 molecule is electrophilic; thus it can be attacked by Lewis bases such as amines. The interaction between CO_2 and amines can be both weak (physisorption) and strong (chemisorption). For this reason, MOFs containing amino groups on their linkers are promising candidates in CO_2 adsorption. An example is the MOF $Zn_2(ATZ)_2(OX)$ [HATZ = 5-aminotetrazole; OX = oxalate] where the CO_2 carbon atom interacts with the nitrogen of amine moieties through a physisorption process[119] [Figure 43]. However, even in this case the adsorption capacity can be influenced by the competitive presence of water.

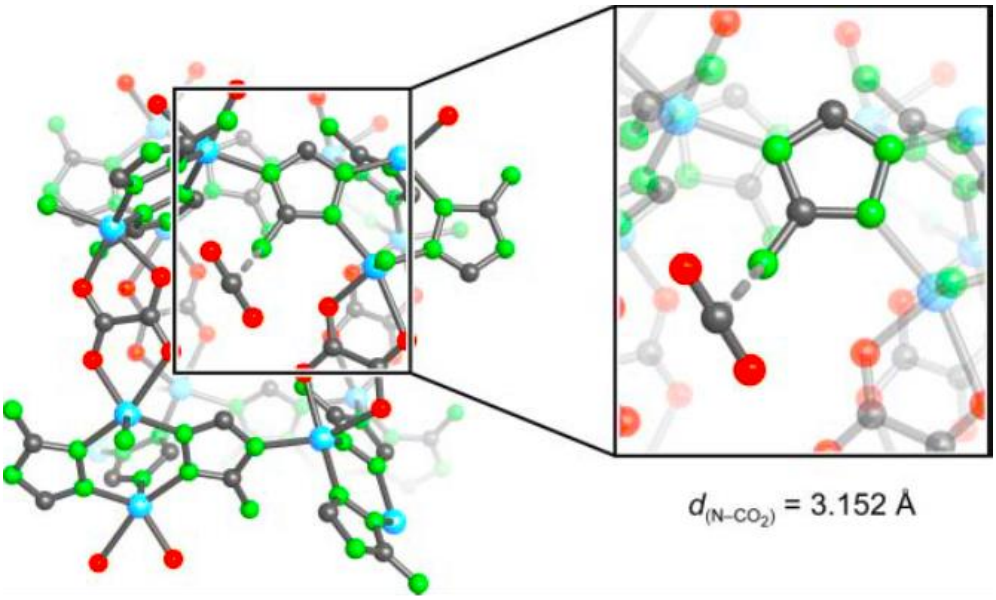

Figure 43: Representation of CO_2 adsorption in MOF $Zn_2(ATX)_2(OX)_2$. CO_2 is physisorbed by the amines that point into the pores. Color code: Zn – blue, C – grey, O – red, N – green. [1]

To solve the problem of the reduction of CO_2 uptake in the presence of water, a successful remedy is to render the pores hydrophobic in order to prevent the entrance of water inside the structure[120]. The best way to obtain a MOF with excellent CO_2 adsorption capacity is to create a compound that gathers all the aforementioned properties together in the same framework. Another important aspect to take into consideration when talking about MOFs application in CO_2 adsorption (but the same applies also for other gases) is the release of the captured gas from the adsorbent. Unlike the aqueous solutions of alkanolamine, MOFs usually need more mild conditions to be regenerated. There are three different methods to remove CO_2 from the pores. The first is Temperature Swing Adsorption (TSA) that uses heat (usually the excess produced during the industrial process) to stimulate the gas desorption [121]. The second is the Pressure Swing Adsorption (PSA) that exploits the decrease of the pressure from the operating pressure to ambient pressure (obtained closing the inlet valve) to trigger the gas release[122]. The third is

the Vacuum Swing Adsorption (VSA) that is like PSA but, in this case, the pressure is lowered to sub-atmospheric pressures to force the gas to get out from the pores[123] [Figure 44]. These three methods can also be used coupled together to obtain a higher efficiency of gas removal.

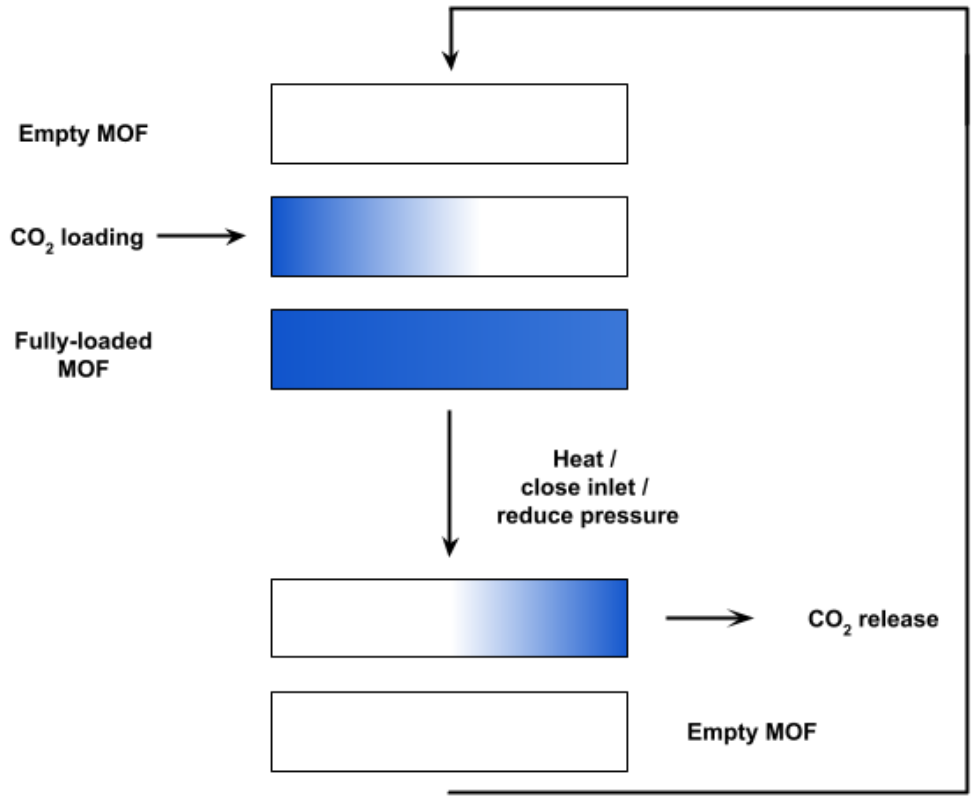

Figure 44: Schematic representation of CO_2 removal from the pores.

3.1.2. Hydrogen Capture and Storage

Hydrogen is considered a very promising clean energy source because the only product obtained from its combustion is water. Even if hydrogen is very abundant on Earth's surface, hydrogen gas (H_2) is very rare, and it is produced mainly by water electrolysis. Since its synthesis requires energy, it is not considered a real energy source, but an energy carrier (or vector). A big issue to solve when dealing with hydrogen is its storage. As seen for CO_2, hydrogen storage can be of physical or chemical nature. The former is represented by cryogenic storage: hydrogen is cooled down to cryogenic temperatures (usually at T = 77 K or below) and then stored as high-density gas or liquid. Consequently, this method is characterized by high operational costs and energy consumption. An alternative to the employ of low temperatures is storage at high pressures in pressurized tanks that are commonly heavy and expansive. Chemical storage relies on the

chemical reaction of hydrogen with lightweight elements from the groups 13/15 of the periodic table (B, Al, N) to form the so-called Lightweight Inorganic Hydrides (like ammonia borane, hydrazine bis(borane), lithium and sodium borohydrides, etc…), solid and easy-to-handle materials featured by high gravimetric H_2 content. They can release high-purity hydrogen upon mild thermal treatment. MOFs could represent a viable alternative storage system because they possess extraordinary properties for storage and reversible gas uptake. Hydrogen is usually adsorbed in MOFs through weak Van der Waals interactions between the gas and the framework (physisorption), but it can also interact strongly with specific polar sites, if present. There are several factors that influence hydrogen adsorption and that must be kept in mind when planning to synthesize a MOF for this purpose. For sure, surface area has a predominant role in the amount of gas that can be adsorbed by the MOF, so the use of longer linkers is to be preferred. Nevertheless, a large pore dimension should be avoided because smaller pores maximize the interaction between hydrogen molecules and the framework resulting in a gain of adsorption capacity (a pore size around 7Å is the optimum)[124]. The presence of coordinatively unsaturated metal centers or open metal sites are proven to enhance the adsorption of hydrogen because the σ-electrons of H_2 interact with the vacant d-metal orbitals, while the occupied d-orbitals of the metal can back-donate electrons into the σ*-orbitals of H_2[125] [Figure 45]. Another method to enhance hydrogen uptake is to incorporate linkers that possess polar or polarizable functional groups.

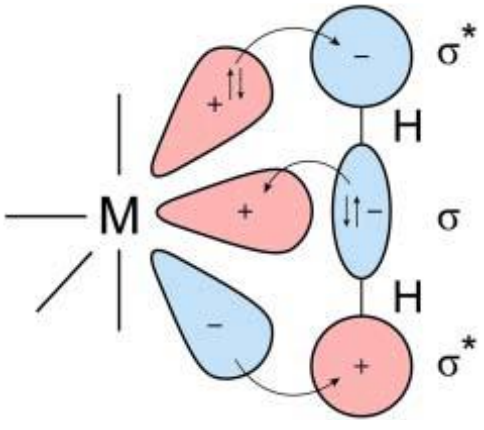

Figure 45: Coordination of H_2 molecule to an open metal site. [1]

MOFs for hydrogen storage must comply the U.S. Department of Energy (DoE) guidelines for hydrogen storage systems. These requirements foresee a gravimetric H_2 uptake of at least

5.5 wt.% with short refueling times and cycling stability at the operating temperatures (between 30° and 50° C). To date, no suitable candidate to satisfy these requirements has been found yet.

3.1.3. Methane Capture and Storage

Methane (CH_4) is the main component of natural gas, and it has the potential to replace gasoline or diesel as car fuel. Methane possesses a high gravimetric heat of combustion, and its combustion releases the smallest amount of CO_2 among all the other hydrocarbons. Even for methane, a big issue to solve is its storage. Currently, the most exploited storage technologies are cryogenic liquefaction and compression at room temperature. However, these methods present the same disadvantages described in the case of hydrogen. Methane storage is of particular interest for automotive applications in which the gas must be stored inside a limited volume tank. For this reason, it is necessary that the MOF not only is able to store copious quantities of gas, but also that the most part of it can be released within the working pressures (high working capacity)[126]. Since the working capacity depends on the structure and on the nature of the MOF, some factors must be taken into account to synthesize a high-performance material for this purpose. As for other gas adsorption applications, even in the case of methane is compulsory to maximize the adsorption sites inside the framework. Methane is typically adsorbed near the polar SBUs or on the faces and edges of the linkers but can also interact with open metal sites [Figure 46]. However, in the case of methane, where the working capacity is of fundamental importance, large surface areas are not always correlated with a large working capacity[127]. A principal factor to consider for a high methane uptake is the optimization of the framework-methane interaction. Based on this, a smaller pores dimension is more desirable because it increases the strength of the dispersion forces between the surface and gas molecules, enhancing the adsorption capacity. For the application in methane storage, MOFs not only have to possess a high adsorption and working capacity, but also, they must have a high cycle stability and low cost of production[128].

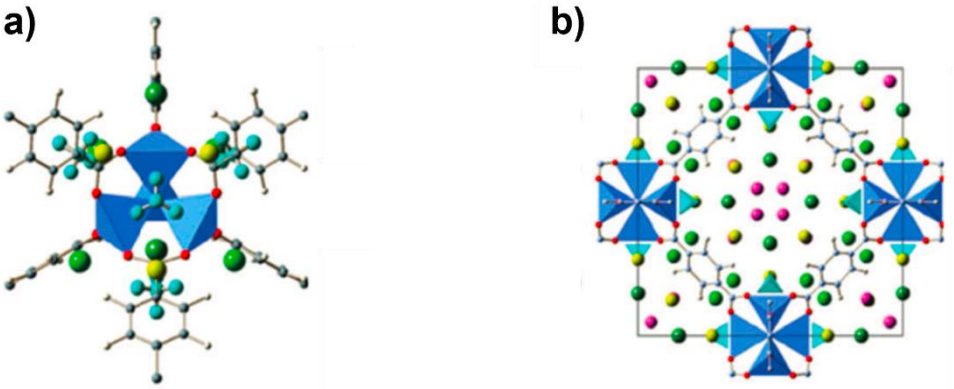

Figure 46: Example of methane adsorption sites in MOF-5. Around the SBU (a) and inside the pores (b). Color code: green spheres – primary adsorption sites, yellow spheres – secondary adsorption sites, violet spheres – extra adsorption sites. [126]

3.2. Gas Separation

The gas adsorption properties of MOFs can also be exploited to separate the individual gases that are part of a gaseous flow. Usual gas separation techniques involve cryogenic distillation or membrane separation[129]. However, in recent years separation methods based on adsorption have become a key tool in industry because of their milder operation conditions. Under this perspective, the well-known tunable properties of MOFs make them very promising candidates in this field of application. The separation can be achieved both through a selective adsorption (physisorption or chemisorption) of one adsorbate to a specific adsorption site of the MOF (thermodynamic separation) or through exploitation of the different diffusivity[6] of the mixture components (kinetic separation). However, in most cases both mechanisms are present together. In addition to the mechanical stability, the high surface area and the pore size, a good adsorbent must show good adsorption capacity and selectivity towards the components of the mixture. The former depends mostly on the nature of the adsorbent, as well as from the operational conditions (pressure and temperature). The latter is related to the strength of the adsorbent-adsorbate interactions.

[6] The rate at which particles can spread through the MOF pores and channels.

3.2.1. Thermodynamic Separation

Thermodynamic separation is a process common for MOFs that have pores large enough to allow all the components of the mixture to freely enter in the framework. In this case, the separation of the components is related to the different thermodynamic affinity the gases have for the MOF surface (mirrored in the related Q_{st} values). A measure of the strength of the adsorbent-adsorbate interaction is given by the value of the Q_{st} that can be experimentally calculated from the adsorption isotherm of a particular gas. The strength of the interaction depends only on the surface characteristics of the material and on the physical characteristics of the target gas (polarizability, dipole, or quadrupole moment).

The advantage of using MOFs is the possibility to tune the selectivity for a particular gas introducing specific functionalities or binding sites inside the framework. Thermodynamic selectivity is based both on chemisorption and physisorption. As an example, let us consider a mixture containing CO_2 and N_2. CO_2 is featured by a higher polarizability and quadrupole moment with respect to N_2. So, the presence of polar sites inside the framework will result in a higher affinity for CO_2 and, consequently, a higher selectivity toward this gas [Figure 47].

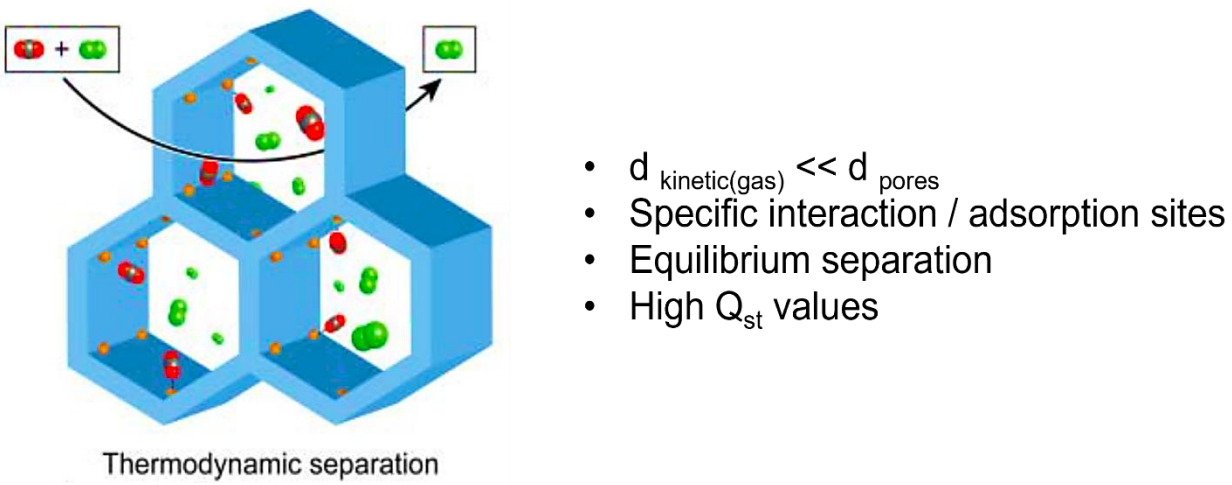

Figure 47: Representation of thermodynamic separation of a mixture of CO_2 (black and red spheres) and N_2 (green spheres). [1]

3.2.2. Kinetic Separation

Kinetic separation [Figure 48] is common for MOFs that possess small pores that do not permit to large molecules to enter inside the structure. However, this kind of separation is always accompanied by a drop in the pressure, so it is usually avoided. The kinetic separation mechanism

is also based on the different diffusion rates of the gases that can enter the pores. Gas molecules with high mobility or diffusivity can permeate the space more quickly with respect to molecules with lower mobility. Diffusion rates are determined mainly by the relationship between the size and shape of the pores and the size and shape of adsorbate molecules and by the affinity to adsorption sites. When the pore size is larger than the kinetic diameters of the gas molecules, we have a "molecular diffusion". In this case, the only resistance to the gases flow is derived from molecule-molecule collisions, because a molecule-pore wall collision is improbable. If the pore size is similar to the kinetic diameter ($d_{kinetic\ (gas)}$) of the gas molecules the diffusion mechanism takes place according to the "Knudsen diffusion". In this case, the molecule-pore wall collisions are more frequent with respect to the molecule-molecule collisions. Kinetic separation is usually applied to mixtures containing gases with significantly different kinetic diameters. For example, it is almost impossible to kinetically separate a mixture of CO_2 and N_2 because they have remarkably similar dimension, but it is possible to do that for a mixture of *iso*-butylene and *trans*-butylene.

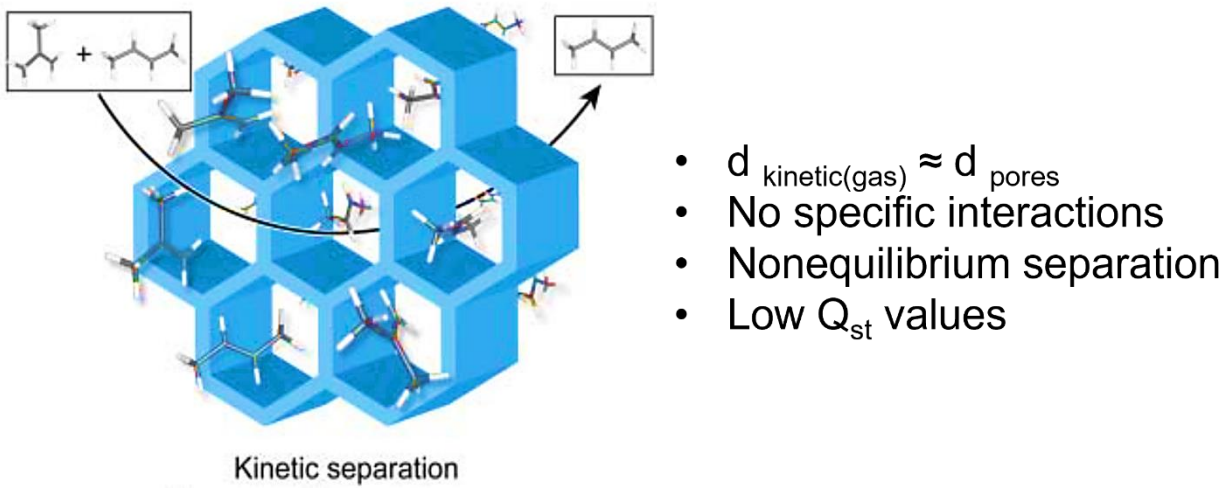

Figure 48: Representation of kinetic separation of a mixture of *iso*-butylene and *trans*-butylene. [1]

3.3. Luminescence Sensing

Luminescent materials are those that, in response of an external stimuli, release energy in the form of electromagnetic radiation in the visible region[130]. These materials have been explored for a number of different applications in displays, sensing and optical devices. Since luminescence

is one of the easiest transduction mechanisms, luminescent materials gained great attention also for their possible use as chemical sensors[7].

Even MOFs can show luminescent properties and thus act as chemical sensors. Among all the other materials used for this purpose, MOFs possess a number of advantageous properties that make them very interesting candidates for this application field. Porosity allows adsorption of luminescent molecules as chromophores, concentrating them in a narrow space and thus increasing the response sensitivity. The tunability of the pore size can be exploited to enhance the selectivity for a specific target molecule. Selectivity can also be achieved through the presence of different functional groups on the linker skeleton responsible for host-guest interactions. Furthermore, MOFs can possess emissive properties by themselves. Luminescence in MOFs can have different origins: (I) metal ion-based, (II) organic linker-based, (III) charge transfer and (IV) guest induced [Figure 49].

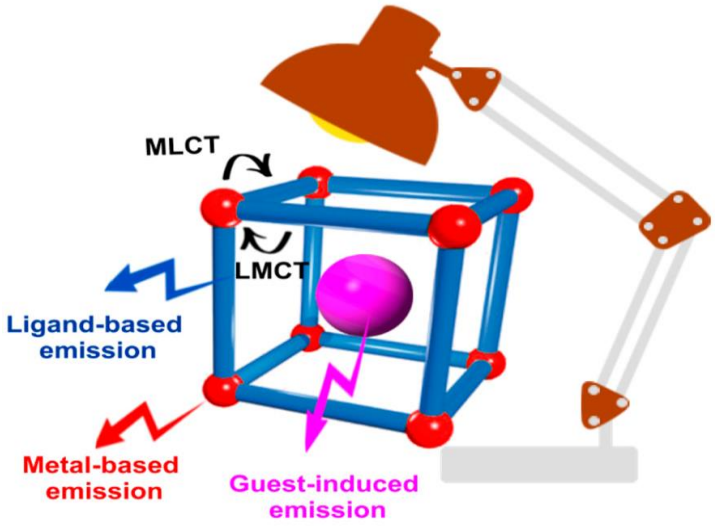

Figure 49: Representation of the mechanisms at the origin of MOFs luminescence. [25]

Metal-based luminescence is obtained using emissive metal ions. Even if there are some example of luminescent MOFs based on d^{10} metal ions[131], the most exploited metals are lanthanides (Ln^{3+}). Lanthanides have characteristic 4f-4f transitions and generate a characteristic color emission in the range from ultraviolet (UV) and near-infrared (NIR). Unfortunately, since f-f transitions are forbidden by the Laporte selection rules, lanthanides suffer from weak light adsorption and for this reason their direct excitation is inefficient. To enhance their emission

[7] Analytical tools that provide information about the chemical composition of the environment in which they are introduced.

intensity, in MOFs it is possible to exploit the presence of the organic linkers that can participate in the energy transfer process in a mechanism called "antenna effect"[132]. In this case, light is adsorbed by the organic linkers around the lanthanides ions, then the energy is transferred to the metal centers that can emit at higher intensity.

Organic linkers-based luminescence of MOFs is attributable to the presence of aromatic heterocycles with highly π-conjugated electrons (thiazoles, thiophenes) that absorb in the UV-visible region. However, the emission properties of these molecules when embedded within a MOF network (emission lifetime and maximum emission wavelength) are different from those of the freestate. In fact, organic linkers emission is affected by the coordination environment: proximity of other molecules in the solid state, size and nature of metal ions and orientation of the linkers[133]. For example, the MOF $[Zn_3(\mu_5\text{-}PTC)_2(\mu_2\text{-}H_2O)_2]$ (H_3PTC = pyridine-2,4,6-tricarboxylic acid) show a strong blue emission at λ_{max} = 467 nm when excited at λ = 338 nm, while the free linker displays a weak emission at 415 nm under the same conditions[134].

Charge-transfer luminescence is generated from a transition from the charge-transfer excited state to the ground state and is frequently observed in MOFs containing d^{10} metals. Typically, in MOFs two different charge-transfer mechanisms can be observed: Metal-Ligand Charge-Transfer (MLCT) and Ligand-Metal Charge-Transfer (LMCT) [Figure 50]. The former happens when an electronic transition occurs between a metal-centered orbital and an organic linker-localized orbital. As an example, the MOF [Mn(HBIDC)] (H_3BIDC = 1H-benzimidazole-5,6-dicarboxylic acid) shows a strong emission at λ_{max} = 726 nm that is red-shifted with respect to the free linker (λ_{max} = 440 nm). In the MOF, there is a charge transfer from the Mn^{2+} ion to the π-conjugated system of benzimidazole [135]. The LMCT mechanism is the opposite of MLCT and involves an electronic transition from an organic linker-localized orbital to a metal-centered orbital. For example, the MOF $[Zn(2,3\text{-}PYDC)(BPP)]\cdot 2{,}5H_2O$ (H_2-2,3-PYDC = pyridine-2,3-dicarboxylic acid and BPP = 1,3-bis(4-pyridyl)propane) shows an intense emission at λ_{max} = 436 nm and λ_{max} = 438 nm upon excitation at λ = 372 nm and λ = 370 nm respectively, while the linker H_2-2,3-PYDC only displays a very weak luminescence for excitation at λ = 370 nm[136].

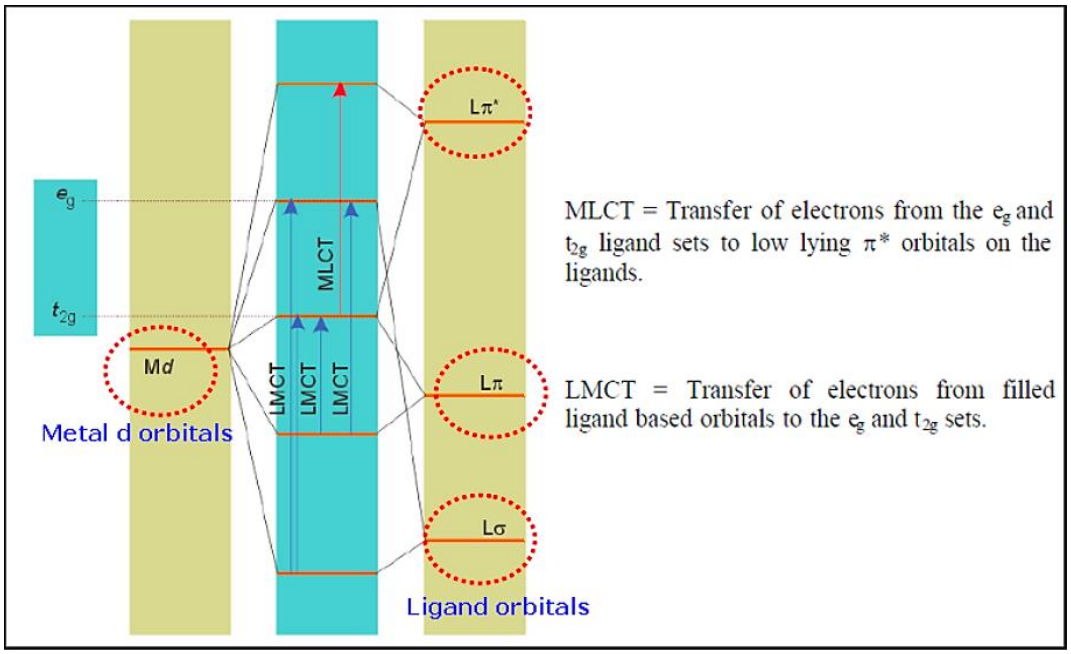

Figure 50: Scheme for the MLCT and LMCT charge transfer.

Guest-induced luminescence is related to the porosity of MOFs and their ability to encapsulate luminescent guest molecules such as lanthanides and fluorescent dyes. In this case, the incorporation inside the MOF structure improves the emission yield. For example, lanthanides suffer from a strong emission quenching in aqueous environments. When encapsulated inside a MOF, this quenching effect is smoothed through the "protection" provided by the MOF walls. This is the case of the lanthanide-doped bio-MOF-1 $[Zn_8(ad)4(BPDC)_6O]\cdot 2Me_2NH_2 8DMF 11H_2O$ (ad = adeninate and H_2BPDC = biphenyl-4,4'-dicarboxylic acid)[137] where different lanthanides (3+) ions were inserted inside the structure of bio-MOF-1 to obtain Ln^{3+}@bio-MOF-1. When excited at λ = 365 nm, the doped MOFs showed an emission (visible at naked eye) characteristic of the element. This emission was even detected in an aqueous environment[138] [Figure 51].

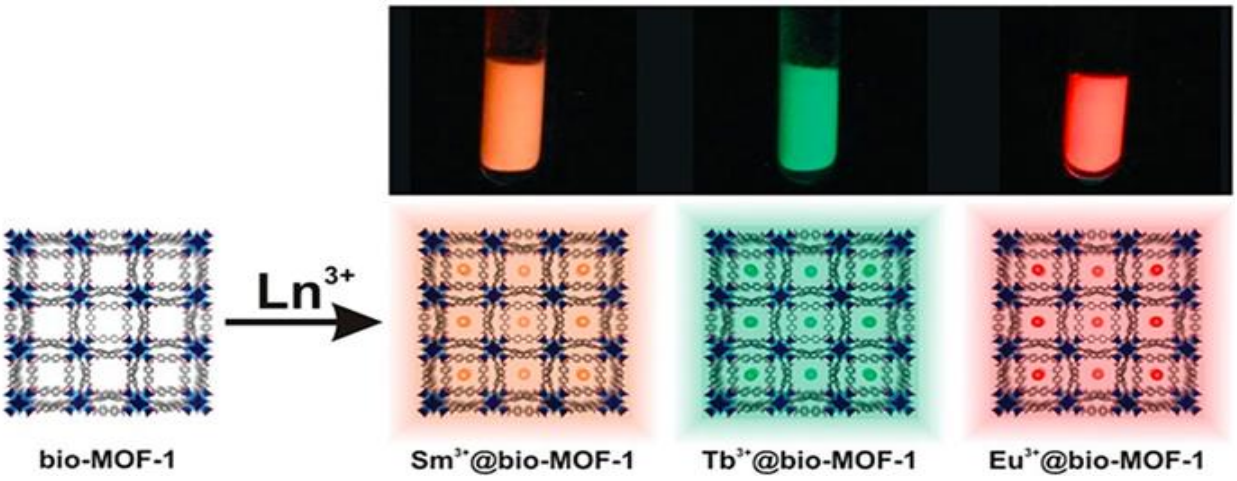

Figure 51: Emission of the lanthanide ions doped bio-MOF-1. [138]

As chemical sensors, MOFs are very promising because their luminescent properties are very sensitive and dependent on their structural characteristics and on the nature of the guest species. Also, the porosity of MOFs allows for a reversible uptake and release of the guests, with easy regeneration and re-utilization. A large number of substances have been successfully detected with MOFs: cations[139] and anions[140], small molecules[141] , gases and vapors[142] and they are also sensitive to variations of the environmental conditions (pH[143] and temperature[144]) [Figure 52].

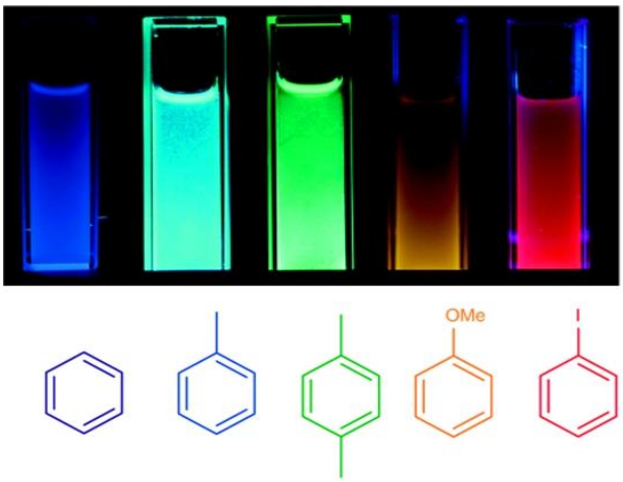

Figure 52: Example of luminescent emission of a Zn MOF in presence of different substances. The resulting luminescence is obtained after the suspension of the MOF in solution of each molecule, and excitation at 365 nm. [141]

The tunability of MOFs luminescence emission find applications in light-emitting devices both for white light (that is important in displays and lighting)[145]and for NIR emitting (useful in consumer electronics and night-vision illumination sources)[146]

3.4. Heterogeneous Catalysis

Inorganic and porous zeolites have always been one of the most important classes of commercially available heterogeneous catalysts [147]. Due to the structural analogy with these compounds, one of the earliest proposed applications for MOFs was catalysis. Although zeolites and MOFs share some of the relevant characteristics for a good catalyst like large internal surface area and porosity, MOFs have all the features to overcome zeolites in an applicative context (at least under mild conditions). In fact, it is possible to synthesize a huge variety of different structures that can also be tuned to include functionalities suitable for catalysis or to achieve an optimum level of control over the reaction environment. Moreover, the structure can be

modified through PSM and pores can be decorated with complex catalysts that would not survive to the synthesis conditions of MOFs[148]. Also, the crystallinity of MOFs allows for a clear investigation of the distribution of catalytically active sites within the framework and of its influence on the catalytic activity.

Catalysis is a very promising application for MOFs, for several reasons: the presence of more than one possible catalytic active site in the structure (metal nodes and the (functionalized) linkers), the possibility to encapsulate molecules of big dimensions, huge quantities of substrate or other catalytically active species (as nanoparticles), the high chemical and thermal stability and the easy post-reaction product separation and catalyst recyclability. [149]. Also, MOFs structure may improve the catalytic efficiency, stabilizing the transition states and orienting reactants in space. Nowadays, MOFs can be used as heterogeneous catalysts for a lot of different reactions as Heck reaction[150], Sonogashira coupling[151], hydrogenation of unsaturated organic compounds[152], in electrocatalysis (they must possess redox-active metal sites)[153] or in photocatalysis (trough LMCT and MLCT mechanisms)[154]. Nevertheless, one of the most interesting applications is Carbon Capture and Utilization (CCU), to capture CO_2 and utilize it as building block for the synthesis of other added-value chemicals such as formic acid or methanol[155]. MOFs with good CO_2 adsorption properties (see paragraph 3.1.1. – Carbon Dioxide Capture and Storage) are able to concentrate a large quantity of gas inside the pores, thus improving the catalytic efficiency. Then, different CO_2-conversion reactions can be catalyzed using MOFs, like epoxidation of olefins[156] or conversion into cyclic carbonates[157] [Figure 53].

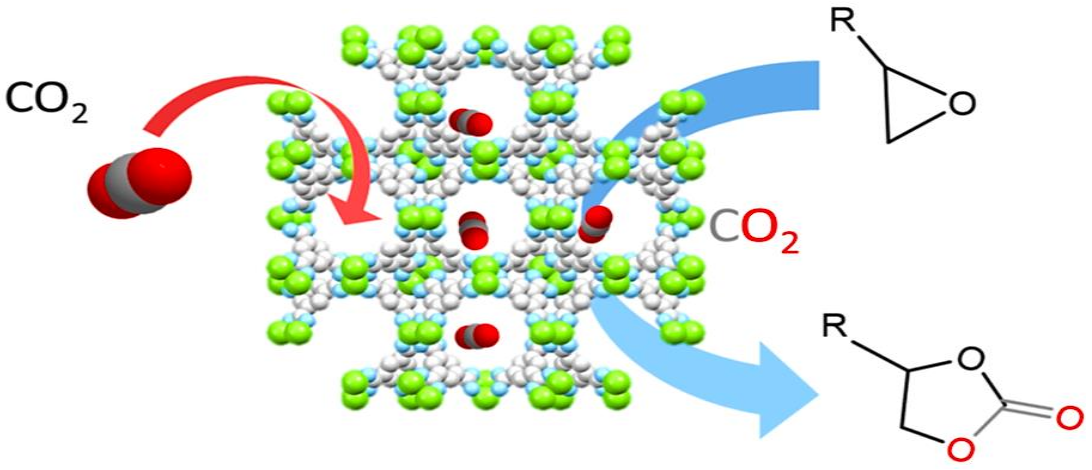

Figure 53: Representation of cycloaddition reaction to epoxides, using CO_2 captured by MOFs.[156]

Examples of the use of MOFs as heterogeneous catalysts will be reported in chapter 8.

3.5. Drug Delivery

In recent years, MOFs have been tested as carriers for drug delivery applications. The high surface area of MOFs and their porosity allow for the loading of a large quantity of drug molecules inside the structure[158]. The possibility to tune the framework permits to improve the stability of the MOF in a biological environment or the loading of the drug, resulting in a desirable high local concentration[159]. MOFs pores can also be designed to accelerate or to slow the diffusion of the therapeutic molecules.

The loading of the drug is governed by physical properties of MOFs (surface area, pore size and void volume), but the stabilization inside the structure is governed by chemical properties (van der Waals forces, π-π stacking or hydrogen bonding). There are two methods to encapsulate the drug inside MOFs: the *one-pot synthesis* and the *post-synthetic encapsulation* (impregnation). The first method foresees the introduction of the target molecule inside the reaction solvent to form a [drug@MOF] composite directly [Figure 54]. This method is useful to incorporate molecules of big dimensions even in MOFs with small pores. However, the synthesis method and reaction conditions must be chosen well to avoid the degradation of the therapeutic molecule[160].

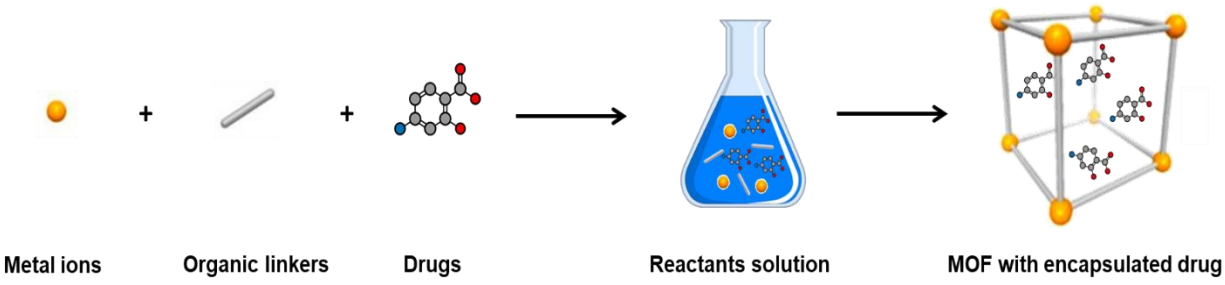

Figure 54: Schematic representation of *one-pot synthesis* of MOF with encapsulated drug molecules.

The second method involves the loading of the drug inside the MOF after its synthesis. To do that, the MOF is soaked in a solution containing the therapeutic molecule that diffuses inside the pores[161] [Figure 55].

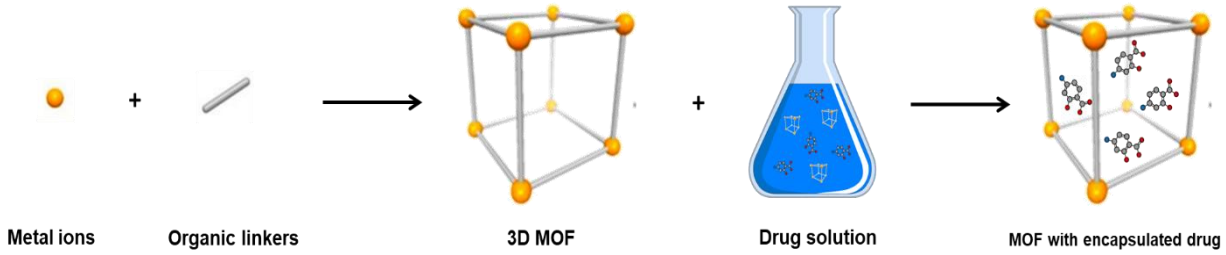

Figure 55: Schematic representation of *post-synthetic encapsulation* of drugs inside MOFs structure.

The loading efficiency (%) can be calculated as (mass of loaded drug / mass of drug loaded MOF)x100. The precise amount of adsorbed drug can be assessed through thermogravimetric analysis (TGA), looking at the step in the thermogravimetric profile relative to the drug mass loss in a certain temperature interval[162].

The use of MOFs as drug-carriers presents a number of advantages. One of the problems faced by drugs is the solubility in physiological conditions, which may limit their application due to a poor absorption. MOFs can load large amounts of the poorly soluble drug and carry it to the site where it will be released, without any solubility problem [163]. Many drugs are sensitive to acids, heat, oxygen and other external factors. It was shown that the stability of the drug significantly improves when loaded inside a MOF[164]. Last, MOFs can be used to control the release of the drug during time. In this way, it is possible to avoid the "burst effect" i.e. the fast release of the active principle and obtain a continuous release of small amounts of drug that can last for days (this could be particularly good after surgery when a slow release of antibiotics could help to prevent the occurrence of infections)[165].

The drug release by MOFs can occur in two different ways. *Spontaneous release* is typical of MOFs that are not very stable under physiological conditions. In this case the release is due to the progressive demolition of the structure of the MOF. *External stimulation release* happens when the release is triggered by a change in environmental conditions like pH or temperature[166] [Figure 56].

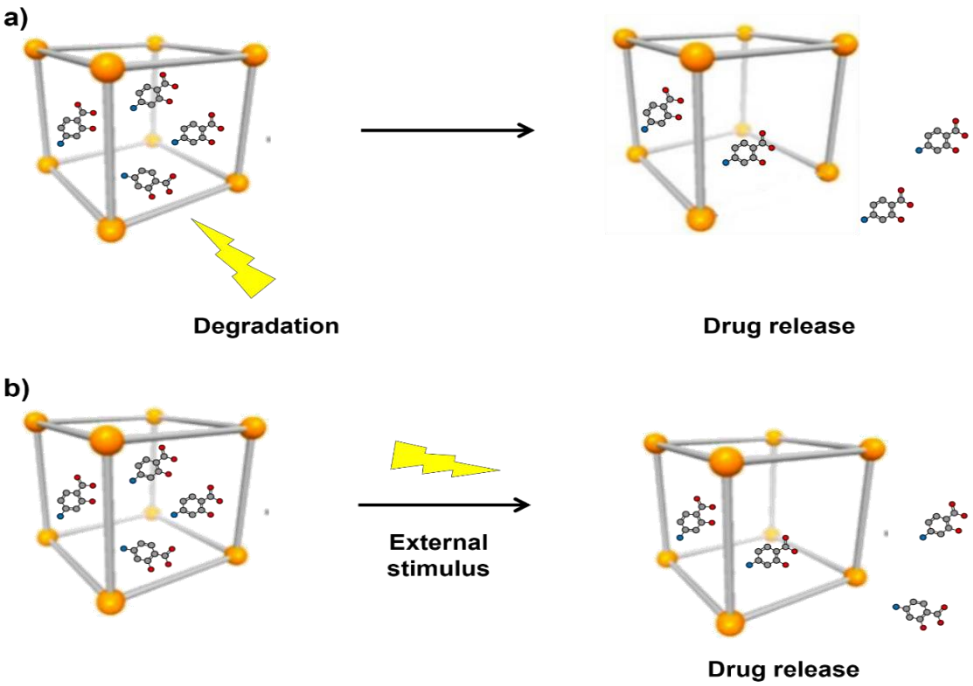

Figure 56: Schematic representation of drug release of MOFs. Spontaneous release happens when the MOF degrades under physiological conditions (a). External stimulation release is triggered by a change in the environmental conditions (b).

3.6. Water Purification

Nowadays, most of the industries (such as paper, textile, food processing, pharmaceutical and so on) discharge a huge number of wastes into water bodies. This is one of the principal causes of scarcity of global freshwater. Currently, almost 50% of the world population is living in water-stressed areas, so that one of the main goals of the Sustainable Development Agenda of United Nations is providing universal access to clean freshwater[167]. The increasing need for freshwater has prompted the development of new methods for the desalination of seawater or for the harvesting from groundwater that are the "natural options" to increment the quantity of available freshwater, as well as development of wastewater management and its recycle[168]. Recycling wastewater means removing all the contaminants of emerging concern (CEC) to make water fit for human consumption. The term "contaminant" is defined, according to the Safe-Drinking Water Act (SDWA), as any physical, chemical or biological matter or substance present in water that can be poisonous or harmful for the living beings[169]. Common contaminants that can be found in water are both inorganic and organic pollutants. The former are usually metal ions (heavy or radioactive)[170] and oxyanions/cations. These contaminants are generally very persistent in the environment because of their high-water solubility and mobility, and hence they are easily bioavailable. Consequently, they show bioaccumulation/biomagnification phenomena

in the food chain and also in the human body[171]. Due to the toxic and sometimes lethal characteristics of these inorganic species also at low concentration levels (ppm), these kind of contaminants are the main focus for water remediation.

Organic pollutants include detergents, oils, dyes pesticides, herbicides, insecticides, hydrocarbons, food additives and personal care products (PCPs)[172]. Organic contaminants are less persistent than inorganic ones; however, they are produced in very large amounts making them pseudo-persistent in our ecosystem.

The ever-increasing presence of pollutants in the water basins led to the setting up of a regulation to establish the acceptable levels of contaminants in water[173]. Nowadays, in order to purify water to fit into these parameters, there are lot of different strategies that can be used: membrane separation[174], photocatalysis[175], ozonation[176], and precipitation[177] among all. All these methods have advantages and disadvantages, but they suffer from high operational cost, low decontamination activity and some of them generate secondary pollutants. Adsorption of pollutants using porous materials represents a low-cost and flexible alternative to remove contaminants from water[178]. Relative to this application, zeolites, mesoporous clays, and porous carbons showed good performances in the adsorption of different pollutants present in wastewater[179]. MOFs have obviously started to be exploited in this context as well. MOFs present a long-lifetime and can be easily recycled and reutilized simply by washing them to remove the adsorbed contaminants. However, water stability is a necessary prerequisite to use MOFs in water purification processes, but this feature is not very common for MOFs[180]. Nevertheless, it is possible to synthesize water-stable MOFs in diverse ways: (I) coupling high-valence metal ions and carboxylate-type linkers or (II) N-containing linkers and divalent metals, (III) the introduction of hydrophobic functionalities on the linkers and (IV) the minimization of the number of open-metal sites[181].

There are many studies on the application of MOFs in the removal of pollutants from wastewater. MOFs show very good performances towards the different (inorganic and organic) contaminants present in aqueous media. As for inorganic pollutants, MOFs are capable to remove toxic heavy metal ions[182,183], inorganic acids[184], oxyanions or oxications[185] and also nuclear wastes[186]. In the case of the organic ones, examples of species that can be removed using MOFs are pharmaceutical and personal care products[187], feed additives (usually organo-arsenic compounds)[188], agricultural products[189], industrial wastes (like bisphenol A)[190] and dyes[191].

Chapter 4

ZIRCONIUM MOFS FOR LUMINESCENT APPLICATIONS

This chapter is based upon the following publication:

Zirconium Metal–Organic Frameworks Containing a Biselenophene Linker: Synthesis, Characterization, and Luminescent Properties.

Inorganic Chemistry; **2020** *59* (21), 15832-15841

Giorgio Mercuri, Marco Moroni, Andrea Fermi, Giacomo Bergamini, Simona Galli, Giuliano Giambastiani and Andrea Rossin

4.1. Aim of the Work

Zirconium(IV) MOFs are a very popular class of compounds that witnessed a widespread diffusion after the discovery of the first member of the family in 2008: UiO-66[192]. In these MOFs, there are [Zr_6] octahedral nodes that show high chemical and thermal stability when combined with carboxylate donors[193]. The coordination bonds present in these compounds are particularly strong because of the oxophilic character of Zr(IV) cation (d^0 valence electronic configuration) that perfectly matches with oxygen-based strong σ donors like the -COO^- groups. Carboxylate-based linkers are usually made of fully carbocyclic spacers and much fewer examples are reported of spacers containing heterocycles like thiazole, thiophene and selenophene. In particular, for selenophene there are only a small number of scientific papers, and they are based on the monocyclic selenophene-2,5-dicarboxylic acid[194]. Fully organic selenophene polymers are featured by peculiar luminescence properties ascribed to the Highest Occupied Molecular Orbital (HOMO) – Lowest Unoccupied Molecular Orbital (LUMO) energy levels[195]. The resulting absorption and emission band ranges make them useful for potential technological applications in organic solar cells and for light-emitting diodes (LEDs).

In this work, a new bicyclic ditopic linker based on selenophene was designed and synthesized in good yield. The new linker 2,2'-biselenophene-5,5'-dicarboxylic acid (H_2SpSp) is isostructural with two other five-membered heterocycles based on thiophene (2,2'-bithiophene-5,5'-dicarboxylic acid, H_2TpTp) and on thiazole (2,2'-bithiazole-5,5'-dicarboxylic acid, H_2TzTz) [Figure 57].

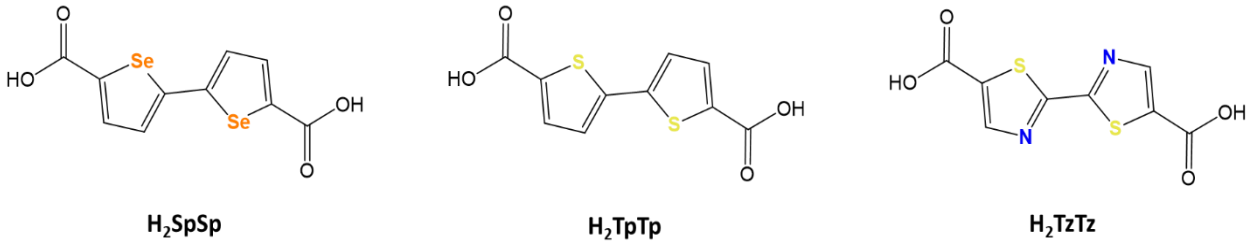

H_2SpSp H_2TpTp H_2TzTz

Figure 57: Molecular structures of the three linkers used in this work.

The selenophene-based linker has been reacted with a zirconium salt under solvothermal conditions to obtain a new zirconium-MOF of formula $[Zr_6O_4(OH)_4(SpSp)_{3.8}Cl_{4.4}]$ that has been fully characterized in the solid state. This MOF is isostructural to the already known analogues with bithiophene[196] and bithiazole[197]. Given the structural analogy between the three linkers and the resulting MOFs, three Zr mixed-linkers MOFs (MIXMOFs) have also been synthesized: two "double-mixed" MOFs (biselenophene – bithiophene $[Zr_6O_4(OH)_4(SpSp)_{2.6}(TpTp)_{1.3}Cl_{4.2}]$ and biselenophene – bithiazole $[Zr_6O_4(OH)_4(SpSp)_2(TzTz)_{1.8}Cl_{4.4}]$) and the "triple-mixed" biselenophene – bithiophene – bithiazole MOF $[Zr_6O_4(OH)_4(SpSp)_{1.6}(TpTp)_{1.2}(TzTz)_{1.4}Cl_{3.6}]$. Unfortunately, all MOFs are defective (missing linkers). As inferred from X-ray fluorescence, elemental analysis and PXRD structure determination, these missing linkers are replaced by chloride anions that are bound to the metal centers. Defects like missing-linkers can occur when modulators are employed during MOF synthesis and are common in UiO-type MOFs[198]. The actual linker composition of the mixed-linker MOFs has been assessed through ^{1}H-NMR signal integration after sample digestion in acidic solutions. This information has been exploited to refine the crystal structures of the compounds, obtained through PXRD analysis.

Finally, the luminescent properties of the four MOFs and of their constitutive linkers has been evaluated in the solid state and in DMF suspension. Both linkers and related MOFs are luminescent under UV irradiation, with an emission wavelength that falls in the blue-green visible region.

4.2. Experimental Details

4.2.1. Materials and Methods

Commercially available reagents were obtained from their vendors, and no further purification was carried out. Literature protocols were followed to make the bithiazole linker H_2TzTz[197], the

bithiophene linker H_2TpTp[196] and ethyl selenophene-2-carboxylate[199]. In the C–C homocoupling reactions, solvents were previously distilled following standard purification procedures.

Deuterated solvents (Sigma-Aldrich) were preliminary dried through storage over 4 Å molecular sieves, and they subsequently underwent three freeze−pump−thaw cycles before use. NMR spectra were recorded on a Bruker AVANCE 400 MHz spectrometer, with tetramethyl-silane as the zero reference for the ^{1}H and ^{13}C-NMR chemical shifts (δ, ppm).

Fourier transform infrared (FTIR) spectra were collected as KBr pellets on a PerkinElmer Spectrum BX Series FTIR spectrometer, in the spectral range 4000 − 400 cm^{-1}, with a resolution of 2 cm^{-1}.

Thermogravimetric analysis (TGA) was made under an inert gas (N_2) flow (flow rate: 100 mL min^{-1}) at a heating rate of 10 K min^{-1} on an EXSTAR Seiko 6200 thermogravimetric analyzer (TG-DTG). Differential scanning calorimetry (DSC) was performed using ∼10 mg of powdered samples placed in alumina crucibles on a Netzsch STA 409 PC analyzer under an N_2 flow (flow rate: 40 mL min^{-1}) in the 303 − 1173 K temperature range (heating rate: 10 K min^{-1}). The raw data were corrected against a background curve ("blank" experiment) acquired under the same experimental conditions.

Elemental analyses (carbon, hydrogen, nitrogen, and sulfur) on all solid samples were obtained through a Thermo FlashEA 1112 Series CHNS-O elemental analyzer, with an accepted tolerance of ±2%.

For the electrospray ionization mass spectrometry (ESI-MS) experiments, acetonitrile solutions of Et_2SpSp were prepared using 0.5 mg of the diester dissolved in 1 mL of acetonitrile in an Eppendorf tube and then diluted to 100 ng μL^{-1} with acetonitrile and 1% formic acid. As for H_2SpSp, aqueous solutions were prepared using 1 mg mL^{-1} and then diluting to 10 ng μL^{-1} with 95% (v/v) water and 5% (v/v) acetonitrile. The as-obtained diluted solutions were directly infused into the ESI interface of the instrument, a Thermo LTQ orbitrap (Thermo, San Jose, CA) equipped with the Xcalibur 2.0 software. Working conditions were as follows. (a) Positive polarity: spray voltage 5 kV, capillary voltage 35 V, capillary temperature 548 K, and tube lens 110 V. (b) Negative polarity: spray voltage 5 kV, capillary voltage −18 V, capillary temperature 563 K, and tube lens −87 V. The sheath gas was set at 10 au, and the auxiliary gas was kept at 3 au.

PXRD qualitative measurements were carried out in the 4 − 50° 2θ region with a Panalytical X'PERT PRO powder diffractometer equipped with a diffracted-beam nickel filter, a PIXcel solid-state detector, and a Cu Kα X-ray source (λ = 1.5418 Å). Slits were used on both the incident

(Soller slit aperture 0.25°; divergence slit aperture 0.5°) and diffracted (anti-scatter slit height 7.5 mm) beams.

X-ray fluorescence (XRF) analyses were performed on powdered batches (ca. 10 mg for each MOF sample) with a Panalytical MINIPAL 2 instrument equipped with a Cr X-ray source. Single crystal X-ray diffraction data were collected at low temperature (T = 100 K) on an Oxford Diffraction XcaliburPX diffractometer equipped with a CCD area detector using the Cu Kα radiation (λ = 1.5418 Å). The program used for the data collection was CrysAlis CCD 1.171. Data reduction was carried out with the program CrysAlis RED 1.171, and the absorption correction was applied with the program ABSPACK 1.17.

Direct methods, as implemented in Sir2014, were used to solve the crystal structure, while the structure refinement was performed by full-matrix least-squares against F^2 implemented in SHELXL-2018. All the non-hydrogen atoms were refined anisotropically while the hydrogen atoms were fixed in calculated positions and refined isotropically with atomic displacement parameters depending on that of the atom to which they are bound. The geometrical calculations were performed by PARST97, and molecular plots were produced by the program ORTEP3.

4.2.2. Compounds Synthesis

Synthesis of Diethyl-2,2'-Biselenophene-5,5'-dicarboxylate (Et_2SpSp): 2,2'-Biselenophene 5,5'-diester was prepared through an Ag(I)/Pd(II)-catalyzed homocoupling of ethyl selenophene-2-carboxylate, following the literature procedure found for its thiophene analogue[200]. The full experimental details are reported hereafter, for the sake of completeness. Ethyl selenophene-2-carboxylate (480 mg, 2.36 mmol) was dissolved in freshly distilled dimethyl sulfoxide (DMSO; 14 mL) in a Schlenk round-bottom flask equipped with a magnetic stirring bar. Then, silver fluoride (AgF; 600 mg, 4.72 mmol) and the Pd(II) catalyst bis(benzonitrile)palladium dichloride [$PdCl_2(C_6H_5CN)_2$; 27.1 mg, 0.07 mmol] were added to this solution while stirring at ambient temperature. Afterward, the resulting mixture was heated at 333 K for 5 h. Then, it was cooled to room temperature and passed through a Celite pad, which was successively washed with chloroform (3 × 10 mL). The dark-yellow organic filtrate was washed with water (3 × 10 mL) and the aqueous layer extracted with chloroform (3 × 10 mL). The combined organic layers were dried over anhydrous sodium sulfate and concentrated under reduced pressure to leave a crude solid that was finally purified through column chromatography on silica gel (eluent: petroleum

ether/ethyl acetate 85:15). The dark-yellow solid residue obtained after solvent removal was recovered and dried under vacuum. Yield: 405 mg (85%). Single crystals suitable for X-ray diffraction were obtained through ambient-temperature slow evaporation of an ethyl acetate concentrated solution [Figure 62].

^{1}H-NMR (400 MHz, CD_2Cl_2, 298 K) [Figure 58a]: δ 1.36 (t, $^{3}J_{HH}$ = 7.1 Hz, 6H, H^{7}), 4.31 (q, $^{3}J_{HH}$ = 7.1 Hz, 4H, H^{6}), 7.37 (d, $^{3}J_{HH}$ = 3.9 Hz, 2H, H^{3}), 7.90 (d, $^{3}J_{HH}$ = 3.9 Hz, 2H, H^{2}).

^{13}C-NMR (400 MHz, CD_2Cl_2, 298 K) [Figure 58b]: δ 14.1 (C^{7}), 61.5 (C^{6}), 128.3 (C^{2}), 136.2 (C^{3}), 139.1 (C^{1}), 150.5 (C^{4}), 162.9 (C^{5}). Elem. Anal. Calc. for Et_2SpSp ($C_{14}H_{14}O_4Se_2$; FW = 404.18 g mol^{-1}): C, 41.60; H, 3.49. Found: C, 41.62; H, 3.52. ESI-MS/MS: *m/z* 405 [(M + H)$^{+}$]. IR (KBr pellet, cm^{-1}): *v* 3043 (w), 2988 (w), 2976 (w), 2901 (w), 2867 [w, *v*(C–H)], 1685 [s, *v*(C=O)], 1525 [m, *v*(C=C)], 1442 [s, δ(CH_2/CH_3)], 1261 [s, δ(O–Et)], 747 [s, γ(C–H)].

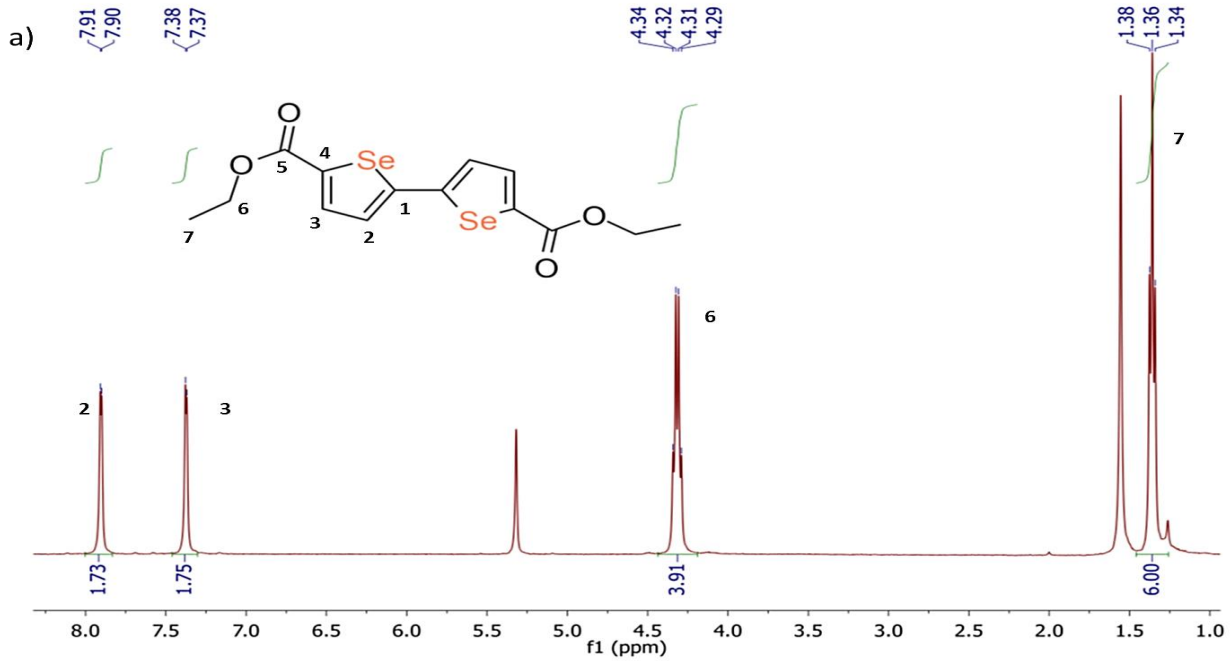

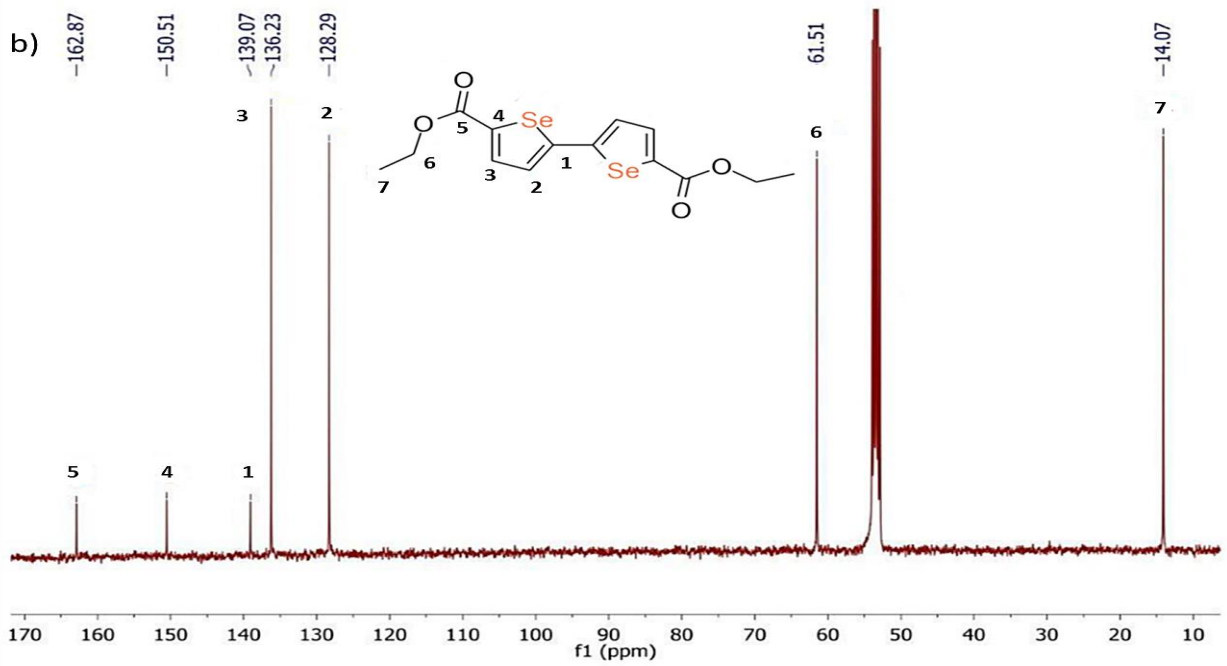

Figure 58: ^{1}H-NMR spectrum (400 MHz, CD_2Cl_2, 298 K) (a) and ^{13}C-NMR spectrum (400 MHz, CD_2Cl_2, 298K) (b) of Et_2SpSp.

Synthesis of 2,2′-Biselenophene-5,5′-dicarboxylic Acid (H_2SpSp): Diethyl 2,2′-biselenophene-5,5′-dicarboxylate (Et_2SpSp; 360 mg, 0.88 mmol) was suspended in 8.5 mL of methanol. An additional 8.5 mL of a freshly prepared Na(OH) 1 M aqueous solution was added to this suspension. Then, the mixture was brought to 328 K and kept at this temperature for 2 h. After that time, the clear yellow solution formed was cooled to ambient temperature. Thin-layer chromatography analysis (petroleum ether/ethyl acetate 5:1) confirmed the absence of the ester starting material. The low-boiling part of the solution (methanol) was removed through rotary evaporation, and the residual (aqueous) phase was treated with 1 M aqueous hydrochloric acid $HCl_{(aq)}$ to reach pH 3 − 4. The final H_2SpSp product started to precipitate from the liquid phase immediately after the first HCl small addition. The reaction flask was kept at 277 K for several hours to complete its precipitation. The yellow solid was eventually filtered on filter paper. Yield: 245 mg (80%).

^{1}H-NMR (400 MHz, DMSO-*d6*, 298 K) [Figure 59a]: δ 7.57 (d, $^{3}J_{HH}$ = 4.1 Hz, 2H, H^3), 7.84 (d, $^{3}J_{HH}$ = 4.1 Hz, 2H, H^2), 13.25 (s, br, 2H, H^6). ^{13}C-NMR (400 MHz, DMSO-d_6, 298 K) [Figure 59b]: δ 129.4 (C^2), 136.5 (C^3), 140.0 (C^1), 149.6 (C^4), 163.8 (C^5). Elem. Anal. Calc. for H_2SpSp ($C_{10}H_6O_4Se_2$, MW = 348.07 g mol^{-1}): C, 34.51; H, 1.74. Found: C, 34.53; H, 1.76. ESI-MS/MS: *m/z* 347 [(M − H)$^-$], 303 [(M − H − CO_2)$^-$], 173 [(M − 2H)$^{2-}$]. IR (KBr pellet, cm^{-1}): ν 3423 [s, br, *ν*(O−H)], 3048 [w, *ν*(C−H)], 1655 [m, *ν*(C=O)], 1526 [m, *ν*(C=C)], 1395 [s, δ(CH)], 763 [m, γ(C−H)], 466 [w, *ν*(C−Se)].

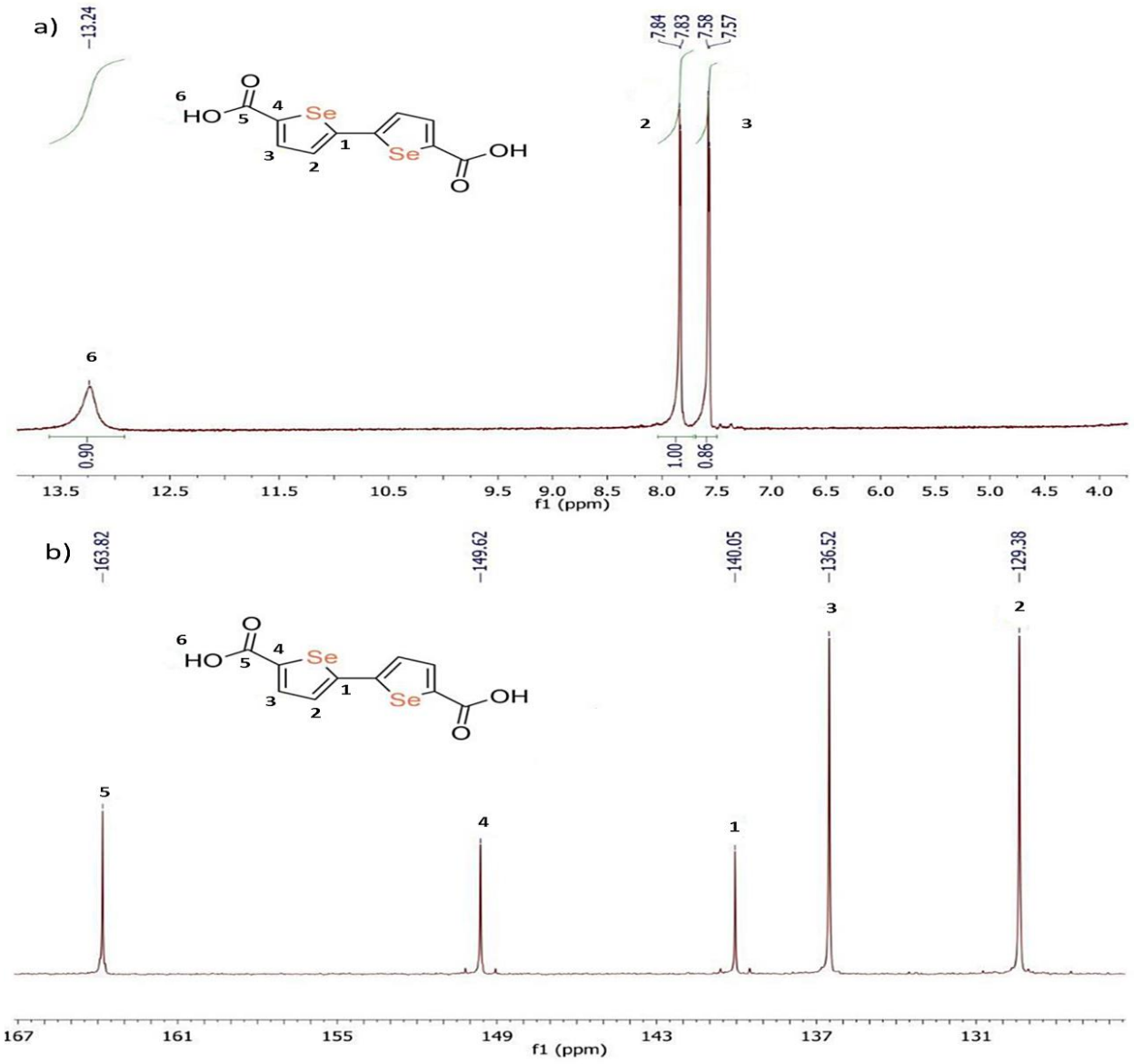

Figure 59: ^{1}H-NMR spectrum (400 MHz, DMSO-d_6, 298 K) (a) and ^{13}C-NMR spectrum (400 MHz, DMSO-d_6, 298K) (b) of H_2SpSp.

Synthesis of $[Zr_6O_4(OH)_4(SpSp)_{3.8}Cl_{4.4}]\cdot 4DMF\cdot 8H_2O$ (1·S): Zirconium(IV) chloride precursor ($ZrCl_4$; 67.6 mg, 0.29 mmol) was mixed together with a concentrated (12 M) $HCl_{(aq)}$ solution (0.5 mL) used as modulator. This mixture was brought to a total volume of 5.5 mL using DMF. The resulting suspension was immersed into an ultrasonic bath and sonicated at ambient temperature for 15 min. At the end of the sonication, the linker H_2SpSp (100 mg, 0.29 mmol) was added to the clear colorless solution; the mixture was further diluted with fresh DMF (7 mL), sonicated for an additional 15 min, and finally transferred to a Teflon-lined stainless-steel autoclave (inner Teflon beaker volume ca. 20 mL). The autoclave was sealed and heated at 363 K for 24 h under autogenous pressure. After slow overnight cooling, a yellow powder of **1·S** formed at the bottom

of the beaker. It was collected, washed with ethanol (4 × 10 mL) and petroleum ether (4 × 10 mL), and finally dried under a N_2 stream at room temperature. Yield: 109 mg (87% based on zirconium). The phase purity of every batch was checked through PXRD. Elem anal. Calc. for **1·S** ($C_{50}H_{63.2}Cl_{4.4}N_4O_{35.2}Se_{7.6}Zr_6$, MW = 2586.88 g mol^{-1}): C, 23.10; H, 2.44; N, 2.16. Found: C, 23.09; H, 2.41; N, 2.12. IR [*ν*(C=O)] band (KBr, cm^{-1}; [Figure 60]): 1651 (m).

Synthesis of $[Zr_6O_4(OH)_4(SpSp)_{2.6}(TpTp)_{1.3}Cl_{4.2}]$·4DMF·6$H_2O$ (2·S): The synthetic protocol followed for the preparation of **2·S** is identical with that reported above for **1·S**, using a 50:50 mixture of H_2SpSp (52.2 mg, 0.15 mmol) and H_2TpTp (38.1 mg, 0.15 mmol) against 0.30 mmol of zirconium chloride (70.0 mg). Yield: 110 mg (90% based on zirconium). The phase purity of every batch was checked through PXRD. Elem anal. Calc. for **2·S** ($C_{51}H_{59.6}Cl_{4.2}N_4O_{33.6}S_{2.6}Se_{5.2}Zr_6$, MW = 2456.42 g mol^{-1}): C, 24.91; H, 2.44; N, 2.28; S, 3.39. Found: C, 25.05; H, 2.46; N, 2.31; S, 3.43. IR [ν(C=O)] bands (KBr, cm^{-1}; [Figure 60]): 1704, 1662 (m).

Synthesis of $[Zr_6O_4(OH)_4(SpSp)_2(TzTz)_{1.8}Cl_{4.4}]$·4DMF·2$H_2O$ (3·S): The synthetic protocol followed for the preparation of **3·S** is identical with that reported above for **1·S**, using a 50:50 mixture of H_2SpSp (52.2 mg, 0.15 mmol) and H_2TzTz (38.4 mg, 0.15 mmol) against 0.30 mmol of zirconium chloride (70.0 mg). Yield: 106 mg (92% based on zirconium). The phase purity of every batch was checked through PXRD. Elem anal. Calc. for **3·S** ($C_{46.4}H_{47.6}Cl_{4.4}N_{7.6}O_{29.2}S_{3.6}Se_4Zr_6$, MW = 2313.51 g mol^{-1}): C, 24.07; H, 2.07; N, 4.60; S, 4.99. Found: C, 24.29; H, 2.06; N, 4.62; S, 4.97. IR [ν(C=O)] bands (KBr, cm^{-1}; [Figure 60]): 1654, 1580 (m).

Synthesis of $[Zr_6O_4(OH)_4(SpSp)_{1.6}(TpTp)_{1.2}(TzTz)_{1.4}Cl_{3.6}]$·5DMF·12$H_2O$ (4·S): The synthetic protocol followed for the preparation of **4·S** is identical with that reported above for **1·S**, using a 33:33:33 mixture of H_2SpSp (34.8 mg, 0.10 mmol), H_2TzTz (25.6 mg, 0.10 mmol), and H_2TpTp (25.4 mg, 0.10 mmol) against 0.30 mmol of zirconium oxychloride octahydrate ($ZrOCl_2$·8H_2O; 96.7 mg). Yield: 110 mg (85% based on zirconium). The phase purity of each batch was checked through PXRD. Elem anal. Calc. for **4·S** ($C_{54.2}H_{77}Cl_{3.6}N_{7.8}O_{41.8}S_{5.2}Se_{3.2}Zr_6$, MW = 2600.99 g mol^{-1}): C, 25.00; H, 2.98; N, 4.20; S, 6.41. Found: C, 25.43; H, 3.01; N, 4.28; S, 6.38. IR [ν(C=O)] bands (KBr, cm^{-1}; [Figure 60]): 1658, 1590, 1520 (s).

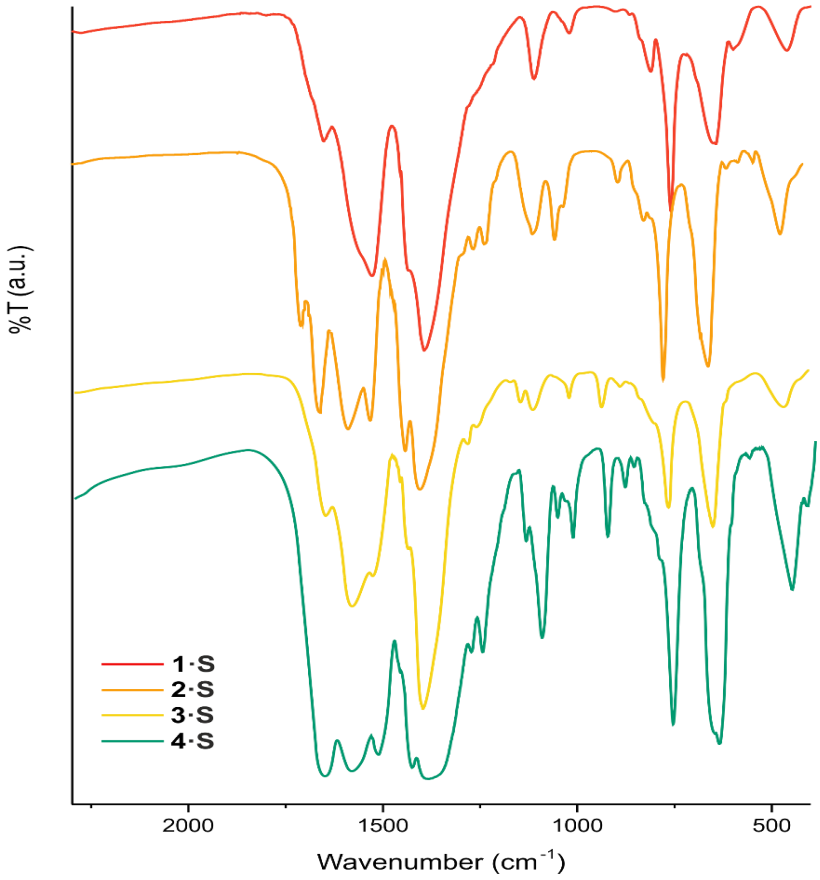

Figure 60: Comparison of IR-spectra of compounds **1 S –4 S** in the 2300 – 400 cm^{-1} wavenumber range.

4.2.3. Linkers Composition Quantification in the Mixed-Linker Phases

The approximate linkers composition in the three MIXMOFs **2·S-4·S** has been assessed through ^{1}H-NMR analysis of the digested samples in acidic solutions (D_2SO_4), following a well-established procedure found in literature[201]. In a typical procedure, 10 mg of sample was dissolved in three drops of sulfuric acid-d_2 solution (D_2SO_4, 96-98 wt. % in D_2O, 99.5 atom % D, Aldrich) and 0.5 mL of DMSO-d_6 directly into an NMR tube. The mixture was heated at T = 333 K for 12 h, to complete the sample digestion. The as-obtained clear yellow solution was analyzed via ^{1}H-NMR (400 MHz, relaxation delay τ = 15 s, 512 scans). In [Figure 61] the NMR spectrum of the triple-mixed MOF **4 S** is reported as an example (no other NMR spectra will be reported).

The stoichiometric coefficients (x, y, k) in the general formula $[Zr_6O_4(OH)_4(SpSp)_{\mathbf{x}}(TpTp)_{\mathbf{y}}(TzTz)_{\mathbf{k}}]$ (where $\mathbf{x} + \mathbf{y} + \mathbf{k} = 6$) were calculated from the integral values (a, b, c) related to the corresponding linker proton signals, according to the following equations:

$$Double-mixed\ MOFs: x = \frac{6a}{(a+b)} \quad and \quad y = \frac{6b}{(a+b)}$$

$$Triple-mixed\ MOFs: x = \frac{6a}{(a+b+c)} \quad and \quad y = \frac{6b}{(a+b+c)} \quad and \quad k = \frac{6c}{(a+b+c)}$$

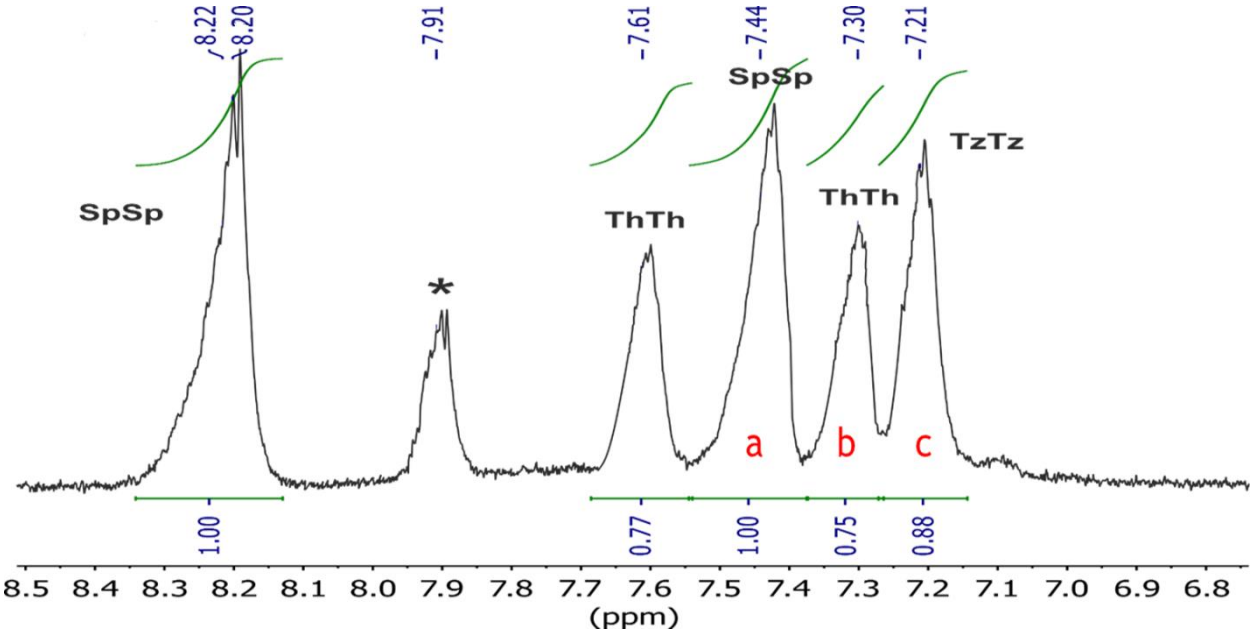

Figure 61: Zoom of the aromatic region used for the quantification of the linkers ratio of the digested **4 S** compound. * Clathrated DMF solvent.

4.2.4. Single-Crystal X-Ray Diffraction Linker Structure Determination

Single crystal X-ray diffraction data were collected at low temperature (T = 100 K) on an Oxford Diffraction XcaliburPX diffractometer equipped with a CCD area detector using the Cu Kα radiation (λ = 1.5418 Å). The program used for the data collection was CrysAlis CCD 1.171. Data reduction was carried out with the program CrysAlis RED 1.171 and the absorption correction was applied with the program ABSPACK 1.17. Direct methods, as implemented in Sir2014[202], were used to solve the crystal structure, while the structure refinement was performed by full-matrix least-squares against F^2 implemented in SHELXL-2018[203]. All the non-hydrogen atoms were refined anisotropically while the hydrogen atoms were fixed in calculated positions and refined isotropically with atomic displacement parameters depending on that of the atom to which they are bound. The geometrical calculations were performed by PARST97[204] and molecular plots were produced by the program ORTEP3[205].

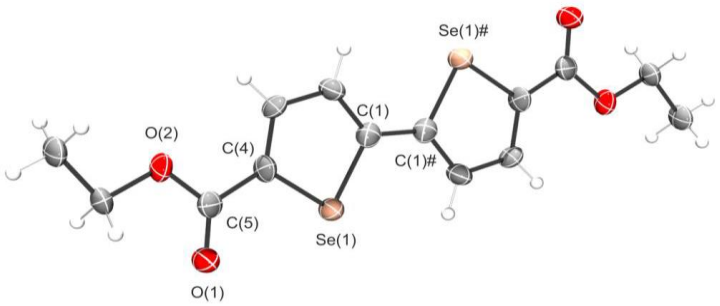

Formula	$C_7 H_7 O_2 Se$
M [g mol^{-1}]	202.09
T [K]	100
Color, habit	Yellow, platelet
Size [mm^3]	0.01 × 0.01 × 0.06
Crystal system	Triclinic
Space group	$P\bar{1}$
a [Å]	5.7879(4)
b [Å]	7.6750(6)
c [Å]	8.7717(6)
α [°]	94.242(6)
β [°]	95.086(5)
γ [°]	109.487(7)
V [Å^3]	363.66(5)

Figure 62: ORTEP drawing of Et_2SpSp and main crystallographic data, experimental details, and structure refinement details.

4.2.5. PXRD (MIX)MOFs Structure Determination

Powdered samples (~50 mg) of **1·S–4·S** were deposited in the 0.2 mm deep hollow of a zero-background silicon sample holder (Assing Srl, Monterotondo, Italy). PXRD data were acquired with a Bruker AXS D8 Advance verticalscan θ:θ diffractometer, equipped with an X-ray source (Cu Kα, λ = 1.5418 Å), a Bruker Lynxeye linear position-sensitive detector, and a nickel filter in the diffracted beam. The following optical components were employed: primary beam Soller slits (2.5°), a fixed divergence slit (0.5°), and an anti-scatter slit (8 mm). The generator was operating at 40 kV and 40 mA. Preliminary PXRD acquisitions were performed in the 2θ range 3.0 – 35.0°, with steps of 0.02° and a time per step of 1 s to unveil the purity and crystallinity of the batches. PXRD acquisitions to determine the crystal and molecular structure were conducted with a time per step of 10 s and steps of 0.02°, spanning the 2θ range 3.0 – 105.0. A visual comparison between the PXRD patterns of the MOFs under study and those of the $[Zr_6O_4(OH)_4(L)_6]\cdot n$DMF analogues [L = $TpTp^{2-}$ or $TzTz^{2-}$] highlighted that the compounds are isostructural. This suggestion was confirmed by performing a whole PXRD pattern refinement adopting the Le Bail approach, as allowed by TOPAS-R V3, starting from the unit cell parameters of the parent bithiophene MOF [Figure 68]. The linker and DMF molecule crystallographically independent portions were described using rigid bodies. In the case of **2·S–4·S**, the copresence of the $SpSp^{2-}$, $TpTp^{2-}$, and $TzTz^{2-}$ linkers was taken into account by including in the structural model the rigid body of $SpSp^{2-}$ and inserting proper vicariant atoms (S vs Se for $TpTp^{2-}$; S vs Se and N vs CH for $TzTz^{2-}$), setting

their molar ratios at the values obtained from the ^{1}H-NMR signal integration of the digested samples (see paragraph 4.2.3.- Linkers composition quantification in the mixed-linker phases).

In the initial steps of the structure determination, both the metal cluster components (i.e., Zr^{4+}, O^{2-}, and OH^-) and spacers were positioned according to the crystal structure of $[Zr_6O_4(OH)_4(TpTp)_6]\cdot n$DMF. Average values were assigned to the bond distances and angles. When permitted by the symmetry, the position and orientation of the independent components of the MOFs were allowed to vary. To account for the possibility of missing-linker defects, a known phenomenon for UiO-type materials[206], the linker site occupation factors were refined, reaching in all compounds a value lower than 1. As assessed by XRF [Figure 64], the missing negative charges are compensated for by chloride anions.

Based on a quest in the Cambridge Structural Database (version 2020.1) for Zr_6Cl_x clusters (no $Zr_6Cl_xO_y$ clusters were found), it was assumed that the chloride anions in **2·S– 4·S** are bound to the Zr(IV) cations as terminal ligands vicariant to the oxygen atoms of the carboxylate groups. They were placed accordingly in all the positions where their site occupation factor did not refine to zero. The site occupation factors of the linkers and chloride anions were correlated so that the total negative charges were set to 12^-, to balance the positive charge coming from the $[Zr_6O_4(OH)_4]^{12+}$ metallic node. For the sake of simplicity, the smeared electronic density within the cavities was modeled by DMF molecules alone. The two crystallographically independent DMF molecules were located using a Monte Carlo/simulated annealing approach[207], implemented in TOPAS-R V3. During the final structure refinement stages, performed with the so-called Rietveld method, the linker and DMF bond distances (but the C−H and C=O bonds) were refined in limited ranges of values, retrieved from the Cambridge Structural Database (version 2020.1) searching for room temperature-determined crystal structures containing the 2,2′- biselenophene, 2-carboxyselenophene, 2,2′-bithiophene-5,5′-dicarboxylate, or 2,2′-bithiazole fragments. (Bonds: C2−C3/N3 and C4−C5, 1.36−1.42 Å; C3/N3−C4, 1.37−1.45 Å; C−Se, 1.84−1.91 Å; C−S, 1.68−1.84 Å; C−C of the carboxylic functionalization, 1.45−1.55 Å; C−C exocyclic, 1.40−1.55 Å; C−N in the DMF molecule, 1.35−1.45 Å). The background was described by a Chebyshev-type polynomial function. An isotropic thermal factor [Biso(M)] was refined for the Zr(IV) metal center; the isotropic thermal factor of lighter atoms belonging to the cluster and ligands was calculated as Biso(L) = Biso(M) + 2.0 (Å^2); the isotropic thermal factor of the DMF atoms was calculated as Biso(S) = Biso(M) + 3.0 (Å^2). The peak profile was described by taking advantage of the Fundamental Parameters Approach[208].

*Crystal data for **1·S**:* cubic, $Pn\bar{3}$, a = 25.7020(6) Å, V = 16979(1) Å^3, Z = 24, Z′ = 4, ρ = 0.991 g cm^{-3}, F(000) = 4555.0, R_{Bragg} = 0.011, R_p = 0.020, and R_{wp} = 0.028 for 4986 data and 73 parameters in the 5.3 – 105.0° (2θ) range. CCDC 2020561.

*Crystal data for **2·S**:* cubic, $Pn\bar{3}$, a = 25.546(1) Å, V = 16671(3) Å^3, Z = 24, Z′ = 4, ρ = 1.005 g cm^{-3}, F(000) = 4925.1, R_{Bragg} = 0.015, R_p = 0.025, and R_{wp} = 0.032 for 4991 data and 86 parameters in the 5.2 – 105.0° (2θ) range. CCDC 2020562.

*Crystal data for **3·S***: cubic, $Pn\bar{3}$, a = 25.564(1) Å, V = 16511(2) Å^3, Z = 24, Z′ = 4, ρ = 1.002 g cm^{-3}, F(000) = 4874.4, R_{Bragg} = 0.015, R_p = 0.020, and R_{wp} = 0.026 for 4981 data and 80 parameters in the 5.4 – 105.0° (2θ) range. CCDC 2020563.

*Crystal data for **4·S**:* cubic, $Pn\bar{3}$, a = 25.416(2) Å, V = 16417(4) Å^3, Z = 24, Z′ = 4, ρ = 1.031 g cm^{-3}, F(000) = 5022.6, R_{Bragg} = 0.005, R_p = 0.019, and R_{wp} = 0.024 for 4991 data and 79 parameters in the 5.2 – 105.0° (2θ) range. CCDC 2020564.

4.2.6. Variable- Temperature PXRD Analysis

As a representative example, the thermal behavior of **1·S** was studied in situ by employing variable-temperature PXRD (VT-PXRD) [Figure 66]. A powdered batch (∼20 mg) of this MOF was deposited on an aluminum sample holder and heated using a custom-made sample heater (Officina Elettrotecnica di Tenno, Ponte Arche, Italy) spanning the 303 – 663 K temperature range with 20 K steps. PXRD patterns were measured at each temperature step in the 2θ range 5.0 − 25.0°, with 0.02° steps and a time per step of 1 s and treated by performing a parametric whole PXRD pattern refinement with the Le Bail method, as provided by TOPAS-R V3.

4.2.7. Gas Adsorption

Before the adsorption measurements were carried out, ∼40 mg each of **1·S** – **4·S** were activated at 403 K under high vacuum (10^{-6} Torr) for 24 h. Volumetric adsorption isotherms were recorded to a maximum pressure of 1.2 bar through the ASAP 2020 instrument (Micromeritics). The textural properties were investigated using N_2 as the adsorbate at 77 K. For BET specific surface area calculation, the 0.01−0.1 p/p_0 pressure range of the isotherm was used to fit the data [Figure 70]. The pore-size distribution was determined on the basis of the non-local DFT (NLDFT) method (Tarazona model for cylindrical pores)

4.2.8. Luminescence Measurements

Photophysical analysis was performed on solids or air-equilibrated suspensions in DMF at 298 K unless otherwise specified. UV−vis absorption spectra were recorded on a PerkinElmer λ40 spectrophotometer making use of quartz cells with 1.0 cm optical path length. Luminescence spectra were collected on a PerkinElmer LS-50 or an Edinburgh FLS920 spectrofluorometer equipped with a Hamamatsu R928 phototube. For analysis of the solid samples, the emission quantum yield was determined from corrected emission spectra collected by the abovementioned Edinburgh FLS920 spectrofluorometer equipped with a $BaSO^{4-}$ coated integrating sphere (4 in. diameter), a 450 W xenon lamp as the light source (the excitation wavelength was properly selected by means of a monochromator), and a R928 photomultiplier. The values of the quantum yield were calculated following the method described by de Mello et al.[209]. Estimated experimental errors: 5% on the molar absorption coefficients; 2 nm on the band maxima; 20% on emission quantum yields of the solid samples.

4.3. Results and Discussion

The new linker 2,2'-biselenophene-5,5'-dicarboxylicacid (H_2SpSp) was synthetized starting from a silver-palladium (silver fluoride and bis(benzonitrile)palladium dichloride) catalyzed homocoupling of ethyl selenophene-2-carboxylate, to obtain the ester 2,2'-biselenophene-5,5'dicarboxylate (Et_2SpSp). Then, the ester was converted into the corresponding dicarboxylic acid through a basic hydrolysis using sodium hydroxide in a water/methanol mixture, followed by acidification with hydrochloric acid [Figure 63]. Unfortunately, it was not possible to obtain a single crystal for the structural determination of the linker through single-crystal X-ray diffraction. However, single crystals of Et_2SpSp were obtained after slow evaporation of an ethyl acetate concentrated solution [Figure 62]. The diester crystallizes in triclinic $P\bar{1}$ space group with the two selenium atoms that lie in a "trans" position. This arrangement was expected because it is typical of other conjugated bicyclic compounds containing heteroatoms like H_2TzTz and H_2TpTp.

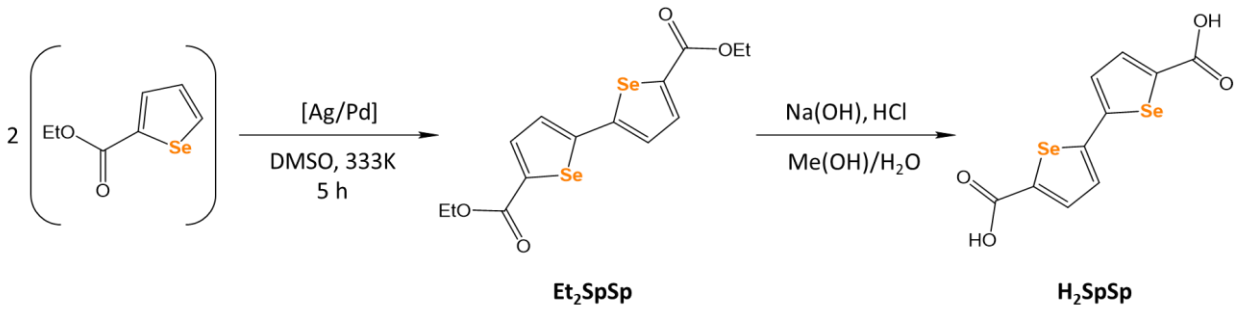

Figure 63: Schematic synthesis of the new H_2SpSp linker.

The reaction between H_2SpSp and $ZrCl_4$ in DMF under solvothermal conditions and using concentrated HCl as modulator led to the formation of the MOF **1 S** as a microcrystalline yellow powder.

Since it is possible to synthesize MOFs with more than one type of linkers inside the structure and exploiting the structural analogy between the H_2SpSp and the H_2TzTz and H_2TpTp linkers, three new mixed-linker MOFs were prepared. Using the same synthesis conditions and setting the initial linker relative stoichiometric ratio as 3:3 for the double-mixed (H_2SpSp + H_2TzTz and H_2SpSp + H_2TpTp) and 2:2:2 for the triple-mixed (H_2SpSp + H_2TzTz + H_2TpTp), the compounds **2 S-4 S** were obtained. Interestingly, for the synthesis of the triple-mixed MOF **4 S**, the use of $ZrCl_4$ as metal source led to the precipitation of an amorphous powder. To overcome this issue, $ZrOCl_2{\cdot}8H_2O$ was used as metal precursor and this choice allowed to obtain a crystalline product. This result can be explained taking into consideration that water plays a significant role in the crystallization mechanism of Zr-MOFs[210] because it is the source of the oxide and hydroxide groups that form the UiO-6x MOFs SBU $[Zr_6O_4(OH)_4]^{12+}$. In this case, we can claim that the tetrameric structure $[Zr_4(OH)_8(H_2O)_{16}]^{8+}$ found in the solid-state structure of zirconium oxychloride[211] provides a faster crystallization kinetics and consequent higher crystallinity degree.

Unfortunately, all the synthesized MOFs are defective. Defects are quite common in UiO-type MOFs[198] and, in general, when modulators are employed during the synthesis. In this case, the missing-linkers are replaced by chloride anions (coming from the HCl used as modulator) that are bound to the metal centers. The replacement of the linkers by these anions can be inferred from elemental analysis and from X-ray fluorescence analysis [Figure 64].

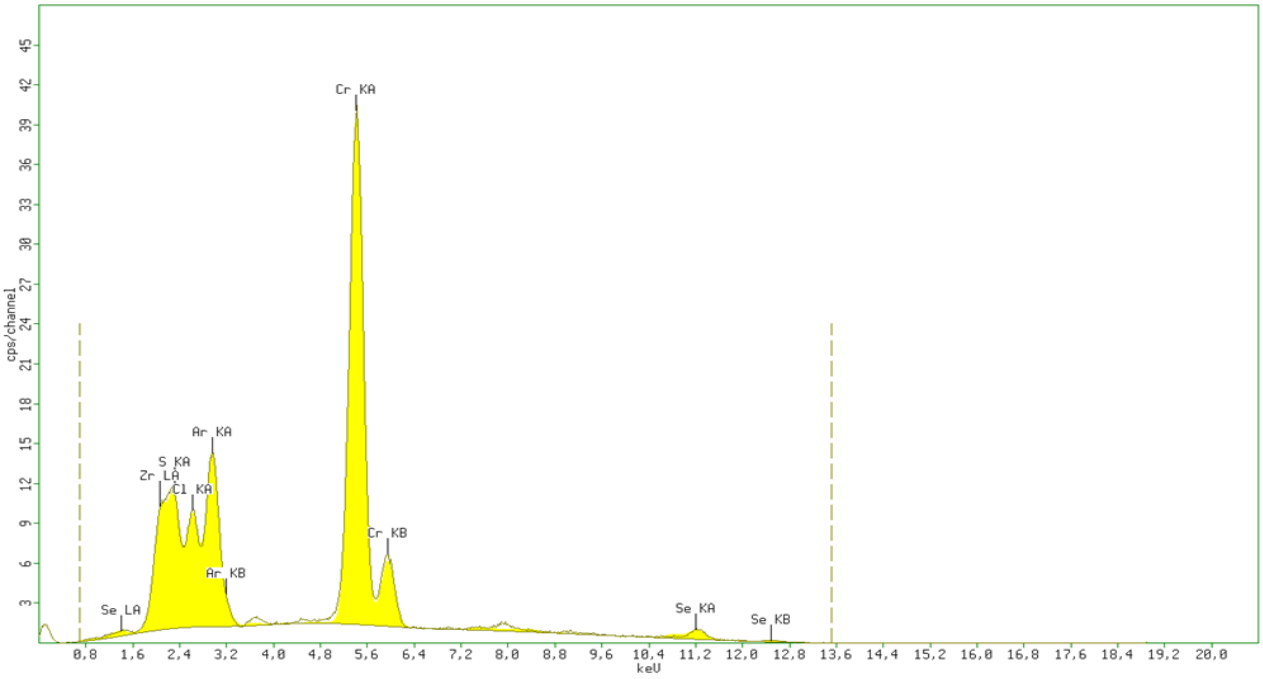

Figure 64: X-ray fluorescence spectrum of **4·S** (chosen as a representative example) measured in air. The characteristic lines of argon come from air, while those of chromium are generated by the anode of the X-ray source (made of this metal).

After the synthesis, the actual linker composition of the mixed-linker MOFs was assessed via ^{1}H-NMR signal integration of the digested samples in acidic solution, in accordance with a well-consolidated experimental methodology already applied for other mixed-metal MOFs. The experimental procedure is reported in a precedent paragraph (see 4.2.3. – Linkers composition quantification in the mixed-linker phases). The calculated linkers composition was also exploited for the refinement of the PXRD data during the crystal structure determination.

The MOFs thermal behavior was evaluated through thermal analyses (TGA and DSC) under N_2 flow [Figure 65]. All the four MOFs follow the same sequence of events: gradual loss of the clathrated solvent in the first part and then decomposition at temperatures that are reported in [Table 1]. The pure biselenophene MOF (**1 S**) has a decomposition temperature of 692 K that is higher than those of pure bithiophene and pure bithiazole analogues ($[Zr_6O_4(OH)_4(L)_6]$ where L= H_2TpTp or H_2TzTz) that are of 663 K and 673 K respectively. This behavior can be related to the different acidities of the carboxylic acid moieties of the linkers and their strength of coordination bonding with zirconium. Low-energy lying empty 4d orbitals on selenium confer to this element a higher polarizability and charge delocalization ability with respect to sulfur. Consequently, the selenophene carboxylate is more basic, resulting in a stronger bonding with the metal atoms.

		1 S	2S	3 S	4S
LOSS OF SOLVENT	*T range (K)*	313-473	313-480	313-550	313-600
	Calc. loss (wt%)	16.9	16.3	14.2	22.4
DECOMPOSITION	T_{dec} *(K)*	692	697	676	692
	Residual mass (%)	24.6	25.0	27.1	29.3

Table 1: Details of the thermal behavior of compounds **1 S-4 S** observed by TGA analysis.

The residual mass remaining after decomposition of the MOFs is likely to be ascribed to simple binary zirconium compounds such as zirconium carbide (ZrC), zirconium oxide (ZrO_2) or zirconium sulfide (ZrS_2) and their mixtures.

The analysis of the DSC curves of compounds **2 S-4 S** reveals the presence of a single peak concomitant with the decomposition of the relative compound [Figure 65]. This indicates that the three mixed-linker MOFs exist as a unique pure phase and not in a solid solution of the single-linker MOFs.

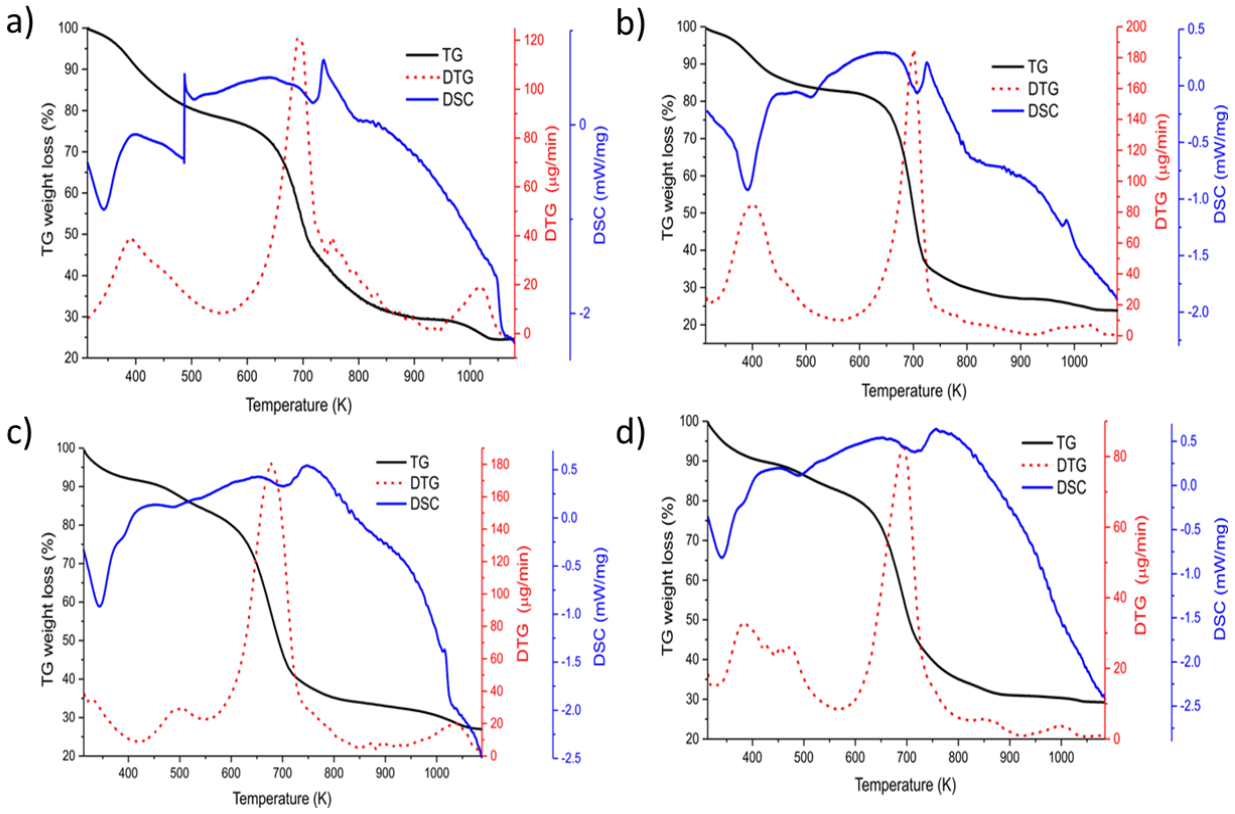

Figure 65: TGA (black line), DSC (blue line) and DTG (dotted red line) acquired under a N_2 flow for the four compounds: **1 S** (a), **2 S** (b), **3 S** (c) and **4 S** (d).

In combination with the TGA analysis, the thermal behavior of the compounds was also checked through variable-temperature powder X-ray diffraction (VT-PXRD) carried out in air on **1·S** chosen as a representative example for all the compounds [Figure 66a]. VT-PXRD highlighted that the MOF gradually loses its crystallinity starting from room temperature, becoming amorphous at 663 K. However, in the temperature range 303 – 423 K, the unit cell volume increment is about 0.4% [Figure 66b]. This low value reveals the high rigidity of the crystal structure when the external stimulus is temperature variation.

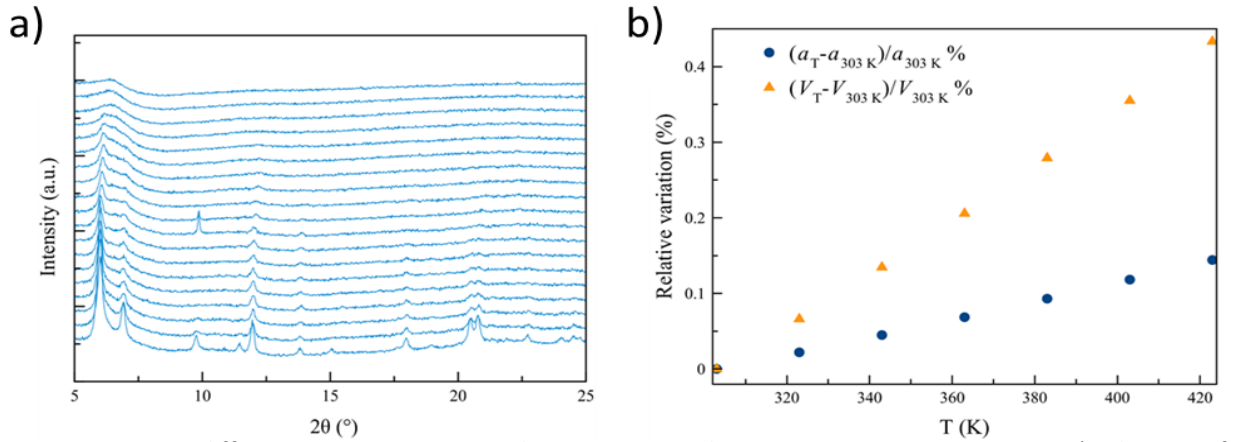

Figure 66: VT-PXRD diffraction patterns measured in air on **1·S** in the temperature range 303-663 K (with steps of 20 K) (a). Percentage relative variation of the unit cell parameters in **1·S** as a function of the temperature (b).

Another proof of the phase purity of the three mixed-linker MOFs is represented by the comparison of their PXRD profiles with those of their single-linker counterparts. [Figure 67] shows the comparison between the main diffraction peaks of compound **3 S** (chosen as representative example) and its pure linker analogs **1 S** and $[Zr_6O_4(OH)_4(TzTz)_6]\cdot n$DMF.

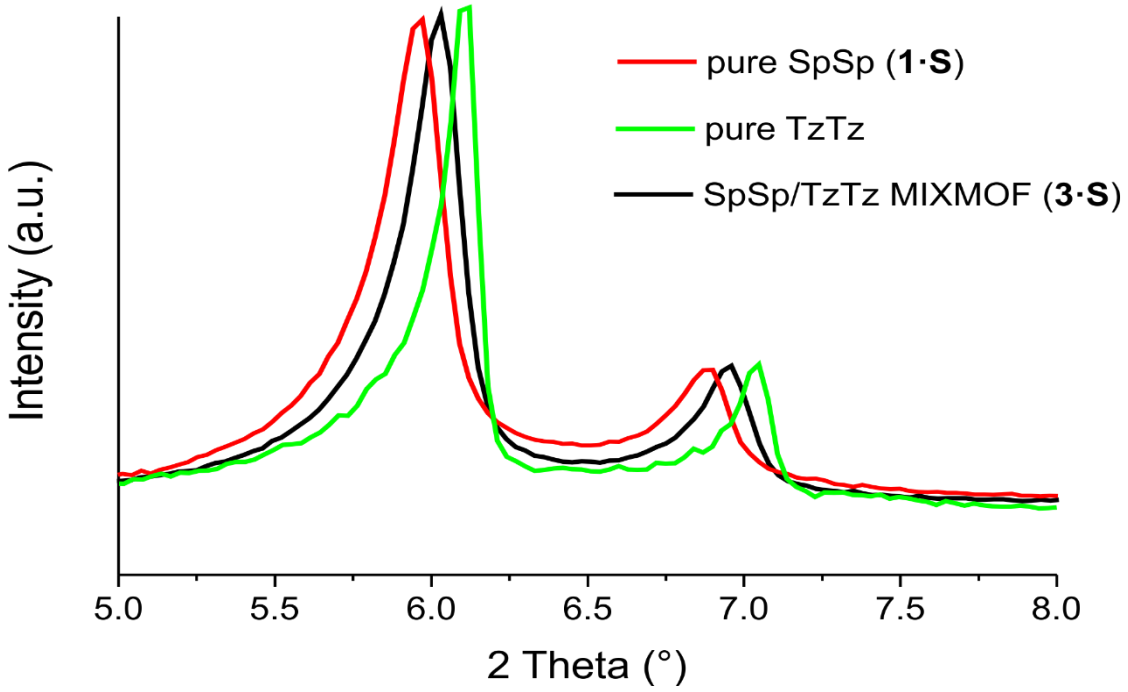

Figure 67: PXRD patterns (5° - 8° 2θ region) of **3·S** (black line) and of its pure-linker parent materials **1·S** (red line) and $[Zr_6O_4(OH)_4(TzTz)_6]\cdot n$DMF (green line) at comparison.

As can be seen, the main diffraction peaks of **3 S** are unique and fall in between those of its parent materials, confirming the formation of a solid phase structurally similar to the others but with different composition. The visual comparison between the PXRD patterns of the new synthesized MOFs and those of the H_2TpTp and H_2TzTz analogues highlights that the compounds are isostructural with one another and with the parent carbocyclic MOF UiO-67 $[Zr_6O_4(OH)_4(PhPh)_6]$ ($PhPh^{2-}$ = 4,4'-biphenyldicarboxylate)[192]. Confirmation of this hypothesis is given by the Rietveld refinement of the whole PXRD pattern [Figure 68]

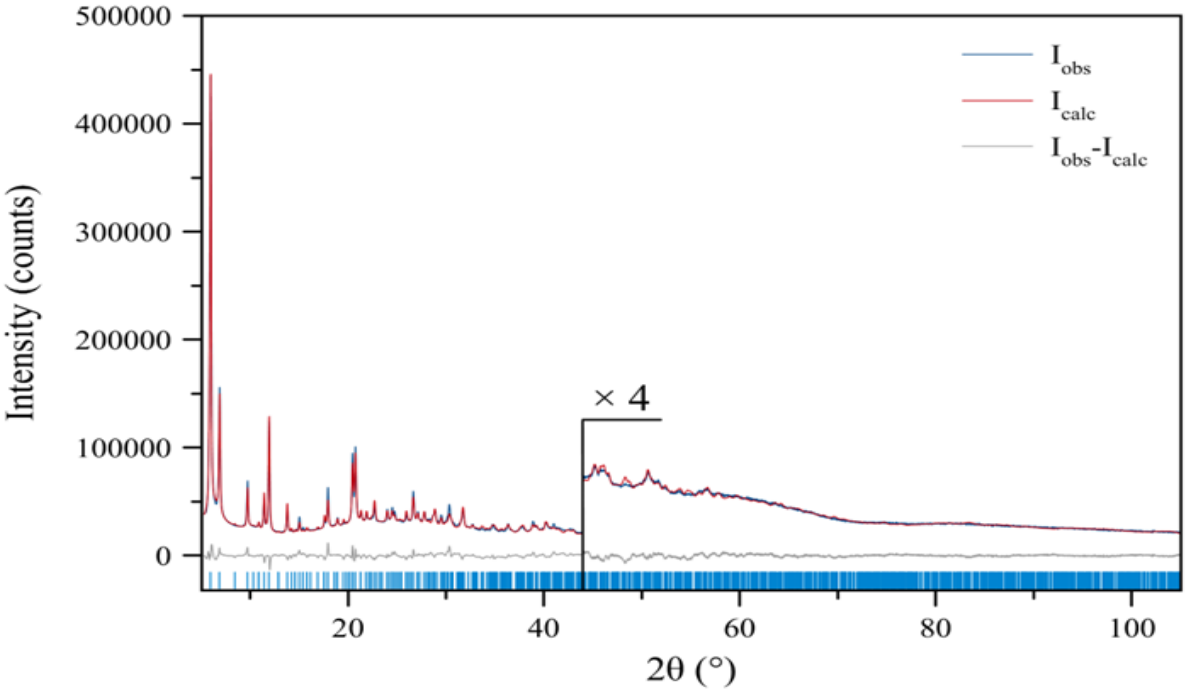

Figure 68: Graphical result of the final structure refinement carried out with the Rietveld method on the PXRD pattern of **1·S** (chosen as a representative example) in terms of experimental (blue), calculated (red) and difference (grey) traces. The blue markers at the bottom indicate the positions of the Bragg reflections.

The actual crystal structures of the four MOFs was assessed through PXRD analysis. Since they are all isostructural, only the structure of compound **1 S** is described in detail here, while the other structures can be checked in section – 4.2.5. PXRD (MIX)MOFs Structure Determination. MOF **1 S** [Figure 69]. crystallizes in the cubic space group $Pn\bar{3}$ and features $[Zr_6O_4(OH)_4]^{12+}$ clusters as SBUs. The Zr(IV) metal centers are eight-coordinated (in a square-antiprismatic coordination geometry) by eight oxygen atoms, with four coming from the carboxylate groups, (which define one square face of the antiprism), and four belonging to μ_3-O and μ_3-OH groups (defining the other square face). The main Zr-O bond distances between the Zr(IV) ion and the carboxylate oxygen atoms in the four MOFs are 2.22 Å (**1·S**), 2.21 Å (**2·S**), 2.21 Å (**3·S**), and 2.14 Å (**4·S**). These values are comparable to those of pure H_2TpTp and H_2TzTz MOFs (2.217 and 2.229 Å, respectively), suggesting the existence of a strong coordinative bond. Each $[Zr_6]$ SBU is surrounded by 12 carboxylate groups belonging to 12 different ditopic linkers, forming a 3D open framework [Figure 69b] of *fcu* topology. The structure features octahedral (~11 Å diameter [Figure 69c]) and tetrahedral (~8 Å diameter [Figure 69d]) cages, occupied by solvent molecules (omitted in the structure images). The cages diameters were estimated by measuring the distances between the nearest carbon atoms of linkers belonging to the apposite cage walls and subtracting the van der Waals radii of the two atoms. Each octahedral cage is edge-sharing and

face-sharing with eight octahedral and eight tetrahedral cavities, respectively. Two crystallographically distinct DMF solvent molecules were located within the octahedral and tetrahedral cavities, respectively. Neglecting the presence of the clathrated solvent, the empty unit cell volume of the four MOFs was estimated in the range 63 – 65%, in agreement with the values found in pure H_2TpTp and H_2TzTz MOFs (61% and 62%, respectively). The estimated pore volumes are 0.88 $cm^3\ g^{-1}$ (**1·S**), 0.87 $cm^3\ g^{-1}$ (**2·S**), 0.99 $cm^3\ g^{-1}$ (**3·S**), and 0.83 $cm^3\ g^{-1}$ (**4·S**). All linkers show a "trans" disposition of their heteroatoms on the two heterocyclic rings, as found in their uncoordinated form [Figure 57]. Linker deviation from planarity (with dihedral angles between the two heterocyclic rings falling in the 6° − 25° range) is observed in all cases, as was already found for other structurally characterized coordination compounds containing the H_2TpTp linker[212].

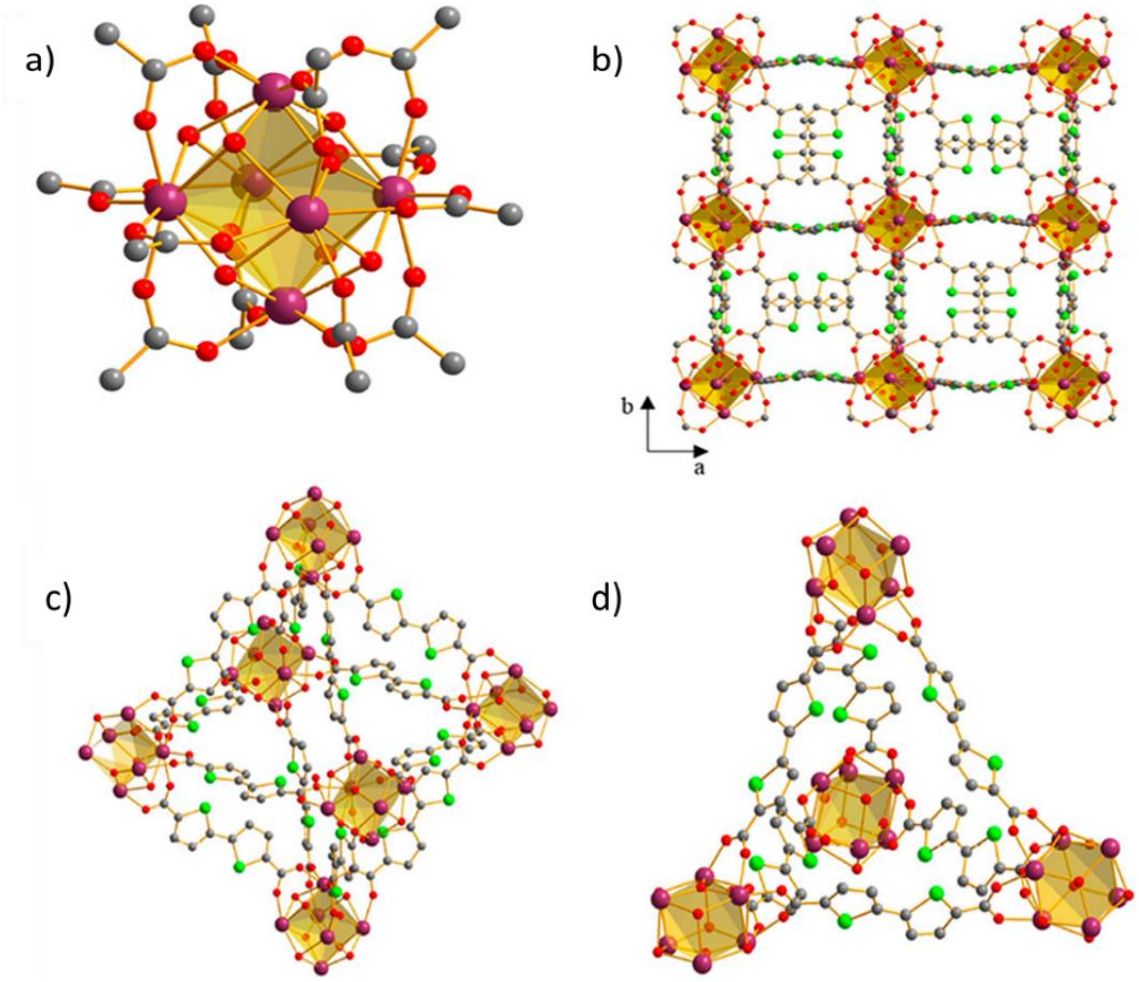

Figure 69: Representation of the crystal structure of **1 S**. The SBU (a), portion of the crystal packing viewed along the [100] crystallographic direction (b), the octahedral cage (c) and the tetrahedral cage (d). Both solvent molecules and hydrogen atoms are omitted for clarity. The model has been built assuming a perfect crystal without defects. Color code: Zr – violet, Se – green, C – grey and O – red.

The texture and the porosity of the four MOFs were then evaluated through volumetric N_2 adsorption at 77 K. Before the analysis, in accordance with the typical methodology, all samples were evacuated using a thermal treatment heating them at 303 K under high vacuum for 24 h. This procedure is necessary to remove the synthesis solvent molecules that might be trapped inside the pores. All the compounds show a type I isotherm typical of microporous materials [Figure 70a]. Calculated BET areas are 541 $m^2\ g^{-1}$ (**1 S**), 380 $m^2\ g^{-1}$ (**2 S**), 306 $m^2\ g^{-1}$ (**3 S**) and 460 $m^2\ g^{-1}$ (**4 S**). These values are lower than those found in literature for the pure linker analogues $[Zr_6O_4(OH)_4(TpTp)_6]$ (2207 $m^2\ g^{-1}$)[196] and $[Zr_6O_4(OH)_4(TzTz)_6]$ (840 $m^2\ g^{-1}$)[197]. This result can be explained by the defective nature of the samples (as explained in paragraph 1.3. – Surface Area of MOFs) combined with a partial loss of crystallinity upon heating (as witnessed by VT-PXRD). The micropore volumes are estimated using the Dubinin – Astakhov model to the N_2 adsorption isotherm, and the found values are: 0.23 (**1 S**), 0.15 (**2 S**), 0.12 (**3 S**) and 0.19 (**4 S**) $cm^3\ g^{-1}$. The total pore volumes evaluated at p/p_0=0.98 are equal to 0.26 (**1 S**), 0.23 (**2 S**), 0.17 (**3 S**) and 0.21 (**4 S**) $cm^3\ g^{-1}$. All the samples present two different micropore sizes (retrieved from the NLDFT analysis; Tarazona model for cylindrical pores) of ca. 18 Å and 22 Å [Figure 70b], in line with the crystallographic results related to the Zr-Zr distances between opposite metallic nodes in the framework and similar to those found in literature for the biphenyl parent MOF UiO-67 (12 Å and 16 Å)[192].

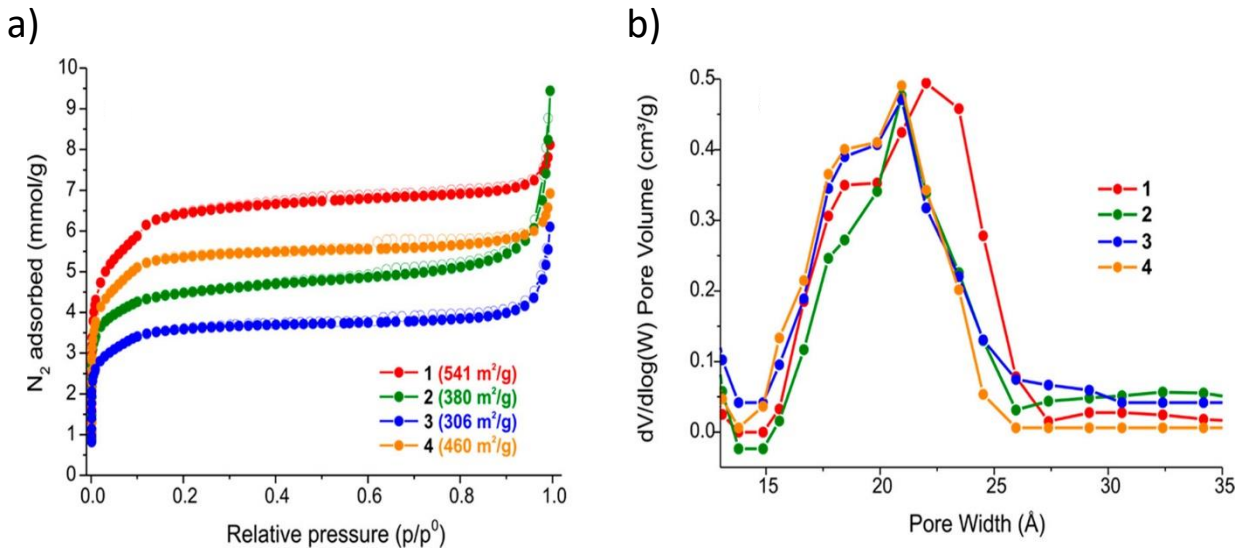

Figure 70: N_2 adsorption isotherms (full symbols) and desorption isotherms (empty symbols) measured at 77 K for **1S-4 S** (a). Pore size distribution calculated with NLDFT Tarazona model for cylindrical pores of **1S-4 S** (b).

Finally, the four MOFs were tested for luminescence applications. Firstly, the luminescent properties of the bare linkers were tested both in DMF solution [Figure 71a] and in the solid state [Figure 71b]. When dissolved in DMF, the three linkers H_2SpSp. H_2TpTp and H_2TzTz show absorption and emission maxima in the 345 nm < $\lambda_{max,abs}$ < 366 nm and 405 nm < $\lambda_{max,em}$ < 435 nm ranges for absorption and emission, respectively. In the solid state, their emissions are red-shifted and present an emission in the range of 450 nm < $\lambda_{max,em}$ < 550 nm. In this emission range, the linkers generate the characteristic blue-green colors under a UV lamp. The CIE chromatic coordinates[8] of these emissions are shown in the upper part of the emission spectra [Figure 71b]. Linkers H_2SpSp and H_2TpTp emit in the green region, while H_2TzTz emits in the blue region.

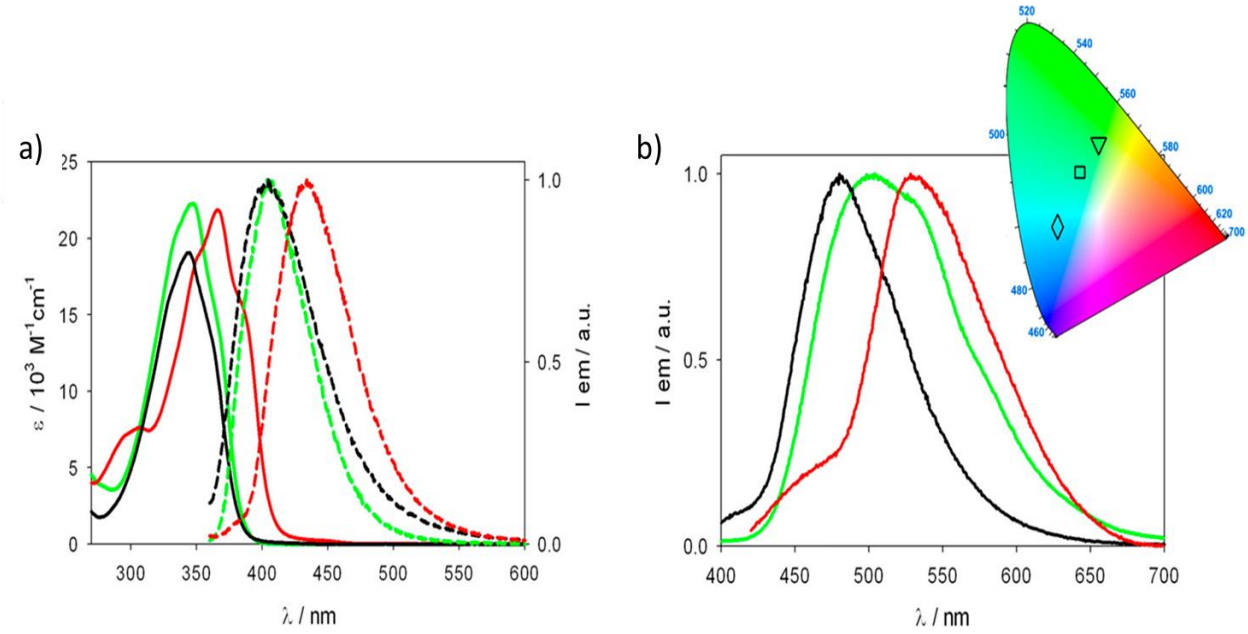

Figure 71: Absorption (solid lines) and normalized emission (dashed lines)spectra of the linkers H_2SpSp (red), H_2TpTp (green) and H_2TzTz (black) in a DMF solution at ambient temperature (λ_{ex}=340 nm) (a). Normalized emission spectra of the same compounds in powder form at room temperature (λ_{ex}=390 nm, 350 and 360 respectively) (b). In the upper part CIE diagram derived from the emission spectra of H_2SpSp (triangle), H_2TpTp (square) and H_2TzTz (diamond).

In a second stage, the luminescent properties of the related MOFs **1 S-4 S** were evaluated in DMF suspension [Figure 72]. The emissions of all samples are red-shifted with respect to that of their constitutive linkers. This shift may be caused by the chromophore coordination to Zr(IV). The maximum emission can be found at λ_{max} = 510 nm, 485 nm, 450 nm and 485 nm for **1 S-4 S**, respectively. As indicated by the CIE diagrams reported, all the emissions fall in the blue – green

[8] System designed in 1931 by "Commission Internationale de l'éclairage" (CIE) to enclose all the colors that are visible from the human eye, regardless their luminance. On the borders are reported the wavelength of a specific color. Close to the borders, the color is at its maximum saturation.

visible region, with **1 S** that is fully in the green region, **2 S** and **4 S** are borderline between green and blue and **3 S** falls completely in the blue region.

Unfortunately, the emission intensities of the mixed-metal MOFs are rather low, with a luminescence quantum yield lower than 0.05. This value falls under the ordinary detection limit set for solid-state materials. This behavior is frequently observed in the solid state, where the presence of emissive organic molecules concentrated in the same structure (fluorophore aggregation) can lead to a self-quenching of the emission[213]. This phenomenon is also common for MOFs where all the organic linkers in the framework are emissive fluorophores[214].

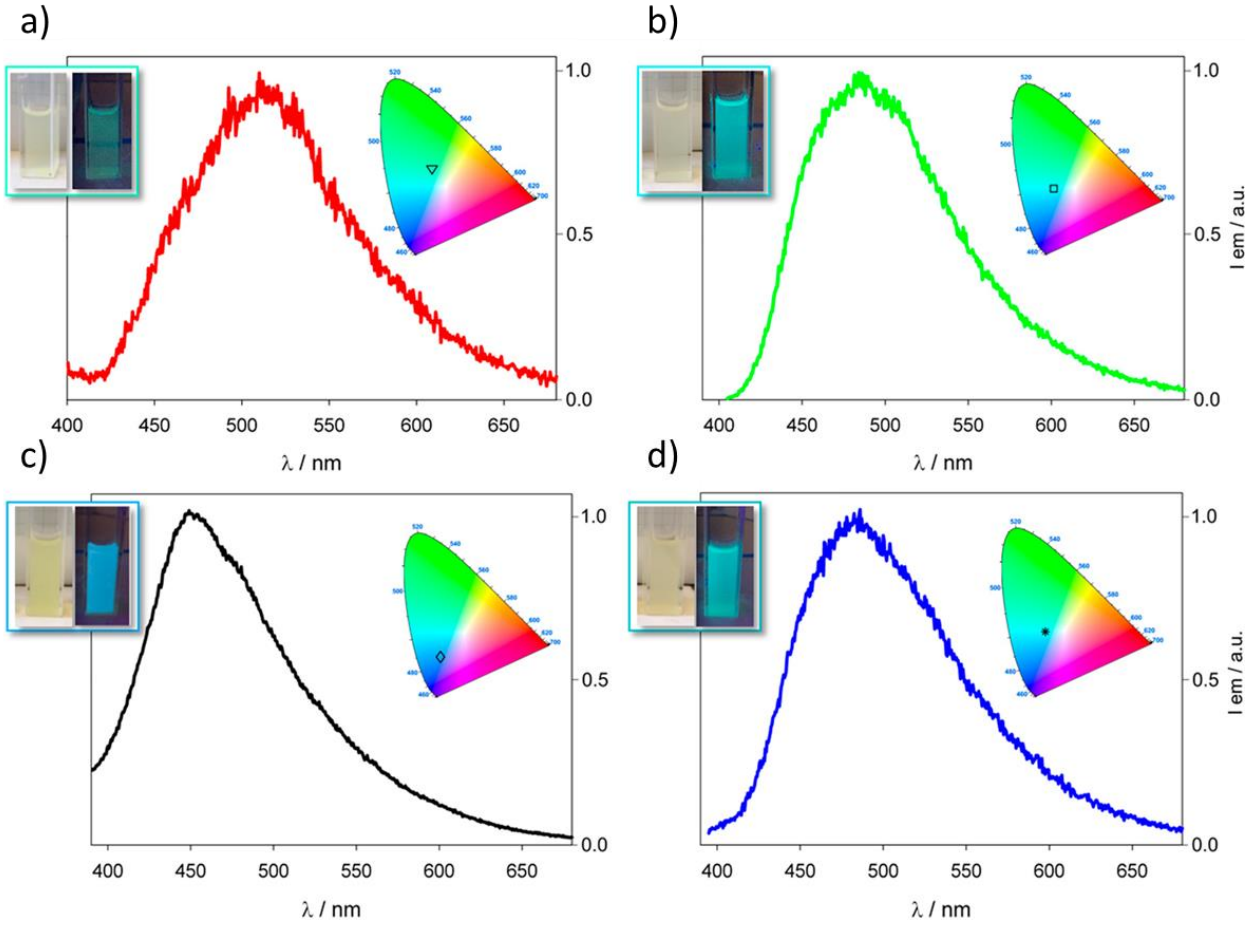

Figure 72: Normalized emission spectra and corresponding CIE diagrams of **1 S** (a), **2 S** (b), **3 S** (c) and **4 S** (d) in DMF suspension. Inset: photographs taken on the suspensions under ambient light (left) and under UV irradiation (right) with 360 nm< λ_{ex} <380 nm.

4.4. Conclusions

In this work, a new zirconium MOF containing the novel 2,2'-Biselenophene-5,5'-dicarboxylic acid linker (H_2SpSp) specifically designed for MOF synthesis has been prepared. Exploiting the

structural analogy of this new linker with other five-membered heterocycles H_2TpTp (2,2'-bithiophene-5,5'-dicarboxylic acid) and H_2TzTz (2,2'-bithiazole-5,5'-dicarboxylic acid), three mixed-linker MOFs have also been synthesized: two-double mixed [H_2SpSp + H_2TpTp] and [H_2SpSp + H_2TzTz] as well as the triple-mixed [H_2SpSp + H_2TpTp + H_2TzTz]. All the four MOFs are isostructural and were fully characterized in the solid state. Selenophene, thiophene and thiazole are luminescent organic molecules, so their inclusion in a MOF structure produces luminescent materials that emit in the blue-green visible region upon excitation by a suitable UV-wavelength. Blue emitters show applications in displays and solid-state lighting[215], while green LEDs can be exploited in medical fields (chromotherapy) because green light helps to lighten hyperpigmentation spots and has calming and anti-inflammatory properties. In addition, the green color is slightly sedative, with beneficial effects for sleep and stress reduction. Unfortunately, the measured emission quantum yields are low in all cases, probably because of the self-quenching effects coming from the formation of nonfluorescent aggregates in the solid state. A viable strategy to solve this problem is the "solid-state dilution" of the chromophore using an excess of another non-emissive spacer for the construction of a mixed-linker MOF[216]. This strategy was applied in a different work and will be presented in the next chapter.

Chapter 5

ZIRCONIUM MOFS FOR LUMINESCENT SENSING AND WASTEWATER REMEDIATION

This chapter is based upon the following publication:

UiO-67-derived bithiophene and bithiazole MIXMOFs for luminescence sensing and removal of contaminants of emerging concern in wastewater.

Inorganic Chemistry Frontiers; **2022** *9*, 90 - 102

Giorgio Mercuri, Marco Moroni, Simona Galli, Clara Piccirillo, Agostina-Lina Capodilupo, Giulia Tuci, Giuliano Giambastiani and Andrea Rossin

5.1. Aim of the Work

One of the most important environmental issues that our society is facing nowadays is the scarcity of clean water. Among all the different contaminants that can be present in water, the class of contaminants of emerging concern (CECs) is one of the most relevant. To CECs belong pharmaceuticals and personal care products. The dangerousness of these compounds lies not only in their intrinsic toxicity and in the toxic by-products or metabolites that are formed after their decomposition, but also because many of them are not fully metabolized by the human body, passing through to contaminate the water system[217]. In fact, in recent years residues of CECs molecules were found in almost every region of the World both in surface and ground waters, as well as in wastewater treatment plants[218]. The worldwide presence of these contaminants is largely due to the increased consumption and use of antibiotics[219]. The concentration of antibiotics in the environment is continuously growing because they are not completely degraded by conventional wastewater treatments[220]. For this reason, it is mandatory to develop a water treatment that is effective in detecting and/or removing CECs from wastewater. From this viewpoint, MOFs have properties that make them applicable in environmental remediation (see paragraph 3.6. – Water purification) and some of them have been studied for CECs removal from water[221]. In the literature, it is also possible to find papers where luminescent MOFs are exploited as sensors for the detection of contaminants in water[222]. However, only few studies are reported on MOFs that can detect and adsorb pollutants at the same time[223] working as a multifunctional material.

In this work, the two intrinsically fluorescent linkers H_2TpTp (2,2'-bithiophene-5,5'-dicarboxylic acid) and H_2TzTz (2,2'-bithiazole-5,5'-dicarboxylic acid) [Figure 73]are used to synthesize two new

"UiO-67-type" Zr(IV) MOFs. Starting from the previous experience (see chapter 4 – Zirconium MOFs for luminescent applications),[224] where MOFs built exclusively with heterocyclic emissive linkers show an emission intensity below the limit required for practical applications, a "solid-state dilution" approach was used. To do that, SALE was applied on UiO-67 to partially replace the H_2PhPh linker (non-luminescent) with the heterocyclic luminescent linkers H_2TpTp and H_2TzTz [Figure73]. The resulting MOFs $[Zr_6O_4(OH)_4(PhPh)_5(TpTp)]$ (**UiO-67-TpTp**) and $[Zr_6O_4(OH)_4(PhPh)_5(TzTz)]$ (**UiO-67-TzTz**) have been thoroughly characterized in the solid state. They show the same structural topology and crystal structure of parent UiO-67, and they maintain the luminescence features of the "inserted-linkers". In this respect, SALE has proved to be extremely effective to avoid the formation of domains of the same linker in the MIXMOFs with the consequent undesired self-quenching caused by the proximity of the emitters in the crystal structure.

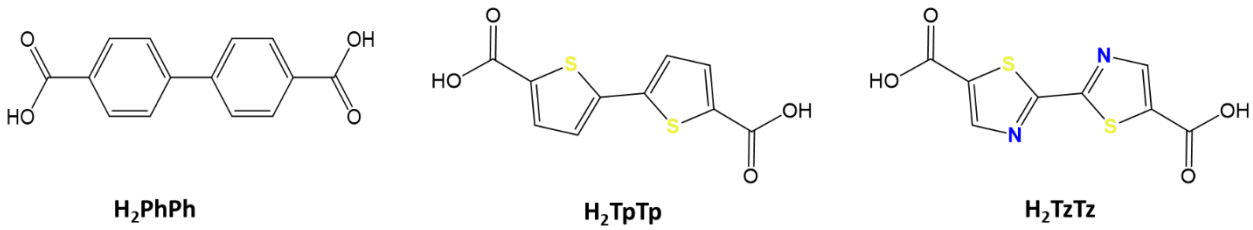

Figure 73: Molecular structure of the different linkers used in this work.

The two mixed-metal MOFs have been tested as luminescent sensors for selected CECs, namely: diclofenac sodium (DCF), fluoxetine (FXT), sulfamethoxazole (SMZ) and ibuprofen (IBR) [Figure 74]. The compounds show an increase of the emission intensity when suspended in water solutions containing the pollutants. Based on the luminescence sensing results, **UiO-67-TzTz** was also evaluated for the adsorption of DCF from water.

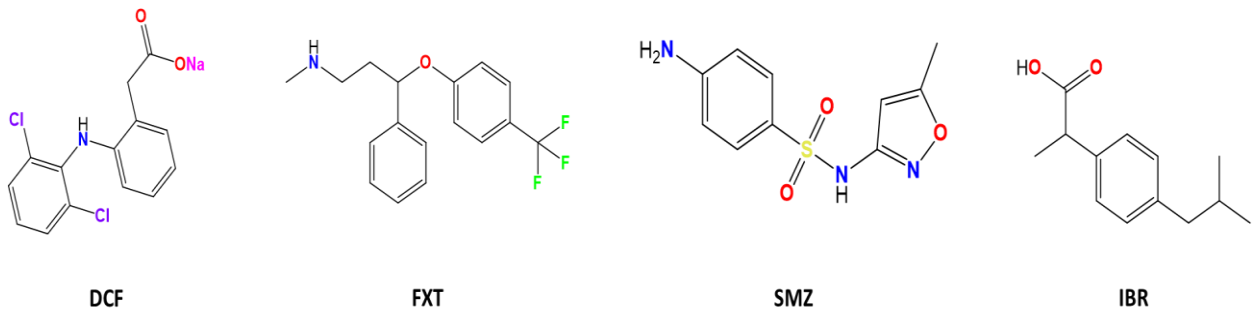

Figure 74: Molecular structures of the CECs studied in this work: diclofenac sodium (DCF), fluoxetine (FXT), sulfamethoxazole (SMZ) and ibuprofen (IBR).

5.2. Experimental Details

5.2.1. Materials and Methods

All the chemicals and reagents employed were used as received from commercial suppliers. Deuterated solvents (Sigma Aldrich) were stored over 4 Å molecular sieves and degassed by three freeze–pump–thaw cycles before use. Literature recipes were followed to prepare UiO-67[225], H_2TpTp[196] and H_2TzTz[197].

^{1}H-NMR spectra were recorded on a BRUKER AVANCE 400 MHz spectrometer, with chemical shifts (δ) reported in parts per million (ppm) downfield of tetramethylsilane (TMS) and calibrated against the residual protiated solvent resonance.

FT-IR spectra (KBr pellets) were recorded on a PerkinElmer Spectrum BX Series FTIR spectrometer, in the 4000–400 cm^{-1} range, with a 2 cm^{-1} resolution.

TGA analysis were performed under a N_2 flow (100 mL min^{-1}) at a heating rate of 10 K min^{-1} with an EXSTAR Thermo Gravimetric Analyzer Seiko 6200. The latter was coupled with a ThermoStarTM GSD 301T for mass analysis of volatile species.

The elemental analyses were performed using a Thermo FlashEA 1112 Series CHNS–O elemental analyzer with an accepted tolerance of ±4% on carbon (C), hydrogen (H), nitrogen (N) and sulfur (S).

PXRD qualitative measurements were carried out in the 2.0 – 50.0° 2θ range with a Panalytical X'PERT PRO powder diffractometer equipped with a sealed X-ray tube (Cu Kα, λ = 1.5418 Å), a filter of nickel in the diffracted beam, and a PIXcel© solid state detector. Slits were used on both the incident (Soller, 0.25°, and divergence, 0.5°) and the diffracted (anti-scatter, 7.5 mm height) beam.

XRF qualitative elemental analysis was performed on a powdered batch (ca. 10 mg) of **UiO-67-TzTz** and [*DCF*@**UiO-67-TzTz**] with a Panalytical MINIPAL 2 instrument equipped with a Cr X-ray source.

5.2.2. Compounds Synthesis

Synthesis of $[Zr_6O_4(OH)_4(PhPh)_5(TpTp)]$·5DMF (UiO-67-TpTp·DMF): UiO-67 {$[Zr_6O_4(OH)_4(PhPh)_6]$, FW = 2120.63 g mol^{-1}, 213 mg, 0.10 mmol} was suspended in a DMF solution (7 mL) of H_2TpTp (FW = 254.27 g mol^{-1}, 25 mg, 0.10 mmol). The obtained suspension

was heated at T = 393 K under gentle magnetic stirring. After 12 h, the mixture was cooled down to ambient temperature and the yellow solid, **UiO-67-TpTp·DMF**, was filtered over a 0.2 µm PTFE filter, subsequently washed with hot DMF (353 K, 2 × 10 mL), ethanol (3 × 10 mL) and petroleum ether (3 × 10 mL), and finally dried under a N_2 flow at ambient temperature. Yield: 213 mg (85% based on zirconium). The phase purity of every batch was checked through PXRD. Elemental analysis (%) calc. for **UiO-67-TpTp·DMF**, $C_{95}H_{83}N_5O_{37}S_2Zr_6$ (MW = 2498.16 g mol^{-1}): C 45.67, H 3.35, N 2.80, S 2.57; found: C 45.68, H 3.35, N 2.83, S 2.58. IR [*ν*(C=O)] band (KBr, cm^{-1}): 1678 (s), 1605 (s).

Synthesis of $[Zr_6O_4(OH)_4(PhPh)_5(TzTz)]$·5DMF (UiO-67-TzTz·DMF): UiO-67 {$[Zr_6O_4(OH)_4(PhPh)_6]$, FW = 2120.63 g mol^{-1}, 268 mg, 0.13 mmol} was suspended in a DMF solution (7 mL) of H_2TzTz (FW = 256.24 g mol^{-1}, 32 mg, 0.13 mmol). The suspension was heated at T = 393 K under gentle magnetic stirring. After 12 h, the reaction mixture was cooled down to ambient temperature and the greyish solid, **UiO-67-TzTz·DMF**, was filtered over a 0.2 µm PTFE filter, subsequently washed with hot DMF (353 K, 2 × 10 mL), ethanol (3 × 10 mL) and petroleum ether (3 × 10 mL), and finally dried under a nitrogen stream at ambient temperature. Yield: 200 mg (61% based on zirconium). The phase purity of every batch was checked through PXRD. Elemental analysis (%) calc for **UiO-67-TzTz·DMF**, $C_{93}H_{81}N_7O_{37}S_2Zr_6$ (MW = 2500.13 g mol^{-1}): C 44.68, H 3.27, N 3.92, S 2.57; found: C 44.66, H 3.23, N 3.89, S 2.54. IR [*ν*(C=O)] band (KBr, cm^{-1}): 1683 (w, sh), 1590 (s).

Synthesis of $[Zr_6O_4(OH)_4(PhPh)_5(TzTz)]$·DCF ([*DCF*@UiO-67- TzTz]): UiO-67-TzTz·DMF (40 mg, 0.016 mmol) was suspended in an aqueous solution (10 mL) of diclofenac sodium (FW = 318.15 g mol^{-1}, 51 mg, 0.16 mmol, 10 equiv.) at T = 343 K under gentle magnetic stirring. After 15 h, the suspension was cooled to ambient temperature and the solid was filtered off, washed with water (1 × 10 mL), ethanol (2 × 10 mL), petroleum ether (2 × 10 mL), and finally dried under a nitrogen stream at ambient temperature. Yield: 39 mg (quantitative).

5.2.3. Linkers Composition Quantification

The approximate linkers composition in the two MIXMOFs has been assessed through ^{1}H-NMR analysis of the digested samples in acidic solutions (48% aqueous HF, Sigma Aldrich/DMSO-d_6) as seen in the previous chapter (see 4.2.3. – Linkers composition quantification in the mixed-linker

phases). In a typical procedure, 10 mg of sample was dissolved in three drops of aqueous hydrofluoric acid and 0.6 mL of DMSO-d_6 directly into an NMR tube. The mixture was heated at T = 343 K for 12 h, to complete the sample digestion. The as-obtained clear yellow solution was analyzed via ^{1}H-NMR (400 MHz, relaxation delay τ = 15 s, 512 scans). [Figure 75] shows the ^{1}H-NMR spectrum of the digested **UiO-67-TzTz** chosen as a representative example.

The stoichiometric coefficients (x, y) in the general formula $[Zr_6O_4(OH)_4(PhPh)_x(L)_y]$ (where x + y = 6 and L = $TzTz^{2-}$ or $TpTp^{2-}$) were calculated from the integral values (*a, b*) related to the corresponding linker proton signals, according to the following equations:

$$x = \frac{6(\frac{a}{2})}{(\frac{a}{2}+b)} \quad and \quad y = \frac{6b}{(\frac{a}{2}+b)}$$

The value of the integral *a* must be divided by 2 because the relative NMR signal is referred to 4 H, while that of thiazole linker is referred only to 2 H.

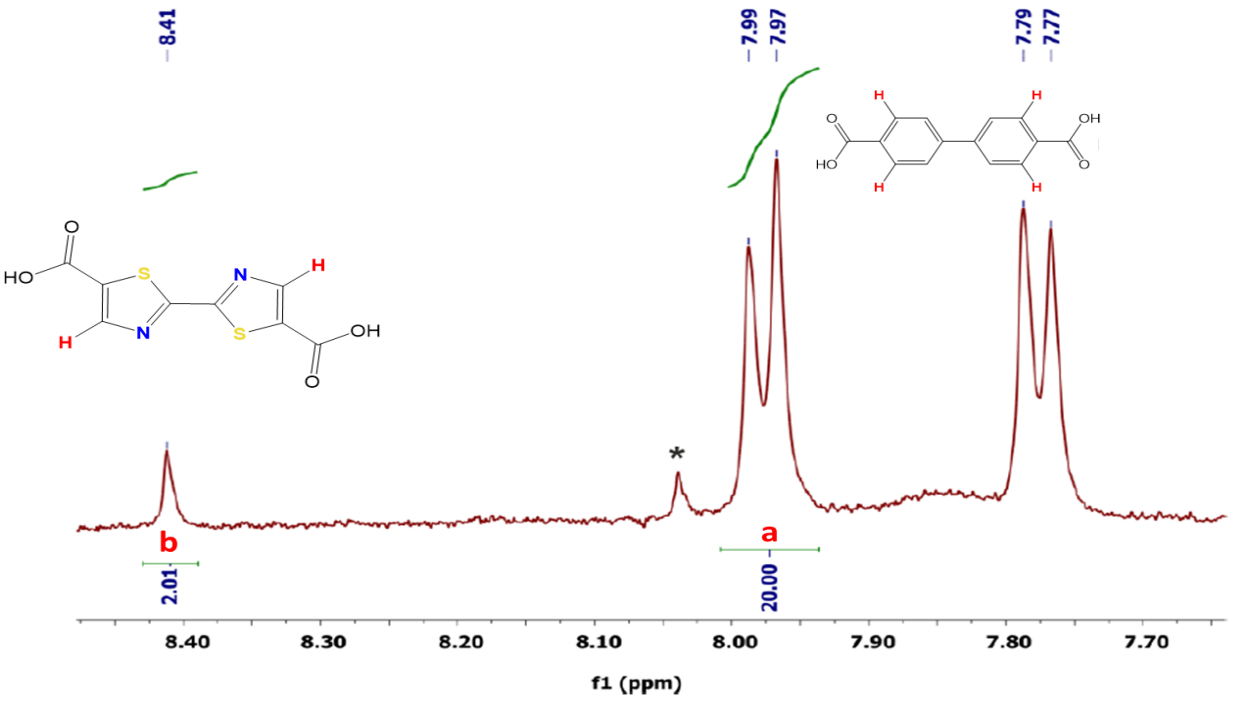

Figure 75: Zoom of the aromatic region used for the quantification of the linkers ratio of the digested **UiO-67-TzTz**. In red are highlighted the hydrogen atoms relative to the integrated NMR signals. * clathrated DMF solvent signal.

5.2.4. PXRD Structure Determination

PXRD data acquisitions were carried out using a Bruker AXS D8 Advance vertical-scan θ:θ diffractometer, equipped with a sealed X-ray tube (Cu Kα, λ = 1.5418 Å), a filter of nickel in the diffracted beam, a Bruker Lynxeye linear position-sensitive detector, and the following optical components: primary beam Soller slits (2.5°), fixed divergence slit (0.5°), anti-scatter slit (8 mm). The generator was set at 40 kV and 40 mA. A powdered sample (~50 mg) of **UiO-67-TzTz·DMF** was introduced into the cavity of a silicon free-background sample-holder 0.2 mm deep (Assing Srl, Monterotondo, Italy). The purity and crystallinity of the sample were checked conducting a preliminary PXRD acquisition in the 2θ range 3.0 – 35.0°, with steps of 0.02° and time per step of 1 s. The PXRD acquisition for the assessment of the crystal structure was performed overnight in the 2θ range 3.0 – 105.0°, with steps of 0.02° and an approximate scan time of about 12 h. A visual comparison between the PXRD pattern of **UiO-67-TzTz·DMF** and that of UiO-67[206] suggested that the two MOFs are isostructural. A whole powder pattern profile refinement with the so-called Le Bail approach[226] performed with TOPAS-R V336 employing the space group and unit cell parameters of UiO-67 confirmed the suggestion [Figure 79]. The crystallographically independent portion of $PhPh^{2-}$, $TzTz^{2-}$ and DMF were modelled as rigid bodies using the z-matrix formalism, assigning to the bond distances and angles Bond distances and angles for the rigid body describing: (a) the ligands: $PhPh^{2-}$ aromatic C–C, 1.39 Å; $TzTz^{2-}$ aromatic C–C and C–N, 1.39 Å; C–S, 1.75 Å; single C–C, 1.54 Å; carboxylic C–O, 1.25 Å; C–H, 0.95 Å; $PhPh^{2-}$ C–C–C internal bond angles, 60.0°; C–C–C and C–C–H external bond angles, 120.0°; $TzTz^{2-}$ C–C–C and C–C–S internal bond angles, 113.2° and 112.1°, respectively; C–C–H external bond angles, 123.4°; C–C–C external bond angles, 128.0°; (b) the DMF molecule: C=O, 1.25 Å; C–N, 1.35 Å; C–H, 0.95 Å; bond angles for sp^2 and sp^3, atoms, 120.0° and 109.5°, respectively. idealized values based on a search in the Cambridge Structural Database (v. 2021) for room-temperature and room-pressure crystal structures containing the three molecules. The molar ratio between the $PhPh^{2-}$ and $TzTz^{2-}$ linkers was set at the value retrieved from the ^{1}H-NMR signal integration of the digested sample. In the initial steps of the structure assessment, both the metal cluster atoms (Zr and O) and the center of mass of the rigid bodies describing the spacers were located according to the crystal structure of UiO-67[206] and $[Zr_6O_4(OH)_4(TzTz)_6]\cdot n$DMF[197], adopting an idealized distribution of the two linkers in both independent positions. The linkers orientation was then allowed to be refined. Two crystallographically independent DMF molecules and a

dummy oxygen atom representing the smeared electron density in the cavities not described by DMF were located using the Simulated Annealing approach[207], implemented in TOPAS-R V3. A Chebyshev-type polynomial function was employed to describe the background. An isotropic thermal factor [Biso(M)] was refined for the Zr(IV) ion; the isotropic thermal factor of the oxygen atoms belonging to the cluster and the ligands was calculated as Biso(L) = Biso(M) + 2.0 ($Å^2$); the isotropic thermal factor of the atoms describing the clathrated solvent was calculated as Biso(S) = Biso(M) + 3.0 ($Å^2$). The peak profile was modelled trough the Fundamental Parameters Approach[208]. The anisotropic peak broadening was described by means of Gaussian and Lorentzian spherical harmonics. During the final stages of the structural refinement, instrumental and structural parameters were collectively refined by means of the so-called Rietveld refinement[227] The final Rietveld refinement plot is shown in [Figure 79]:

*Crystal data for **UiO-67-TzTz·DMF***, $C_{78}H_{46}N_2O_{32}S_2Zr_6$·Solv, cubic, $Pn\bar{3}$, a = 26.842(1) Å, V = 19 339(3) $Å^3$, Z = 24, Z′ = 4, ρ = 0.922 g cm^{-3}, F(000) = 5404.8, R_{Bragg} = 0.005, R_p = 0.019 and R_{wp} = 0.024, for 5051 data and 78 parameters in the 4.0–105.0° (2θ) range. CCDC no. 2103802.

5.2.5. Gas Adsorption

Before the adsorption measurements were carried out, ~40 mg of each MIXMOF were activated at 453 K under high vacuum (10^{-6} Torr) for 12. The textural properties were evaluated through volumetric N_2 adsorption at 77 K on an ASAP 2020 Micromeritics instrument. For the BET specific surface area calculation, the 0.01–0.1 p/p_0 pressure range of the isotherm was used. The micro- and mesopore size was evaluated through NLDFT methods (Tarazona model for cylindrical pores).

5.2.6. Luminescence Sensing Experiments

Luminescence experiments were performed on pre-activated MIXMOF samples using a Cary Eclipse fluorescence spectrometer. As a preliminary test of the MIXMOFs water stability, a weighted amount (5 mg) of material was dispersed into 25 mL of distilled water and sonicated for about 30 minutes. After this time, the suspension was transferred into a fluorimetric 1 cm path cuvette and luminescence spectra were registered with a 380 nm excitation source. To evaluate the sensing properties of the materials, the protocol reported by Zhong et al.[228] was

used, with some modifications. The MIXMOF aqueous suspension (2 mL) was placed in the cuvette, as described above. Subsequently, aliquotes of an aqueous solution (100 mg L^{-1}) of each pollutant (DCF, FXT, SMZ and IBR) were gradually added, and the cuvette was shaken for about 30 seconds. Then, the luminescence spectrum of the MIXMOF-pollutant system was registered. Wavelength shifts and/or signal intensity changes were monitored.

5.2.7. Testing of Pollutant Adsorption and Desorption

Based on the results of luminescence sensing, **UiO-67-TzTz** was tested for the adsorption of DCF using the following protocol. An activated sample (4 mg) of the MIXMOF was suspended in an aqueous solution of the pollutant (2 mL) in a glass vial. The mixture was gently stirred for 6 h at room temperature; this time interval was chosen as it is considered ideal to reach a plateau in the adsorption profile, according to what is reported in the literature[229]. Experiments with different pollutant concentrations (in the range 5 – 200 mg L^{-1}) were carried out. At the end of the experiments, the suspension was centrifuged to separate **UiO-67-TzTz** from the solution; the supernatant was analyzed with UV-Vis spectroscopy (λ_{max} = 276 nm) to determine the residual pollutant concentration. The experiments were performed in duplicate; an average value of the two results was adopted for the discussion. The data were fitted with the Langmuir model, according to the equation:

$$\frac{C_e}{q_e} = \frac{1}{X_m K} + \frac{C_e}{X_m}$$

where C_e is the concentration of the contaminant at the equilibrium (mg L^{-1}), q_e is the amount of contaminant adsorbed for unit of material (mg g^{-1}), X_m is the maximum adsorption capacity of the material for the specific pollutant (mg g^{-1}) and K is a parameter related to the affinity between the pollutant and the adsorbent.

DCF desorption from **UiO-67-TzTz** was evaluated for selected pollutant concentrations. At the end of the adsorption process, the supernatant was separated from the solid by centrifugation; the solid was dried, then suspended in distilled water (2 mL) and left under stirring at ambient temperature. After 6 h, the solid was separated by centrifugation and the supernatant was analyzed in terms of its DCF concentration as described above.

5.3. Results and Discussion

The two new mixed-linker MOFs **UiO-67-TpTp** and **UiO-67-TzTz** were synthesized using the SALE technique starting from UiO-67[225]. To test the possible exchange between the different linkers, a preliminary experiment was made using ^{1}H-NMR analysis. To do that, a small amount of UiO-67 and the H_2TzTz linker (in a 1:1 - MOF : linker molar ratio) are placed in an NMR tube and diluted with DMF-d_7. The NMR spectrum recorded before the reaction shows only the linker's hydrogen signals at δ_H = 8.60 ppm [Figure 76b]. Then, the tube was heated at 393 K for 12 h to favor linker exchange. After this reaction time, another NMR spectrum was recorded [Figure 76a]. The two doublets ascribed to the two different proton sets of H_2PhPh at δ_H = 7.95 and 8.17 ppm were clearly visible in solution, while the signal of H_2TzTz has disappeared, indicating a successful linker exchange.

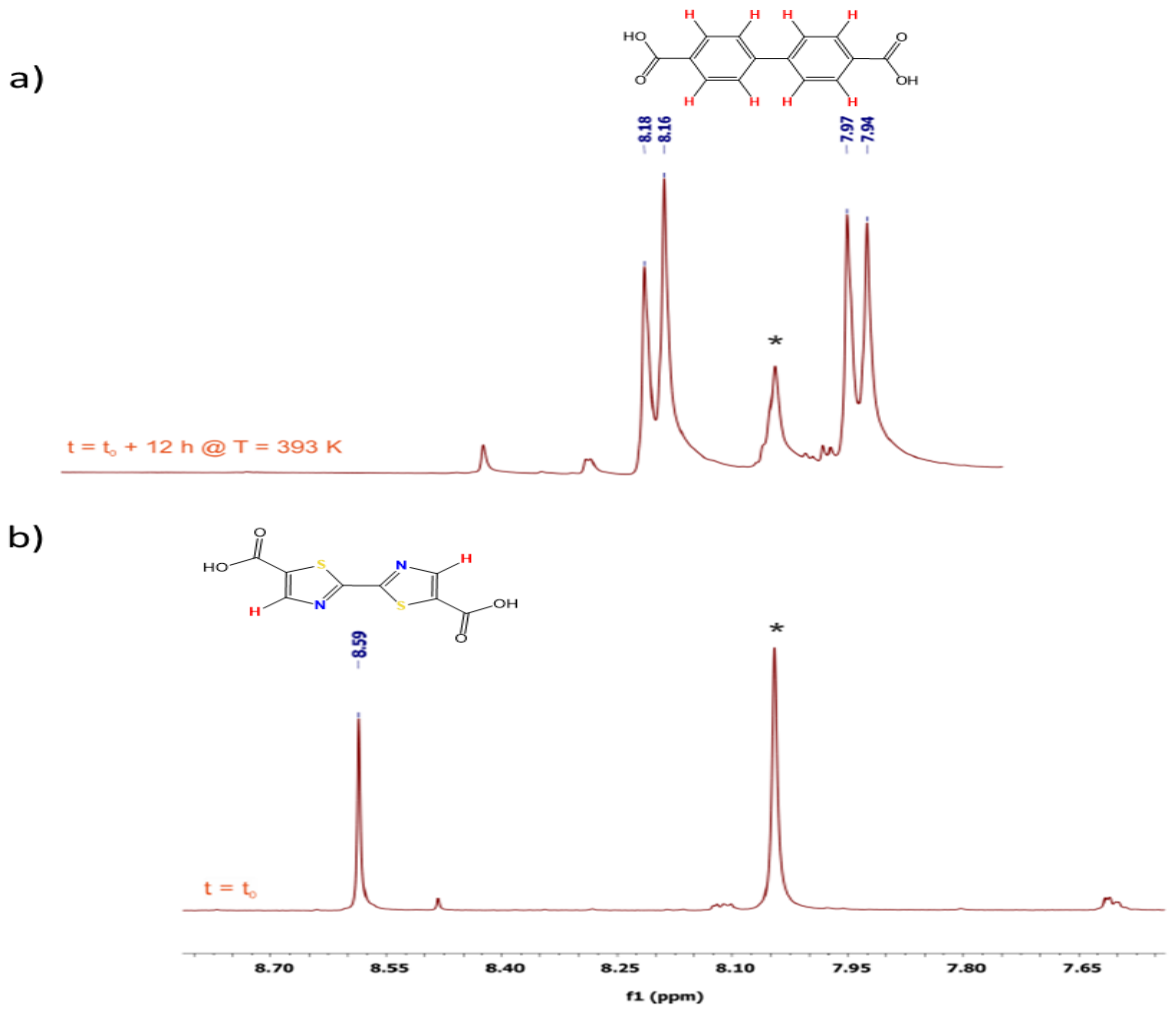

Figure 76: Test for the SALE synthesis of **UiO-67-TzTz** monitored through ^{1}H-NMR spectroscopy in DMF-d_7 solution (400 MHz, T=298 K). Zoom of the aromatic region of the spectrum of the initial solution before the synthesis (b). Zoom of the aromatic region of the spectrum recorded after keeping the same NMR tube at T= 393 K for 12 h (a).

After the positive response of the test, the two MIXMOFs were prepared suspending UiO-67 in a DMF solution of the linkers H_2TpTp and H_2TzTz keeping the 1:1 – MOF : linker molar ratio. The solutions were heated at 393 K for 12 h under gentle magnetic stirring, leading to the formation of the new MOFs of minimal formulae $[Zr_6O_4(OH)_4(PhPh)_5(TpTp)]\cdot 5DMF$ (**UiO-67-TpTp**) and $[Zr_6O_4(OH)_4(PhPh)_5(TzTz)]\cdot DMF$ (**UiO-67-TzTz**). The 5:1 ratio of the two linkers was expected from the initial stoichiometry adopted from the synthesis and it was confirmed through elemental analysis and the digestion of the sample in acidic solution, following the procedure reported in a precedent paragraph (see 5.2.3. – Linker composition quantification). The choice of this linkers ratio was made to "dilute" the heterocyclic linkers and to avoid emission self-quenching caused by the proximity of the emitters in the crystal structure previously observed in other MOFs (see chapter 4 – Zirconium MOFs for luminescent applications)[224].

The two MOFs **UiO-67-TpTp** and **UiO-67-TzTz** have been thoroughly characterized in the solid state. The thermal behavior was assessed through TGA and DTG analysis [Figure 77]. The two MOFs show the same thermal stability of pure UiO-67 (T_{dec} = 819 K); thus, the partial linker substitution does not affect the stability of the material. However, after an initial weight loss due to the synthesis solvent evaporation, both **UiO-67-TpTp** and **UiO-67-TzTz** show another weight loss at 630 K and 670 K respectively. The latter can be ascribed to the loss of $TpTp^{2-}$ and $TzTz^{2-}$ linkers because the two heterocyclic linkers are more weakly coordinated to the Zr atoms than $PhPh^{2-}$ because of their shorter length.

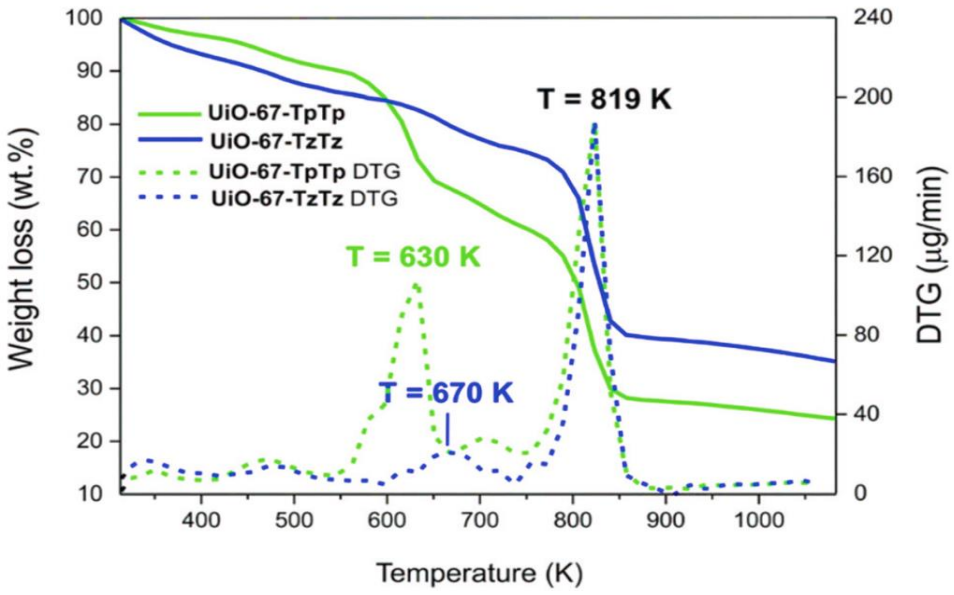

Figure 77: TGA (solid line) and DTG (dotted line) profiles of **UiO-67-TpTp** (green) and **UiO-67-TzTz** (blue).

The phase purity of the MIXMOFs was checked through PXRD analysis [Figure 78]. The pattern comparison confirms that the parent crystallographic symmetry of UiO-67 is maintained in both cases after SALE.

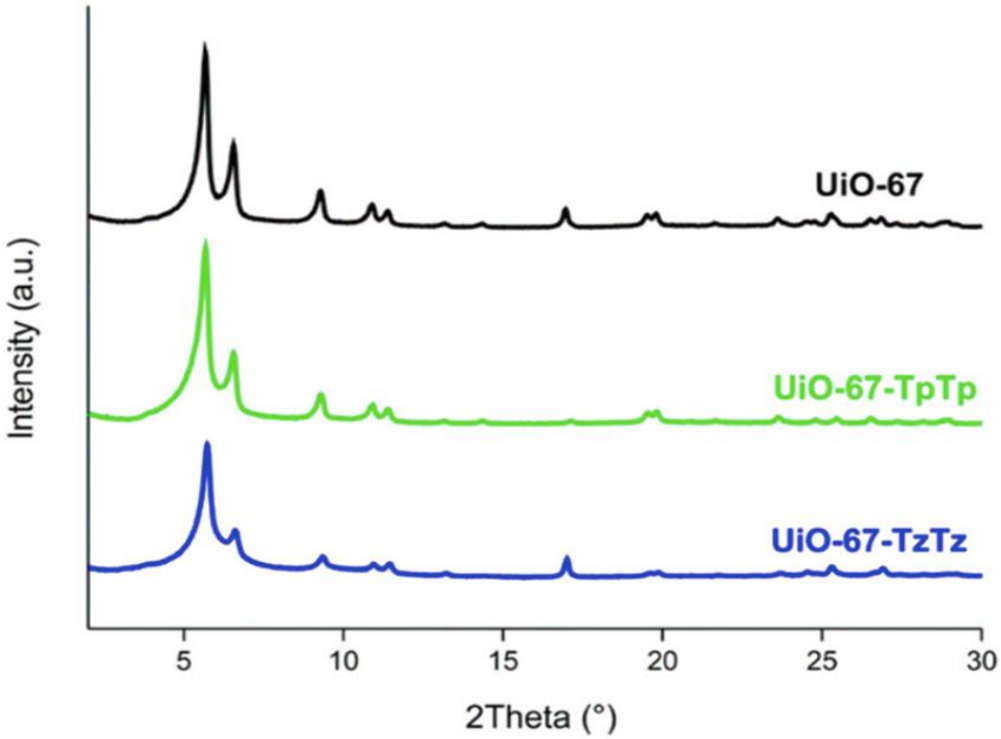

Figure 78: PXRD pattern of UiO-67 (black), **UiO-67-TpTp** (green) and **UiO-67-TzTz** (blue) at comparison.

However, X-ray diffraction alone is not enough to assess whether the two linkers in the two MOFs adopt a random or a cluster distribution. However, given the results obtained in the luminescence tests (which will be analyzed later), we can assume that the linkers are present in a "random" distribution in the solid phase, as no self-quenching of the emission was observed. The structure of the thiazole-functionalized MIXMOF was assessed through the refinement of its whole PXRD pattern [Figure 79].

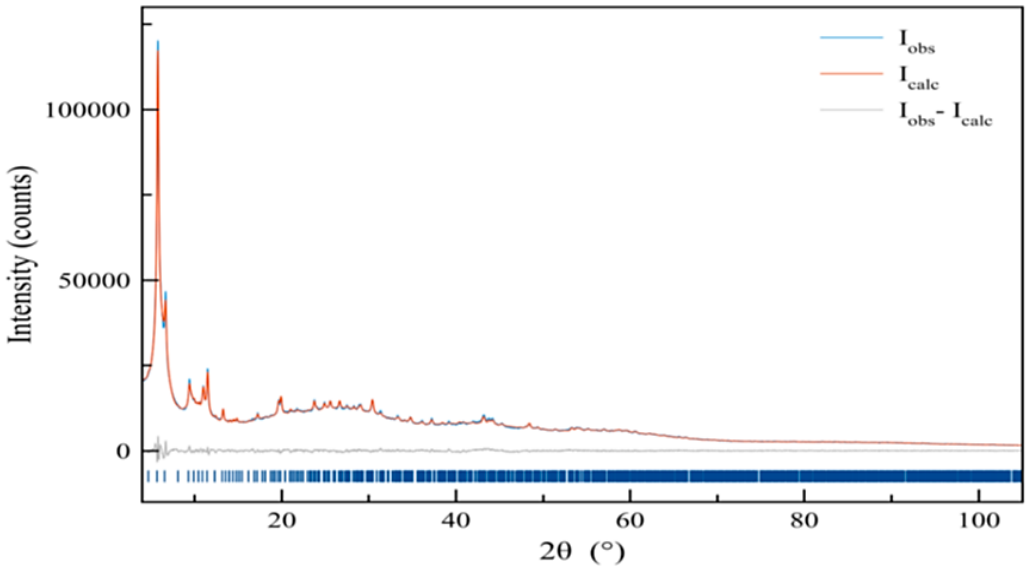

Figure 79: Graphical result of the final structure refinement conducted with the Rietveld method on the PXRD pattern of **UiO-67-TzTz** in terms of experimental (blue), calculated (red) and difference (grey) traces. The blue markers at the bottom indicate the position of the Bragg reflections.

UiO-67-TzTz·DMF crystallizes in the cubic space group $Pn\bar{3}$. The unit cell parameter of the MOF (26.842 Å) is comparable with that of the pure UiO-67 (26.880 Å), in agreement with the predominant presence of the $PhPh^{2-}$ linker. The crystal structure contains $[Zr_6O_4(OH)_4]^{12+}$ clusters as nodes [Figure 80a]: each Zr(IV) ion of the node is connected, in a square-antiprismatic fashion, to eight oxygen atoms, four belonging to the carboxylate groups, which build up one square face of the antiprism, and four coming from μ_3-O and μ_3-OH groups, which form the other square face. The $[Zr_6]$ node is connected to twelve others by the linkers. The $PhPh^{2-}$ linker is longer than $TzTz^{2-}$, so the Zr–O distances involving $TzTz^{2-}$ are longer than those involving $PhPh^{2-}$ [Zr–O_{PhPh} 2.024 – 2.397 Å vs. Zr–O_{TzTz} 2.395 – 2.592, respectively]. Nevertheless, they are still compatible with the formation of Zr–O coordination bonds. The framework [Figure 80b] features octahedral and tetrahedral cages (with diameter of ~12 Å and ~9 Å, respectively). The diameter of the cages was estimated by measuring the distance among the nearest atoms of linkers belonging to opposite cage walls and subtracting the van der Waals radii of the two atoms. The cages are occupied by clathrated solvent. Neglecting the solvent molecules, the empty volume estimated at ambient conditions with the software PLATON[230] is ~66%, in agreement with those found in UiO-67 (64%)[206]. As in the crystal structure of H_2TzTz[197], the heterocycles in $TzTz^{2-}$ adopt a reciprocal trans disposition, even though the two heterocyclic rings are not coplanar (with a deviation of about 9.5°), as in the other heterocycle-based UiO-67-type MOFs[224].

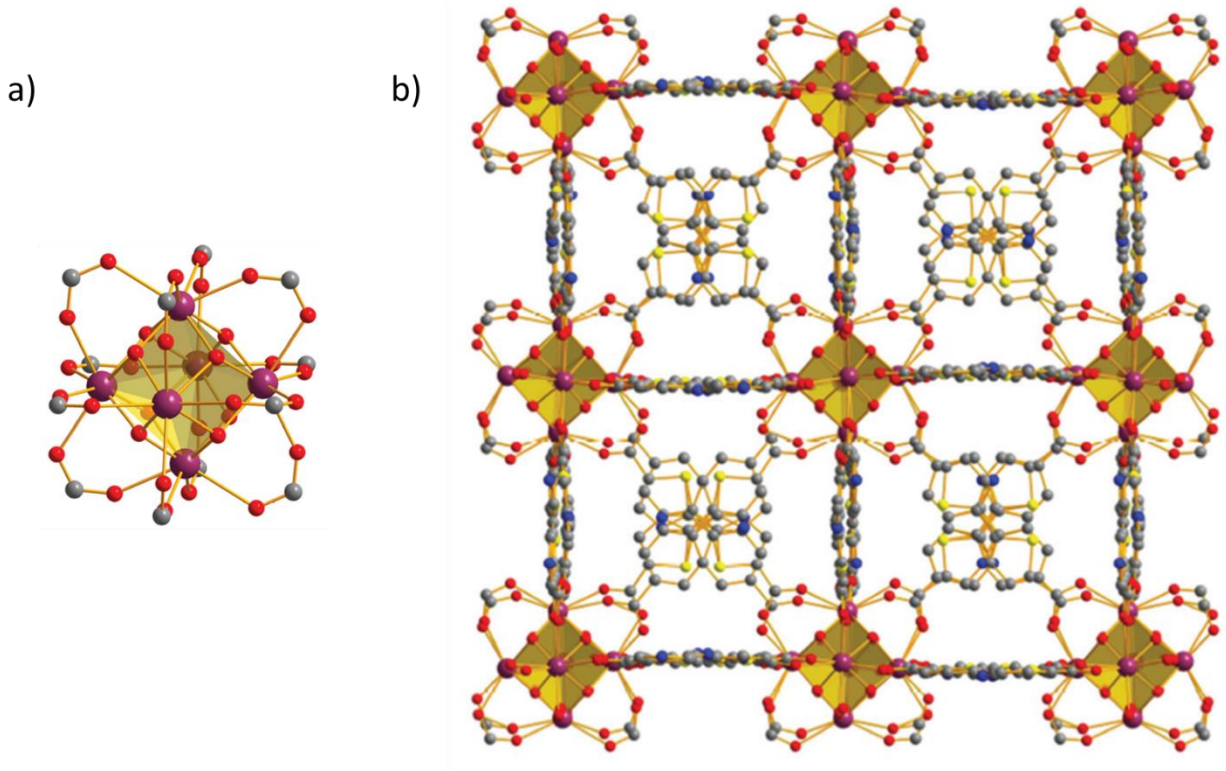

Figure 80: Representation of the crystal structure of **UiO-67-TzTz**. The SBU (a), a portion of the crystal packing viewed along one of the unit cell axes (b). Both solvent molecules and hydrogen atoms are omitted for clarity. Color code: Zr – violet, S – yellow, N – blue, C – grey, O – red.

The texture and the porosity of the two MOFs **UiO-67-TpTp** and **UiO-67-TzTz** was evaluated through volumetric N_2 adsorption at 77 K. Before the analysis, in accordance with the typical methodology, all samples were evacuated using a thermal treatment, heating them at 303 K under high vacuum for 24 h. The isotherms shape [Figure 81a] are of type I, typical of microporous materials. The calculated BET specific surface areas are 1700 m^2g^{-1} for **UiO-67-TpTp** and 1310 $m^2\ g^{-1}$ for **UiO-67-TzTz**, values that are lower than that of pristine UiO-67 of 1877 $m^2\ g^{-1}$. This result may be due to a partial MOF degradation during the linker exchange process, forming structural defects.

The total pore volume calculated at $p/p_0 = 0.98$ is of 0.86 $cm^3\ g^{-1}$ (**UiO-67-TpTp**) and 0.63 $cm^3\ g^{-1}$ (**UiO-67-TzTz**) (vs. 0.95 $cm^3\ g^{-1}$ for UiO-67)[225]. The NLDFT mesopore size (Tarazona model for cylindrical oxide-like pores) shows a slight variation when passing from UiO-67 (22 Å)[225] to **UiO-67-TpTp** or **UiO-67-TzTz** (24 Å) [Figure 81b]. This proves that SALE does not alter the mesopores morphology in the exchanged materials.

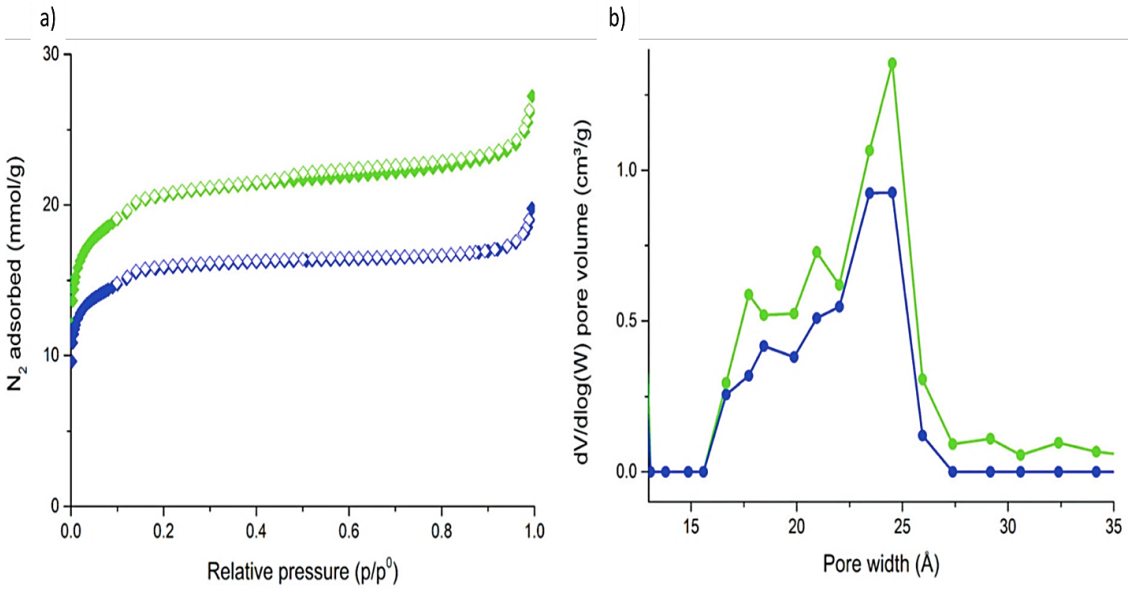

Figure 81: N_2 adsorption isotherms of **UiO-67-TpTp** (full green diamonds) and **UiO-67-TzTz** (full blue diamonds) and desorption isotherms (empty diamonds) measured at 77 K (a). Pore size distribution plots, calculated with NLDFT Tarazona model for cylindrical oxide-like pores, for **UiO-67-TpTp** (green) and **UiO-67-TzTz** (blue) at comparison (b).

Before testing the two MIXMOFs for the application as luminescent sensor in wastewaters, their stability in water was preliminary assessed. To do that, both MIXMOFs were soaked in distilled water at ambient temperature for 12 h. The PXRD patterns measured before and after the soaking [Figure 82] showed that the pristine crystallinity was maintained under the experimental conditions.

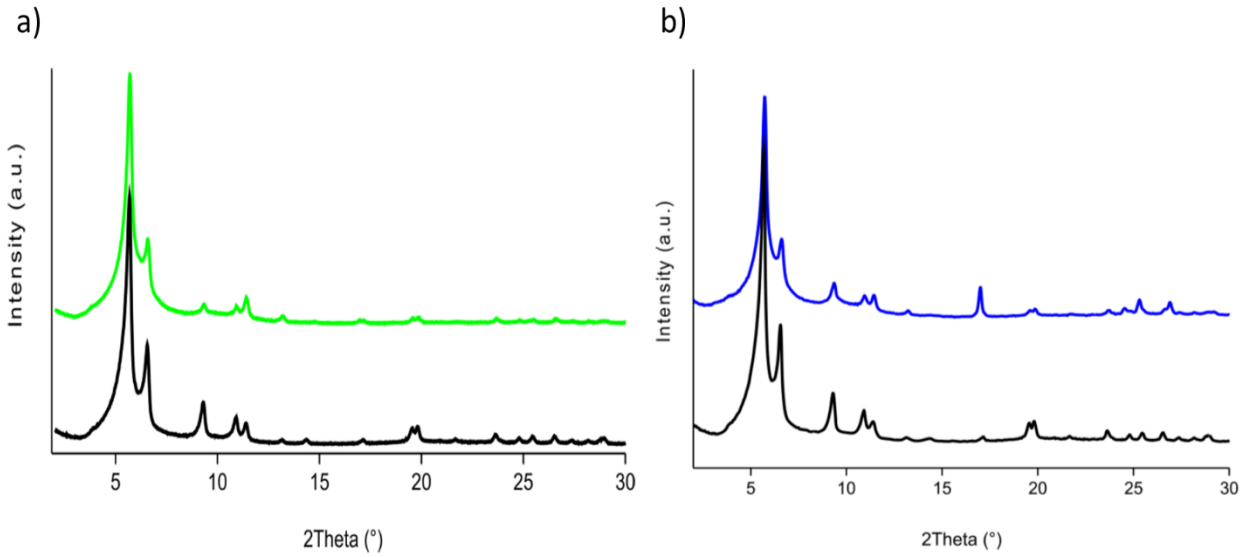

Figure 82: PXRD patter of **UiO-67-TpTp** before (black) and after (green) soaking in water for 12 h at room temperature (a). PXRD pattern of **UiO-67-TzTz** before (black) and after (blue) soaking in water at the same experimental conditions (b).

[Figure 83] depicts the emission spectra of the two MIXMOFs suspended in distilled water. Both materials show an intense and well-defined signal with λ_{max} equal to 442 nm for **UiO-67-TpTp** and 420 nm for **UiO-67-TzTz**, respectively. These values match well with those of the bare linkers in DMF solution[224], falling in the same spectral range and generating characteristic blue/green colors upon irradiation under UV lamp. This result proves that the luminescence of these MOFs is linker-based (see paragraph 3.3. – Luminescence sensing) and arises from the presence of the heterocyclic linkers only (H_2PhPh does not emit in the visible region). Also, that this is an indirect confirmation of the random linkers distribution in the crystal structure; indeed, formation of single-linker domains would induce an emission self-quenching.

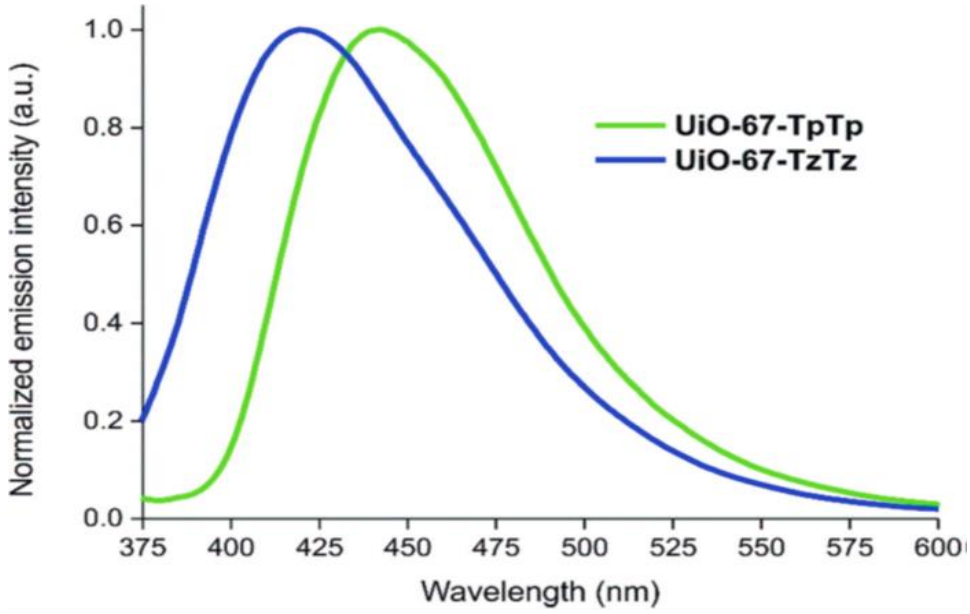

Figure 83: Emission spectra of **UiO-67-TpTp** (green) and **UiO-67-TzTz** (blue) suspended in distilled water.

Luminescence sensing experiments were performed on four of the most common CECs found in wastewaters: diclofenac sodium, fluoxetine, sulfamethoxazole, and ibuprofen [Figure 74]. The changes of the luminescent properties of the MIXMOFS were monitored in water upon addition of increasing amounts of the specific pollutants. Both compounds show an emission intensity increase when in contact with the contaminants, probably ascribed to the enhancement of the rigidity of the MOF heterocyclic linkers when a guest is present into the pores, with consequent elimination of non-radiative decay processes (responsible for signal quenching) [Figure 84].

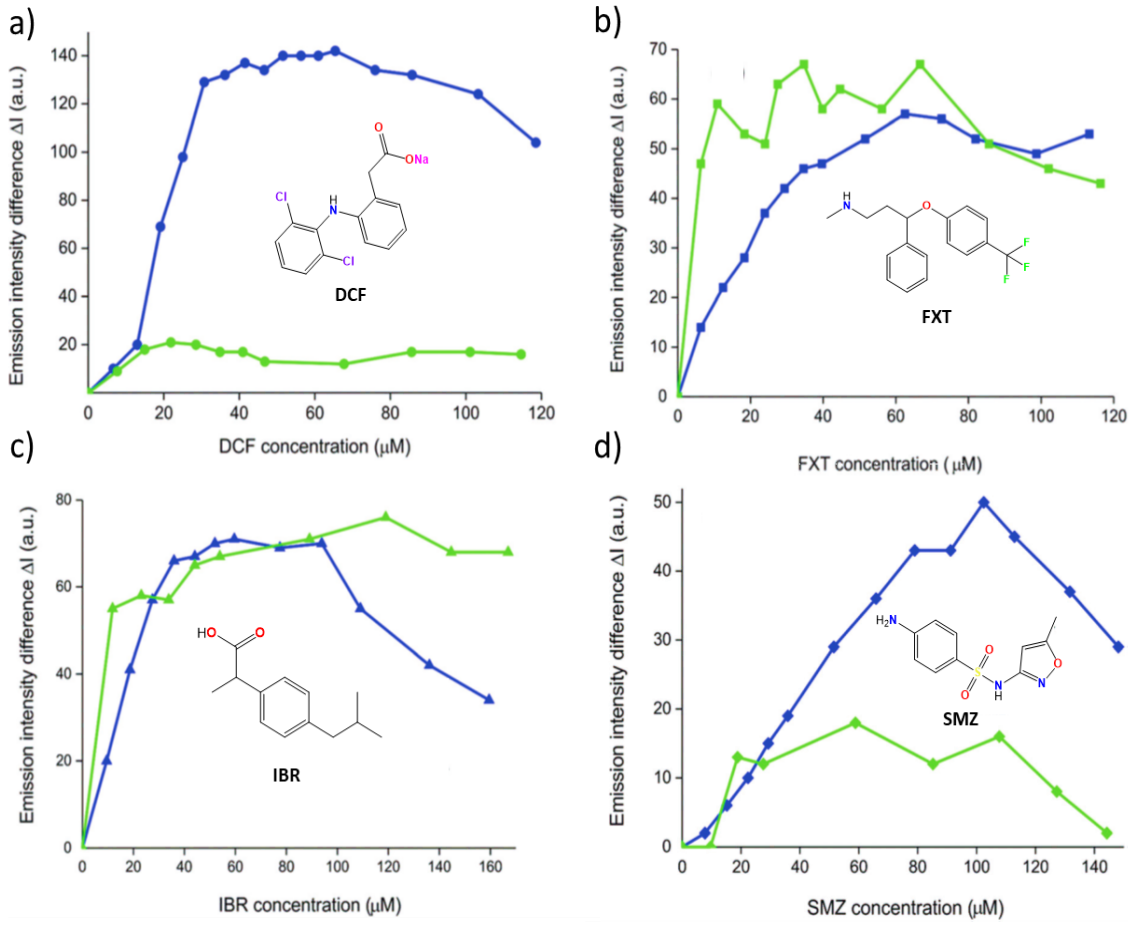

Figure 84: Emission spectra of **UiO-67-TpTp** (green) and **UiO-67-TzTz** (blue) as a function of the CECs concentration: diclofenac sodium (a), fluoxetine (b), ibuprofen (c) and sulfamethoxazole (d).

With DCF [Figure 84a], a similar intensity increase was observed with both materials for concentrations up to 20 µM. However, at higher concentrations, no further increase in intensity was observed with **UiO-67-TpTp** and the signal reached a plateau. On the other hand, for **UiO-67-TzTz** a stronger emission intensity was still measured for concentrations up to 30 µM before reaching saturation. This result can be explained because the negatively charged carboxylate group in DCF engages in stronger electrostatic interactions with **UiO-67-TzTz** where the presence of the thiazole N atom increases the heterocycle polarity if compared with thiophene. In **UiO-67-TzTz**, the emission intensity increase for concentrations up to 30 µM can be fitted with a linear correlation [Figure 86a]. This means that the material acts as a quantitative luminescent sensor in the concentration range 0 – 30 µM.

Considering FXT [Figure 84b], a comparable intensity trend was observed for both materials, although the highest intensity was registered for different contaminant concentrations of about 40 µM and 60 µM for **UiO-67-TpTp** and **UiO-67-TzTz**, respectively. Moreover, at the signal saturation there is a larger oscillation for **UiO-67-TpTp** than for **UiO-67-TzTz**. Consequently, only

the latter was considered for a linear fitting, as reported in [Figure 86b]. A good correlation was observed for concentrations up to 40 µM, a range comparable to that of DCF. However, the slope of the FXT curve is smaller (1.3 vs. 4.4 $\Delta I/\mu M^{-1}$ for FXT vs. DCF, respectively), indicating that the sensitivity of **UiO-67-TzTz** for this contaminant is lower than that for DCF. This difference in sensing response can be explained considering the lower FXT polarity in comparison with DCF. FXT does not have an integer charge, although the presence of the C–F bonds still confers polarity to the molecule. On the basis of the experimental data and the aforementioned considerations, we can claim that there are still significant electrostatic interactions between FXT and **UiO-67-TzTz**, but their strength is lower than those involving DCF.

Considering IBR [Figure 84c], for concentrations up to 45 µM, both MIXMOFs show a similar behavior with a linear increase followed by a plateau. Taking into consideration only the concentration range with a linear increase (up to almost 40 µM), the fitting performed for **UiO-67-TzTz** showed a good correlation [Figure 86c]. The sensitivity is slightly higher than that measured for FXT (the slopes of the fitting are 1.9 vs. 1.3 $\Delta I/\mu M^{-1}$ for IBR vs. FXT, respectively). This difference can again be explained by invoking polarity. IBR is more polar than FXT due to the presence of a carboxylic group.

Tests with SMZ showed that **UiO-67-TzTz** has again higher sensitivity than **UiO-67-TpTp**, as the emission intensity variation is more enhanced in the former case [Figure 84d]. A linear increase for concentrations up to almost 100 µM was measured, that is the larger value registered among the scrutinized CECs. This reveals that higher amounts of SMZ can be included in the MIXMOF pores before reaching saturation. Since there are no significant size differences among the tested contaminants, the origin of the observed behavior may be due to the formation of aggregates into larger micelles in solution, a phenomenon that has already been described for some pharmaceuticals. The size of the aggregates depends on several factors, including the solution concentration and the presence of other molecules able to form micelles like dodecylphosphocholine[231]. The formation of these aggregates can limit the diffusion through the MOF pores and is more common for DCF or IBR than for SMZ. Even if the linear fitting in this case showed a low sensitivity (0.5 $\Delta I/\mu M^{-1}$) [Figure 86d], the sensing capability extends to a larger concentration range, as stated above.

For an easier understanding, the results of the luminescence sensing experiments are summarized in [Figure 85] where they are reported all together and divided for each MOF. From

these graphics, it is clear that **UiO-67-TpTp** gives good performances only for FXT and IBR, while **UiO-67-TzTz** generally gives better performances against all the examined pollutants.

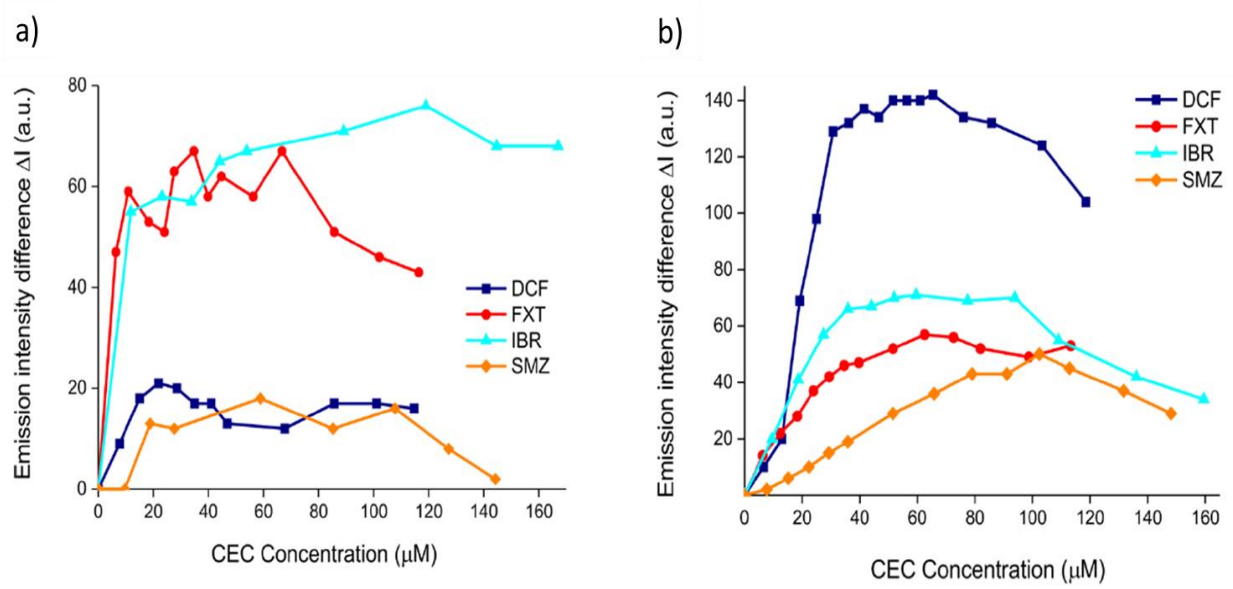

Figure 85: Emission intensity variation vs CEC concentration in the luminescent response of **UiO-67-TpTp** (a) and **UiO-67-TzTz** (b).

In particular, **UiO-67-TzTz** shows a very good linear correlation between the emission intensity and the CECs concentration [Figure 86]. For DCF, FXT and IBR, the range of linear emission response extends for concentrations up to 30 μM – 40 μM, while for SMZ the quantitative detection limit is almost 100 μM.

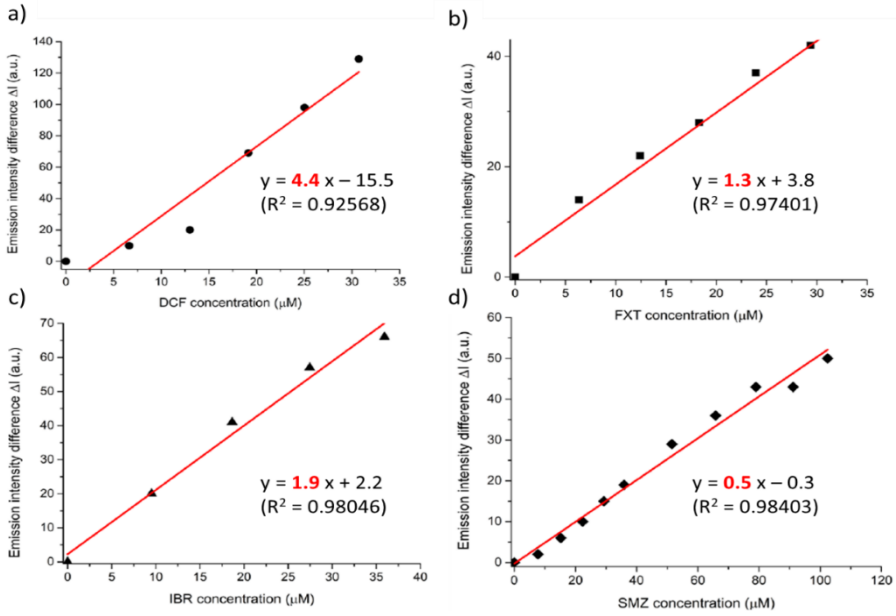

Figure 86: Linear data fitting for the dependance of the emission intensity from the CEC concentration for **UiO-67-TzTz** (chosen based on the results). Diclofenac sodium (a), fluoxetine (b), ibuprofen (c) and sulfamethoxazole (d).

Given the higher DCF sensitivity and related capacity to detect lower concentrations in solution observed for **UiO-67-TzTz** [Figure 85], this MOF was also tested for DCF adsorption from aqueous solutions.

First, it was necessary to prove the effective drug inclusion into the MOF. To do that, a sample of **UiO-67-TzTz** was suspended on an aqueous solution containing an excess of DCF (10 equivalents with respect to MOF) and kept under gentle stirring at T = 343 K for 15 h. The non-ambient temperature was chosen to promote the diffusion of DCF molecules into MOF pores. The resulting powder [*DCF*@**UiO-67-TzTz**] was washed with water to remove the unreacted DCF and then analyzed. The comparison between the IR difference spectrum of **UiO-67-TzTz** and [*DCF*@**UiO-67-TzTz**] and that of DCF [Figure 87a] reveals the presence of the typical DCF vibrational modes at ~1570 [ν(COO$^-$)], 1450 [ν(C=C)] and 750 cm^{-1} [γ(CH)] in the composite. The TGA-DTG profile recorded for [*DCF*@**UiO-67-TzTz**] [Figure 87b] shows an additional weight loss at T= 545 K that is not present in the pristine MOF [Figure 77] that perfectly matches with DCF decomposition temperature (around 544 K)[232].

Furthermore, the weight loss observed for this step (~13.0 wt%) is in excellent agreement with the hypothetical formula $[Zr_6O_4(OH)_4(PhPh)_5(TzTz)]\cdot(DCF)$.

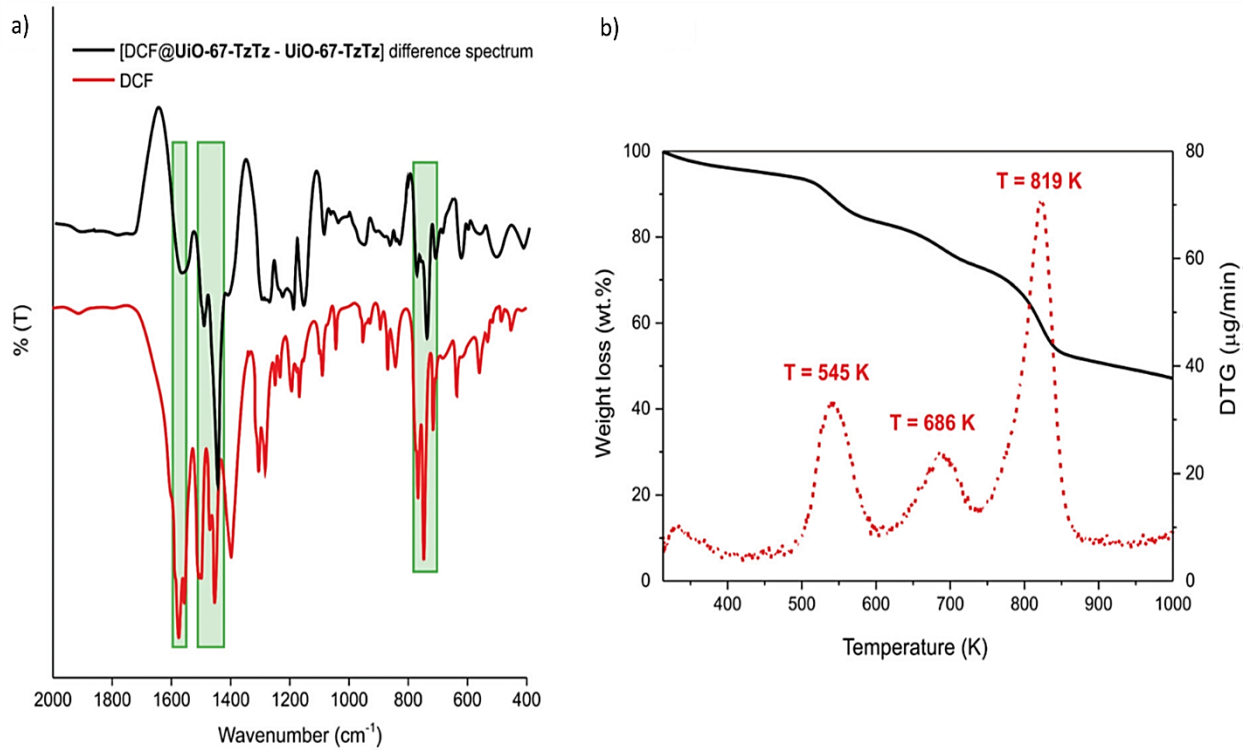

Figure 87: [*DCF*@**UiO-67-TzTz** – **UiO-67-TzTz**] IR difference spectrum (KBr pellet) in comparison with IR spectrum of pure DCF. The most typical vibrational modes of DCF are highlighted with green boxes (a). TGA-DTG profile of [*DCF*@**UiO-67-TzTz**] (b).

Moreover, the XRF spectrum of [*DCF*@**UiO-67-TzTz**] presents the characteristic lines of sodium and chlorine that are absent in the pristine MOF [Figure 88]. All these analyses confirm the successful inclusion of DCF into **UiO-67-TzTz**.

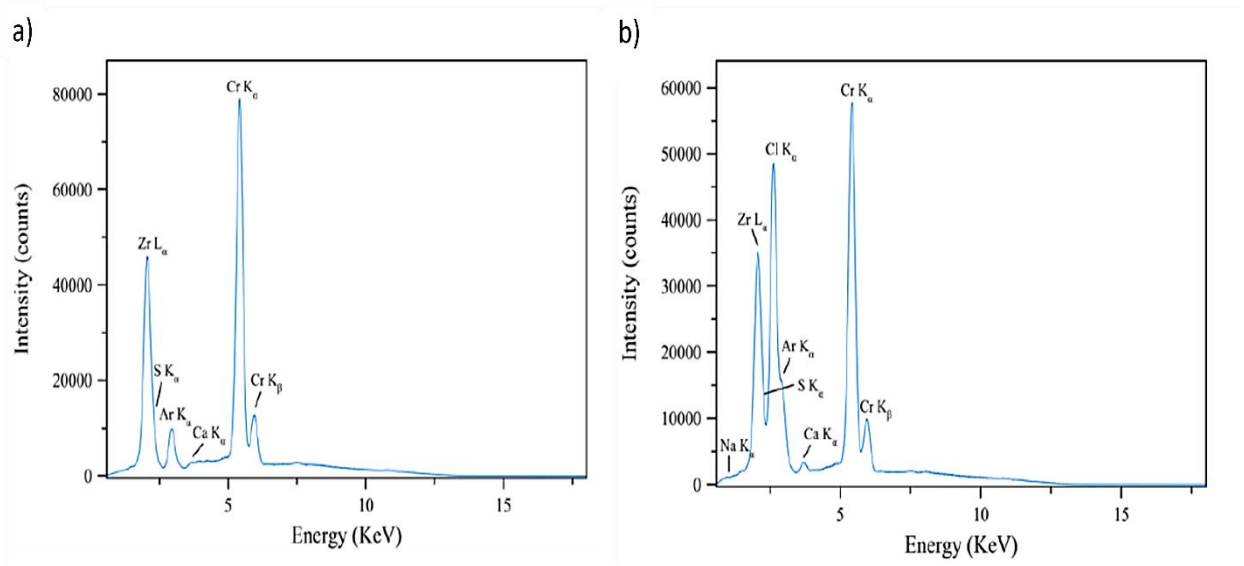

Figure 88: X-ray fluorescence spectra of **UiO-67-TzTz** (a) and [*DCF*@**UiO-67-TzTz**] (b) measured in air. The characteristic lines of argon come from air, those of chromium from the anode of the X-ray source and those of calcium from the sample holder.

The crystallinity degree of the drug-loaded sample was assessed through PXRD analysis [Figure 89]. Unfortunately, the low crystallinity degree shown by the composite did not permit structure determination from powder X-ray data.

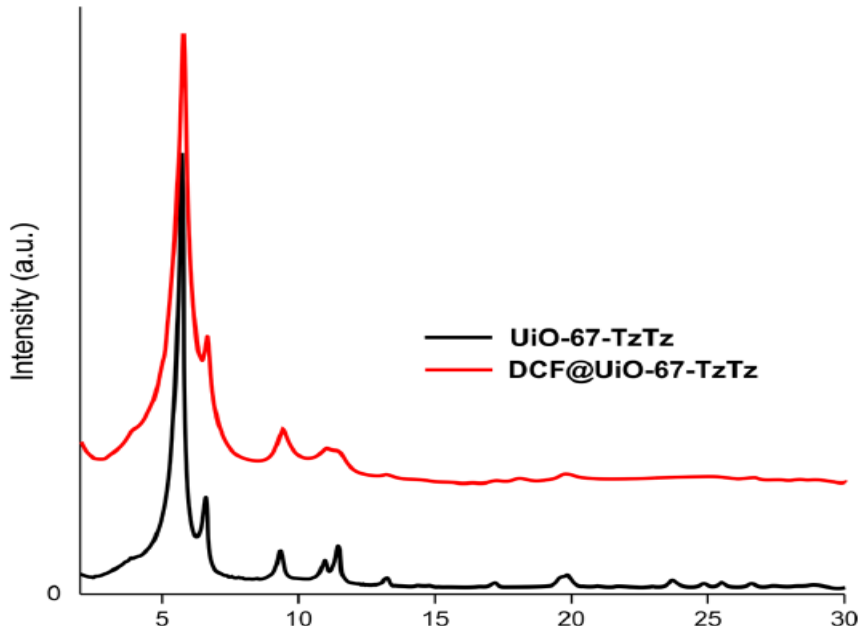

Figure 89: PXRD pattern of **UiO-67-TzTz** (black) and [*DCF*@**UiO-67-TzTz**] at comparison.

Once the drug-inclusion inside the MOF structure has been proved, **UiO-67-TzTz** was evaluated in its ability to act as a DCF "sponge". The adsorption experiments were performed as reported previously (see paragraph 5.2.7. – Testing of pollutant adsorption and desorption), by simply dissolving diclofenac sodium in water. Under these conditions, the solution is slightly acidic (pH between 5 and 6). At this pH, the carboxylic groups of DCF are almost completely deprotonated [p*Ka*(diclofenac) ∼4]. Further lowering the pH leads to DCF complete protonation followed by precipitation, as the acid is much less soluble in water than the corresponding sodium salt[233]. Therefore, performing adsorption experiments at pH lower than 5 is unviable. On the other hand, in highly basic solutions **UiO-67-TzTz** is not stable because the strongly nucleophilic OH^- anions tend to replace carboxylates in the zirconium coordination sphere, leading to the MOF framework collapse.

The experiments were carried out at different pollutants concentrations in the range of 5 – 200 mg L^{-1} and the results are reported in [Figure 90a] together with the percentage removal efficiency [Figure 90b]. Diclofenac sodium is completely removed at low concentrations up to 20 mg L^{-1}, while for higher values the removal efficiency decreases until the only 30% registered for a concentration of 200 mg L^{-1}. Since nowadays the monitored DCF concentration in wastewater or environment is around 1 – 2 mg L^{-1} [234], **UiO-67-TzTz** could be exploitable for real water sample remediation.

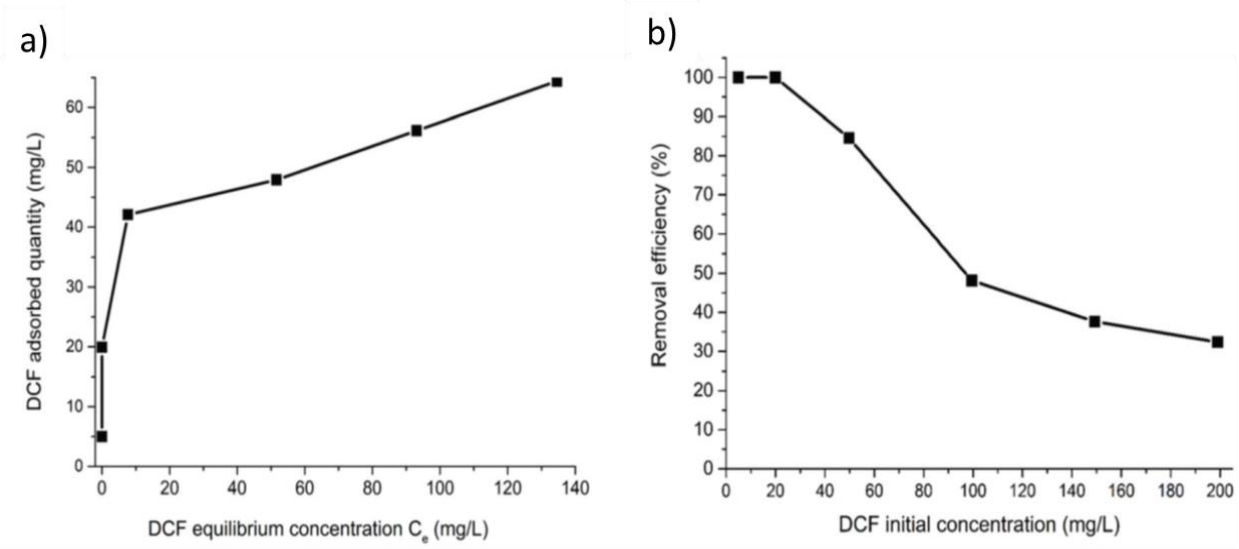

Figure 90: DCF adsorption of **UiO-67-TzTz** (a). Percentage removal efficiency as a function of DCF initial concentration (b).

The experimental data were fitted according to Langmuir model [Figure 91], following the equation:

$$\frac{C_e}{q_e} = \frac{1}{X_m K} + \frac{C_e}{X_m}$$

Where C_e is the concentration of the contaminant at the equilibrium (mg L^{-1}), q_e is the amount of contaminant adsorbed for unit of material (mg g^{-1}), X_m is the maximum adsorption capacity of the material for the specific pollutant (mg g^{-1}) and K is a parameter related to the affinity between the pollutant and the adsorbent.

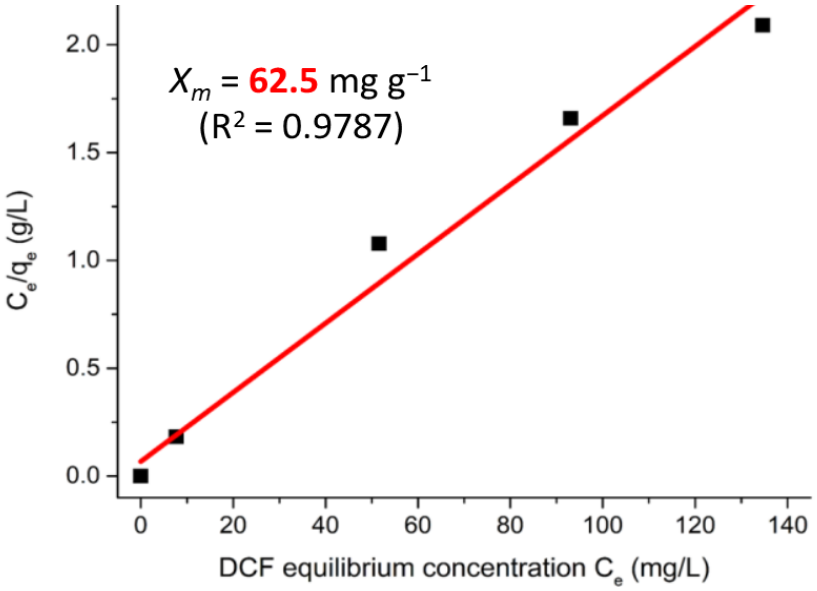

Figure 91: Linear data fitting according to Langmuir model of the DCF adsorption of **UiO-67-TzTz**.

The data show a good correlation with R^2 = 0.98 and from the fitting the maximum adsorption capacity (X_m) of 62.5 mg g^{-1} was found. This value is lower than that found in other MOFs like in Zr–BTC (MOF-808; X_m = 833 mg g^{-1}; BET specific surface area = 1517 m^2 g^{-1})[235]. Nonetheless, the X_m value found is comparable or even higher than that measured for other commercially available porous materials such as activated carbon or carbon nanotubes[236].

For the sake of completeness, desorption tests were performed, following the procedure reported in a previous paragraph (see 5.2.7. – Testing of pollutant adsorption and desorption), for selected DCF concentrations. Desorption was evaluated for initial concentrations of the pollutant of 100 mg L^{-1}, 150 mg L^{-1} and 200 mg L^{-1}, obtaining a percentage of release of 10.7, 16.9 and 18.0 % respectively. These values show that the amount of desorbed DCF increases with its

increasing initial concentration in the aqueous solution; however, even for the highest concentration essayed, desorption is lower than 20%. Such low desorption values seem to indicate the formation of relatively strong host–guest interactions, possibly triggered by the highly polar nature of the host (namely, the bithiazole linker) and the guest (DCF), as already highlighted above[237]. Nevertheless, the number of studies on pollutants desorption from MOFs is limited. In most of the adsorption studies, the adsorbents are simply regenerated through extensive washing with solvents to favor the guest exchange[236], while desorption is not thoroughly investigated.

5.4. Conclusions

In this work, Solvent-Assisted Linker Exchange (SALE) was applied on the UiO-67 MOF to replace one biphenyl dicarboxylate linker with its bithiophene (2,2'-bithiophene-5,5'-dicarboxylic acid) or bithiazole (2,2'-bithiazole-5,5'-dicarboxylic acid) analogues. As a result of this reaction, the two new mixed-linker MOFs **UiO-67-TpTp** and **UiO-67-TzTz**, featured by a 5 : 1 ratio between their carbocyclic and heterocyclic spacers, were obtained. The MIXMOFs maintain the same structural properties of their parent MOF with the added value of being emitters in the blue-green visible region, with spectral features that closely resemble those of the bare heterocyclic linkers. The two MIXMOFs have been tested as luminescent sensors for a series of common water pollutants: diclofenac sodium (DCF), fluoxetine (FXT), ibuprofen (IBR) and sulfamethoxazole (SMZ). While **UiO-67-TpTp** gives good performances only for FXT and IBR, **UiO-67-TzTz** generally gives better performance against all the examined pollutants. In particular, it shows a very good sensing capacity toward DCF. For this reason, **UiO-67-TzTz** was also evaluated as DCF "sponge", showing a satisfactory adsorption ability. Diclofenac sodium poses an environmental risk for surface and ground waters because it is one of the most effective non-steroidal anti-inflammatory drug. So, the extensive human consumption of this medicine led to the increase of its concentration in wastewaters with consequent serious threats to the ecosystem. Given the importance of wastewater treatments to detect and remove CECs (especially when present in small quantities), it is essential to design stable and efficient materials for this scope. In this context, this study has demonstrated that luminescent MOFs can be exploited as multifunctional materials for environmental remediation acting both as a detector and as an adsorbent for the pollutants.

Chapter 6

NU-1000-FUNCTIONALIZED MOF FOR CYANIDE LUMINESCENT SENSING AND CO_2 ADSORPTION

This chapter is based upon the following publication:

Benzothiazolium-functionalized NU-1000: a versatile material for carbon dioxide adsorption and cyanide luminescence sensing.

Journal of Materials Chemistry C; **2020** *8*, 7492

Giorgio Mercuri, Lapo Luconi, Timur Islamoglu, Andrea Fermi, Giacomo Bergamini, Giuliano Giambastiani and Andrea Rossin

6.1. Aim of the Work

Post-synthetic modification is a very useful approach to introduce new or different chemical entities inside MOFs structures to obtain a material that cannot be synthesized through a "direct synthesis". Besides covalent linker modification[238] or linker replacement using SALE, another versatile technique is the metal node functionalization using Solvent-Assisted Ligand Incorporation (SALI). SALI foresees the replacement of inorganic terminal ligands (-OH or -OH_2 groups) by a functional organic ligand (see paragraph 1.1.4 – Post-synthetic modification). This approach is particularly exploited for Zr-based MOFs that usually form SBUs rich of such terminal groups.

In this work, a tailor-made benzothiazolium bromide salt ligand (3-(4-carboxybenzyl)benzo[*d*]thiazolium bromide; **BzTz**) is inserted *via* SALI within the lattice of NU-1000. NU-1000 is a zirconium mesoporous MOF of general formula $[Zr_6(\mu_3\text{-}OH)_4(\mu_3\text{-}O)_4(H_2O)_4(OH)_4(TBAPy)_2]$ containing $[Zr_6(\mu_3\text{-}OH)_4(\mu_3\text{-}O)_4(H_2O)_4(OH)_4]^{8+}$ nodes where eight of the twelve coordination sites are occupied by $TBAPy^{4-}$ linkers (H_4TBAPy = 1,3,6,8-tetrakis(*p*-benzoic-acid)pyrene), while the other four from terminal -OH/-OH_2 groups that are reactive and can be exploited for SALI. The resulting MOF **NU-1000-BzTz** [Figure 92] has been thoroughly characterized in the solid state. After SALI, the sample maintains the same crystallinity of the pristine MOF but with a lower BET specific surface area due to the presence of the new ligand inside the pores. The actual ligand insertion has been proved through ^{1}H-NMR signal integration after the digestion of the MOF in acidic solution. The maximum value achieved is 1.7 **BzTz** ligand per $[Zr_6]$ node (the maximum value based on the stoichiometry of the node is 4).

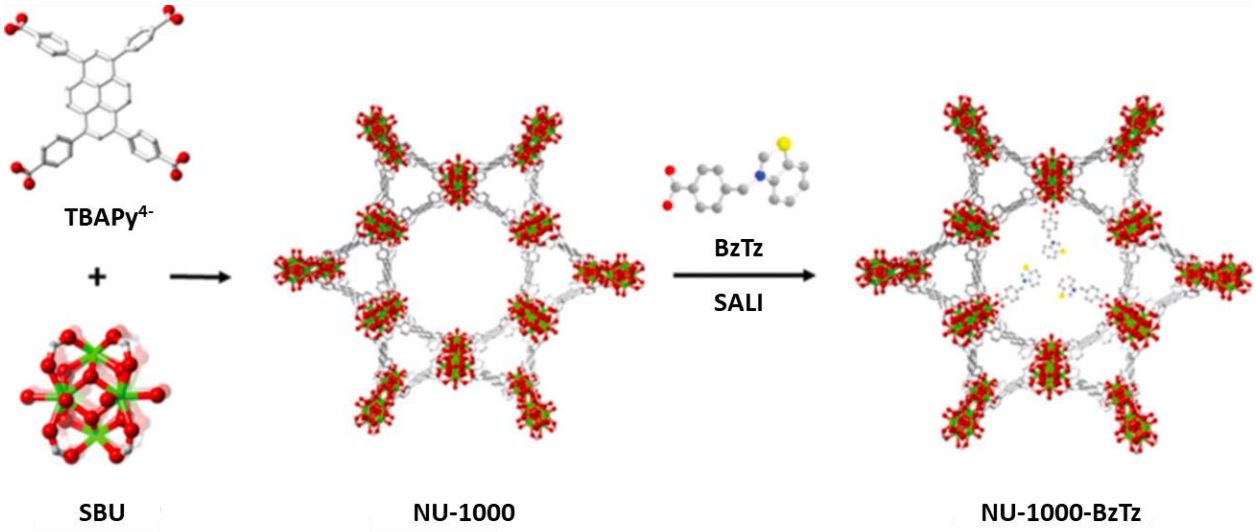

Figure 92: Schematic representation of NU-1000 synthesis and its SALI functionalization with **BzTz** ligand. (The structure is only idealized because there are no X-ray data available). Color code: Zr – green, N – blue, S – yellow, O – red.

Finally, the MOF was tested for CO_2 adsorption showing a better performance than NU-1000 despite the lower surface area. This result confirms that the presence of a polar functional group inside the MOF pores improves the interaction with CO_2.

Moreover, the presence of a luminescent thiazole in the **BzTz** structure has been exploited to test the luminescent properties of **NU-1000-BzTz**. This compound shows good performance in detecting some common polluting ions as CN^-, SCN^-, OCN^- and $SeCN^-$ (when present as sodium or potassium salts). Noteworthy, the process occurs even in the presence of other competing ions (i.e. simulating the real samples of ordinary tap water).

6.2. Experimental Details

6.2.1. Materials and Methods

All the chemicals and reagents employed were purchased from commercial suppliers and used as received without further purification. NU-1000 was prepared according to the published procedures[239]. For the organic syntheses, solvents were purified through standard distillation techniques. Deuterated solvents (Sigma Aldrich) were stored over 4 Å molecular sieves and degassed by three freeze–pump–thaw cycles before use. NMR spectra were recorded on a BRUKER AVANCE 400 MHz spectrometer. ^1H and ^{13}C-NMR chemical shifts are reported in parts per million (ppm) downfield of tetramethylsilane (TMS) and were calibrated against the residual resonance of the protiated part of the deuterated solvent.

FT-IR spectra (KBr pellets) were recorded on a PerkinElmer Spectrum BX Series FTIR spectrometer, in the 4000 – 400 cm^{-1} range, with a 2 cm^{-1} resolution.

Thermogravimetric analysis measurements were performed under a N_2 atmosphere (100 mL/min) at a heating rate of 10 K min^{-1} on an EXSTAR Thermo Gravimetric Analyzer (TG-DTG) Seiko 6200.

The C, H, N, and S elemental analyses were carried out using a Thermo FlashEA 1112 Series CHNS-O elemental analyzer with an accepted tolerance of ±2% for carbon (C), hydrogen (H), nitrogen (N) and sulfur (S).

ESI-MS spectra were recorded using direct introduction (10 mL min^{-1}) on a FinniganLTQ mass spectrometer (Thermo, San Jose, CA). The instrument was equipped with a conventional ESI source. The working conditions were the following: positive polarity: spray voltage 5 kV, capillary voltage 35 V, capillary temperature 548 K and tube lens 110 V. Sheath gas was set at 10 a.u. and auxiliary gas was kept at 3 a.u. For acquisition, Xcalibur 2.0 software (Thermo) was used. Aqueous sample solutions of **BzTz** were diluted to 20 ng μL^{-1}.

PXRD qualitative measurements were carried out using a Panalytical X'PERT PRO powder diffractometer equipped with a diffracted beam Ni filter and a PIXcel© solid state detector in the 4 – 50° 2θ region, operating with Cu Ka radiation (λ = 1.5418 Å). Anti-scatter slits were used both on the incident (0.251 and 0.51 divergence) and the diffracted (7.5 mm height) beams.

6.2.2. Compounds Synthesis

Synthesis of 3-(4-carboxybenzyl)benzo[*d*]thiazolium bromide (BzTz): 4-(Bromomethyl)benzoic acid (0.950 g, 4.43 mmol, 1.2 eq.) was added to a solution of benzo[*d*]thiazole (0.400 mL, 3.7 mmol, 1.0 eq.) in dry and degassed acetonitrile (17 mL) [Figure 93]. The reaction mixture was left under solvent reflux for 48 h with stirring. During this time, formation of a white precipitate was observed. Afterwards, the mixture was cooled to room temperature and the precipitate was filtrated on a Buchner funnel and washed with fresh acetonitrile (3 x 10 mL) and diethyl ether (3 x 10 mL). The white solid residue was recovered and dried under vacuum (1.100 g, yield: 84.1%). Crystals suitable for X-ray diffraction were obtained from a concentrated methanolic solution at 277 K [Figure 96].

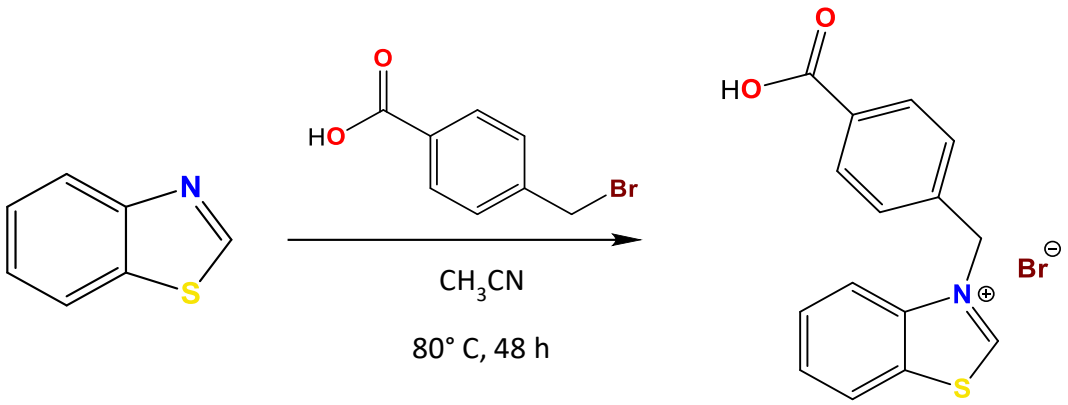

Figure 93: Schematic synthesis of **BzTz** ligand.

^{1}H-NMR (400MHz, DMSO-d_6, 298 K) [Figure 94a]: δ 6.26 (s, 2H, CH_2, H^{8}), 2.59 (d, $^{3}J_{HH}$ = 8.2 Hz, 2H, CH Ar, $H^{10,14}$), 7.83 (m, 2H, CH Ar, $H^{4,5}$), 7.94 (d, $^{3}J_{HH}$ = 8.2 Hz, 2H, CH Ar, $H^{11,13}$), 8.23 (d, $^{3}J_{HH}$ = 8.1 Hz, 1H, CH Ar, H^{3}), 8.56 (d, $^{3}J_{HH}$ = 8.1 Hz, 1H, CH Ar, H^{6}), 10.87 (s, 1H, CH Ar, H^{1}), 13.10 (brs, 1H, COOH). ^{13}C-NMR (100MHz,DMSO-d_6, 298 K) [Figure 94b]: δ 54.7 (CH2, C^{8}), 117.3 (CH Ar, C^{3}), 125.5 (CH Ar, C^{6}), 128.3 (CH Ar, $C^{10,14}$), 128.5 (CH Ar, C^{4}), 129.7 (CH Ar, C^{5}), 129.9 (CH Ar, $C^{11,13}$), 131.2 (C Ar, C^{2}), 131.8 (C Ar, C^{12}), 137.6 (C Ar, C^{9}), 140.0 (C Ar, C^{7}), 165.8 (CH Ar, C^{1}), 166.7 (COOH, C^{15}). Elem. anal. calc. for **BzTz** ($C_{15}H_{12}BrNO_2S$ (FW = 350.23 g mol^{-1}): C 51.44, H 3.45, N 4.00, S 9.16; found: C 51.21, H 3.39 N 3.98, S 8.75. IR (KBr pellet, cm^{-1}): n = 2996 [s, *ν*(C–H)], 1701 [s, *ν*(COO)], 1609 [m, *ν*(C=C)], 1417 (m), 1380 (s), 1233 [s, δ(O–H)], 1177 (m), 1115 (m), 771 [s, γ(C–H)]. ESI-MS: m/z = 270.3 $(M - Br)^{+}$.

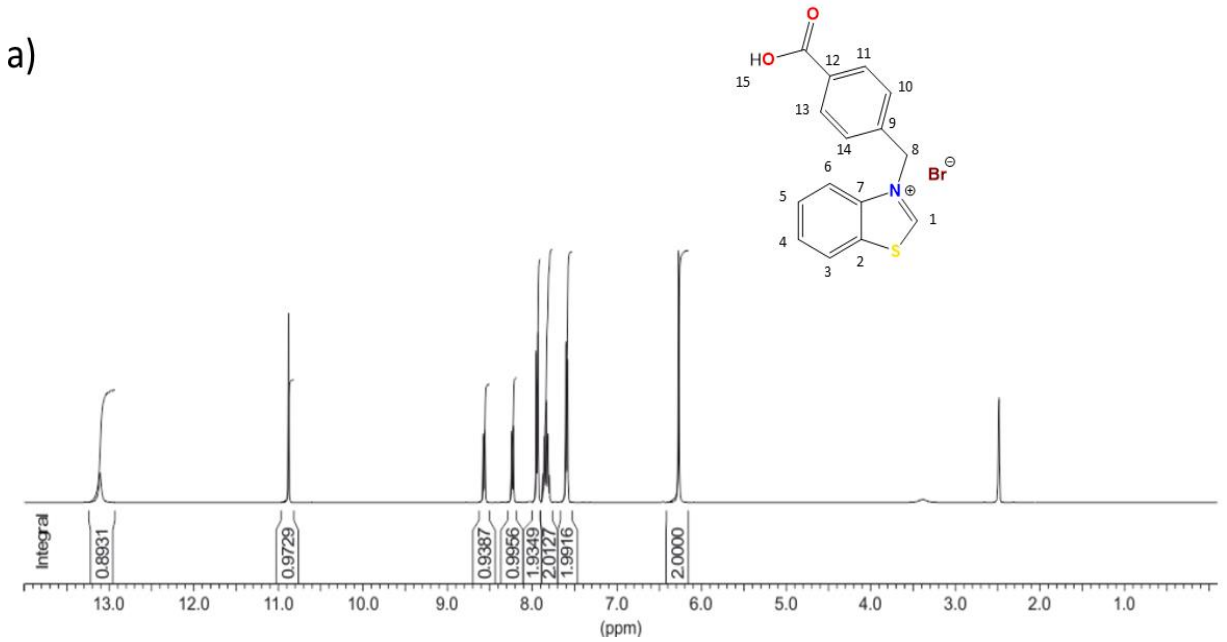

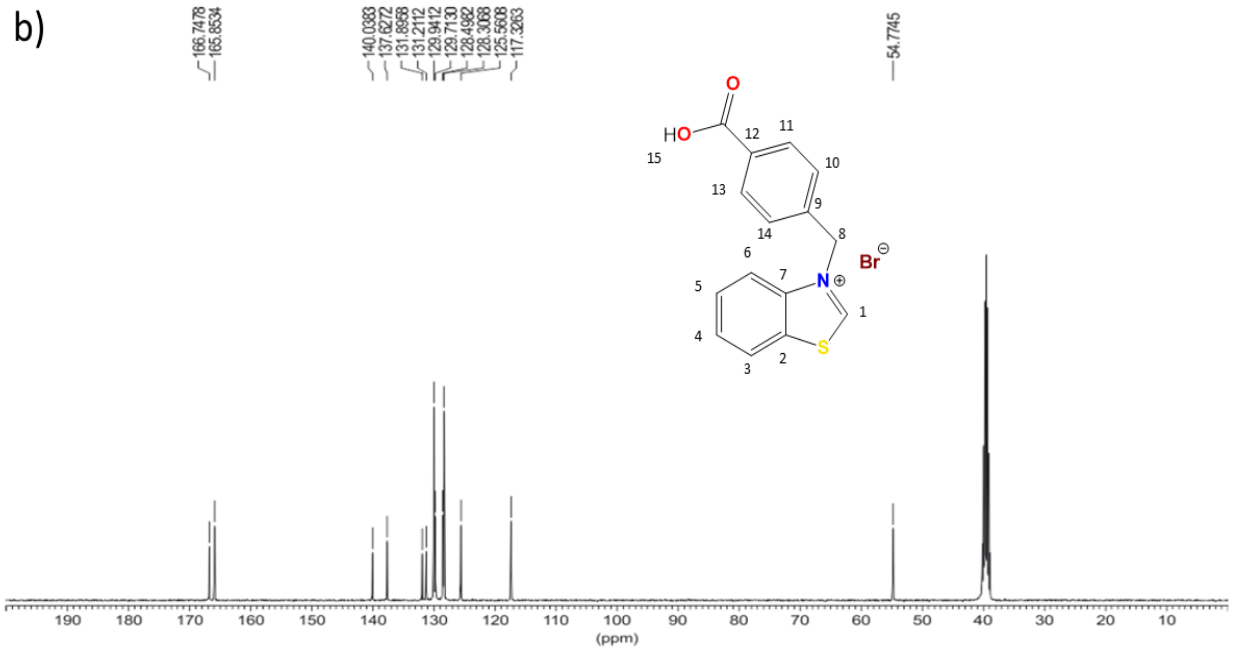

Figure 94: ^{1}H-NMR spectrum (400 MHz, DMSO-d_6, 298 K) (a) and ^{13}C-NMR spectrum (400 MHz, DMSO-d_6, 298 K) (b) of **BzTz**.

Synthesis of NU-1000-BzTz: Following the general SALI procedure reported by Hupp, Farha et al.[240], the benzothiazolium salt **BzTz** (0.163 g, 0.46 mmol, 10 eq.) was added to a suspension of benzoate-free[9] NU-1000 (0.100 g, 0.046 mmol) in a dry and degassed polar solvent mixture (total volume 45 mL, acetonitrile : dimethylsulfoxide = 90 : 10). The reaction mixture was heated at 353 K for 24 h with occasional gentle stirring. After that time, the mixture was brought back to room temperature and the precipitate was filtered over a 0.2 mm PTFE filter. The bright yellow solid residue was sequentially washed with hot acetonitrile, acetone and dichloromethane (3 x 20 mL each) and finally dried in air. IR (KBr pellet, cm^{-1}): 3387 (w, br) [ν(N–H)], 3095 (w) [ν(C–H$_{aromatic}$)], 2928 (w) [ν(C–H$_{aliphatic}$)], 1655 (vs) [ν(C=O)], 1500 (s) [ν(C=C + C=N)], 1435 (w), 1384 (s), 1275 (m), 1250 (m), 1204 (w), 1163 (w), 1123 (s), 1093 (m), 1056 (s), 1014 (w), 946 (s), 839 (m).

6.2.3. Ligand Incorporation Quantification

The extent of benzothiazolium salt incorporation was estimated through signal integration of the ^{1}H-NMR spectrum of the digested sample in acidic solution (5% HF-DMSO-d_6). In a typical

[9] The as-synthesized form of NU-1000 contains residual benzoate ligands at the node sites. Benzoate is present because benzoic acid was used as a modulator in the synthesis of NU-1000. SALI is possible only after removal of coordinated benzoate by extended treatment of the as-synthesized material with aq. HCl in DMF at 353 K

procedure, 5 mg of sample was dissolved in three drops of concentrated hydrofluoric acid and 0.75 mL of DMSO-d_6 directly into an NMR tube. The mixture was heated at T = 343 K for 30 min, to complete the sample digestion. The as-obtained clear solution was analyzed via ^{1}H-NMR (400 MHz, relaxation delay τ = 15 s, 512 scans) [Figure 95]. The maximum loading achieved was 1.7(**BzTz**) per [Zr_6] node.

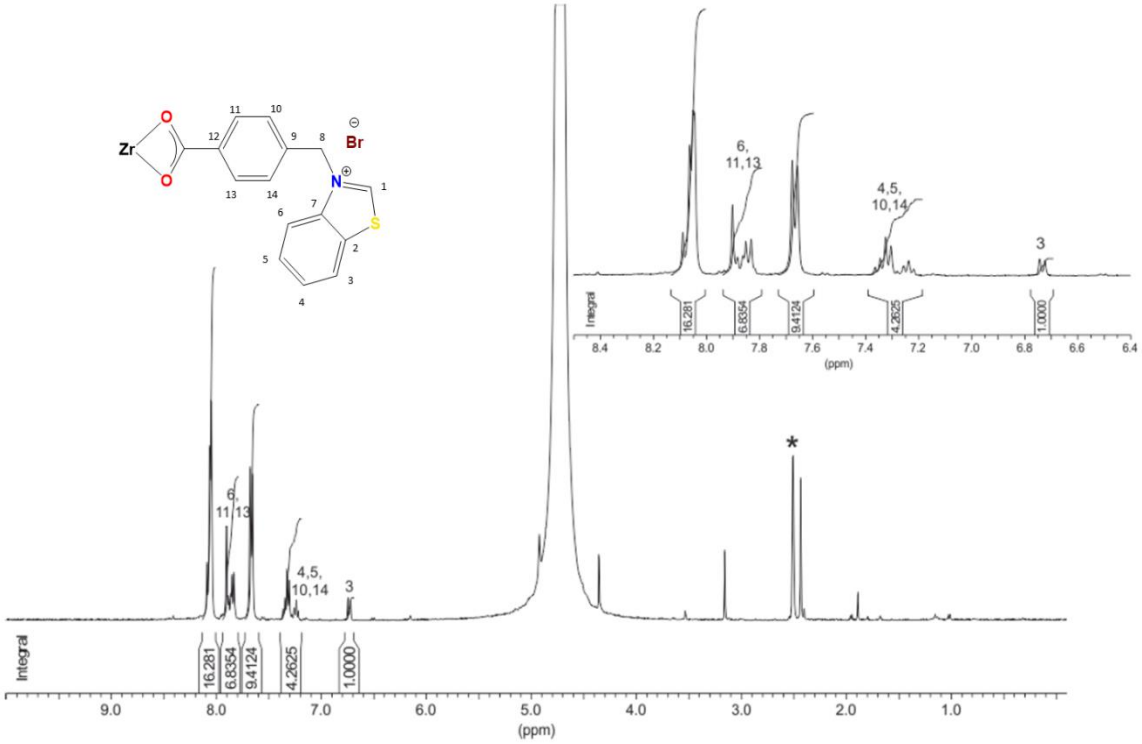

Figure 95: ^{1}H-NMR spectrum (400 MHz, 5% HF-DMSO-d_6, 298 K) of the digested **NU-1000-BzTz**. Inset: zoom of the aromatic region used for the quantification of the functionalization degree. *residual solvent peak.

6.2.4. Single-Crystal X-Ray Diffraction Structure Determination

The structure of **BzTz** was determined *via* single-crystal XRD of crystals obtained from a concentrated methanolic solution at T = 277 K [Figure 96]. Single crystal X-Ray data were collected at low temperature (T = 100 K) on a Bruker APEX-II CCD diffractometer using a Cu Kα radiation (λ = 1.5418 Å). The program used for the data collection and reduction was the Bruker SAINT software package. Data were corrected for absorption effects using the Multi-Scan method (SADABS). Direct methods implemented in Sir20141 were used to solve the structures and the refinements were performed by full-matrix least-squares against F^2 implemented in SHELXL-2018.2 All the non-hydrogen atoms were refined anisotropically while the hydrogen atoms were fixed in calculated positions and refined isotropically with the thermal factor depending on the

one of the atom to which they are bound. The -COOH hydrogen atom was located on the residual density maps and then included with fixed bond distances and U_{iso} values constrained at the level of 1.5×U_{eq} of the carrier oxygen atom. The geometrical calculations were performed by PARST97 and molecular plots were produced by the program ORTEP3.

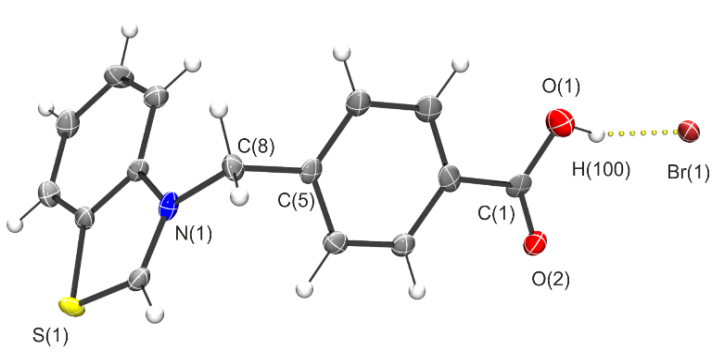

Formula	$C_{15}H_{12}BrNO_2S$
M [g mol^{-1}]	350.23
T [K]	100
Color, habit	Colorless prisms
Size [mm^3]	0.01 x 0.01 x 0.02
Crystal system	Monoclinic
a [Å]	7.3944(5)
b [Å]	14.8659(9)
c [Å]	13.0018(8)
β [°]	91.5700(10)
V [Å^3]	1428.68(16)
D_{calc} [g cm^{-3}]	1.628
Space group	$P2_1/c$

Figure 96: ORTEP drawing of **BzTz** and main crystallographic data, experimental details and structure refinements details.

6.2.5. Gas Adsorption

Before the adsorption measurements were carried out, ~40 mg of **NU-1000-BzTz** was activated at 393 K under high vacuum (10^{-6} Torr) for 12 h. The textural properties were estimated by volumetric adsorption carried out using an ASAP 2020 Micromeritics instrument, using N_2 as adsorbate at 77 K. For BET specific surface area calculation, the 0.01–0.1 p/p_0 pressure range of the isotherm was used to fit the data [Figure 99]. The pore size distribution was determined on the basis of the NLDFT method (Tarazona model for cylindrical pores). CO_2 adsorption isotherms were recorded at 273 and 298 K at a maximum pressure of 1.2 bar. The isosteric heat of adsorption (Q_{st}) was calculated from the CO_2 isotherms measured at 273 and 298 K according to a variant of the Clausius–Clapeyron equation[241]:

$$\ln\left(\frac{p_1}{p_2}\right) = Q_{st} * \frac{T_2 - T_1}{R * T_1 * T_2}$$

where p_n (n = 1 or 2) is the pressure value for isotherm n; T_n (n = 1 or 2) is the temperature value for isotherm n; R is the gas constant (8.314 J K^{-1} mol^{-1}).

6.2.6. Luminescence Measurements

The experiments were carried out in air-equilibrated water suspensions at 298 K unless otherwise noted. UV-vis absorption spectra were recorded using a PerkinElmer l40 spectrophotometer using quartz cells with path length of 1.0 cm. Luminescence spectra were recorded using a PerkinElmer LS-50 or an Edinburgh FLS920 spectrofluorimeter equipped with a Hamamatsu R928 phototube. Lifetimes shorter than 10 ms were measured by the above-mentioned Edinburgh FLS920 spectrofluorimeter equipped with a TCC900 card for data acquisition in time-correlated single-photon counting experiments (0.5 ns time resolution). For solid samples, the emission quantum yield was calculated from the corrected emission spectra registered using an Edinburgh FLS920 spectrofluorimeter equipped with a barium sulfate coated integrating sphere (4 inch), a 450 W Xe lamp (l excitation tunable by a monochromator supplied with the instrument) as light source, and an R928 photomultiplier tube, following the procedure described by De Mello et al.[209]. The estimated experimental errors are 2 nm for the band maximum, 5% for the molar absorption coefficient and luminescence lifetime, and 20% for the emission quantum yield of a solid.

6.3. Results and Discussion

The new ligand 3-(4-carboxybenzyl)benzo[*d*]thiazolium bromide (**BzTz**) was synthesized starting from benzo[*d*]thiazole through a *N*-alkylation by 4-(bromo-methyl)benzoic acid in acetonitrile at 353 K [Figure 93]. Subsequently, this ligand was incorporated into the structure of NU-1000 through SALI [Figure 92]. To do that, an activated NU-1000 sample was suspended in an excess solution of **BzTz** (10 eq.) in MeCN/DMSO 90:10 solvent mixture and heated at 353 K for 24 h. The solvents used for this reaction were previously dried because the presence of water hampers SALI completion (being a condensation reaction between the -OH/-OH_2 groups dangling from the [Zr_6] node and the carboxylic group of **BzTz**) [240]. The actual extent of ligand inclusion was assessed *via* ^{1}H-NMR signal integration of the **BzTz** signals against that of the $TBAPy^{4-}$ linker, after the digestion of the sample in acidic solution (see paragraph 6.2.3. – Ligand incorporation quantification). The experimental conditions of the SALI process were optimized to obtain the maximum incorporation as possible. Under these conditions, the amount of **BzTz** that is incorporated into the NU-1000 structure is reproducible and reaches 1.7 **BzTz** ligands per [Zr_6]

node. This value is lower than the theoretical limit of 4 which is allowed by the stoichiometry and that has been reached in literature[240], but it can be explained invoking the steric hindrance of **BzTz** that interferes with further functionalization.

The new synthesized MOF **NU-1000-BzTz** has been thoroughly characterized in the solid state. The thermal behavior was evaluated through TGA-DTG analysis under N_2 flow [Figure 97]. The thermal stability of NU-1000 is slightly higher than that of **NU-1000-BzTz** (T_{dec} 800 K vs 780 K, respectively). The latter shows a weight loss and a DTG peak around T = 532 K, probably due to the degradation of the **BzTz** group whose decomposition temperature is around 510 K.

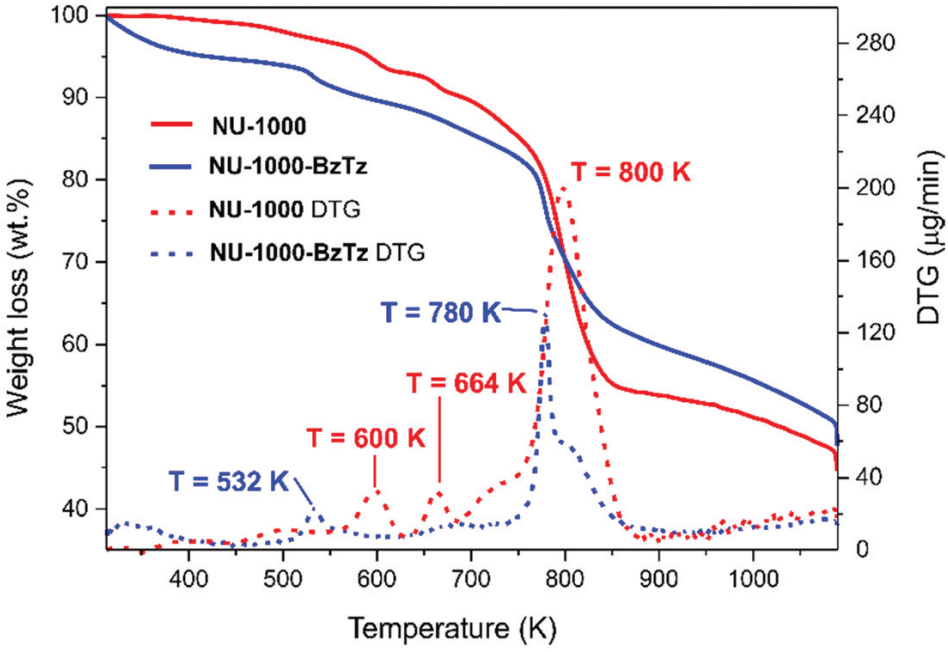

Figure 97: TGA and DTG profiles of NU-1000 (red lines) and **NU-1000-BzTz** (blue lines).

The crystallinity of **NU-1000-BzTz** was evaluated through PXRD analysis [Figure 98]. The crystallographic pattern of the new MOF is only slightly different from that of the pristine MOF, witnessing that the material remains intact after SALI functionalization. The differences in the two patterns can be ascribed to the modification of the unit cell parameters after the inclusion of the bulky **BzTz** ligand.

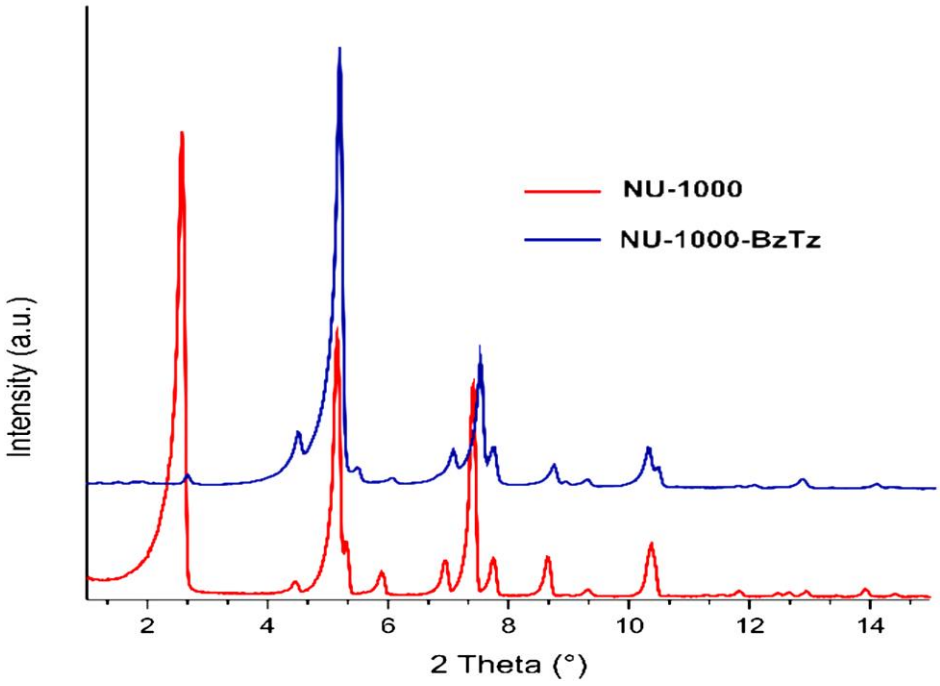

Figure 98: PXRD patterns of NU-1000 (red) and **NU-1000-BzTz** (blue) at comparison.

The texture and the porosity of **NU-1000-BzTz** were evaluated through volumetric N_2 adsorption at 77 K. Before the analysis, in accordance with the typical methodology, the sample was evacuated using a thermal treatment, heating it at 393 K under high vacuum for 12 h [Figure 99a]. The isotherm shape of the MOF is of type IV, typical of mesoporous materials and the same as that of NU-1000. The calculated BET specific surface area is 1530 $m^2\ g^{-1}$, lower than that of NU-1000 that is equal to 2140 $m^2\ g^{-1}$. This result is in accordance with the presence of the **BzTz** groups inside the structure. Their presence also modifies the total pore volume and the pore size distribution [Figure 99b]. The total pore volume at p/p_0 = 0.98 is equal to 1.53 $cm^3\ g^{-1}$ and 0.93 $cm^3\ g^{-1}$ for NU-1000 and **NU-1000-BzTz** respectively. The pore size distribution was evaluated through NLDFT model and show slightly reduced mesopore size for the functionalized material (w = 33 Å vs. 28 Å for NU-1000 and **NU-1000-BzTz**, respectively), while the micropore size is practically unchanged. This result is interesting because it reveals that SALI functionalization occurs only in the MOF mesopores.

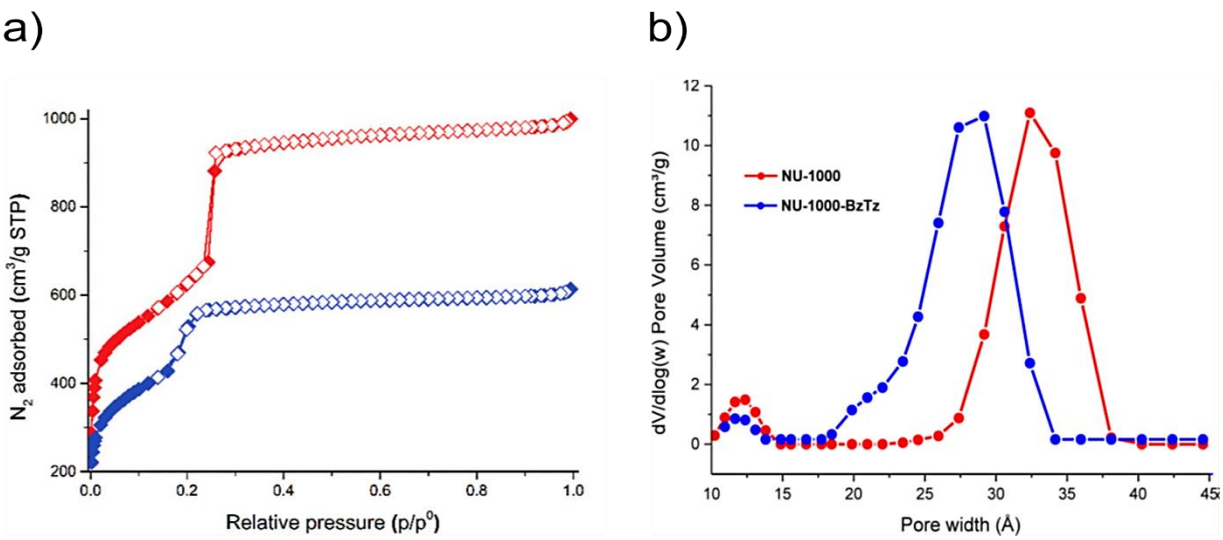

Figure 99: Comparison between N_2 adsorption isotherms of NU-1000 (red diamonds) and **NU-1000-BzTz** (blue diamonds) and desorption isotherms (empty diamonds) measured at 77 K (a). Pore size distribution plots, calculated with NLDFT Tarazona model for cylindrical pores, for NU-1000 (red) and **NU-1000-BzTz** (blue) at comparison (b).

CO_2 adsorption isotherms were measured at the temperatures of 298 K and 273 K [Figure 100]. **NU-1000-BzTz** show a total gas uptake at p_{CO_2} = 1 bar of 8.7 wt% (2.0 mmol g^{-1}) at 298 K and of 10.8 wt% (2.5 mmol g^{-1}) at 273 K. This value is lower than that measured for the simple NU-1000 of 3.0 mmol g^{-1} [44], but it can be reasonably explained taking into account the higher surface area of the latter. Nevertheless, when the isosteric heat of adsorption (Q_{st}) is considered, **NU-1000-BzTz** has a higher Q_{st} than NU-1000 (25 KJ mol^{-1} *vs* 17 KJ mol^{-1} respectively). The higher affinity of the functionalized-MOF with CO_2 can be ascribed to the presence of the polar benzothiazolium molecule inside the pores.

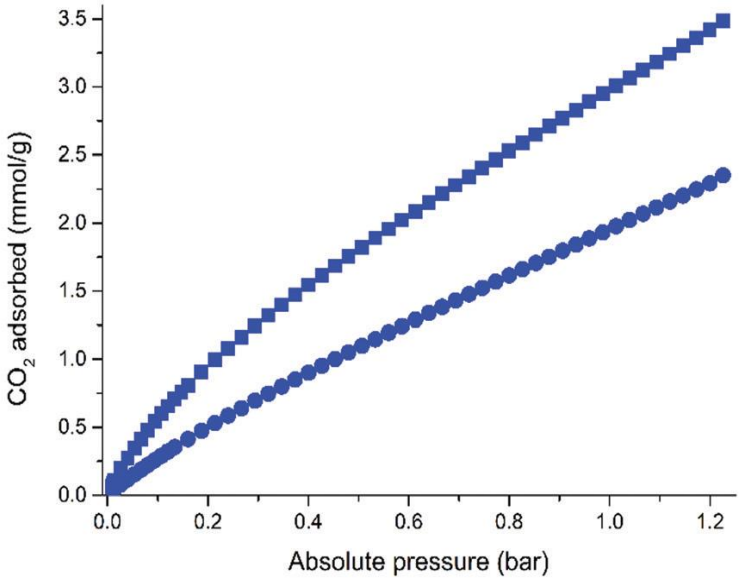

Figure 100: CO_2 adsorption isotherm of **NU-1000-BzTz** calculated at T = 273 K (blue squares) and 298 K (blue circles).

Besides exploiting the MOF in CO_2 adsorption, **NU-1000-BzTz** was also tested as luminescent ion sensor in aqueous solutions. To do that, firstly the water stability of the MOF was evaluated through PXRD analysis after soaking the sample in water for 24 h at ambient temperature [Figure 101]. After this time, the functionalized MOF maintains the crystallinity and the structural texture.

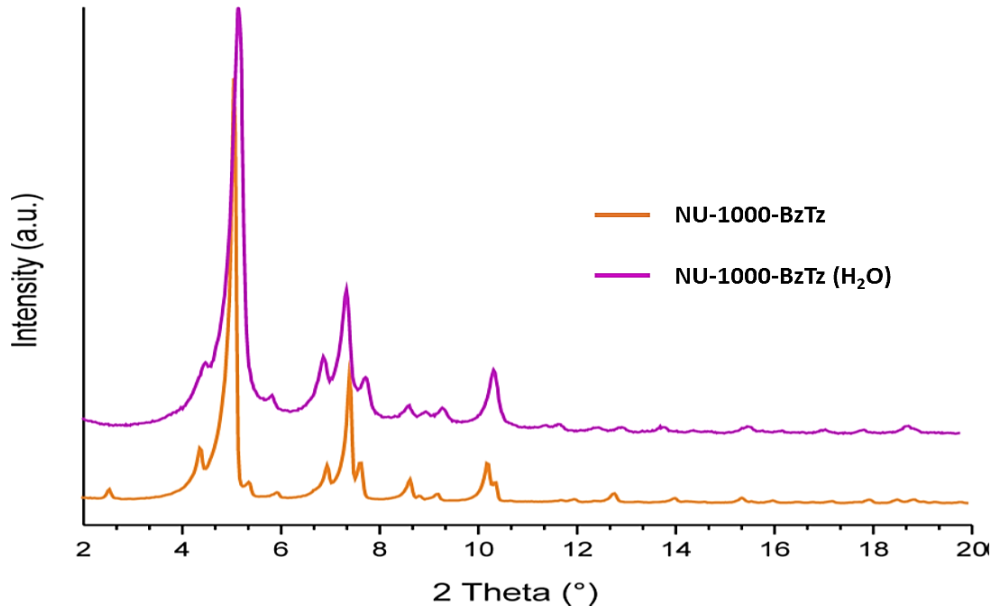

Figure 101: PXRD patterns of the as synthesized **NU-1000-BzTz** (orange) and after soaking in water for 24 h (violet).

Then, the luminescent properties of **BzTz** were evaluated in aqueous suspension [Figure 102a], while that of NU-1000 and of **NU-1000-BzTz** were evaluated both in aqueous suspension and in the solid state [Figure 102b]. Under both experimental conditions, the two MOFs exhibited similar emissions with only slight variations in the profiles and in the emission maxima. However, there were distinct differences in the emissions between the two MOFs, with NU-1000 showing a peak wavelength ($\lambda_{max,em}$) of 450 nm (blue emission) and **NU-1000-BzTz** displaying a peak wavelength of 490 nm (light green emission). As other studies have demonstrated, the strong emission of NU-1000 at 450 nm is originated from the tetrasubstituted pyrene linker present in the structure[242]. Instead, the small redshift in the absorption and emission spectra of **NU-1000-BzTz** compared to that of the pristine MOF could be explained by the presence of the positively charged **BzTz** subunit, which perturbs the electronic environment of the emitting pyrene linker and slightly stabilizes its excited state[243].

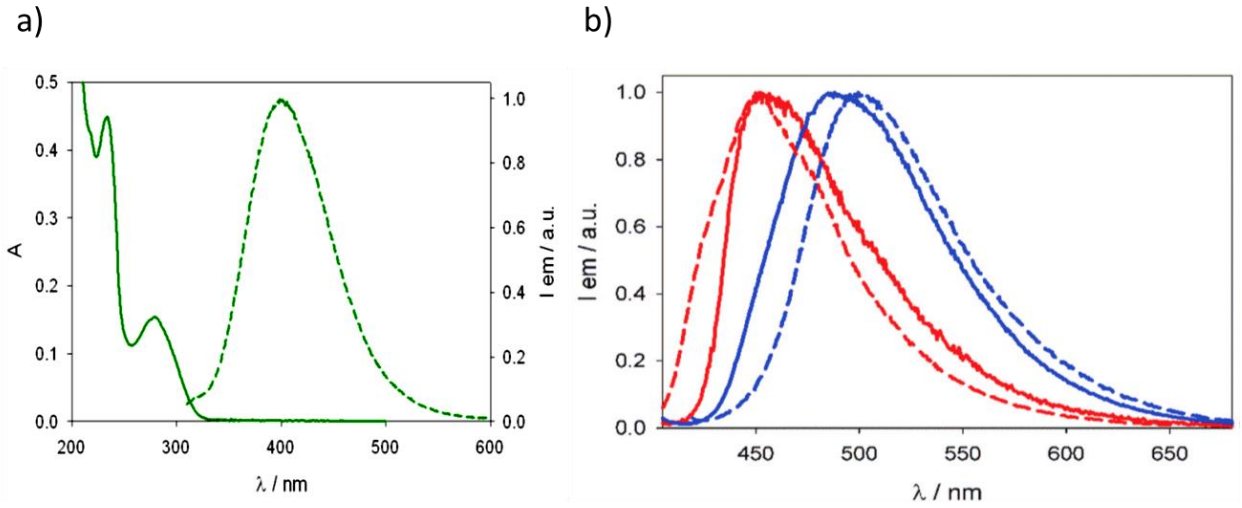

Figure 102: Qualitative absorption (solid line) and normalized emission spectra (dashed line) of **BzTz** in H_2O, λ_{ex} = 280 nm (a). Comparison between normalized emission spectra recorded in water suspension (solid lines) and on powders (dashed lines) of NU-1000 (red) and **NU-1000-BzTz** (blue).

Both NU-1000 and **NU-1000-BzTz** were tested against highly toxic cyanides in aqueous solution. The sensing ability and emission behavior of the bare ligand **BzTz** in the presence of polluting anions in aqueous solutions was first checked [Figure 103]. The consecutive additions of increasing amounts of aqueous KCN (until a maximum of 0.20 mM) to a 1.05 X 10^{-4} M solution of **BzTz** led to small changes in the absorption spectra with the shift of $\lambda_{max,em}$ from 280 to 275 nm, and to the progressive quenching of the emission intensity that, however, keeps the same profile (no λ shift in the fluorescence band upon cyanide addition).

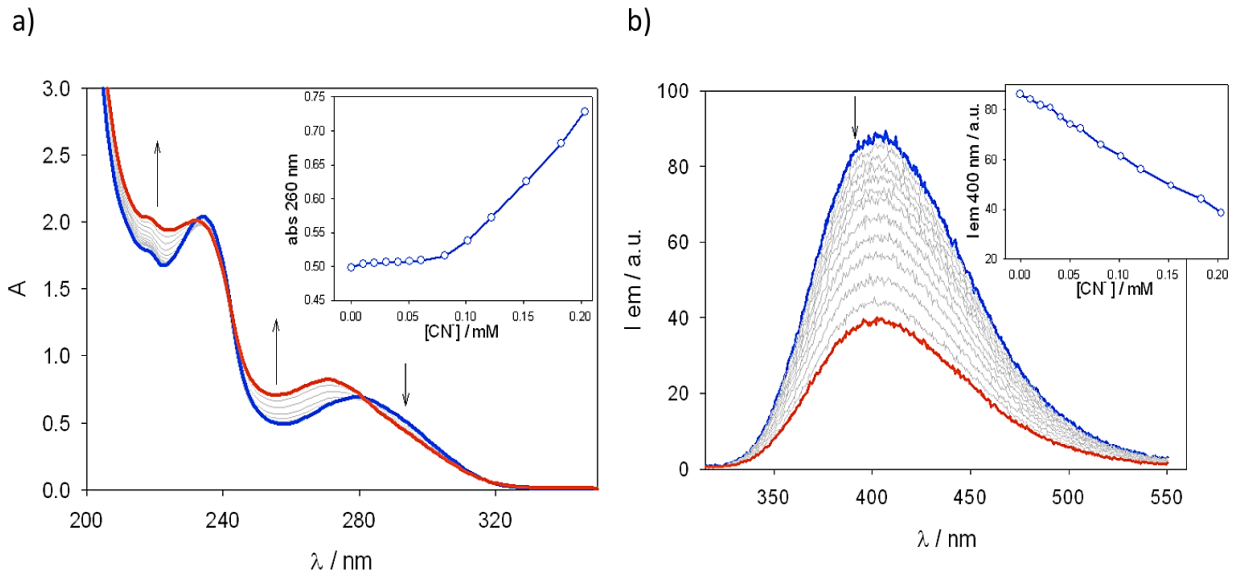

Figure 103: Absorption (a) and emission (b) spectra of a water solution of **BzTz** and their evolution upon additions of KCN until a maximum of 0.20 mM (blue to red lines). Inset: absorption profile at 260 nm (a) and emission intensity profile at 400 nm (b).

When the tests were made for the MOFs under the same conditions, changes in the emission intensities were observed in both cases. In fact, upon addition of KCN, NU-1000 shows an increase in the emission quantum yield, but no changes in the emission profile, keeping the value of $\lambda_{max,em}$ equal to 450 nm, [Figure 104a]. On the contrary, **NU-1000-BzTz** not only displays a higher emission intensity, but it also shifts its emission profile to shorter wavelengths, basically restoring the luminescence of the pristine MOF [Figure 104b]. This behavior is probably due to the $Br^- \leftrightarrow CN^-$ anion exchange within the framework promoted by the presence of the positively charged **BzTz** ligand.

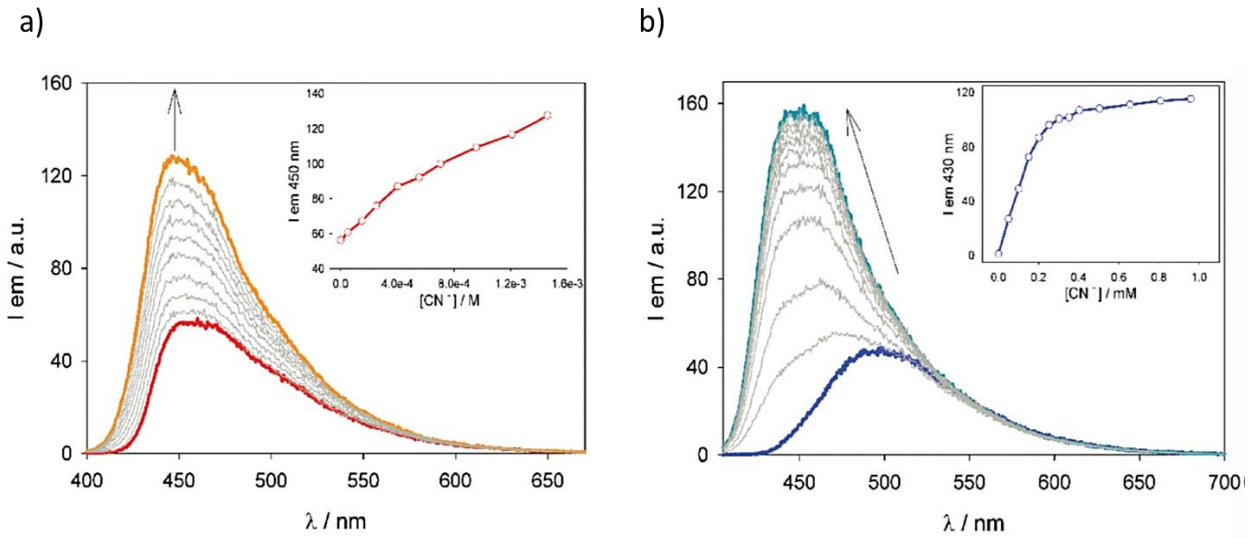

Figure 104: Evolution of the emission spectra recorded for a suspension of NU-1000 upon addition of KCN from 0 to 1.4 mM (orange to red line, respectively) in water at λ_{ex} = 385 nm. Inset: dependence between the [CN^-] and the emission intensity at 450 nm (a). Evolution of the emission spectra recorded for a suspension of **NU-1000-BzTz** upon addition of KCN from 0 to 1.0 mM (blue to green line, respectively) in water at λ_{ex} = 385 nm. Inset: dependence between the [CN^-] and the emission intensity at 430 nm (b).

The luminescent properties of **NU-1000-BzTz** were also tested in the presence of different cyanide anions like cyanate (OCN^-), thiocyanate (SCN^-) and seleno-cyanate ($SeCN^-$) [Figure 105]. The luminescent behavior is the same in all the cases with the emission that is higher in intensity and shifted to lower wavelengths even for low concentrations of pollutants.

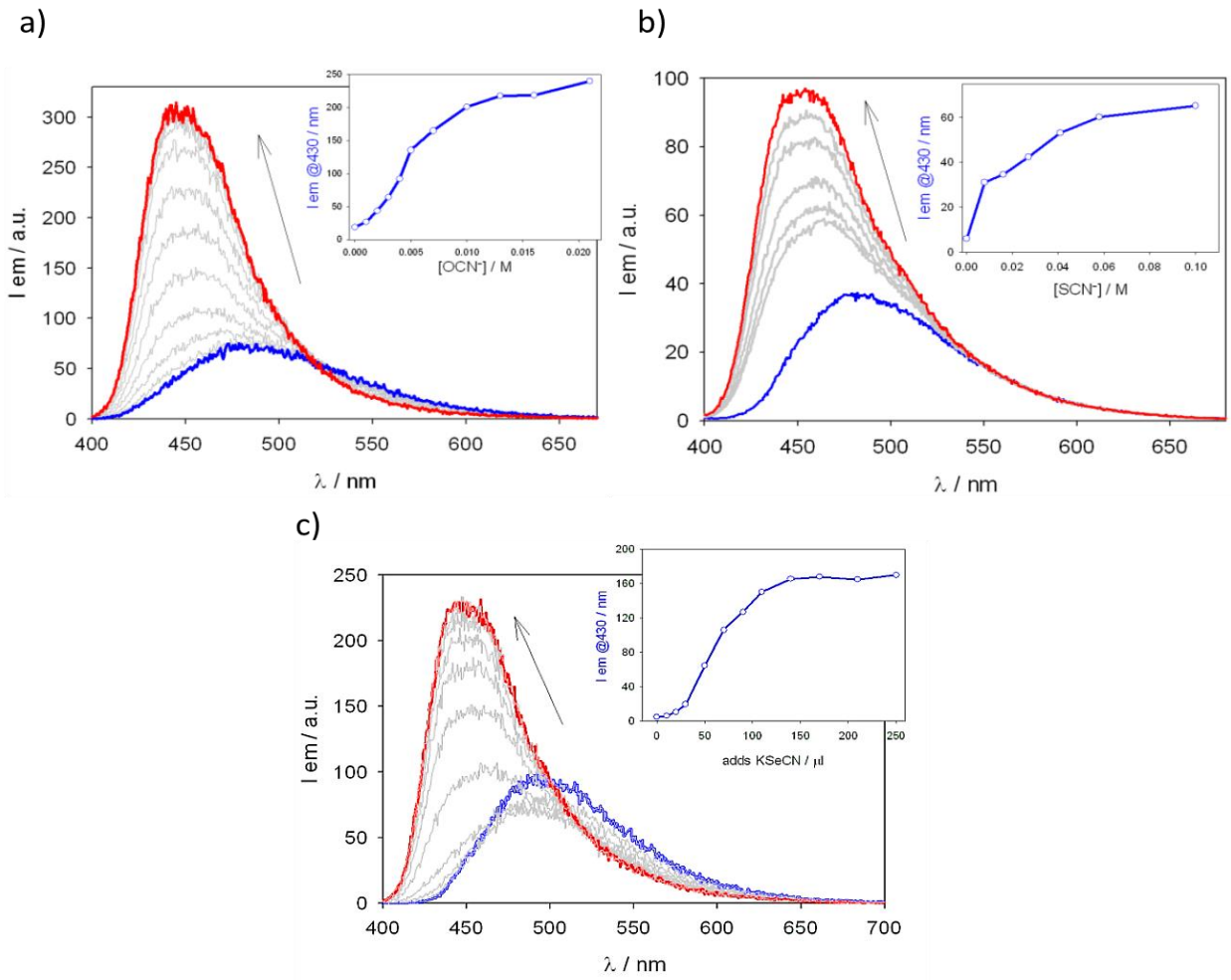

Figure 105: Evolution of the emission spectra recorded for a suspension of **NU-1000-BzTz** upon additions of different pollutants from 0 to a variable maximum concentration (blue to red lines, respectively) in water at λ_{ex} = 385 nm. In the insets: dependence between the anions concentration and the emission intensity at 430 nm. Additions of KOCN from 0 to 21.0 mM (a), NaSCN from 0 to 0.1 M (b) and KSeCN from 0 to 250 µL (c).

In a further study, the dependence of the emission intensity from the anion concentration was studied. Aqueous solutions containing the cyanate salts were gradually added to an aqueous suspension of **NU-1000-BzTz** and the resulting emission spectra were collected at ambient conditions and at λ_{ex} = 430 nm [Figure 106]. This study reveals that the luminescence response is proportional to the relative basicity of the anions, following the order CN^- >>OCN^- > SCN^- [244]. In fact, among all the tested anions, CN^- gives the strongest change in the emission intensity, while the change due to SCN^- is almost negligible. On the basis of this result, we can tentatively ascribe the enhancement of the emission intensity to a partial deprotonation of the H in 2-position (the one between the sulfur and the nitrogen of the thiazole) that is the most acidic present in the **BzTz** ligand. The deprotonation can be speculated to increase the delocalization of the electrons in the framework ligands, which leads to the enhancement of the fluorescence intensity upon

increasing the anions concentration. The same behavior has also been observed in other similar literature examples [245].

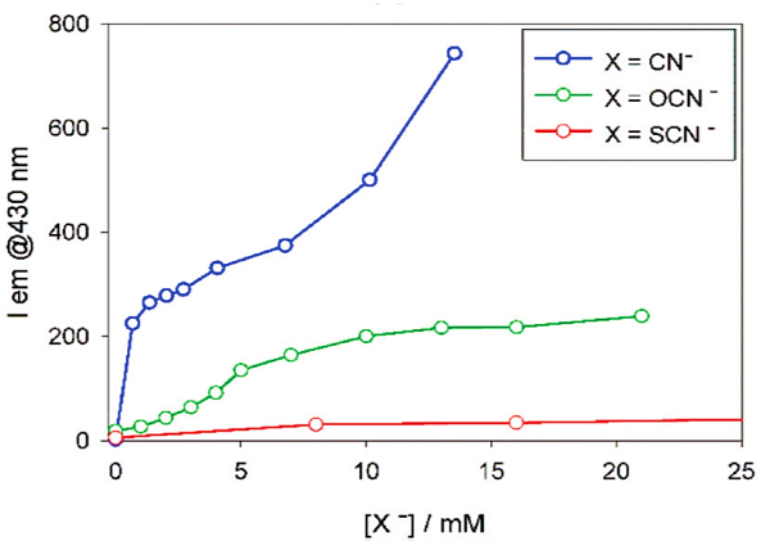

Figure 106: Variation of the emission intensities recorded at 430 nm for suspension of **NU-1000-BzTz** in water upon addition of increasing quantities of KCN, KOCN and NaSCN (λ_{ex} = 385 nm).

Given the elevate response of **NU-1000-BzTz** for CN^- anions, the cyanide limit of detection (LOD) was determined recording the emission spectra upon addition of small concentrations of KCN and plotting this value against the concentration of CN^- anions [Figure 107]. The resulting straight line was used to calculate the LOD value as: LOD = 3σ/*K* (where σ is the standard deviation of the intercept and *k* is the slope of the line calculated with a linear fitting)[246]. The as-calculated LOD for CN^- sensing of **NU-1000-BzTz** is 1.08×10^{-6} M, a value that is in line with the parameters of the World Health Organization that sets the limit of the level of CN^- anions in drinking water at 2×10^{-6} M[247]. Thus, this MOF is suitable for practical applications in CN^- detection in real wastewaters.

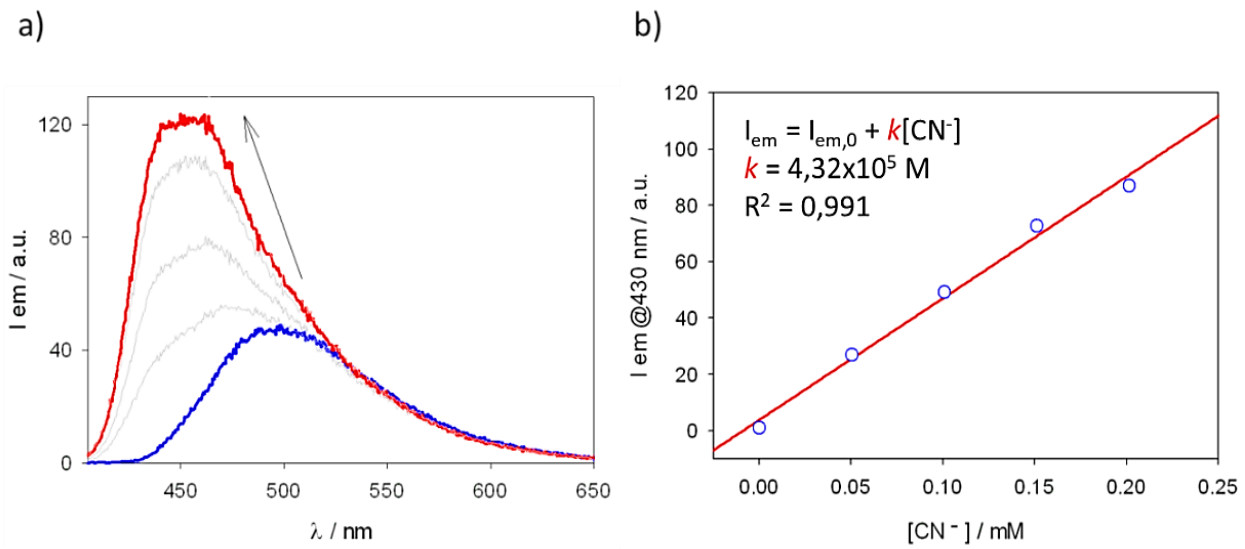

Figure 107: Emission spectra recorded for a suspension of **NU-1000-BzTz** upon addition of increasing quantities of KCN from 0 to 0.2 mM (blue to red lines) in water and λ_{ex} = 385 nm (a). Dependence between [CN^-] and emission intensity at 430 nm. The slope *k* was used to calculate the LOD (b).

The reversibility of the adsorption process was also evaluated for **NU-1000-BzTz**. The test was made adding increasing quantities of silver triflate [$Ag(CF_3SO_3)$] in the aqueous suspension of the MOF with cyanide anions, in order to form the insoluble AgCN salt and remove the anions from the solution. Upon addition of Ag^+ ions, it is possible to notice a decrease in the emission intensity of the MOF and also its shift to the original maximum value of 490 nm [Figure 108a]. The change in color is clearly visible even by naked eyes (as showed in the inset in figure), making the detection process very straightforward (a factor that could be really important for the application as luminescent sensor), and it is a proof of the cyanide removal. The reversible luminescence sensing of **NU-1000-BzTz** was also tested upon repeated additions of KCN and $Ag(CF_3SO_3)$ under monitored fluorescence emission [Figure 108b]. The MOF shows a very good reversibility.

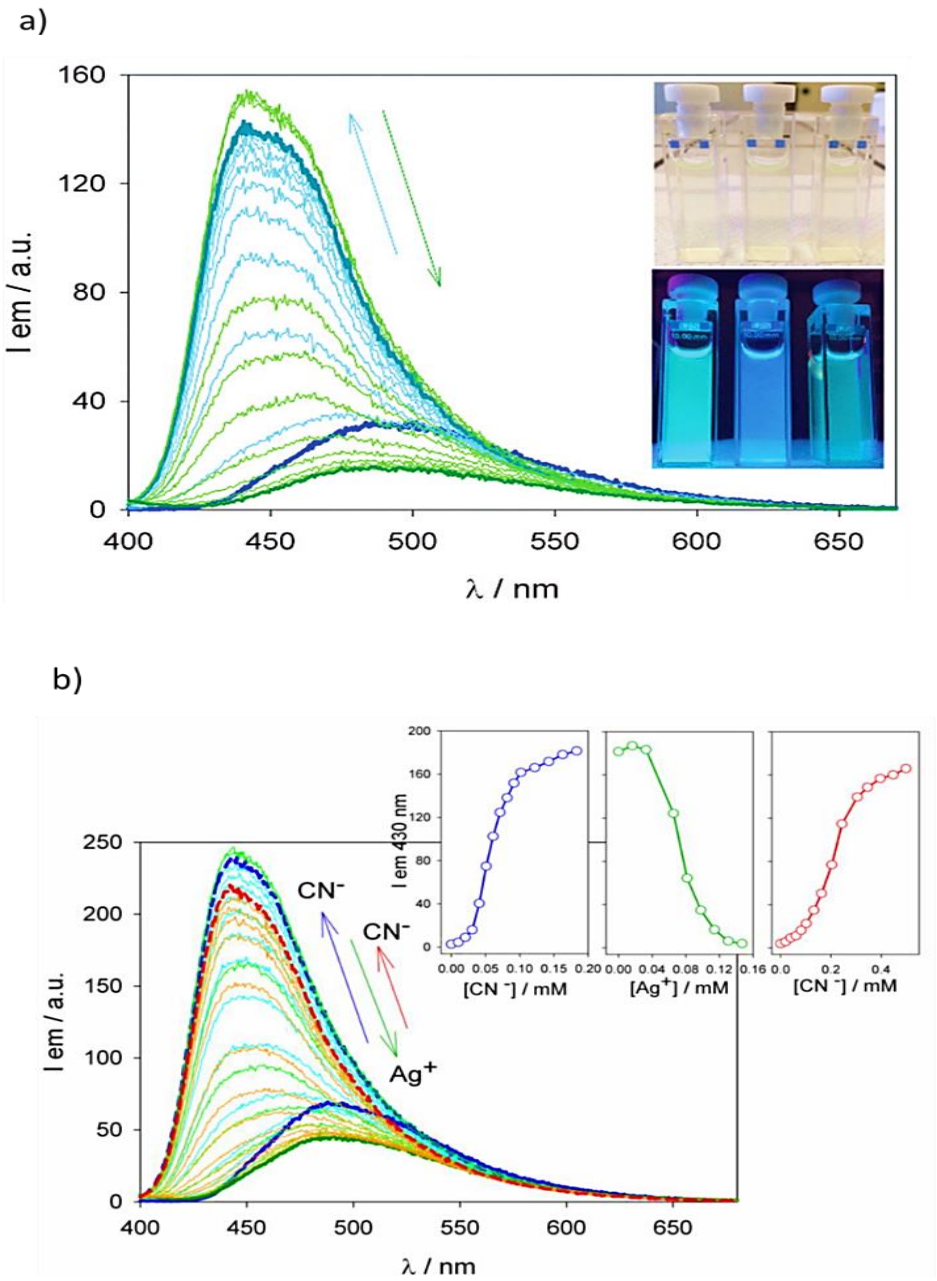

Figure 108: Evolution of the emission spectra recorded for a suspension of **NU-1000-BzTz** upon addition of KCN from 0 to 0.33 mM (blue to turquoise lines, respectively) in water and λ_{ex} = 385 nm, followed by addition of $Ag(CF_3SO_3)$ up to ca. 1.3 mM (dark green line). Inset: photos taken of three suspensions of **NU-1000-BzTz** in pure water (left), 0.5 mM KCN (center) and 0.5 mM KCN plus excess of $Ag(CF_3SO_3)$ (right), under ambient light (top) and under UV excitation (bottom) (a). Evolution of the emission spectra recorded for a suspension of **NU-1000-BzTz** upon additions of KCN from 0 to 0.19 mM (blue lines - from solid to dashed, respectively) in water and λ_{ex} = 385 nm, Followed by additions of $Ag(CF_3SO_3)$ up to ca. 0.15 mM (green lines). To the so-obtained mixture further amounts of KCN were added up to total 0.69 mM (red lines). Inset: dependence between $[CN^-]$, $[Ag^+]$ and the emission intensity at 430 nm (b).

Finally, **NU-1000-BzTz** was tested also in ordinary tap water, showing a good sensing efficiency even in the presence of other competing ions [Figure 109] and demonstrating its capability to act as a selective cyanide luminescent probe even in complex ions matrices.

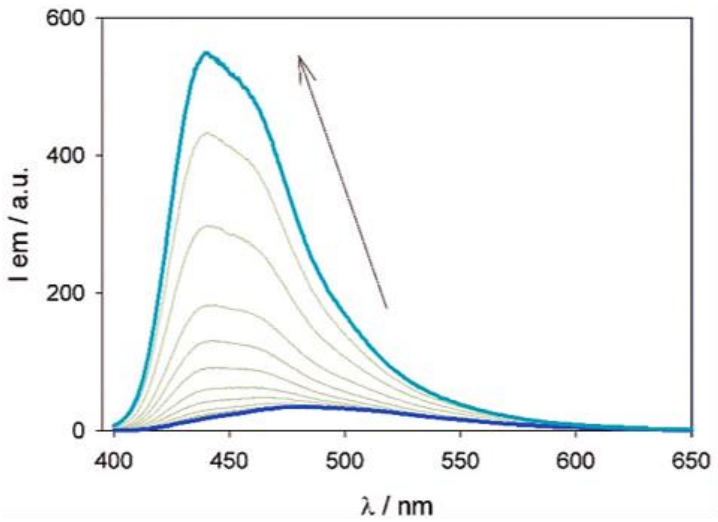

Figure 109: Evolution of the emission spectra recorded for a suspension of **NU-1000-BzTz** upon addition of KCN from 0 to 1.6 mM (blue to turquoise lines, respectively) in tap water at λ_{ex} = 385 nm.

6.4. Conclusions

In this work, the SALI technique has been successfully exploited to incorporate the new specifically designed ligand 3-(4-carboxybenzyl)benzo[*d*]thiazolium bromide (**BzTz**) inside the structure of the well-known NU-1000. The new **NU-1000-BzTz** has a maximum functionalization degree of 1.7 **BzTz** per [Zr_6] node and it keeps the same crystallinity of the parent MOF. **NU-1000-BzTz** was then tested for carbon dioxide storage with good results, since the presence of the polar **BzTz** group inside the pores enhances the thermodynamic affinity for CO_2 with respect to NU-1000 (Q_{st} values of 25 kJ mol^{-1} *vs* 17. kJ mol^{-1}, respectively). The presence of a luminescent thiazolium core in **NU-1000-BzTz** opens to additional applications in luminescence sensing. **NU-1000-BzTz** shows good sensitivity against polluting cyanide anions in aqueous solution. **NU-1000-BzTz** was tested for different anions CN^-, SCN^-, OCN^- and $SeCN^-$, showing a very sensitive, reversible and selective response to cyanide anions even in the presence of other competing anions. The emission color of the MOF changes from light green to blue (the color of the pristine NU-1000) under a UV lamp in the presence of trace amounts of CN^-, making the detection process very straightforward. The high sensitivity and its low cyanide LOD ($1.08x10^{-6}$ M) make **NU-1000-BzTz** suitable for application in real drinking water samples.

Chapter 7

NU-1000-FUNCTIONALIZED MOF FOR A TEMPERATURE-DEPENDENT N_2O/CO_2 PREFERENTIAL ADSORPTION

This chapter is based upon the following publication:

Temperature-Dependent Nitrous Oxide/Carbon Dioxide Preferential Adsorption in a Thiazolium-Functionalized NU-1000 Metal–Organic Framework.

ACS Applied Materials & Interfaces; **2021** *13*, 58982 – 58993

Giorgio Mercuri, Marco Moroni, Simona Galli, Giulia Tuci, Giuliano Giambastiani, Tongan Yan, Dahuan Liu and Andrea Rossin

7.1. Aim of the Work

Nitrous oxide (N_2O) is a major scavenger of stratospheric ozone and the third most important long-lived greenhouse gas after methane and carbon dioxide[248]. Nitrous oxide's atmospheric concentration has been constantly growing during recent years. The major anthropogenic sources of this gas are related to the agriculture and to its use as propellant[249] The contribution of N_2O to global warming is comparable to that of CO_2 because, despite it is present in the atmosphere in much smaller concentration, it has almost 300 times the heat-trapping ability of CO_2. Moreover, from a chemical point of view the two molecules are very similar since they are isoelectronic, have the same "stick-like" linear shape and have the same molecular weight (44 amu). However, CO_2 is quadrupolar while N_2O possesses a small dipole moment (0.166 D), and the distribution of its electron density is enhanced by the existence of two resonance forms with integer charges $\{N{\equiv}N^{+}\text{-}O^{-} \leftrightarrow {}^{-}N{=}N^{+}{=}O\}$ [250]. Consequently, the presence of a polar linker in a porous MOF should be beneficial for the exploitation of the latter as N_2O uptake material (as seen for CO_2).

In this work, the tailor-made ditopic thiazolium carboxylate salt 5-carboxy-3-(4-carboxybenzyl)thiazolium bromide (**H_2PhTz**)Br [Figure 110] was prepared and incorporated into NU-1000 applying the SALI technique, using the same approach described in the previous chapter. NU-1000 has two different kind of pores: wide hexagonal mesopores of ∼30 Å width (along the crystallographic *a*-axis and *b*-axis) and smaller micropores of ∼8 Å width (along the crystallographic *c*-axis). The (**H_2PhTzB**)Br linker has been anchored to the NU-1000 nodes in a bridging fashion between the adjacent [Zr_6] cluster which are only at an 8 Å distance apart in the *c*-crystallographic direction and therefore lying in the materials micropores. The new

NU-1000-PhTz MOF has been thoroughly characterized in the solid state. After SALI reaction, the sample maintains the same crystallinity of the pristine MOF but shows a lower BET specific surface area due to the presence of the new linker inside the pores. The actual linker composition has been determined through ^{1}H-NMR signal integration after the digestion of the MOF in acidic solution.

NU-1000-PhTz has been tested for the capture and separation of CO_2 and N_2O, showing an unprecedented temperature-dependent preferential adsorption capacity, loading more N_2O in a temperature range of 298 K ≤ T ≤ 313 K and more CO_2 at temperatures falling out of this range.

Simulations of the adsorption isotherms using the Grand Canonical Monte Carlo method showed that the preferred adsorption sites for both gases are near the polar inserted-linker.

7.2. Experimental Details

7.2.1. Materials and Methods

All the chemicals and reagents employed were purchased from commercial suppliers and used as received without further purification. NU-1000 was prepared according to the published procedure[239]. For organic syntheses, solvents were purified through standard distillation techniques. Deuterated solvents (Sigma-Aldrich) were stored over 4 Å molecular sieves and degassed by three freeze−pump−thaw cycles before use. NMR spectra were recorded on a Bruker Avance 400 MHz spectrometer. ^{1}H-and ^{13}C-NMR chemical shifts are reported in parts per million downfield of tetramethylsilane and were calibrated against the residual resonance of the protiated part of the deuterated solvent.

FT-IR spectra (KBr pellets) were recorded on a PerkinElmer Spectrum BX Series FTIR spectrometer, in the 4000 − 400 cm^{-1} range, with a 2 cm^{-1} resolution.

Thermogravimetric analyses were performed under N_2 flow (100 mL min^{-1}) at a heating rate of 10 K min^{-1} on an EXSTAR TG Analyzer (TG-DTG) Seiko 6200.

Elemental analyses were carried out using a Thermo FlashEA 1112 Series CHNS-O elemental analyzer with an accepted tolerance of ±2% on carbon (C), hydrogen (H), nitrogen (N), and sulfur (S).

ESI-MS spectra were recorded by direct sample introduction (10 µL min^{-1}) in a Finnigan LTQ mass spectrometer (Thermo, San Jose, CA). The instrument was equipped with a conventional ESI source. The working conditions were the following: positive polarity–spray voltage, 5 kV; capillary voltage, 35 V; capillary temperature, 548 K; tube lens, 110 V. The sheath gas pressure was set at

10 au and the auxiliary gas pressure was kept at 3 au. For the acquisitions, the Xcalibur 2.0 software (Thermo) was used. DMSO solutions of (**H_2PhTz**)Br (1 mg/mL) were diluted to 10 ng/µL with a MeOH/H_2O 1:1 v/v solution.

Powder X-ray diffraction qualitative measurements were carried out in the 2 − 50° 2θ region with a Panalytical X'PERT PRO diffractometer equipped with a diffracted beam Ni filter, a PIXcel© solid-state detector, and a sealed X-ray tube (Cu Kα, λ = 1.5418 Å). Slits were used on both the incident beam (Soller slits aperture: 0.25°; divergence slits aperture: 0.5°) and the diffracted beam (anti-scatter slit aperture: 7.5 mm).

Xray fluorescence qualitative elemental analysis was performed on a powdered batch (ca. 10 mg) of **NU-1000-PhTz** with a Panalytical MINIPAL 2 instrument equipped with a Cr X-ray source.

X-ray photoelectron spectroscopy (XPS) analyses were conducted in an ultrahigh vacuum spectrometer equipped with a VSW Class WA hemispherical electron analyzer and a monochromatic Al Kα X-ray source (1486.6 eV) as the incident radiation. Survey and high-resolution spectra were recorded in constant pass energy mode (90 and 44 eV, respectively). Binding energy (BE) values for all spectra were calibrated using the C 1s sp^2 component at 284.8 eV. Signal fitting was performed with the CasaXPS software using mixed Gaussian−Lorentzian curves.

7.2.2. Compounds Synthesis

Synthesis of 5-Carboxy-3-(4-carboxybenzyl)thiazolium Bromide (H_2PhTz)Br: A stirred solution of thiazole-5-carboxylic acid (0.4 g, 3.1 mmol) and 4-bromomethyl benzoic acid (0.8 g, 3.7 mmol, 1.2 eq.) in acetonitrile (25 mL) was kept at 353 K for 48 h. During this time, an off-white solid formed and precipitated out of the solution [Figure 110]. Afterward, the mixture was cooled down to ambient temperature, and acetonitrile was removed after decantation. The remaining solid was washed with acetone (3 × 10 mL) to remove any impurities or unreacted starting material. Finally, the solid was dried in vacuo to give pure (**H_2PhTz**)Br as an off-white powder (yield: 0.9 g, 84% based on thiazole-5-carboxylic acid).

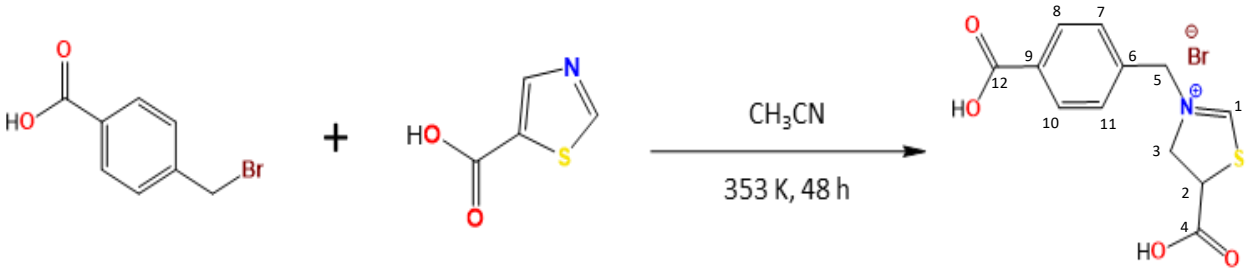

Figure 110: Schematic representation oh (**H_2TzPh**)Br linker synthesis.

^{1}H-NMR (400 MHz, DMSO-d_6, 298 K): δ (ppm) 10.54 (s, 1H, H^1), 9.21 (s, 1H, H^3), 7.99 (d, $^3J_{HH}$ = 8.25 Hz, 2H, $H^{8,10}$), 7.63 (d, $^3J_{HH}$ = 8.25 Hz, 2H, $H^{7,11}$), 5.87 (s, 2H, H^5). ^{13}C-NMR (400 MHz, DMSO-d_6, 298 K): δ (ppm) 167.49 (C^4), 164.25 (C^1), 160.16 (C^{12}), 141.42 (C^3), 138.86 (C^2), 136.31 (C^9), 132.05 (C^6), 130.51 ($C^{8,10}$), 129.49 ($C^{7,11}$), 58.10 (C^5).

Elem. Anal. Calcd (%) for (**H_2TzPhB**)Br $C_{12}H_{10}BrNO_4S$ (FW = 344.18 g/ mol): C, 41.88; H, 2.93; N, 4.07; S, 9.32. Found: C, 41.91; H, 2.96; N, 4.11; S, 9.30. IR (KBr pellet, cm^{-1}): ν = 3067 [m, ν(C–H)$_{aromatic}$], 2896 [m, ν(C–H)$_{aliphatic}$], 1726 [s, ν(COO)], 1709 [s, ν(COO)], 1612, 1582 [m, ν(C=C)], 1420 (m), 1406 (s), 1377 (s), 1224 [s, δ(O–H)], 1151(m), 1108 (m), 796 [s, γ(C–H)]. ESI-MS: m/z = 264 $(M\text{-}Br)^+$, 220 $(M\text{-}Br-CO_2)^+$, 176 $(M\text{-}Br-2CO_2)^+$. Crystals suitable for X-ray diffraction was obtained from a concentrated methanolic solution layered with acetonitrile at 298 K [Figure 112]

Synthesis of $[Zr_6O_4(OH)_6(H_2O)_2(TBAPy)_2(PhTz)]Br\cdot 8(H_2O)$ (NU-1000-PhTz): According to the general SALI procedure previously reported[240], the thiazolium bromide dicarboxylate salt (**H_2PhTz**)Br (0.127 g, 0.370 mmol, 10 eq.) was added to a suspension of benzoate-free NU-1000 (0.080 g, 0.037 mmol) in a dry and degassed polar solvent mixture (total volume, 37 mL; acetonitrile/dimethylsulfoxide = 90:10 v/v). The reaction mixture was heated at 353 K for 24 h with occasional gentle swirling. After that time, the mixture was brought back to room temperature, and the precipitate was filtered over a 0.2 µm PTFE filter. The bright yellow solid residue of **NU-1000-PhTz** was sequentially washed with hot acetonitrile, acetone, and dichloromethane (3 × 20 mL each) and finally dried in air. Yield: 90 mg (94%, based on zirconium). The phase purity of every batch was checked through PXRD. IR (KBr pellet, cm^{-1}): ν = 1676 (sh), 1604 (m), 1542 (m) [*ν*(C=O)], 1419 (s), 1384 (s), 1275 (m), 1261 (s), 1182 (w), 1148 (w), 1106 (w), 784 (m), 716 (m), 659 (m).

7.2.3. Linker Incorporation Quantification

The approximate linker composition of the MOF was assessed through signal integration of the ^{1}H-NMR spectrum of the digested sample in acidic solution (D_2SO_4 in D_2O, DMSO-d_6) [Figure 111]. In a typical procedure, 5 mg of sample were dissolved in three drops of concentrated sulfuric acid and 0.75 mL of DMSO-d_6 directly into an NMR tube. The mixture was heated at T = 363 K for 2 h, to complete the sample digestion. The as-obtained clear yellow solution was analyzed via ^{1}H-NMR (400 MHz, relaxation delay τ = 15 s, 512 scans).

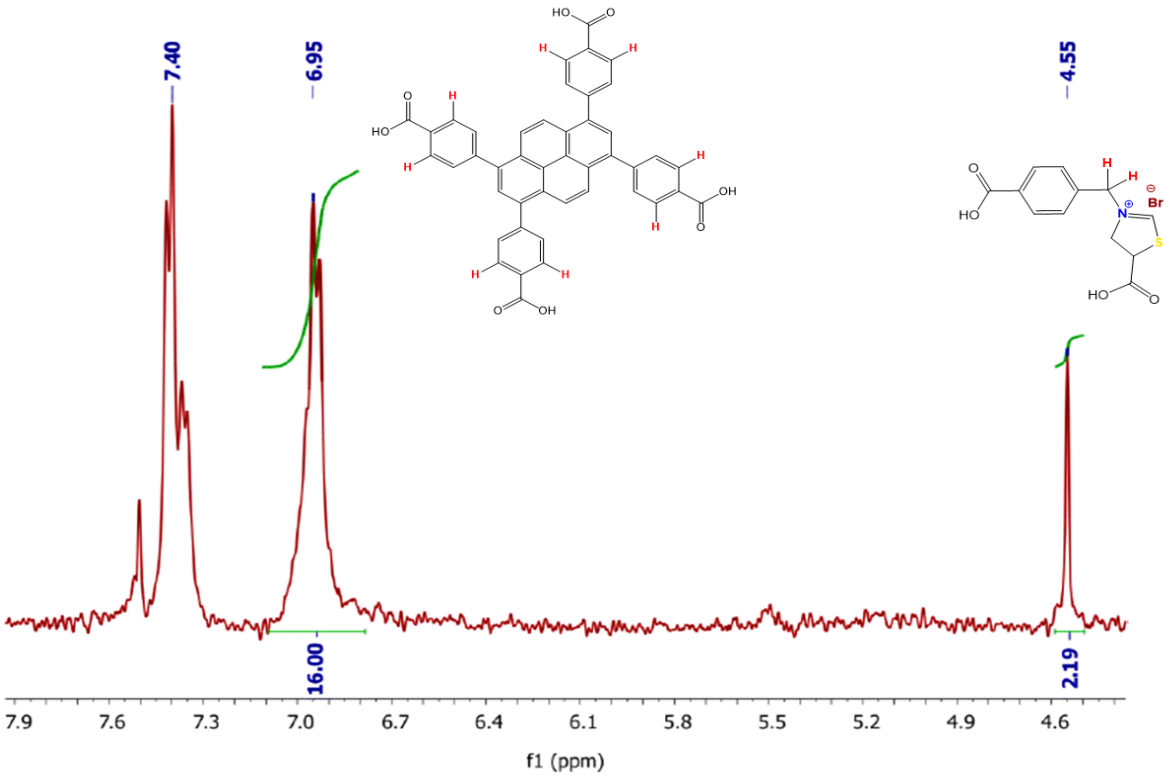

Figure 111: ^{1}H-NMR spectrum (400 MHz, D_2SO_4/D_2O/DMSO-d_6, 298 K) of the digested **NU-1000-PhTz** used for the quantification of the functionalization degree.

7.2.4. Single-Crystal X-Ray Diffraction Structure Determination

Single crystals of the zwitterionic neutral form **HPhTz** suitable for X-ray diffraction were obtained from a concentrated methanolic solution layered with acetonitrile at 298 K [Figure 112]. Single crystal X-ray diffraction data were collected at T = 100 K on an Oxford Diffraction XcaliburPX diffractometer equipped with a CCD area detector and a sealed X-ray source (Cu Kα, λ = 1.5418 Å). The program used for the data collection was CrysAlis CCD 1.171. Data reduction

was carried out with the program CrysAlis RED 1.171, while the absorption correction was applied with the program ABSPACK 1.17. Direct methods as implemented in SIR2014[202] were used to solve the crystal structure, while the structure refinement was performed by full-matrix least-squares against F^2, as implemented in SHELX2018[203]. All the non-hydrogen atoms were refined anisotropically. The hydrogen atoms of the carboxylic groups and of the crystallization water molecule with site occupation factor equal to 1 were located on the difference electron density maps and refined isotropically with $U_{iso} = 1.5U_{eq}(O)$, while all the other hydrogen atoms were fixed in calculated positions (riding model) and refined isotropically with $U_{iso} = 1.2U_{eq}(C)$ (C = carbon atom to which H is bound). As for the water molecule with site occupation factor equal to 0.25, no hydrogen atoms were either located in the electron density map or added in calculated positions. The geometrical calculations were performed by PARST97[251] and molecular plots were produced by the program ORTEP3[205].

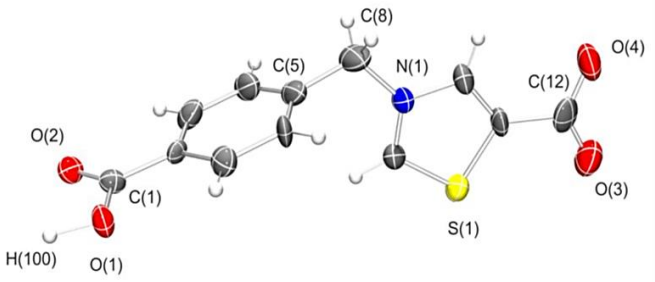

Formula	$C_{24}H_{20.5}N_2O_{9.25}S_2$
M [g mol^{-1}]	549.04
T [K]	100
Color, habit	Colorless platelets
Size [mm^3]	0.005 × 0.01 × 0.01
Crystal system	Monoclinic
Space group	$P2_1/c$
Z	4
a [Å]	28.383(14)
b [Å]	7.780(5)
c [Å]	10.692(6)
β [°]	91.439(4)
V [Å^3]	2360.3(2)

Figure 112: ORTEP drawing of **HPhTz** and main crystallographic data, experimental details and structure refinements details.

7.2.5. PXRD Structure Determination

A powdered sample (~50 mg) of **NU-1000-PhTz** was inserted in the cavity of a silicon-free background sample holder 0.2 mm deep (Assing Srl, Monterotondo, Italy) and analyzed by means of PXRD using a Bruker AXS D8 Advance vertical-scan θ/θ diffractometer, equipped with a sealed Xray tube (Cu Kα, λ = 1.5418 Å), a Bruker Lynxeye linear position sensitive detector, a Ni filter in the diffracted beam, and the following optical components: primary beam Soller slits (2.5°), fixed divergence slit (0.5°), and anti-scatter slit (8 mm). The generator was operated at 40 kV and

40 mA. A preliminary PXRD acquisition to check the purity and crystallinity of the sample was carried out in the 2θ range 2.0 – 35.0°, with steps of 0.02° and time per step of 1 s. The PXRD acquisition for the crystal structure assessment was then performed overnight in the 2θ range 2.0 − 105.0°, with steps of 0.02° and an overall scan time of about 12 h. As witnessed by a visual comparison among the PXRD patterns, **NU-1000-PhTz** shares the same 3D architecture of NU-1000. This suggestion was confirmed by performing an independent indexing procedure consisting in a standard peak search, allowing for the estimation of the first 20 low-to-medium angle peak maximum positions that were then processed with the software TOPAS-R V3.0 through the singular value decomposition algorithm[252], yielding approximate unit cell parameters. The space group was assigned on the basis of the observed systematic absences. The crystallographically independent portion of the pyrene-based linker and the thiazolium-based ligand was described using rigid bodies built up through the z-matrix formalism, assigning average values to bond distances and angles. Bond lengths and angles for the rigid body describing the tetrapyrene-based ligand: endocyclic C−C, 1.39 Å; exocyclic C−C, 1.48 Å; C−O, 1.25 Å; C−H, 0.95 Å; C−C−C, C−C−H and C−C−O angles, 120°. Bond lengths and angles for the rigid body describing the thiazolium-based ligand: phenylic endocyclic C−C, 1.39 Å; thiazolic endocyclic C−C and C−N, 1.35 Å; thiazolic endocyclic C−S 1.70 Å; exocyclic C−C and C−N, 1.48−1.50 Å; C-O, 1.25 Å; phenylic internal and external bond angles, 120°; thiazolic internal and external bond angles, 112 – 113° and 123°, respectively; sp^2 and sp^3 exocyclic bond angles, 120° and 109.5°, respectively. In the initial steps of the structure determination, both the metal cluster constituents (i.e., Zr^{4+}, O^{2-}, H_2O, and OH^-) and the pyrene-based linker were positioned according to the crystal structure of another NU-1000-functionalized MOF NU-1000-NDC (H_2NDC = naphthalene-2,6-dicarboxylic acid)[253]. The thiazolium-based ligand, the bromide anion, and a number of oxygen atoms with variable site occupancy factor modeling smeared electron density in the triangular channels and in the cavities containing **PhTz**$^-$ were located using the simulated annealing approach[207] implemented in TOPAS-R V3. During the structure refinement stages, carried out with the Rietveld method, rotations about the single bonds of the pyrene-based and the thiazolium-based ligands were allowed, and the position of the metal cluster constituents was refined according to the symmetry constraints. The background was modeled by using a Chebyshev type polynomial function. A unique isotropic thermal factor [B_{iso}(M)] was refined for the Zr(IV) ions; the isotropic thermal factor of the other atoms was calculated as $B_{iso}(L) = B_{iso}(M) + 2.0$ (Å^2). The peak profile was modeled through the fundamental parameters approach[208].

*Crystallographic data for **NU-1000-PhTz***: hexagonal, *P6/mmm, a* = 39.602(2) Å, c = 16.440(1) Å, V = 22 329(2) Å^3, Z = 24, Z' = 3, ρ = 0.567 g cm^{-3}, *F*(000) = 3771.8, R_{Bragg} = 0.014, R_p = 0.053, and R_{wp} = 0.075, for 5151 data and 45 parameters in the 2.0 − 105.0° (2θ) range. CCDC no. 2085493

7.2.6. Variable- Temperature PXRD Analysis

The thermal behavior of **NU-1000-PhTz** was studied in situ by means of variable-temperature PXRD, depositing a powdered sample (∼20 mg) on an aluminum sample holder and heating it through a custom-made sample heater (Officina Elettrotecnica di Tenno, Ponte Arche, Italy) in the temperature range 303 − 763 K, with steps of 20 K. A PXRD pattern was acquired under isothermal conditions at each step, in the 2θ range 4.0 − 20.0°, with steps of 0.02° and a time per step of 1 s. A parametric whole powder pattern refinement carried out with the Le Bail approach allowed to unveil the relative variations of the unit cell parameters in the investigated thermal range.

7.2.7. Gas Adsorption

Before the adsorption measurements were carried out, ∼40 mg of **NU-1000-PhTz** were activated at 393 K under a high vacuum (10^{-6} Torr) for 12 h. The textural properties were evaluated through volumetric N_2 adsorption isotherms recorded at 77 K on an ASAP 2020 Micromeritics instrument. For the BET specific surface area calculation, the 0.01 − 0.1 p/p_0 pressure range of the isotherm was used to fit the data. Within this range, all the Rouquerol consistency criteria are satisfied[57]. The total pore volume was estimated at p/p_0 = 0.98. The micro- and mesopore sizes were evaluated through NLDFT methods (Tarazona model for cylindrical pores). CO_2 and N_2O adsorption isotherms were recorded at 213 K, 253 K, 273 K, 298 K, 313 K, and 323 K at a maximum pressure of 1.2 bar. The isosteric heat of adsorption (Q_{st}) values of both gases were calculated from the six isotherms according to the differential form of the Clausius−Clapeyron equation[241]:

$$\left[\frac{\partial(\ln p)}{\partial\left(\frac{1}{T}\right)}\right]_{\theta} = -\frac{Q_{st}}{R}$$

Where R is the gas constant (8.314 J K^{-1} mol^{-1}).

The "Ideal Adsorption Solution Theory" (IAST) method for A/B adsorption selectivity (A, B = CO_2, N_2O, or N_2) of binary mixtures at a total pressure of 1 bar (arbitrary chosen for the sake of simplicity) and at T = 298 K and 323 K was determined as the ratio of the adsorbed molar fractions of the two gases divided by the ratio of the gas-phase initial molar fractions[254]:

$$S_{A/B} = \frac{\left(\frac{\chi_A}{\chi_B}\right)_{ads}}{\left(\frac{\chi_A}{\chi_B}\right)_{gas}}$$

The $(\chi_A)_{ads}$ and $(\chi_B)_{ads}$ values were derived from the application of the free software pyIAST to the experimental single-component isotherms collected at the chosen temperature. The initial compositions (%) for the calculation were the following: [15:85] for the [CO_2/N_2] and [N_2O/N_2] pairs and [50:50] for the [N_2O/CO_2] pair. These ratios were selected to mimic the general feed composition of the landfill and flue gases, respectively[255]. The Henry model was employed for the isotherm fitting. For a detailed explanation of these models and the related parameters, see the pyIAST Web page and documentation.

7.2.8. Grand Canonical Monte Carlo Simulation

The adsorption of CO_2 and N_2O was simulated by Grand Canonical Monte Carlo (GCMC) methods using the RASPA software package[256]. The framework was assumed to be rigid (i.e., atoms were frozen in the position assessed by crystal structure determination), and part of the point charges of the framework were distributed according to the QEq method using the code of Wells et al.[257] Dispersive and electrostatic interactions between the framework and the adsorbed molecules were taken into consideration during the simulations. The Lennard-Jones equation was used to describe dispersive interactions, and its parameters were calculated by the Lorentz–Berthelot mixed rule. For the framework, the Lennard-Jones parameters of the metal atoms were taken from the UFF force field[258], while those of the other elements were taken from the DREIDING force field[259]. This combination of force field parameters has already been successfully used to simulate gas adsorption in porous materials[260]. A rigid three-point charged Lennard-Jones linear model was used for CO_2 and N_2O. The energy parameters of CO_2 were taken from the EPM2 force

field[261], and the C−O bond length was set at 1.149 Å. The energy parameters of N_2O were adopted from the work of Chen et al.[262], with the N−N and N−O bond lengths of 1.1282 Å and 1.1842 Å, respectively. The number of MOF unit cells in the simulation box was 1 × 1 × 2 to ensure that the simulation unit was extended to be at least 28.0 Å along each dimension. Periodic boundary conditions were applied. The dispersive interactions were calculated using a long-range correction with a spherical cutoff radius of 14.0 Å, while the Ewald sum was used to consider the electrostatic interactions. The Peng−Robinson equation of state was used to convert the fugacity. 50 000 cycles of simulations were performed, including 25 000 equilibrium cycles and 25 000 ensemble average cycles. In each cycle, the adsorbed molecules underwent three types of trials: translation, rotation, and regeneration. Further increasing the number of cycles had no significant effect on the adsorption results. Molecular dynamics simulations were performed according to the experimental conditions. One molecule was inserted into the unit cell of each MOF using a canonical (NVT) ensemble to study the diffusion behavior of CO_2 and N_2O. Constant temperature conditions were maintained using a Nosé−Hoover chain thermostat[263]. The velocity Verlet algorithm was used to integrate Newton's equation of motion. The simulation steps and the time per step of each molecular dynamic simulation were 6 ns cycles and 1 fs, respectively, preceded by an equilibration of 3 ns. Finally, the slope of the molecular mean-square displacement (MSD) versus time plot (in its initial time interval, where a satisfactorily linear trend can be observed) was used to calculate the molecular self-diffusion coefficient, averaging over 10 independent trajectories[264].

7.3. Results and Discussion

The new linker 5-Carboxy-3-(4-carboxybenzyl)thiazolium Bromide (**H_2PhTz**)Br was synthesized starting from the commercially available thiazole-5-carboxylic acid and 4-bromomethyl benzoic acid through a simple thiazole N-quaternization in CH_3CN at 353 K. [Figure 110]. This linker was then incorporated into the structure of NU-1000 using SALI. An activated sample of NU-1000 was suspended in an excess solution of (**H_2PhTz**)Br (10 eq.) in a dry and degassed MeCN/DMSO 90:10 solvent mixture and heated at 353 K for 24 h. The actual linker composition was assessed via ^{1}H-NMR signal integration of the (**H_2PhTz**)Br signals against that of the $TBAPy^{4-}$ linker after the digestion of the sample in acidic solution (see paragraph 7.2.3. – Linker incorporation quantification). To confirm the success of the SALI inclusion, an XRF analysis was conducted to

the MOF sample [Figure 113], showing the presence of both sulfur and bromine inside the structure, confirming the successful functionalization. The presence of the bromide anion is necessary to balance the overall framework charge.

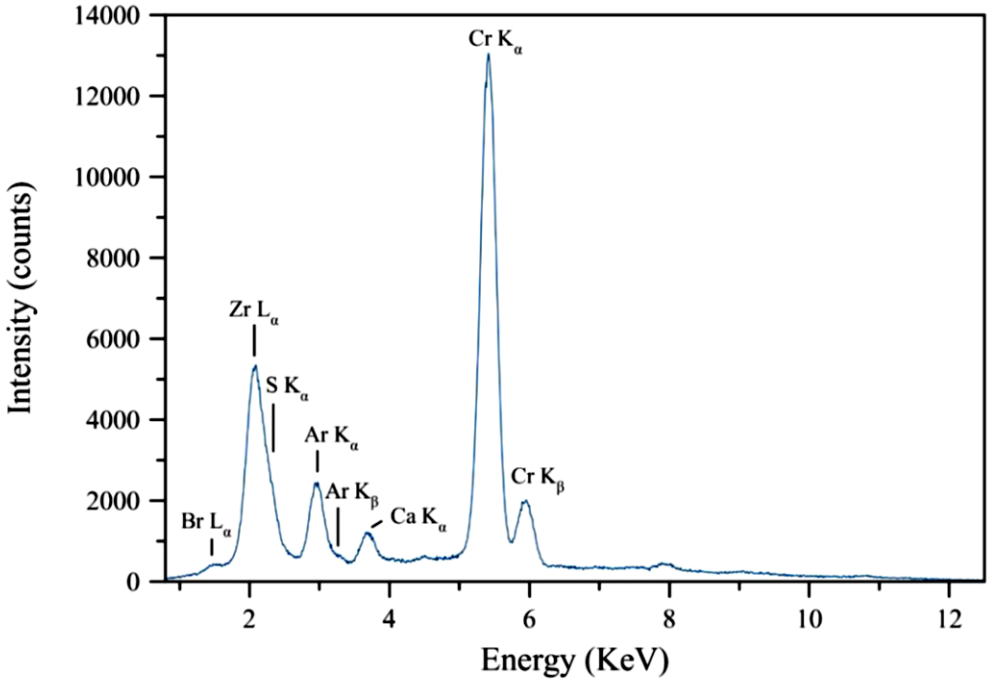

Figure 113: XRF spectrum of **NU-1000-PhTz** measured in air. The characteristic lines of argon come from air, those of chromium from the anode of the X-ray source and those of calcium from the ample holder.

The newly synthesized MOF **NU-1000-PhTz** has been thoroughly characterized in the solid state. The thermal behavior was evaluated through TGA-DTG analysis under N_2 flow [Figure 114]. The thermal stability of **NU-1000-PhTz** is slightly higher than that of NU-1000 (T_{dec} = 820 K vs 800 K, respectively). The former also shows also a weight loss and a DTG peak around T = 580 K that can be ascribed to the degradation of the (**H_2PhTz**)Br linker, whose composition temperature is around 545 K.

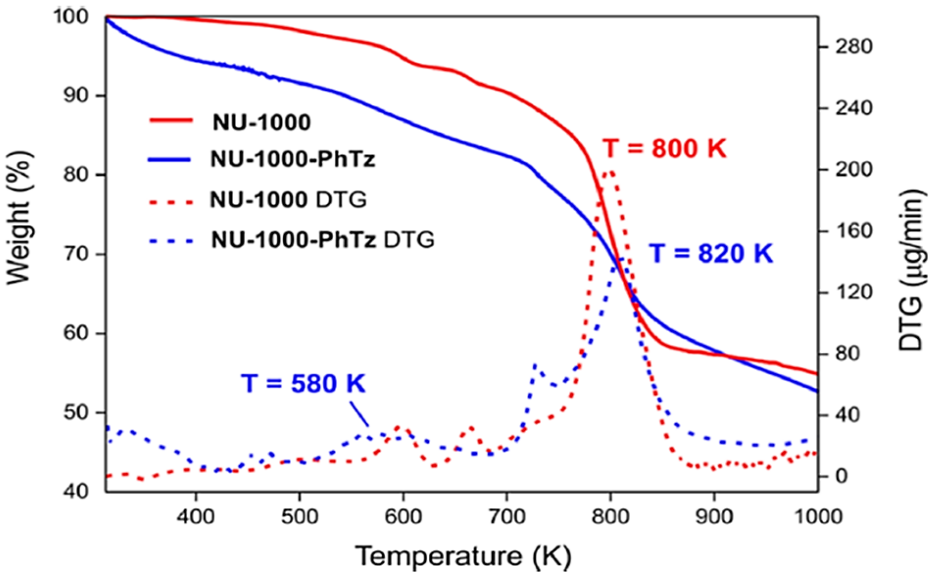

Figure 114: TGA and DTG profiles of NU-1000 (red lines) and **NU-1000-PhTz** (blue lines).

After TGA analysis, the MOF thermal behavior was also checked through VT-PXRD analysis. This experiment, carried out in air, evidenced that the material maintains its crystallinity until temperatures up to 763 K [Figure 115a]. In the temperature range 303 – 583 K, the unit cell parameters variation is very low (around 1.4%), witnessing the structural rigidity of the MOF [Figure 115b]. However, starting from a temperature around 583 K, which is the degradation temperature of (**H_2PhTz**)Br, there is a significant decrease in parameters (around -7%) in the *c*-axis that can be associated to the loss of the inserted linker. Indeed, applying the so-called Kempster-Lipson rule[265], the volume occupied by the **PhTz**$^-$ linker was estimated as ~324 Å^3, a value that is in accordance with the volume shrinkage of 4.5% (~324 Å^3 per formula unit) registered in the range of temperature 303 – 643 K. It is worthy of note that this decrease in the *c*-axis registered upon the loss of the linker is an additional proof of the insertion of (**H_2PhTz**)Br and that the latter is bridging adjacent [Zr_6] nodes in the ~8 Å cavities.

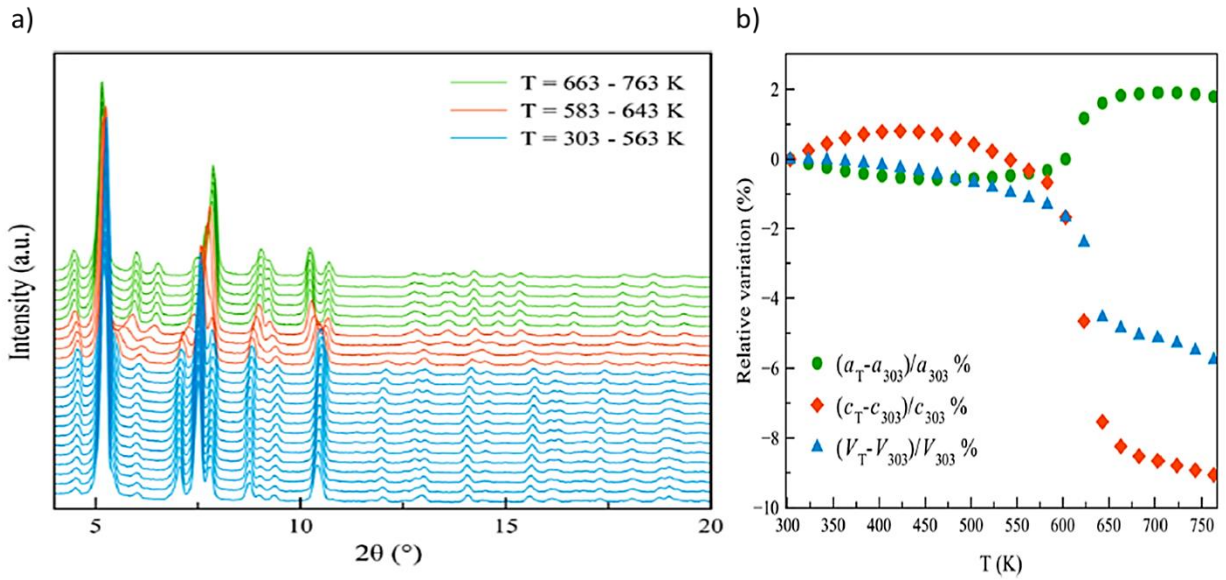

Figure 115: VT-PXRD pattern of **NU-1000-PhTz** acquired in air and in the temperature range 303 – 763 K (a). Percentage relative variation of the unit cell parameters as a function of the temperature (b).

The crystallinity of **NU-1000-PhTz** was evaluated trough a preliminary PXRD analysis; the pristine crystallographic symmetry and structural motif remain almost unaltered after SALI, with only small differences in the relative intensities of the diffraction peaks that are due to the changes in the electronic density distribution induced by the presence of (**H_2PhTz**)Br linker within the unit cell. The structure of the MOF was determined from the powder X-ray data through the refinement of a whole PXRD pattern of the compound, adopting the Le Bail approach [Figure 116].

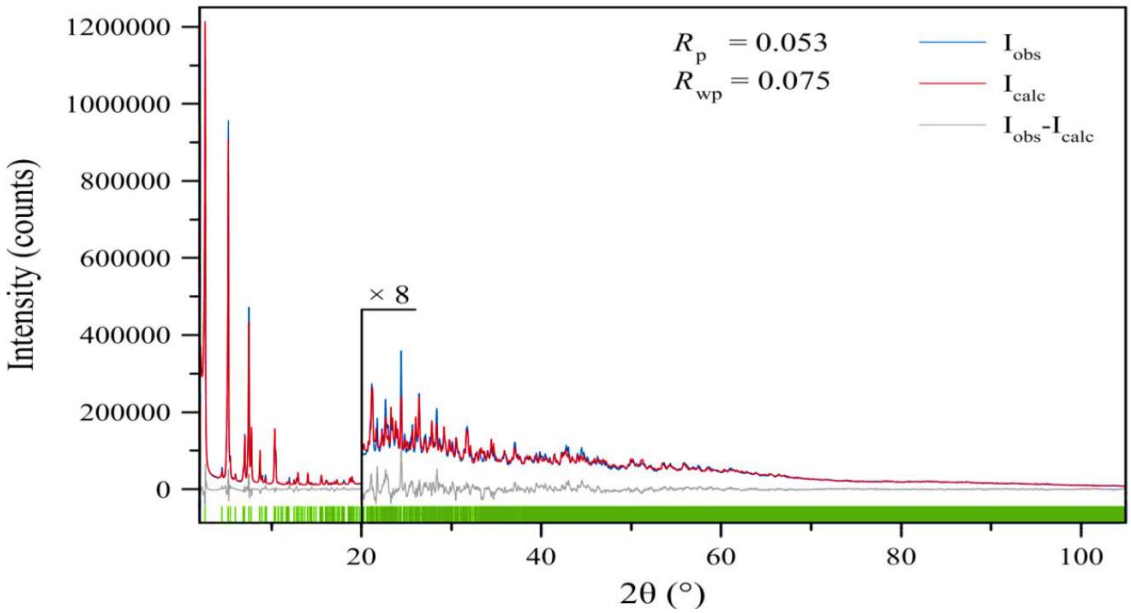

Figure 116: Graphical result of the final structure refinement performed with the Rietveld approach on the PXRD pattern of **NU-1000-PhTz** in terms of experimental (blue), calculated (red) and difference (grey) traces. The green markers at the bottom indicate the positions of the Bragg reflections.

NU-1000-PhTz crystallizes in hexagonal space group *P6/mmm*, with the inorganic SBU composed by an oxo-hydroxy cluster made of six octahedrally coordinated Zr(IV) cations connected to four μ_3-O^{2-} and four μ_3-OH^- anions [Figure 117a]. The framework structure is built through the coordination of each [Zr_6] node to eight different carboxylates coming from $TBAPy^{4-}$ linker. The **PhTz**$^-$ linker occupies the ~8 Å cavities along the *c*-axis of NU-1000 and it is bonded to the [Zr_6] nodes through its carboxylate groups (Zr-O distance is in the 2.027 – 2.433 Å range) in a bridging fashion [Figure 117b]. The node-to-node distance along the *c*-axis in NU-1000 is ~8.5 Å, a value that is comparable to that of the carboxylate-to-carboxylate distance of free **HPhTz** (~8.5 – 11.5 Å). The insertion of the linker in the cavities is made possible by the flexibility of the linker itself, given by the presence of the methylenic -CH_2- that connects the two aromatic rings. The presence of a dicarboxylate linker coordinated to the [Zr_6] nodes and not as a clathrated entity inside the pores is witnessed by the presence of bromine detected *via* XRF. Indeed, the bromide anion with its negative charge is necessary to guarantee electro-neutrality in the final MOF molecular formula in the presence of a doubly deprotonated (**PhTz**)$^-$ linker: $[Zr_6O_4(OH)_6(H_2O)_2(TBAPy)_2$(**PhTz**)]Br.

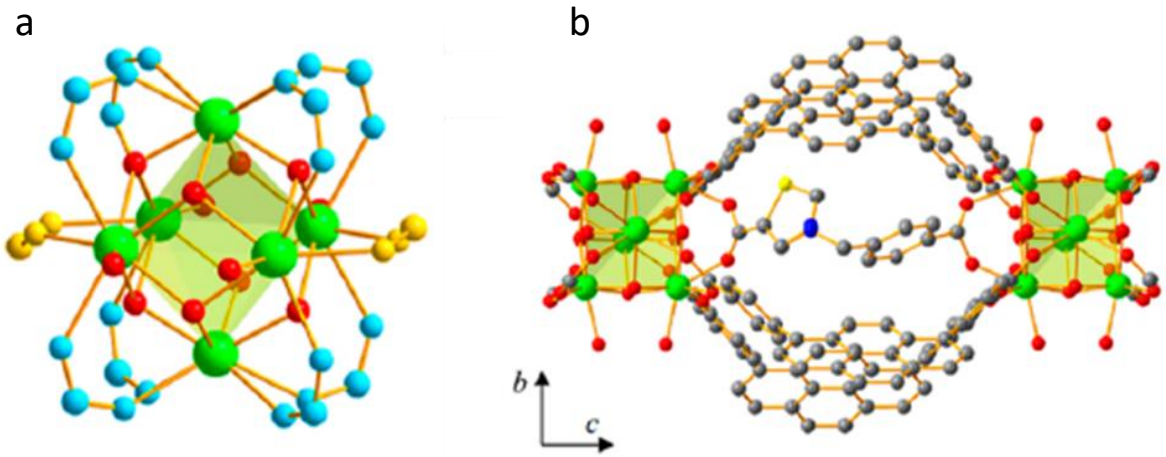

Figure 117: Representation of the crystal structure of **NU-1000-PhTz**. Zr-based oxo−hydroxo cluster coordinated by the carboxylate groups belonging to the $TBAPy^{4-}$ linkers (blue atoms) and to **PhTz**$^-$ (yellow atoms); (a). Bridging coordination mode of **PhTz**$^-$ in the ~8.5 Å cavity along the c-axis (b). Color code: Zr – light green, Br – brown, N – blue, S – yellow, O – red and C – grey.

The remaining free coordination sites of [Zr_6] cluster are saturated by four hydroxide/aquo ligands that are oriented toward the wide hexagonal pores [Figure 118]. These ligands interact with the Br^- anions coming from the **PhTz**$^-$ linker (distance O···Br equal to 2.79 Å). The location of

the framework counterions in the hexagonal channels was already observed in other NU-1000-functionalized MOFs[266].

The empty pore volume was estimated with the software PLATON[230] and is ~69%, a value that is lower than that of NU-1000 but expected for the presence of the added linker.

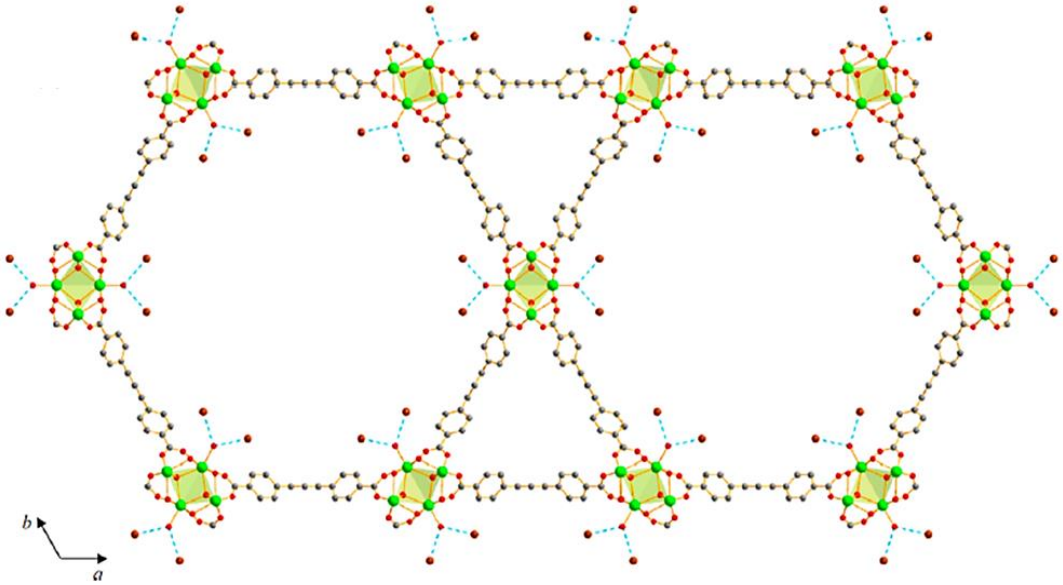

Figure 118: Representation of the crystal structure of **NU-1000-PhTz** viewed along the [001] crystallographic direction. Hydrogen bonds involving OH^-/H_2O and Br- are highlighted with blue dashed lines. Hydrogen atoms are omitted for the sake of clarity. Color code: Zr – light green, Br – brown, N – blue, S – yellow, O – red and C – grey.

The texture and the porosity of **NU-1000-PhTz** were evaluated through volumetric N_2 adsorption at 77 K. Before the analysis, in accordance with the typical methodologies, the sample was evacuated using a thermal treatment, heating it at 393 K under high vacuum for 12 h [Figure 119a]. The isotherm shape of the MOF is of type IV, the same of NU-1000. The calculated BET specific surface area is 1560 $m^2\ g^{-1}$, lower than that of the pristine MOF (2140 $m^2\ g^{-1}$). This result was expected because of the presence of the **PhTz** linker inside the structure. The added bridging thiazolium also modifies NU-1000 pristine pore volume and pore size distribution [Figure 119b]. The total pore volume of **NU-1000-PhTz** calculated at p_o/p_0 = 0.98 is equal to 0.93 $cm^3\ g^{-1}$ (vs 1.53 $cm^3\ g^{-1}$ of NU-1000). The pore size distribution was evaluated through NLDFT model. Despite the presence of the **PhTz**$^-$ linker in the cavities, the micropore size remains practically unchanged with values of 12.4 Å vs 11.6 Å for NU-1000 and **NU-1000-PhTz**, respectively. On the other hand, the mesopores of this latter are smaller than that of NU-1000 (29 Å vs 33 Å, respectively), a result expected due to the presence of bromide counter ions in the mesopores.

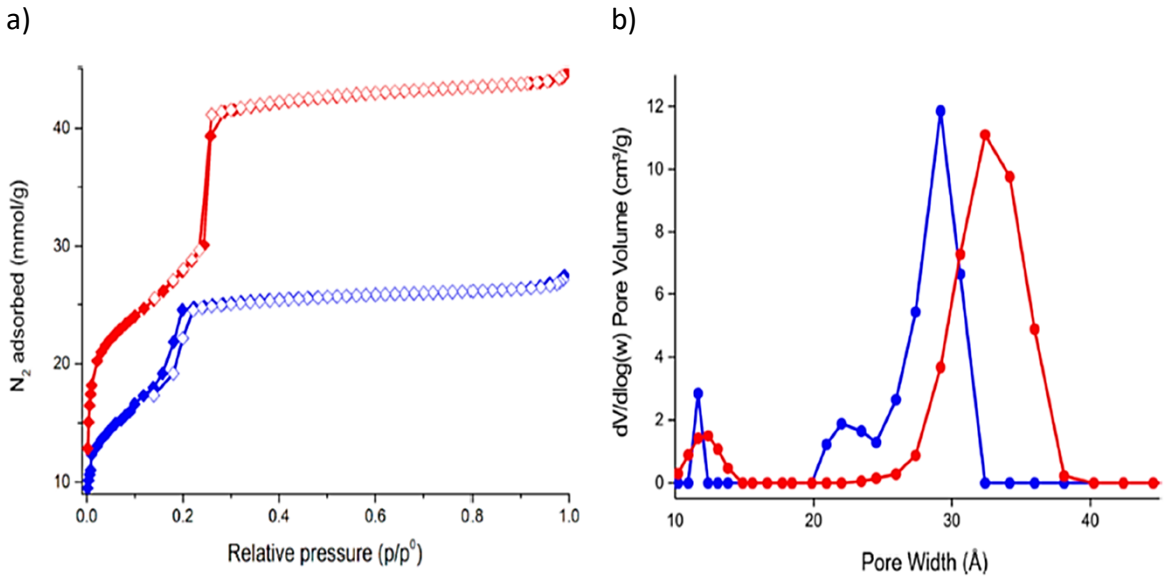

Figure 119: Comparison between N_2 adsorption isotherms of NU-1000 (red diamonds) and **NU-1000-PhTz** (blue diamonds) and desorption isotherms (empty diamonds) measured at 77 K (a). Pore size distribution plot, calculated with NLDFT Tarazona model for cylindrical pores, for NU-1000 (red) and **NU-1000-PhTz** (blue) at comparison (b).

Then, **NU-1000-PhTz** has been tested for the adsorption of the two different polluting gases CO_2 and N_2O, at two different temperatures (T = 213 K and 298 K) and p_{max} = 1.2 bar. For what concern the results of CO_2 adsorption, **NU-1000-PhTz** show a total carbon dioxide uptake at p_{CO_2} = 1 bar of 6.2 wt% (1.4 mmol g^{-1}) and 9.5 wt% (2.2 mmol g^{-1}) at 298 K and 273 K, respectively. These values are lower than that of NU-1000 (2.8 mmol g^{-1} at 298 K, for example) but can be explained by the lower surface area of the functionalized MOF. However, the Q_{st} calculated for **NU-1000-PhTz** is higher with a value of 25 kJ mol^{-1} vs 17 kJ mol^{-1} of NU-1000. This value is the same found in NU-1000-BzTz (treated in the precedent chapter 6) and can be explained by the similarities between the two inserted linkers.

The adsorption of N_2O was measured at the same pressure and temperature conditions. The maximum uptake recorded is 7.2 wt% (1.6 mmol g^{-1}) and 9.4 wt% (2.1 mmol g^{-1}) at 298 K and 273 K, respectively. These values are higher than that found for other MOFs in literature[267]. The Q_{st} value for N_2O is 27 kJ mol^{-1}, a value that is slightly higher than that of CO_2 and also to that found for other MOFs in literature[267].

The results obtained in gas adsorption are really interesting since **NU-1000-PhTz** not only show an overall higher thermodynamic affinity for N_2O respect to CO_2 (higher Q_{st}), but also display a preferential adsorption of this latter gas at lower temperatures (273 K), while a better adsorption of N_2O at higher temperatures (298 K). This behavior led to a deeper investigation. For this

reason, the gas adsorption properties were also investigated for others different temperatures: 213 K, 253 K, 313 K and 323 K [Figure 120]. Moreover, the adsorption isotherms and the gases adsorption quantities at these temperatures were simulated using GCMC method following the procedure previously reported (see paragraph 7.2.8.- Grand Canonical Monte Carlo Simulation). The obtained values are compared to the experimental ones and reported in [Table 2].

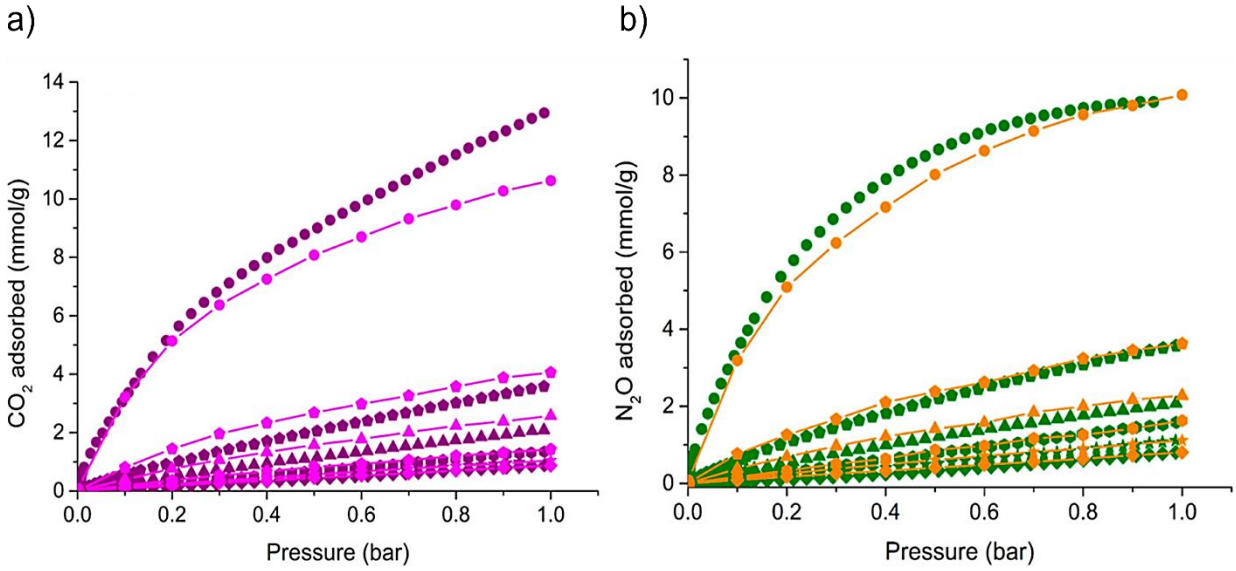

Figure 120: Comparison between experimental (purple and green symbols) and simulated (magenta and orange lines + symbols) of CO_2 (a) and N_2O (b) adsorption isotherms of **NU-1000-PhTz** measured at T = 323 K (diamonds), 298 K (hexagons), 273 K (triangles), 253 K (pentagons) and 213 K (dots).

	CO_2 adsorbed [mmol g^{-1}]		**N_2O adsorbed [mmol g^{-1}]**	
Temperature [K]	Experiments	Simulations	Experiments	Simulations
323	0.9 (4.0 wt%)	0.9 (4.0 wt%)	0.8 (3.6 wt%)	0.8 (3.6 wt%)
313	1.1 (4.7 wt%)	1.0 (4.7 wt%)	1.2 (5.0 wt%)	1.1 (5.0 wt%)
298	1.4 (6.2 wt%))	1.4 (6.2 wt%)	1.6 (7.2 wt%)	1.6 (7.2 wt%)
273	2.2 (9.5 wt%))	2.6 (11.1 wt%)	2.1 (9.4 wt%)	2.3 (10.2 wt%)
253	3.7 (16.2 wt%)	4.0 (17.7 wt%)	3.6 (16.0 wt%)	3.6 (16.0 wt%)
213	13.1 (57.7 wt%)	10.6 (46.8 wt%)	9.9 (43.4 wt%)	10.1 (44.2 wt%)

Table 2: CO_2 and N_2O experimental and simulated data at p = 1 bar for **NU-1000-PhTz**.

The adsorbed gases amounts obtained through GCMCS are in good agreement with the experimental values. **NU-1000-PhTz** show a better adsorption of N_2O in the interval 298 K < T < 313 K, while a higher affinity for CO_2 for temperatures out of this range. The study of the adsorption sites conducted by GCMS, reveals that the preferential adsorption sites of both gases at T = 273 K [Figure 121] and 298 K [figure 122] are located at the corners of the triangular channels and in proximity to the inserted linker, a result that confirms the positive effect of the inclusion of a thiazole-derivative linker. Both the gases molecules interact strongly with the framework, but with different adsorption modes. Carbon dioxide interacts with the thiazolium N and S atoms in an "end-on" configuration trough one of its oxygen atoms, revealing a partial positive charge delocalized all over the thiazolium ring. Nitrous oxide prefers a "side on" configuration by which all its three atoms interact with the S of thiazole ring. The different behavior can be ascribed to the polarity of N_2O. Regardless, at the investigated temperatures, both gases preferentially interact through their oxygen atoms (in N_2O the negative charge is more likely localized on O than on N atoms for electronegativity reasons) and with the S atom that is less sterically hindered than the N^+ atom of thiazole.

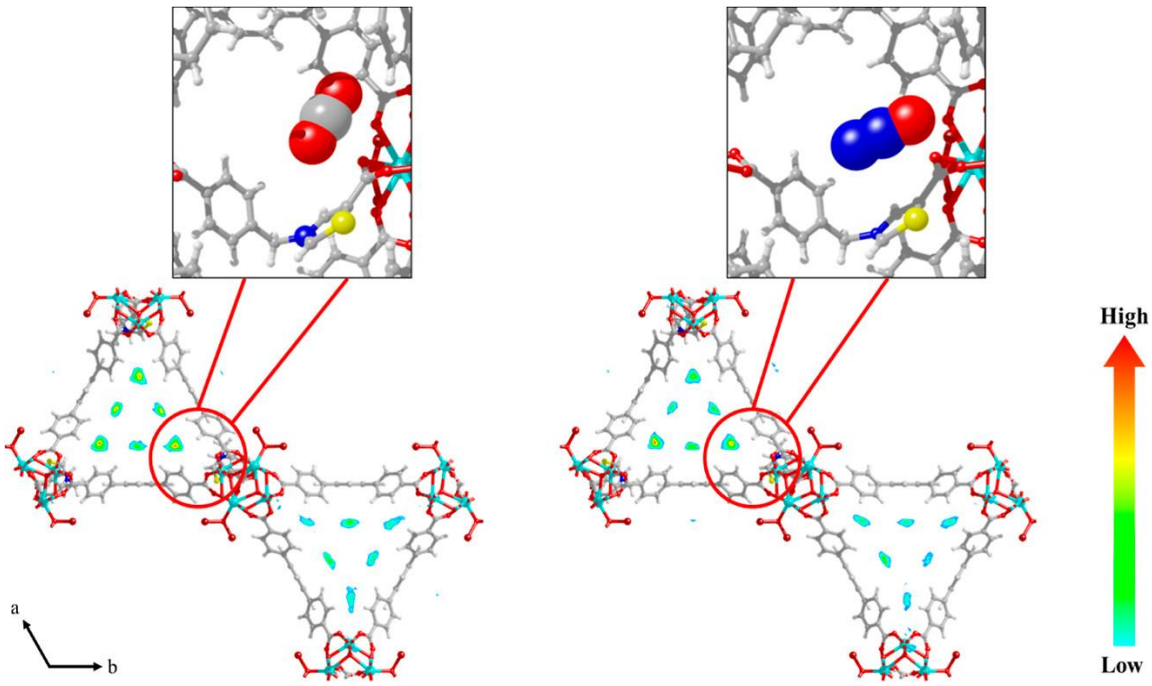

Figure 121: Contour plots of the center-of-mass probability densities of adsorbed CO_2 and N_2O in **NU-1000-PhTz** at T = 273 K and *p* = 1 bar

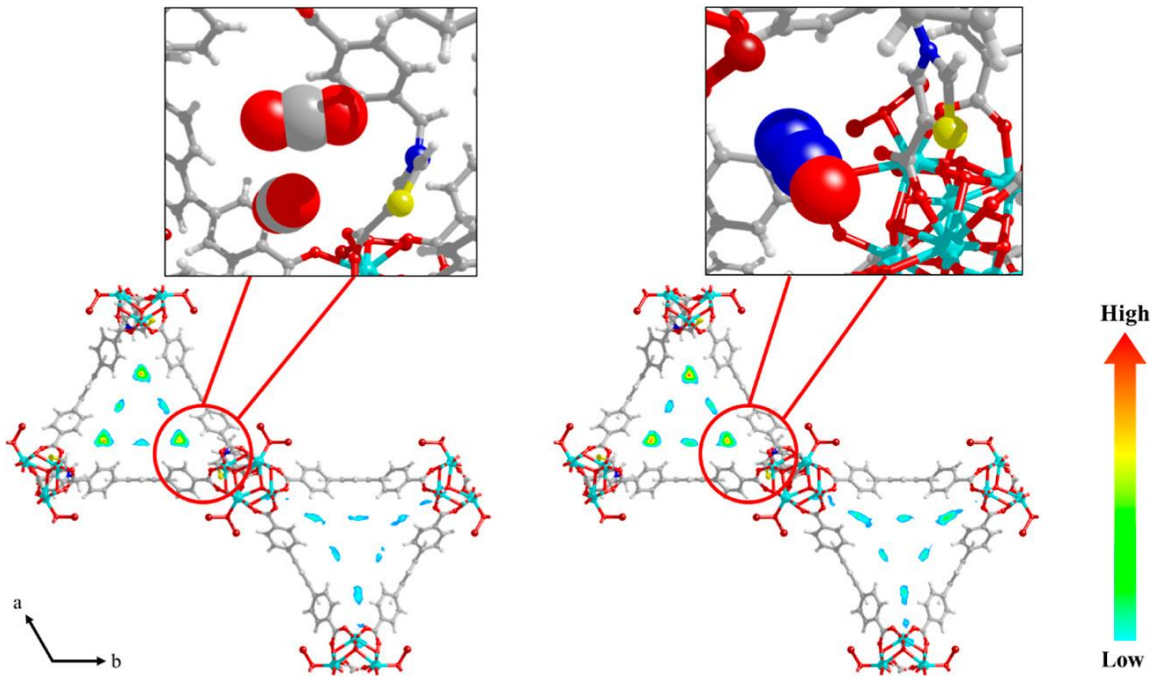

Figure 122: Contour plots of the center-of-mass probability densities of adsorbed CO_2 and N_2O in **NU-1000-PhTz** at T = 298 K and *p* = 1 bar

Other studies on the diffusion of the two gases in **NU-1000-PhTz** have revealed that at all the assayed temperatures below the ambient, the diffusion coefficient (D_S) of CO_2 is larger than that of N_2O (faster diffusion). However, at 298 K the D_S of this latter increases significantly, exceeding that of CO_2. Therefore, at this temperature, N_2O diffuse faster, first occupying the MOF primary adsorption sites. This result is in line with the higher N_2O adsorption capacity, thermodynamic affinity , and selectivity observed experimentally at 298 K. Conversely, the D_s values of N_2O calculated for NU-1000 are smaller at all the other investigated temperatures. The results are shown in [Table 3].

	Ds [m^2 s^{-1}]			
Temperature [K]	NU-1000		**NU-1000-PhTz**	
	CO_2	**N_2O**	**CO_2**	**N_2O**
213	7.9×10^{-10}	2.7×10^{-10}	8.1×10^{-10}	8.7×10^{-11}
253	1.5×10^{-9}	1.0×10^{-9}	1.5×10^{-9}	2.1×10^{-10}
273	7.9×10^{-9}	2.2×10^{-9}	3.2×10^{-9}	9.2×10^{-10}
298	1.9×10^{-8}	3.9×10^{-9}	3.1×10^{-9}	7.6×10^{-9}

Table 3: Derived D_s values of CO_2 and N_2O in NU-1000 and **NU-1000-PhTz** at different temperatures. The ambient temperature values (where a faster N_2O over CO_2 diffusion is observed for the thiazolium-functionalized material) are highlighted in red.

The temperature-dependent adsorption behavior showed by **NU-1000-PhTz**, may be exploited for the discrimination of chemically similar polluting gases, opening new horizons in the field of molecular recognition and gas mixture separation. To further study the adsorption behavior of the MOF, also the selectivity ($S_{A/B}$) data for three different binary mixture ([CO_2/N_2] 15:85, [N_2O/N_2] 15:85, [N_2O/CO_2] 50:50) at T = 298 K and 323 K were estimated using the IAST method. The results of this analysis are reported in [Table 4]

Temperature [K]	CO_2/N_2 [15:85]	N_2O/N_2 [15:85]	N_2O/CO_2 [50:50]
298	12	14	1.1
323	37	32	0.9

Table 4: IAST adsorption selectivity data of binary gas mixtures for **NU-1000-PhTz**.

The selectivity value between N_2O and CO_2 has its maximum at T = 298 K, and it is equal to 1.1, a value higher than that of NU-1000 (0.8) proving again the beneficial effects of the introduction of the new linker. At T = 323 K the same selectivity is 0.9, in accordance with the experimental results, because at this temperature, the selectivity for CO_2 is higher. For what concern the comparison with N_2 adsorption, both S_{CO_2/N_2} and S_{N_2O/N_2} have absolute values that are much higher than those of S_{N_2O/CO_2}, a behavior that can be ascribed to the non-polar nature of nitrogen. the highest values were recorded at T = 323 K. At this temperature, the amount of N_2 adsorbed is close to zero. Therefore, N_2 separation from both greenhouse gases is more efficient if compared with that achieved at ambient temperature.

7.4. Conclusions

In this work, SALI has been successfully employed to incorporate the new specifically designed linker 5-carboxy-3-(4-carboxybenzyl)thiazolium bromide [(**H_2PhTz**)Br] inside the structure of NU-1000. The SALIed material **NU-1000-PhTz** contains one (**H_2PhTz**)Br linker per [Zr_6] node (as assessed through ^{1}H-NMR analysis of the digested sample) and keeps the same crystallinity of the pristine MOF. The inserted linker bridges two adjacent [Zr_6] nodes along the *c*-axis. The MOF was then tested for capture and separation of the two polluting gases CO_2 and N_2O, showing a higher thermodynamic affinity for both gases with respect to NU-1000. This result can be ascribed to the presence of the polar thiazolium salt inside the pores that interacts with the polar

gases. Indeed, as proven by Grand canonical Monte Carlo simulations the preferential adsorption sites for both gases are in close proximity of the inserted linker. Moreover, **NU-1000-PhTz** shows an unprecedented temperature-dependent selectivity for the two gases, adsorbing more N_2O at temperatures between 298 K and 313 K, but more CO_2 at temperatures outside of this range. So, the functionalized MOF can discriminate between different polluting gases through selective adsorption simply by switching the temperature. With the aim of reducing the Greenhouse Effect on the planet, **NU-1000-PhTz** may represent a functional material for the efficient adsorption and discrimination of chemically similar polluting gases like CO_2 and N_2O.

Chapter 8

ZINC BIPYRAZOLATE MOF FOR CARBON CAPTURE AND UTILIZATION

This chapter is based upon the following publication:

Carbon Dioxide Capture and Utilization with Isomeric Forms of Bis(amino)-Tagged Zinc Bipyrazolate Metal–Organic Frameworks.

Chemistry – A European Journal; **2021** *27*, 4764 – 4754. Part of the "Metal-Organic Frameworks: Special Collection 2020" Special Issue (Wiley VCH) dedicated to the MOF2020^{web} conference.

Giorgio Mercuri, Marco Moroni, Simona Galli, Kostiantyn V. Domasevitch, Corrado di Nicola, Patrizio Campitelli, Claudio Pettinari, Giuliano Giambastiani and Andrea Rossin

8.1. Aim of the Work

The issue of greenhouse gases is a pressing global concern, as these gases trap heat in the Earth's atmosphere and contribute to climate change. The most significant greenhouse gas is carbon dioxide, which is primarily emitted through the burning of fossil fuels. To reduce the level of this greenhouse gas in the Earth's atmosphere, one of the most used methods nowadays is the trapping of CO_2 within porous solid-state sponges, a process named "carbon capture and storage" (CCS)[268]. In addition to CCS, another field of research that is gaining significance advancement is "carbon capture and utilization" (CCU), where the CO_2 is exploited as primary building block for the synthesis of other valuable chemicals, such as formic acid, methanol and methane[269]. From this point of view, carbon dioxide is considered an abundant and "renewable" resource that can be harvested and recycled. MOFs are considered ideal compounds for both CCS and CCU applications, because they can act as efficient CO_2 sponges and heterogeneous catalysts for CO_2 transformation at the same time [270]. Moreover, the possibility to include suitable functionalities inside the framework enhances the properties of the material. Given the acidic nature of CO_2, to improve the interaction strength between the solid and the gas, the simplest and easiest functionality that can be used is a primary amino group ($-NH_2$).

In this work, two different zinc MOFs featuring amino-decorated bipyrazolate linkers have been synthesized. These linkers are the already known 3,5-diamino-4,4'-bipyrazole (**3,5-H_2L**)[271] and its (newly prepared) isomeric form 3-3'-diamino-4-4'-bipyrazole (**3,3'-H_2L**) [Figure 123].

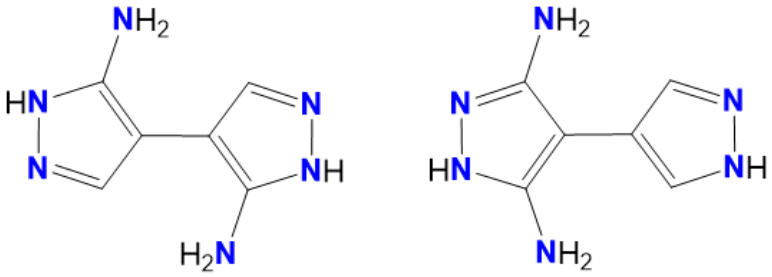

3,3'-H_2L **3,5-H_2L**

Figure 123: Molecular structures of the two isomeric linkers used in this work.

The corresponding zinc MOFs (**Zn(3,3'-L)** and **Zn(3,5-L)**) have been used as heterogenous catalysts for the [CCS+CCU]application. In particular, the MOFs have catalyzed CO_2 cycloaddition to the two halogenated epoxides epichlorohydrin and epibromohydrin, to produce the corresponding cyclic carbonates[272]. Cyclic carbonates are industrially important chemical intermediates that have a wide range of applications, such as monomers for polymerization, electrolytes in lithium batteries, and high-boiling aprotic green solvents[273]. Additionally, the synthesis of five-membered cyclic carbonates from epoxides under catalytic conditions is a relatively straightforward process with 100% atom economy[274]. Both MOFs show good results in the reaction of CO_2 with the epoxides at 393 K and p_{CO_2} of 5 bar under solvent and co-catalyst free conditions.

8.2. Experimental Details

8.2.1. Materials and Methods

3,3'-Dinitro-4,4'-bipyrazole[275] and 3,5-diamino-4,4'-bipyrazole [272] were synthesized as reported in literature. All the chemicals and reagents employed in the syntheses purchased from commercial suppliers were used as received without further purification, while the epoxides used in the catalytic tests were distilled prior to use and stored over 4 Å a molecular sieves under nitrogen.

IR spectra were recorded as neat from 4000 to 600 cm^{-1} with a Perkin- Elmer Spectrum One System instrument.

Elemental analyses (C, H, N %) were performed with a Fisons Instruments 1108 CHNS-O elemental analyzer.

The ^{1}H-NMR spectrum of 3,3'-diamino-4,4'-bipyrazole was recorded in deuterated dimethylsulfoxide-d_6 on a Bruker Ascend 400 instrument operating at 400 MHz and 298 K. The chemical shifts are reported in ppm from TMS as internal standard.

TGA-DTA analysis was performed with a PerkinElmer STA 6000 Simultaneous Thermal Analyzer. The samples were heated from 303 to 923 K at a heating rate of 10 K min^{-1} under a nitrogen flow (20 mL min^{-1}).

PXRD qualitative analysis was carried out with a Bruker AXS D8 Advance diffractometer, acquiring data at room temperature in the 3 – 35° 2θ range, with steps of 0.02°, and time per step of 1 s. The nature and purity of all the batches employed for the functional characterization were assessed by elemental analysis, IR spectroscopy and PXRD.

Gas-chromatography/Mass (GC/MS) analyses of the reaction mixtures after the catalytic runs were performed on a Shimadzu QP2010S apparatus equipped with a flame ionization detector and a Supelco SPB-1 fused-silica capillary column (30 m length, 0.25 mm internal diameter, 0.25 mm film thickness).

8.2.2. Compounds Synthesis

Synthesis of 3,3'-diamino-4,4'-bipyrazole (3,3'-H_2L): 3,3'-Dinitro-4,4'-bipyrazole (24.64 g, 0.11 mol) were prepared following the literature method[275] and slurred in water (2 L) at 343 K. An aliquot (1 mL) of a Raney 2800 nickel aqueous slurry was then added, followed by the dropwise addition of an aqueous solution of hydrazine hydrate (48.5 mL, 1 mol, in 200 mL of water) during a 4-hour period at 343 K and under vigorous stirring. Fresh portions (1 mL) of nickel catalyst were repeatedly added at one-hour time intervals. The dissolution of the starting material was complete after the first 2 h, with the mixture turning orange due to the presence of the nitropyrazolate anion in solution. The reduction progress was readily monitored by the gradual fading of the solution color over the following 2 h. After the complete addition of hydrazine, the mixture was further stirred for 2 h. Then, it was filtered while hot and the precipitate was thoroughly washed with hot water (1.5 L, 343 – 353 K). The colorless filtrates were combined and reduced to 150 mL on a rotary evaporator. The colorless crystals of the product were filtered, washed with small portions of cold water and air-dried. Yield: 17.11 g (95 %). Elem. anal. calc. for $C_6H_8N_6$ (MW = 164.2 gmol^{-1}): C, 43.89; H, 4.91; N, 51.20%. Found: C, 43.64;

H, 5.03; N, 50.94%. ^{1}HNMR (400 MHz, 298 K, DMSO-d_6): d(ppm) = 7.99 (2 H, CH), 7.75 (4 H, NH_2), 12.80 (2 H, NH).

Synthesis of 3,5-diamino-4,4'-bipyrazole (3,5-H_2L): the linker was prepared in nearly quantitative yield following the procedure reported in literature[271]. The experimental details are reported hereafter for the sake of completeness. 3,5-Dinitro-4,4'-bipyrazole (33.00 g, 136 mmol) were prepared following the literature method[275] and dissolved in a mixture of 96% ethanol (2 L) and water (200 mL) at 333 K; then a Raney 2800 nickel slurry in water (1 mL) was added. A solution of hydrazine hydrate (48.5 mL, 1 mol) in 96% ethanol (200 mL) was added dropwise in 10 h at 333 K under magnetic stirring. Upon hydrazine addition, the solution turned from light-yellow to deep-orange, and orange crystals of the hydrazinium salt of nitrobipyrazole[276] separated from the reaction mixture. The crystals dissolved in a period of 6 – 7 h. The reaction progress was monitored by the gradual discoloration of the reaction mixture. After every hour of the reaction, a new portion (1 mL) of nickel catalyst was added to the mixture. After reduction completion, water (200 mL) was added to the colorless solution and the mixture was filtered while hot. The solvents were distilled off on a rotary evaporator giving the product as white powders (yield: 21.24 g, 95%). Single crystals suitable for an X-ray diffraction analysis were obtained in the form of colourless thin needles after recrystallization from hot water (32 g per 1 L) with charcoal. Elem. Anal. Calc. for $C_6H_8N_6$ (MW = 164.17 g·mol^{-1}): C, 43.89%; H, 4.91%; N, 51.20%. Found: C, 43.57%; H, 5.01%; N, 51.03%. ^{1}H-NMR(DMSO-d_6), ppm: 4.45 (4H, NH_2), 7.69 (2H, CH), 10.23 (1H, NH), 12.67 (1H, NH).

Synthesis of Zn(3,3'-L)·DMF: In a 50 mL reaction flask equipped with a reflux condenser, 3,3'-H_2L (0,164 g, 1 mmol) was dissolved in DMF (15 mL). After 10 min of stirring, zinc(II) acetate dihydrate $Zn(CH_3COO)_2{\cdot}2H_2O$ (0.220 g, 1 mmol) was added to this solution. The reaction mixture was kept under stirring at 393 K for 3 h and subsequently slowly cooled to room temperature. A white precipitate was obtained, filtered off, washed twice with DMF and dried under vacuum. Yield: 86%. Elem. anal. calc. for $C_9H_{13}N_7OZn$ (MW = 300.6 gmol^{-1}): C, 35.96; H, 4.36; N, 32.61%. Found: C, 35.79; H, 4.31; N, 32.55%. IR (n, cm^{-1}): 3388(w), 3322(w) [ν(N-H)], 3097–2926 [ν(C-$H_{aromatic}$) + $\nu(CH_{aliphatic})$], 1662(s) [ν(C=O)], 1615(m), 1526(m) [ν(C=C) + ν(C=N)], 1489(s), 1384(s), 1293(w), 1254(w), 1096(s), 979(s), 660(s), 636(m), 467(s).

Synthesis of Zn(3,5-L)·DMF: The same procedure described for **Zn(3,3'-L)·DMF** was applied for the synthesis of **Zn(3,5-L)·DMF**, using 3,5-H_2L instead of 3,3'-H_2L. Yield: 84%. Elem. anal. calc. for $C_9H_{13}N_7OZn$ (MW = 300.6 $gmol^{-1}$): C, 35.96; H, 4.36; N, 32.61%. Found: C, 36.11; H, 4.42; N, 32.57%. IR (n, cm^{-1}): 3324(w) [ν(N-H)], 3096–2927 [$\nu(CH_{aromatic})$ + $\nu(C\text{-}H_{aliphatic})$], 1662(s) [$\nu$(C=O)], 1615(s), 1514(s) [ν(C=C) + ν(C=N)], 1436(m), 1383(s), 1256(m), 1133(s), 1095(s), 1010(w), 954(s), 843(m), 754(m), 657(s).

Preparation of [epibromohydrin@Zn(3,3'-L)]: an activated (at 473 K, 10^{-6} torr, 12 h) sample of **Zn(3,3'-L)** (60 mg) was suspended in dry and degassed epibromohydrin (5 mL) under a nitrogen atmosphere in a Schlenk flask. The suspension was gently stirred and kept at 393 K for 24 h, to facilitate the epoxide diffusion into the MOF pores. After that time, the flask was brought back to ambient temperature, the solid was left to decant and the liquid supernatant removed. [epibromohydrin@**Zn(3,3'-L)**] was finally recovered in quantitative yield, washed with petroleum ether (3x10 mL) and dried under a nitrogen stream.

8.2.3. Single-Crystal X-Ray Diffraction Structure Determination

Single crystals of **(3-3'-H_2L)** suitable for an X-ray diffraction analysis were obtained after recrystallization from water [Figure 124]. X-ray diffraction data were collected at T = 173 K using a Stoe Image Plate Diffraction System instrument equipped with a sealed X-ray source [graphite-monochromated Mo Kα radiation (λ = 0.71073 Å)] and an Oxford Cryosystems Cryostream 700 Cooler. ϕ oscillation scans were performed with the following conditions: ϕ = 0 -> 185°; Δϕ = 1.1°; exposure time = 8 min per frame. The crystal structure was solved by direct methods and refined by full-matrix least-squares on F^2 using the programs SHELXS-97 and SHELXL-2014/7, respectively[203]. Anisotropic atomic displacement parameters were assigned to all carbon and nitrogen atoms. All the hydrogen atoms were located in difference Fourier maps and freely refined with isotropic atomic displacement parameters. 3,3'-diamino-4,4'-bipyrazole crystallizes in the monoclinic space group $P2_1/c$. The asymmetric unit contains half of a molecule, lying about an inversion center. Consequently, the anti-relative disposition of the two amino groups is the thermodynamically favored conformation in the free linker.

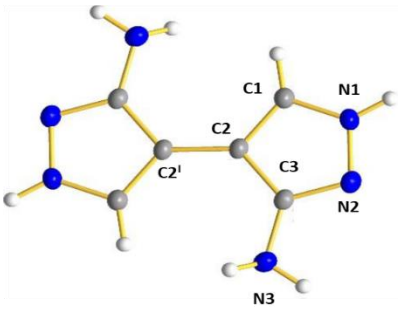

Figure 124: ORTEP drawing at 50% probability level of **3,3'-H_2L**. Color code: N – blue, C – grey, H – white.

Crystal data for 3,3'-diamino-4,4'-bipyrazole: $C_6H_8N_6$, FW = 164.18 g mol^{-1}, monoclinic, $P2_1/c$, a = 8.1992(10) Å, b = 4.5320(5) Å, c = 9.7004(12) Å, β = 108.777(10)°, V = 341.27(7) Å^3, Z = 2, ρ = 1.598 g cm^{-3}, F(000) = 172, *R1* = 0.036, w*R2* = 0.093 [I>2σ(I)] and *R1* = 0.046, w*R2* = 0.096 (all data) for 941 data and 72 parameters in the 5.2 – 59.1° (2θ) range.

8.2.4. PXRD Structure Determination

A powder sample (~50 mg) of **Zn(3,3'-L)·DMF** and [epibromohydrin@ **Zn(3,3'-L)**] were placed in the cavity of a silicon free background sample-holder 0.2 mm deep (Assing Srl, Monterotondo, Italy) and analyzed by means of PXRD with a Bruker AXS D8 Advance vertical-scan q:q diffractometer, provided with a sealed X-ray tube (Cu Kα, λ = 1.5418 Å), a Bruker Lynxeye linear position-sensitive detector, a filter of nickel in the diffracted beam and the following optical components: primary beam Soller slits (aperture = 2.5°), fixed divergence slit (aperture = 0.5°), anti-scatter slit (aperture = 8 mm). The generator was operated at 40 kV and 40 mA. After preliminary PXRD acquisitions to verify the samples purity and crystallinity as described above, data acquisitions for a deeper data treatment were performed in the 2θ range 5 – 105°, with steps of 0.02° and an overall scan time of about 12 hours. A standard peak search on the **Zn(3,3'-L)·DMF** PXRD pattern allowed for the estimation of the maximum positions of the first 20 low-to-medium angle peaks that were analyzed with the software TOPAS-R V3.0 through the Singular Value Decomposition algorithm[252], to retrieve the unit cell parameters. The space group was assigned based on the systematic absences. The space group and unit cell parameters were then confirmed by a whole powder pattern refinement carried out with TOPAS-R V3.0 employing the Le Bail method. Based on the space group and unit cell values, **Zn(3,3'-L)·DMF** is isostructural with Zn(BPZNO$_2$) (H_2BPZNO$_2$ = 3-nitro-4,4'-bipyrazole)[277], so that the crystal structure characterization was carried out only for [epibromohydrin@**Zn(3,3'-L)**]. The latter shares the

same space group and unit cell parameters of the parent **Zn(3,3'-L)** MOF. Hence, the structure refinement of the framework was achieved with TOPAS-R V3.0 applying the Rietveld method starting from the crystal structure of Zn(BPZNO$_2$). Then, the position and orientation of epibromohydrin were retrieved through the Simulated Annealing approach[207]. The crystallographically independent portion of the ligand and epibromohydrin were described through a rigid body built up using the z-matrix formalism, initially setting bond lengths and angles to average values. Bond lengths and angles for the rigid body describing the ligand: C – C and C – N of the pyrazole ring, 1.36 Å; exocyclic C – C and C – N, 1.40 Å; C – H and N – H, 0.95 Å; pyrazole ring internal and external bond angles, 108° and 126°, respectively; angles at the nitrogen atom of the amino group 120°. Bond lengths and angles for the rigid body describing epibromohydrin: C – C and C – O of the epoxide ring, 1.44 Å; exocyclic C – C, 1.50 Å; C – Br, 1.94 Å; C – H, 0.95 Å; epoxide ring internal bond angles, 60°; exocyclic O-C-H and O-C-C angles, 116°; angles around the sp^3 exocyclic carbon, 109.5°. The center of mass of the ligand was located on a 2/*m* symmetry element, an occurrence which implies that the two -NH$_2$ groups and the two hydrogen atoms share the four crystallographically equivalent positions (the four carbon atoms) with 50% probability each. The ligand orientation was allowed to vary along the crystallographic *c*-axis. During the final Rietveld refinement stages, pyrazole C-C and C-N bond lengths were refined in restrained ranges (1.34 – 1.38 Å), retrieved with a search in the Cambridge Structural Database (v. 2020) for room-temperature crystal structures containing the M(pyrazolate) (M = *3d* transition metal ion) moiety. The torsion angle among the two pyrazolate rings was free to refine, but no sensible variation from planarity or significant lowering of the figures of merit were observed, so that the ligand was eventually kept planar. The background curve was modelled using a polynomial function of the Chebyshev-type. An isotropic thermal factor [B_{iso}(M)] was refined for the metal ion, while for the ligand and epoxide atoms the isotropic thermal factor was calculated as B_{iso}(L) = B_{iso}(M) + 2.0 (Å^2). The peak profile was described using the Fundamental Parameters Approach[208]. The anisotropic peak broadening was described using second-order Lorentzian and fourth-order Gaussian spherical harmonics, modulating their contribution based on the reflections Miller indices. The final Rietveld refinement plot is reported in [Figure 125].

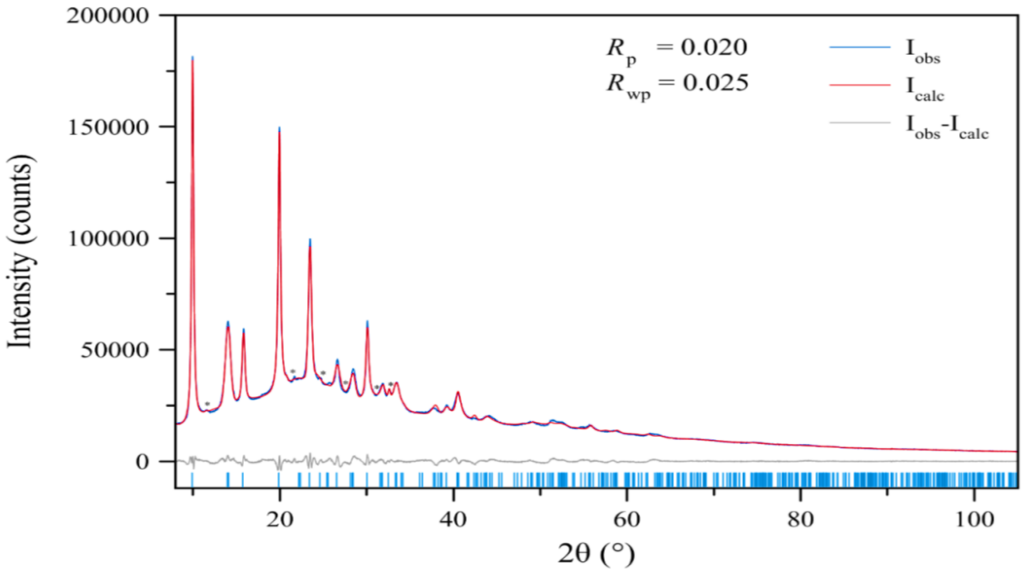

Figure 125: Graphical result of the final structure refinement conducted with the Rietveld method on the PXRD pattern of [epibromohydrin@**Zn(3,3'-L)**] in terms of experimental (blue), calculated (red) and difference (grey) traces. The blue markers at the bottom indicate the position of the Bragg reflections. Black asterisks indicate peaks belonging to impurities and the silicon sample-holder, respectively.

*Crystal data for [epibromohydrin@**Zn(3,3'-L)**]*, **Zn(3,3'-L)** 0.7 (C_3H_5OBr): $C_{8.1}H_{9.5}Br_{0.7}N_6O_{0.7}Zn$, MW = 323.4 gmol^{-1}, orthorhombic, *Cccm*, a = 12.566(2) Å, b = 12.681(2) Å, c = 7.2365(7) Å, V = 1153.2(3) Å^3, *Z* = 16, *Z'* = 4, *ρ* = 1.855 gcm^{-3}, *F*(000) = 629.2, R_{Bragg} = 0.007, R_p = 0.020 and R_{wp} = 0.025, for 4851 data and 76 parameters in the 8.0 – 105.0° (2θ) range.

8.2.5. Variable-Temperature PXRD Analysis

A variable-temperature PXRD experiment was carried out with the diffractometer described above on a ~20 mg sample of **Zn(3,3'-L)·DMF** heating in air with a custom-made sample heater (Officina Elettrotecnica di Tenno, Ponte Arche, Italy), in the temperature range 303 – 763 K with steps of 20 K. At each step, the data were acquired in isothermal conditions in the 2θ range 8.5 – 27.5°, with steps of 0.02° and a time per step of 1 s. The persistence of the room-temperature porous framework was assessed through whole powder pattern refinements performed with the Le Bail method, as implemented in TOPAS-R V3.0

8.2.6. Water Vapor Stability

After activation (at 423 K, 10^{-3} bar, 24 h) to remove the guest solvent and preliminary PXRD data acquisitions, ~10 mg samples of **Zn(3,3'-L)** and **Zn(3,5-L)**, left deposited on the PXRD aluminum sample-holders, were introduced into an air-tight cell saturated with moisture. Their behavior towards water vapor was monitored at given time intervals by measuring PXRD diffraction patterns with the same conditions applied for the preliminary acquisitions. All the acquired data were treated through a whole powder pattern refinement with the Le Bail method using the software TOPAS-R V3.0.

8.2.7. Gas Adsorption

Both MOFs (~40 mg) were activated at 473 K under high vacuum (10^{-6} torr) for 12h before each measurement. The BET specific surface area and porosity were estimated through volumetric N_2 adsorption at 77 K with an ASAP 2020 (Micromeritics) instrument. For the BET specific surface area calculation, the 0.01–0.1 p/p_0 pressure range of the isotherm was used for data fitting to satisfy all the Rouquerol consistency criteria[57]. The materials porosity was determined based on the BJH method (Halsey thickness equation) for the mesopores and with the Tarazona NLDFT—cylinder-like pore shape (typical of inorganic oxide materials) for the micropores. CO_2 and N_2 adsorption isotherms were also recorded at 273 K and 298 K at a maximum pressure of 1.2 bar. The isosteric heat of adsorption (Q_{st}) was calculated from the CO_2 isotherms measured at 273 K and 298 K according to a variant of the Clausius–Clapeyron equation:

$$ln\left(\frac{P_1}{P_2}\right) = Q_{st}\, x\, \frac{T_2 - T_1}{R\, x\, T_1\, x\, T_2}$$

where P_n (n = 1 or 2) is the pressure value for isotherm n; T_n (n = 1 or 2) is the temperature value for isotherm n; R is the gas constant.

The CO_2/N_2 selectivity at 298 K was calculated based on the Henry method as the ratio of the initial slopes of the adsorption isotherms. The IAST selectivity for an equimolar CO_2/N_2 mixture at a total pressure of 1 bar was determined as the ratio of the (adsorbed) molar fractions of the two gases[254] as derived from the application of the free software pyIAST to the experimental N_2

and CO_2 isotherms of **Zn(3,3'-L)** and **Zn(3,5-L)** collected at 298 K. A BET (CO_2) and a Henry (N_2) model were employed for the isotherms fitting, with root mean square deviations = 0.0040 (K_a = 4.40; K_b = 0.13; M = 4.12)/0.0013 (K_H = 0.602) and 0.0039 (K_a = 4.26; K_b = 0.13; M = 3.80)/0.0021 (K_H = 0.344) for **Zn(3,3'-L)** and **Zn(3,5-L)**, respectively.

8.2.8. Catalytic CO_2 Epoxidation

For a comparative analysis with Zn(BPZNH$_2$)[272], the reaction temperature and pressure was kept identical to the literature. The two MOF **Zn(3,3'-L)** and **Zn(3,5-L)** catalysts were activated at 473K under high-vacuum (10^{-6} torr) for 12 h before running the catalytic tests, keeping them under N_2 atmosphere after activation. The MOF catalyst (0.05 mmol, 11.4 mg) and the epoxide substrate (10 mmol, ca. 800 µL for epichlorohydrin, MW = 92.52 gmol^{-1} and ca. 860 µL for epibromohydrin, MW = 136.98 gmol^{-1}) were placed in a Teflon sample holder inside a stainless-steel reactor under an inert atmosphere. The reactor was then pressurized with 5 bar CO_2 and kept at 393 K for 24 h under stirring, in a closed system. The reagent in defect that limits the conversion was CO_2 (ca. 7 mmol against 10 mmol of epoxide), because of the reactor shape limitations. At the end of the reaction, the reactor was cooled in an ice/water bath and bis(2-chloroethyl) ether (10 mmol) was added to the mixture as internal standard. The as-obtained suspension was finally filtered over a Celite pad and analyzed by gas chromatography. For the recycling tests, after the first catalytic run the supernatant liquid was carefully removed under an inert atmosphere. The solid catalyst was washed with dry and degassed acetone (3x5 mL), and it was then dried under vacuum for 1 h to remove all volatile compounds before re-using it for further catalytic cycles. The amount of zinc leached in solution after catalysis was determined by Grafite Furnace Atomic Absorption Spectroscopy (GF-AAS) on a GBC 908AA instrument.

8.3. Results and Discussion

The new linker 3-3'-diamino-4-4'-bypirazole (**3,3'-H_2L**) was synthesized following the same procedure as the known analogue 3,5-diamino-4,4'-bypirazole (**3,5-H_2L**)[271] through a two stage reaction [Figure 126]. The first step involves the nitration of 4,4'-bypirazole, followed by the catalytic reduction of the intermediate 3,3'-dinitro-4,4'-bypirazole.

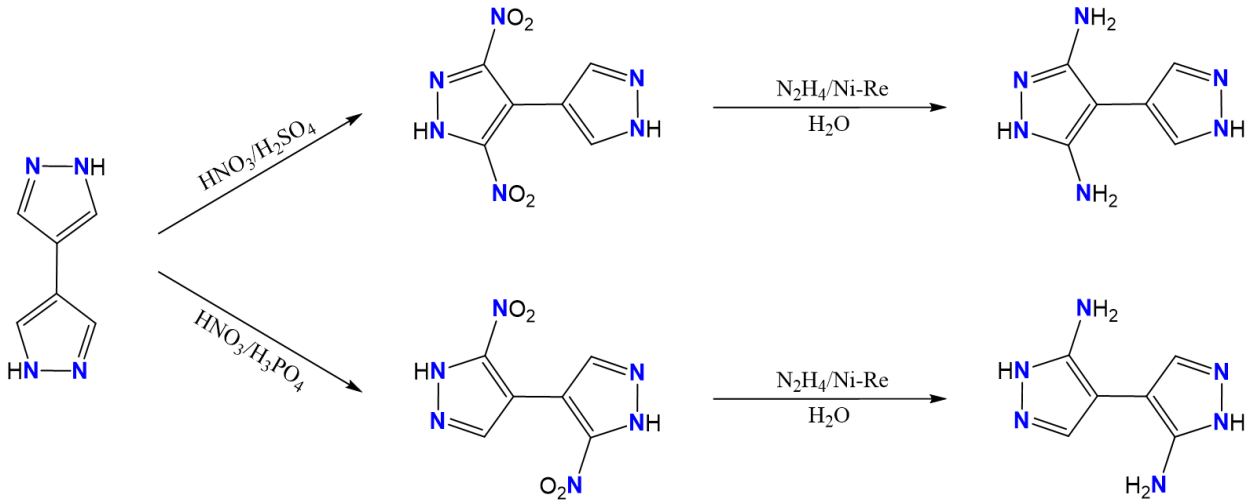

Figure 126: Schematic representation of **3,3'-H_2L** and **3,5-H_2L** synthesis.

Then, also the two relative MOFs **Zn(3-3'-L)·DMF** and **Zn(3-5-L)·DMF** where synthesized under solvothermal conditions making react the llinkers with zinc(II) acetate dihydrate.

The thermal behavior of **Zn(3,3'-L)·DMF** MOF was evaluated via thermal analysis (TGA, DTG, DTA) under N_2 flow [Figure 127]. The compound show a first weight loss of ~ 22.3% in the range 358 K < T < 583 K, ascribed to the loss of 0.85 moles of clathrated DMF per formula unit (calculated quantity = 22.6%). The decomposition temperature is around 773 K, a value that is almost the same of that of **Zn(3,5-L)** (726 K [271]). This result suggests that, despite their position on the linker skeleton, the two amino groups have a similar effect on the strength of the Zn – N bond. Moreover, the decomposition temperatures are slightly higher than those of their mono-amino parent Zn(BPZNH_2) (703 K [272]), confirming the beneficial effect of the -NH_2 group in the stability of the metal-pyrazolate bond.

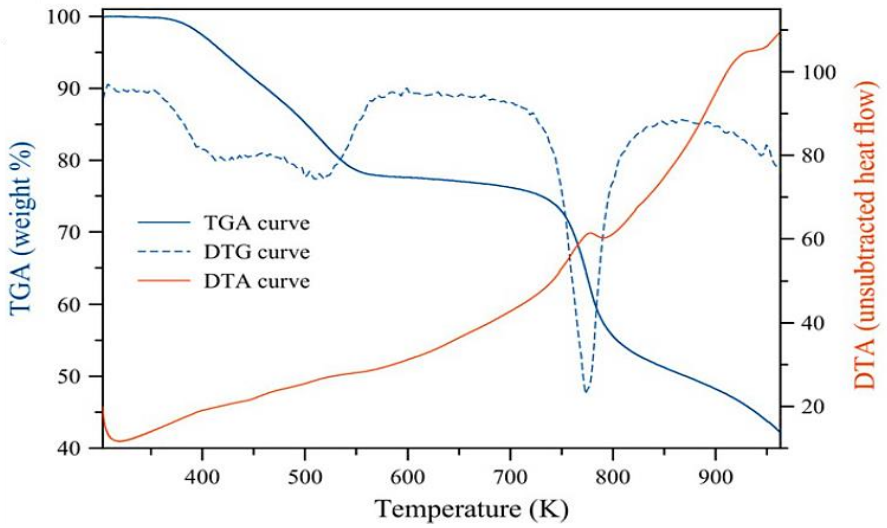

Figure 127: TGA (solid blue line), DTG (dotted blue line) and DTA (red line) profile of **Zn(3,3'-L)·DMF**.

In combination with the TGA analysis, the thermal behavior of **Zn(3,3'-L)·DMF** was also checked through VT-PXRD carried out in air [Figure 128]. This analysis has confirmed the high thermal stability of the MOF that maintains the same crystal structure at temperatures up to 763 K that is the highest temperature that it is possible to reach with the heating chamber.

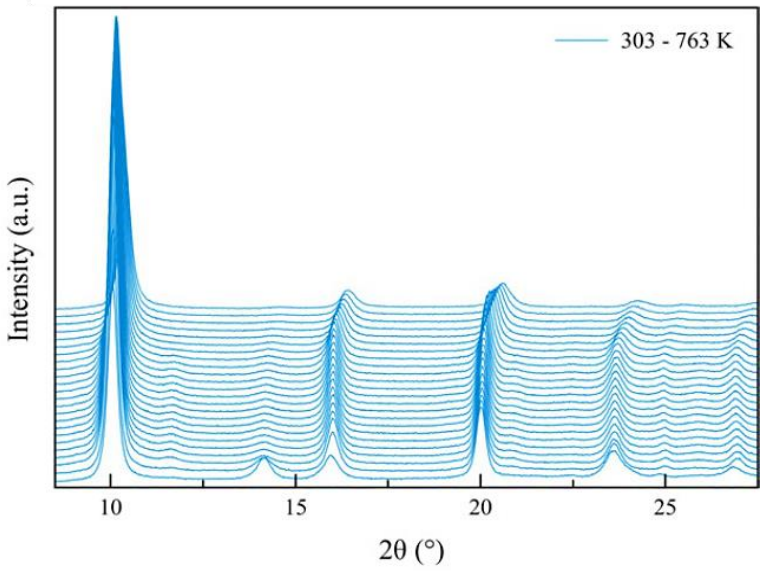

Figure 128: VT-PXRD diffraction pattern measured in air of **Zn(3,3'-L)·DMF** in the temperature range 303 – 763 K (with steps of 20 K).

The structure of **Zn(3,3'-L)·DMF** was assessed through the refinement of a whole PXRD pattern of the compound, adopting the Le Bail approach [Figure 129].

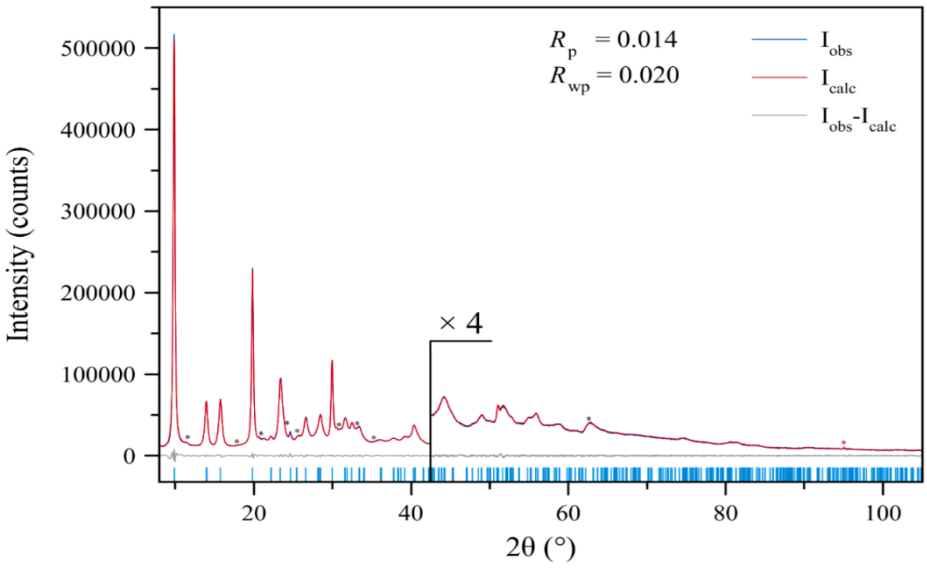

Figure 129: Graphical result of the final structure refinement conducted with the Rietveld method on the PXRD pattern of **Zn(3,3'-L)·DMF** in terms of experimental (blue), calculated (red) and difference (grey) traces. The blue markers at the bottom indicate the position of the Bragg reflections. Black and red asterisks indicate peaks belonging to impurities and the silicon sample-holder, respectively.

Zn(3,3'-L)·DMF crystallizes in the orthorhombic space group *Cccm* and has the same structural motif of the isomeric **Zn(3,5-L)·DMF** [271]. It features tetrahedral ZnN_4 nodes [Figure 130a] and *exo*-tetradentate linkers. A 3D (4,4)-connected network [Figure 130b] is formed with 1D square channels running along the [001] crystallographic direction [Figure 130c]

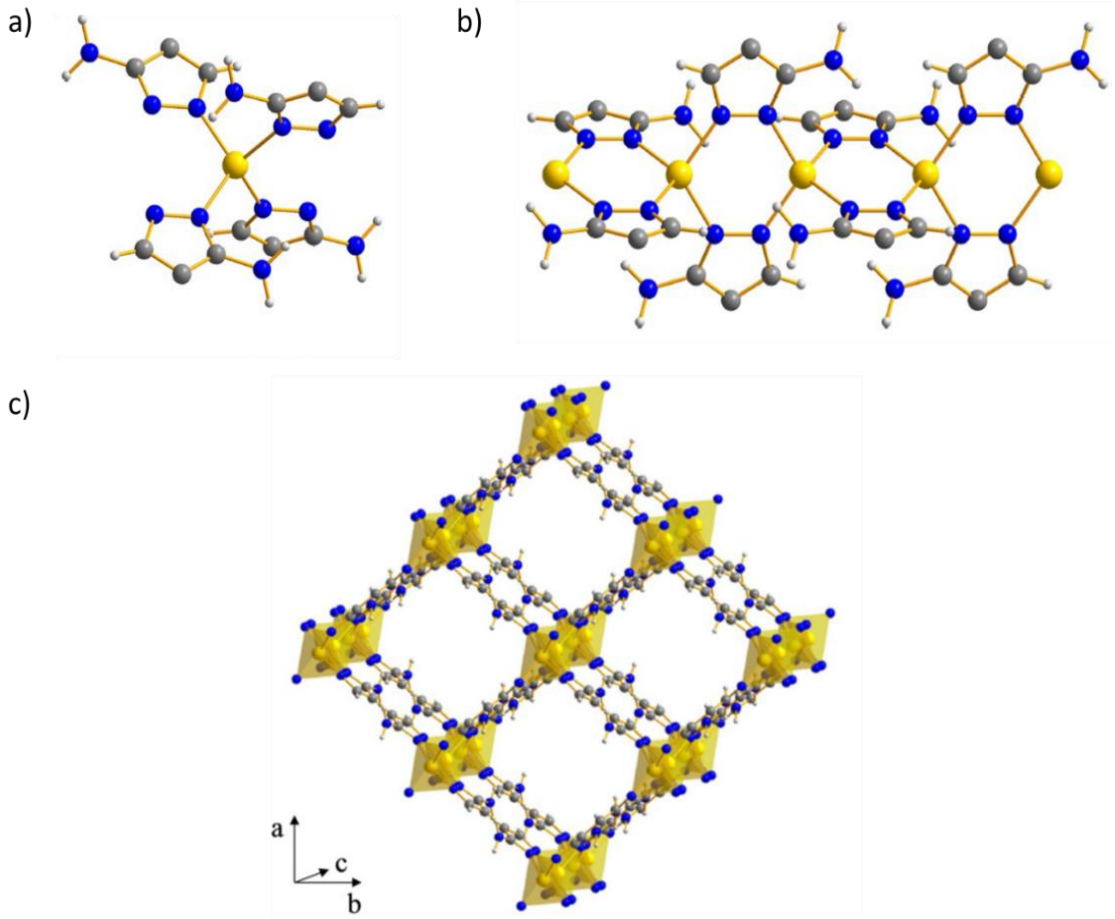

Figure 130: Representation of the crystal structure of **Zn(3,3'-L)**. The tetrahedral ZnN_4 node (a). The 1D chain running along the crystallographic c-axis (b). The packing, viewed in perspective along the crystallographic *c*-axis (c). Color code: Zn – yellow, Br – brown, N – blue, O – red, C – grey.

The texture and the porosity of both **Zn(3,3'-L)·DMF** and **Zn(3,5-L)·DMF** where then evaluated through volumetric N_2 adsorption at 77 K. Before the analysis, in accordance with the typical methodology, all samples were evacuated using a thermal treatment heating them at 303 K under high vacuum for 24 h. Both MOFs show an isotherm shape of type IV [Figure 131a] typical of micro-mesoporous materials. The calculated BET specific surface areas are very similar, with values of 463 $m^2\ g^{-1}$ for **Zn(3,3'-L)·DMF** and 504 $m^2\ g^{-1}$ for **Zn(3,5-L)·DMF**.

The total pore volume calculated at p/p_0 = 0.98 is equal to 0.53 $cm^3\ g^{-1}$ and 0.47 $cm^3\ g^{-1}$ for **Zn(3,3'-L)** and **Zn(3,5-L)**, respectively. The NLDFT micropores size (Tarazona model for cylindrical pores)[Figure 131b] is almost identical for both MOFs (1.3 nm *vs* 1.2 nm for **Zn(3,3'-L)** and

Zn(3,5-L), respectively). These values (~ 13 Å) are in line with the Zn – Zn distance found in the crystal structure between opposite vertices of the channels (13.2 Å). On the contrary, the mesopore size (estimated through BJH model) of the two MOFs is fairly different with values of 13 nm for **Zn(3,3'-L)** and of 34nm for **Zn(3,5-L).**

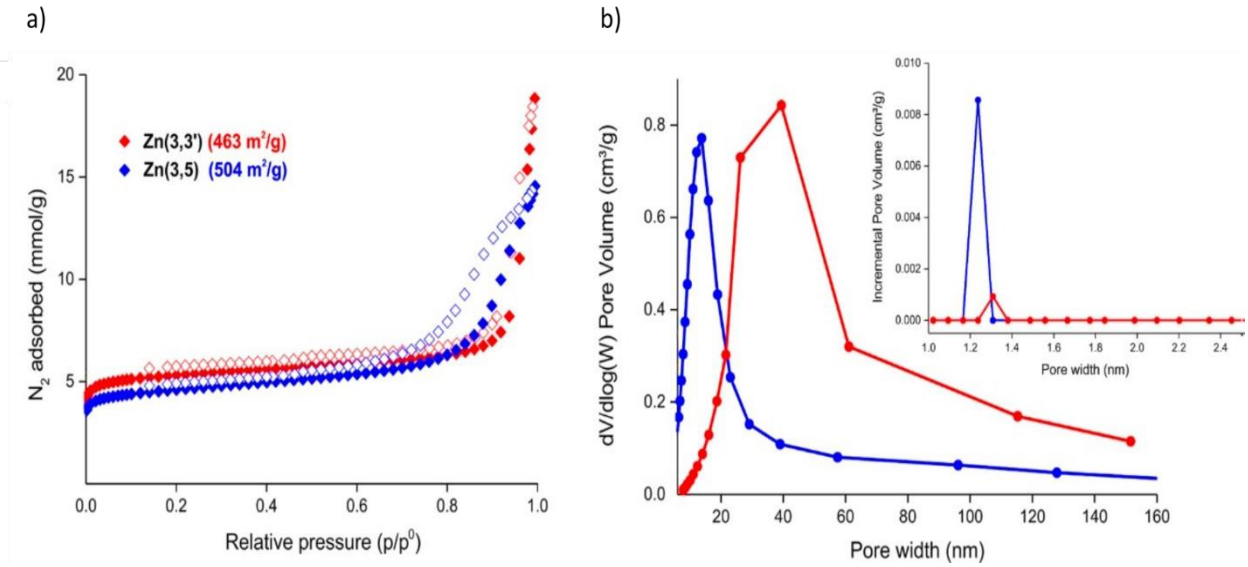

Figure 131: N_2 adsorption isotherms of **Zn(3,3'-L)** (full red diamonds) and **Zn(3,5-L)** (full blue diamonds) and desorption isotherms (empty diamonds) measured at 77 K (a). Mesopore size distribution plots, estimated by BJH model for **Zn(3,3'-L)** (red) and **Zn(3,5-L)** (blue) at comparison (b). Inset: micropore size distribution calculated with NLDFT Tarazona model for cylindrical pores, for **Zn(3,3'-L)** (red) and **Zn(3,5-L)** (blue) at comparison.

Then, the CO_2 adsorption isotherms of both MOFs were measured at the temperatures of 298 K and 273 K at p_{CO_2} = 1.2 bar [Figure 132]. **Zn(3,3'-L)** show a total gas uptake of 19.7 wt% (4.5 mmol g^{-1}) at 273 K, while **Zn(3,5-L)** adsorbs 19.3 wt% (4.4 mmol g^{-1}) of CO_2 under the same conditions. Both MOFs have very similar capacity and the values of gas adsorbed are comparable with that found for the "mono-amino" analogue Zn($BPZNH_2$) (H_2BPZNH_2 = 3-amino-4,4'-bipyrazole) of 21.0 wt% of CO_2 (4.8 mmol g^{-1})[272]. This result witnesses that, even if the presence of one amino group on the linker skeleton favor the adsorption of CO_2 (through non-covalent interactions between the -NH_2 dangling group and the CO_2) as already found out in literature[272], the introduction of two amino groups does not have beneficial effects in terms of CO_2 adsorption capacity. This behavior can be ascribed to the formation of N-H···N hydrogen bonds between amino groups that are in close proximity within the pores, suggesting that the interaction between the substituents prevails on that with the adsorbate. This result was already observed for **Zn(3,5-L)**[271]. The same trend can be found for the isosteric heat of adsorption that was calculated applying a variant of the Clausius-Clapeyron equation (see paragraph 8.2.7. – Gas

Adsorption). The Q_{st} values calculated are equal to 24.8 kJ mol^{-1} and 25.4 kJ mol^{-1} for **Zn(3,3'-L)** and **Zn(3,5-L)**, respectively, values that are higher than that of the untagged analogue Zn(BPZ) (H_2BPZ = 4,4'-bypirazole) that is equal to 23.7 kJ mol^{-1} [278], but lower than that of Zn($BPZNH_2$) (35.6 kJ mol^{-1})[272].

Taking into consideration the ratio of the initial slopes in the Henry region of both CO_2 and N_2 adsorption isotherms at 298 K, also the CO_2/N_2 selectivity was estimated. In this case, the presence of two amino groups is beneficial and the Henry selectivity values calculated are 20 and 32 for **Zn(3,3'-L)** and **Zn(3,5-L)**, respectively, values higher than that of Zn($BPZNH_2$) of 17[272]. This selectivity can be ascribed to the steric hindrance of the pores that hampers N_2 diffusion more than that of CO_2 because of the larger kinetic diameter of the former.

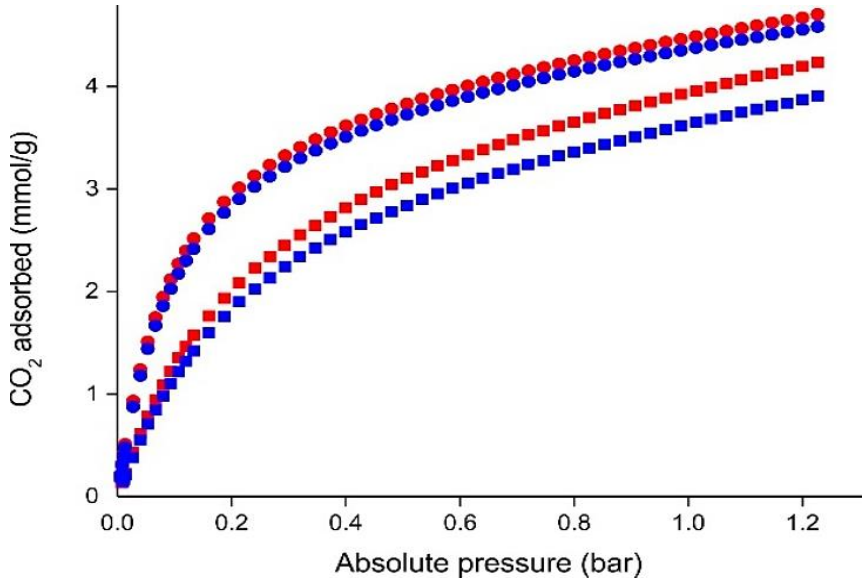

Figure 132: CO_2 adsorption isotherms measured at 298 K (squares) and 273 K (circles) of **Zn(3,3'-L)** (red symbols) and **Zn(3,5-L)** (blue symbols).

Then, before running the catalytic experiments, the stability of the two MOFs toward humidity was monitored through PXRD analysis [Figure 133]. In a water-vapor-saturated atmosphere, both the MOFs do not show nor variations in crystallinity or phase transitions for at least 120 days.

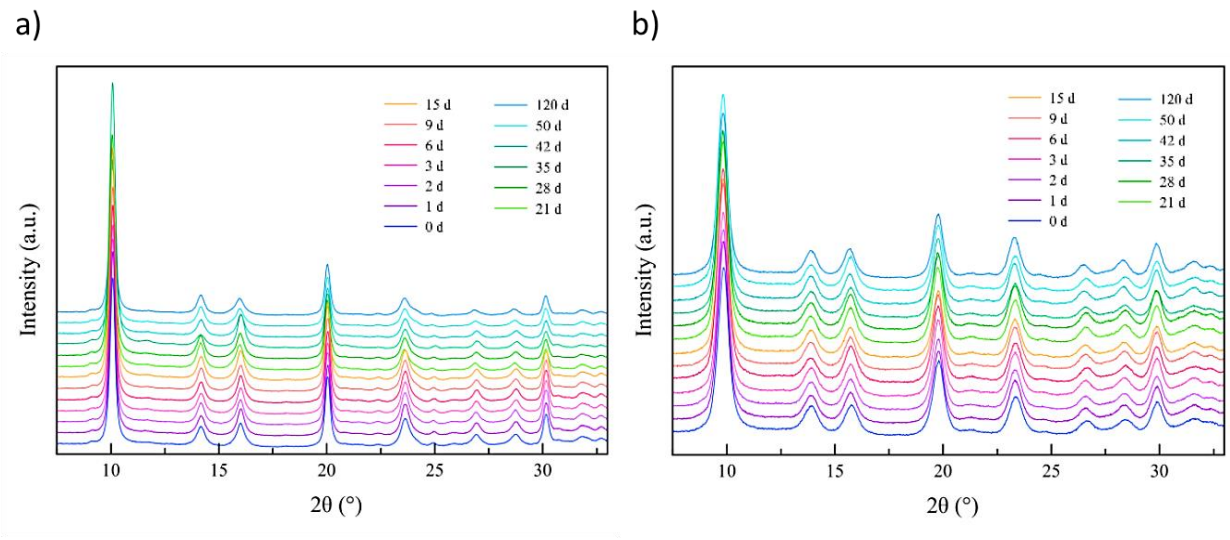

Figure 133: PXRD patterns acquired at certain time intervals on **Zn(3,3'-L)** (a) and **Zn(3,5-L)** (b) kept into a water-vapor saturated atmosphere for 120 days.

Finally, the (preactivated) MOFs have been tested as heterogeneous catalysts for the synthesis of cyclic carbonates via CO_2 addition to two halogenated epoxides (epichlorohydrin and epibromohydrin) [Figure 134]. The catalytic tests were performed following a previously reported procedure[272] under solvent-free conditions (the two liquid epoxides act as solvent) at 393 K, pressure of CO_2 = 5 bar and without the use of any other co-catalyst. For the reactions, 0.05 mmol of catalyst and 10 mmol of halogenated epoxides were used.

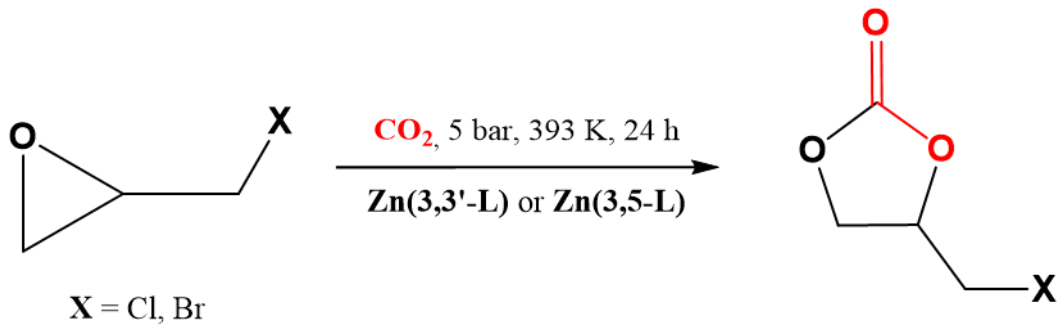

Figure 134: Schematic representation of the catalytic transformation of halogenated epoxides into the corresponding cyclic carbonates.

A proposal of the reaction mechanism to explain the interaction between the substrate and the reactants is provided in [Figure 135]. Initially, the epoxide coordinates to the Lewis acidic metal nodes, while the CO_2 is activated by the basic amino-groups of the linkers (the basicity of the amino group attached to a pyrazole ring is enhanced if compared with that of an amino group linked to a phenyl ring, as witnessed by the comparison of the pK_b values of 3-aminopyrazole (pK_b = 7.84) and aniline (pK_b = 9.37)) with the subsequent formation of a zwitterionic

carbamate[279]. The coordination to the metal site and the presence of an O-nucleophilic species on the carbamate moiety, triggers the epoxide ring opening. Then, an intramolecular addition-elimination reaction on the carbamate intermediate closes the cycle, generating the new cyclic carbonate product and regenerating the catalytically active sites.

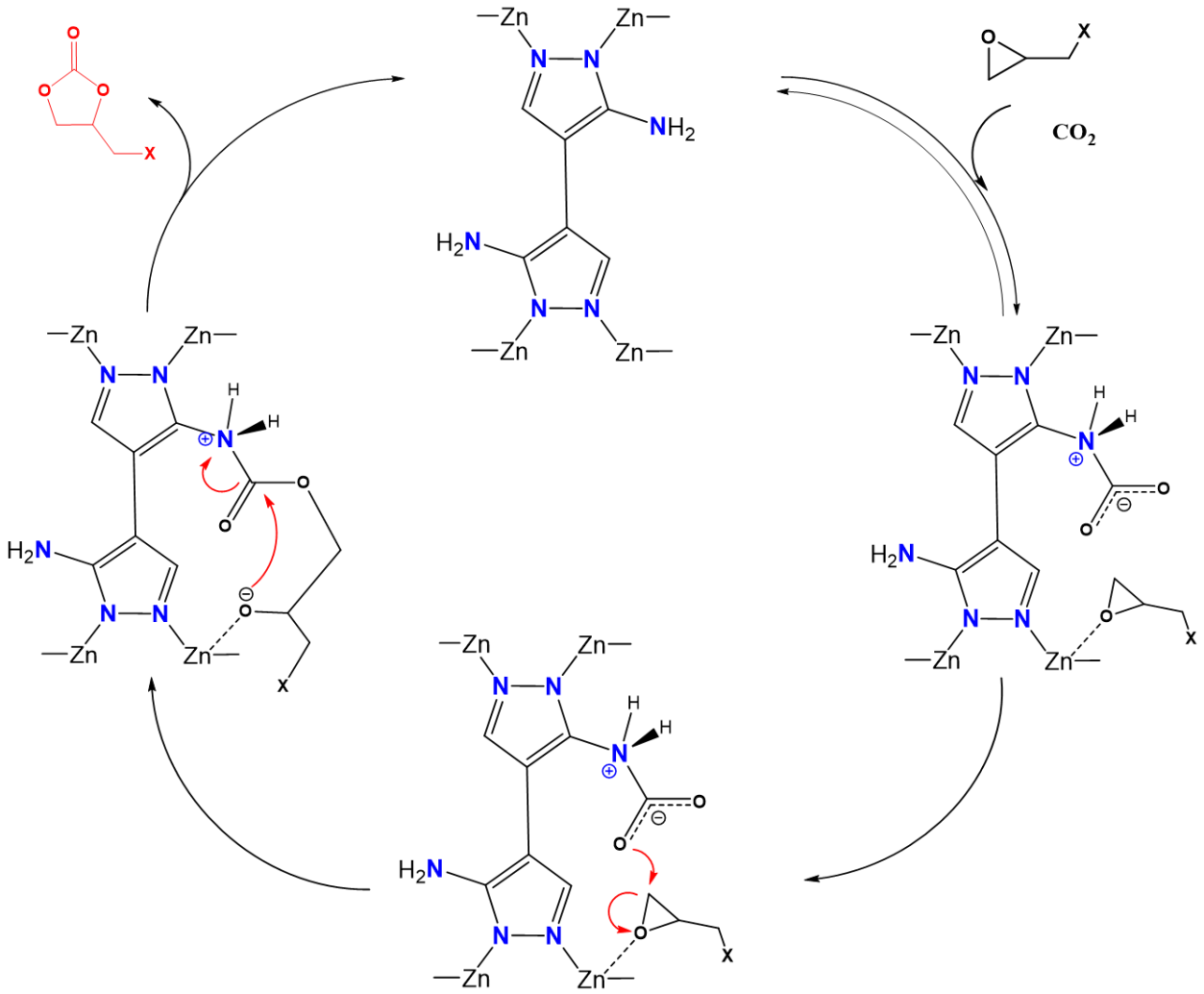

Figure 135: Schematic representation of the proposed reaction mechanism between epoxides and CO_2 catalyzed by **Zn(3,3'-L)**.

The results of the catalytic reactions are showed in [Table 5] where they are compared with that of Zn(BPZNH$_2$) found in literature[272].

Catalyst	X	Yield (%)	TOF[10]
Zn(3,3'-L)	Cl	49	4.0
Zn(3,5-L)	Cl	64	5.3
Zn(3,3'-L)	Br	41	3.4
Zn(3,5-L)	Br	49	4.0
Zn($BPZNH_2$)	Cl	32	2.6

Table 5: Summary of the catalytic results.

Based on the results, it seems clear that the presence of an additional amino group on the linker skeleton of **Zn(3,3'-L)** and **Zn(3,5-L)** is beneficial for the catalytic performance.

Considering only the two MOFs under study, **Zn(3,5-L)** show a better catalytic activity than **Zn(3,3'-L)** regardless of the epoxide used. This behavior may be ascribed considering the relative disposition of the amino groups in the MOF [Figure 136]. According to the reciprocal arrangements of the amino groups in the structure, hydrogen bonds with varying strength (d(N···N) ~ 2.5–3.2 Å) are formed between $NH_2\cdots NH_2$. Although the number of *syn*-oriented bipyrazolates in the actual structure is probably low (as the *anti*-conformation is more thermodynamically stable, as seen in the crystal structure of the bare linker **3,3'-H_2L** [Figure 124]), in the case **of Zn(3,3'-L)**, the possibility of a random occurrence of a *syn* conformation and subsequent *intramolecular* $NH_2\cdots NH_2$ hydrogen bonds cannot be ruled out, which would weaken the interaction between the amino groups and the reagents (the same *intramolecular* hydrogen bonds are not possible in the case of **Zn(3,5-L)**).

[10] TurnOver Frequency (TOF): number of catalytic reactions that occur per unit of time. It is a measure of the efficiency of a catalyst and is often used to compare the activity of different catalysts or to evaluate the performance of a single catalyst under different conditions. A higher TOF value indicates that the catalyst is converting more substrate into product per unit of time and is therefore more efficient.

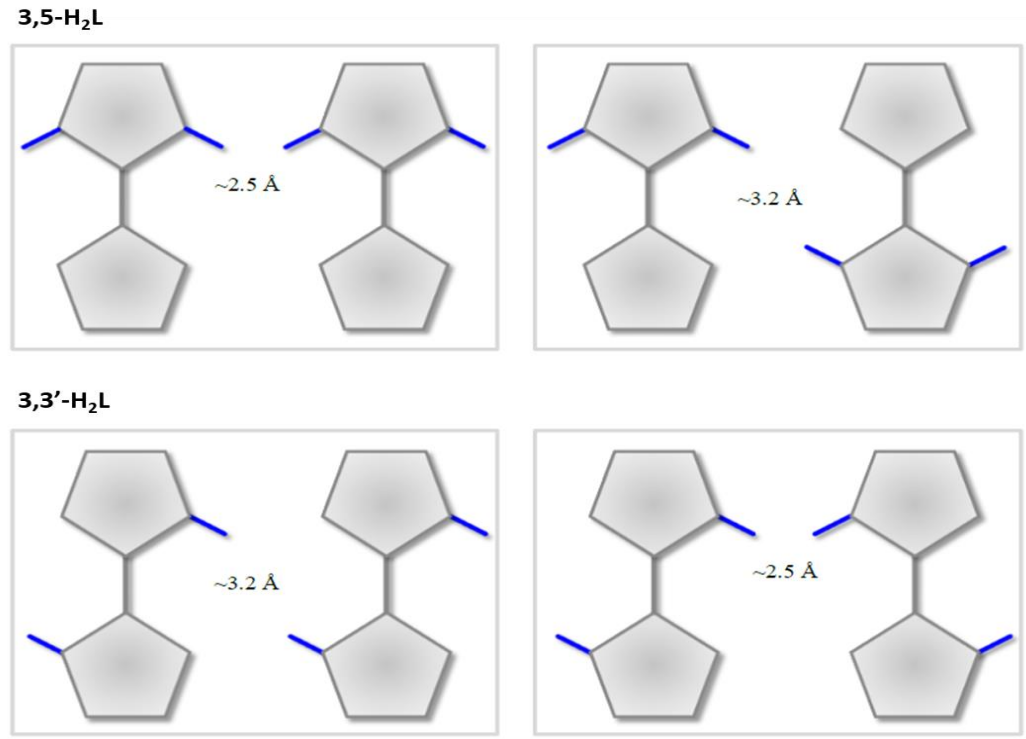

Figure 136: Pictorial representation of the reciprocal disposition of **3,5-H_2L** (top) and **3,3'-H_2L** (bottom) linkers in a hypothetical ordered domains in the crystal structure of the two MOFs.

The comparison between the conversion of epichlorohydrin and epibromohydrin reveals that, for the same catalyst, the conversion of the former is always higher than that of the latter. This can be ascribed to the higher chlorine electronegativity, its stronger hydrogen bonding interaction with the amino groups and its harder nature (with respect to bromine) towards the electrophilic sites (Zn(II)).

To further investigate the interaction between the halogenated epoxides and the MOFs, the structure of the [epibromohydrin@**Zn(3,3'-L)**] adduct (chosen as representative example) was resolved through PXRD analysis as described previously (see paragraph 8.2.4. – PXRD structure determination) [Figure 137]. The MOF with the adsorbed epoxides keeps the same structural motif of the **Zn(3,3'-L)** MOF (crystallizes in the orthorhombic space group *Cccm* and features tetrahedral ZnN_4 nodes and exo-tetradentate linkers [Figure 130]). Epibromohydrin molecules are hosted inside the 1D square channels running along the [001] crystallographic direction. N–H···Br and N–H···O nonbonding interactions between the amino groups and the guest epoxide molecules are present [*d*(N···Br) and *d*(N···O) = 3.03 Å and 3.02 Å, respectively]. In this model, which represents an ideal crystal structure, the epoxide does not interact with the metal sites. However, it is reasonable to expect that some degree of defective metal sites may be present in the actual sample (due to missing linkers), where the metal ions are linked to terminal acetate

anions or to -OH groups resulting from their basic hydrolysis, as has been observed in other Zn(II) MOFs in the literature[280]. These defects may serve as additional activation sites for the epoxide substrate. Further activation may also occur due to a temporary expansion of the Zn(II) coordination number from four to five or six during catalysis, leading to local distortion of the crystal structure, which would allow the epoxide O atom to be included within its coordination sphere. Five-[281] or six-coordinated[282] Zn(II) coordination compounds are well-known in the literature and are often associated with (pyr)azole linkers.

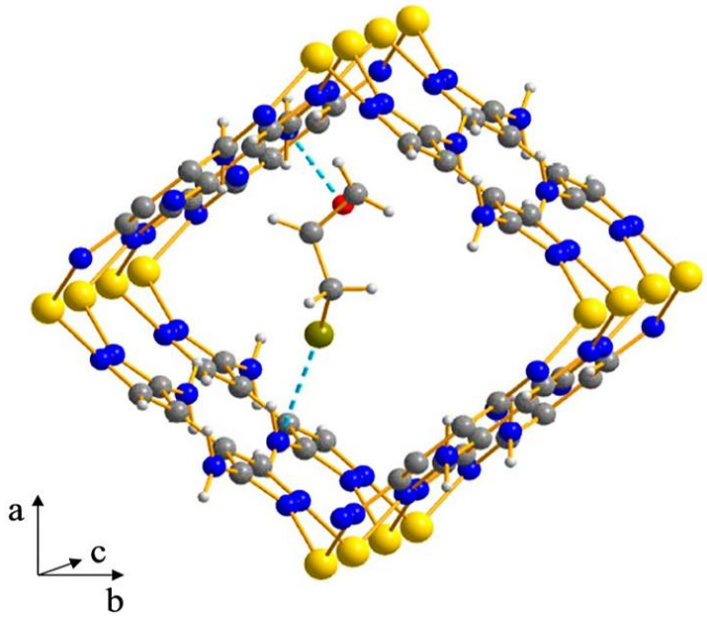

Figure 137: A guest molecule of epibromohydrin in the 1D channel of **Zn(3,3'-L)**. Color code: Zn – yellow, Br – brown, N – blue, O – red, C – grey. The N – H···Br and N – H···O interactions are depicted with cyan dashed lines.

Catalyst recovery and recycling experiments have been carried out with **Zn(3,3'-L)** in the carbonation of epibromohydrin. The recycling process is straightforwardly conducted through the complete removal of the supernatant at the conclusion of the first catalytic cycle and after centrifugation. The solid residue is subsequently washed with dry and de-gassed acetone, filtered, and dried at room temperature under a vacuum before running another catalytic experiment. It has been shown that the MOF retains its catalytic activity almost unchanged throughout three successive epoxidation cycles. If the epoxide conversion in the first run is normalized to 100%, the values for the second and third runs were found to be 92% and 90%, respectively. The slight decrease in catalytic activity for subsequent cycles can reasonably be attributed to a partial loss of the catalyst during the recycling process.

The amount of leached zinc was directly quantified via GF-AAS analysis after each catalytic cycle, and it was found to be negligible in all cases, with a maximum content of ~ 0.005% of leached Zn(II) ions detected in the most contaminated sample examined. Overall, these results confirm the truly heterogeneous nature of the process and the substantial stability of the catalyst throughout several catalytic cycles.

Another proof of the MOF's stability under the catalytic conditions applied is provided by the PXRD profile before and after catalysis [Figure 138]. As it is clearly visible, the PXRD profile of **Zn(3,3'-L)** (chosen as a representative example) remains almost unaltered after the catalytic reaction.

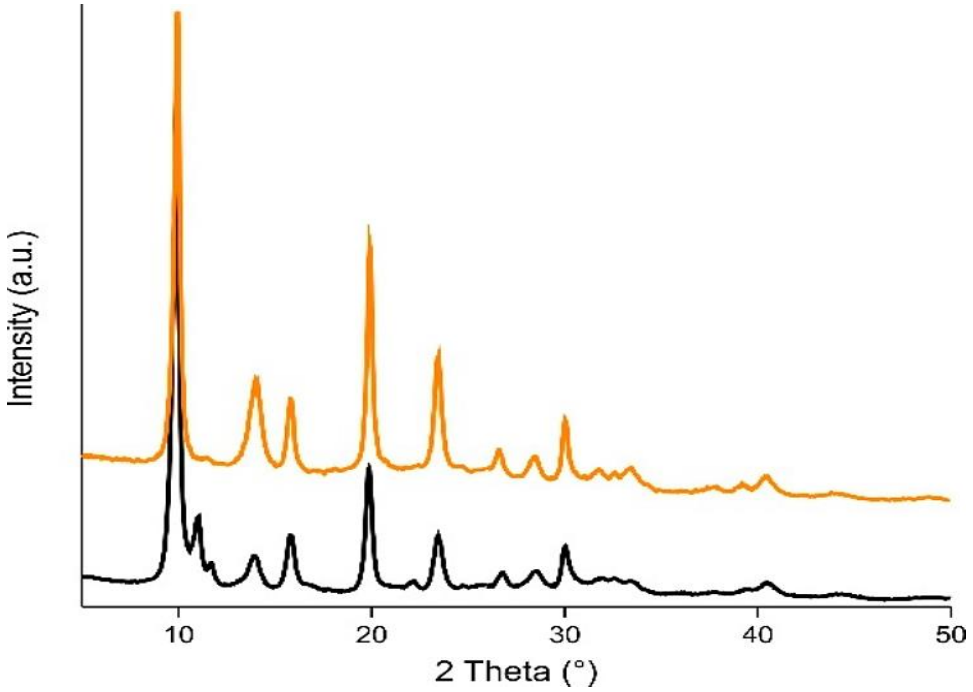

Figure 138: PXRD profiles of Zn(3,3'-L) collected before (black) and after (orange) the catalytic experiment.

8.4. Conclusions

In this work, the brand new 3-3'-diamino-4-4'-bipyrazole (**3,3'-H_2L**) linker and the corresponding Zn(II) MOF have been synthesized. This new MOF **Zn(3,3'-L)** is isostructural to the already known Zn(BPZNH_2)[272] and the analogue **Zn(3,5-L)**[271], and it has been tested as heterogeneous catalyst for the CO_2 cycloaddition to the two halogenated epoxides epichlorohydrin and epibromohydrin to produce the corresponding cyclic carbonates. From the obtained results, it is clear that the catalytic activity of the two amino-tagged bipyrazolate Zn(II) MOFs in CO_2 epoxidation has been

enhanced by the incorporation of two -NH_2 groups on the linker skeleton. The addition of a further amino group on the linker, is an approach based on the widely recognized and universally accepted reaction mechanism that involves a Lewis acid (CO_2) – Lewis base (-NH_2) interaction. Despite the CO_2 adsorption capacity is nearly equivalent to that of their mono(amino) parent Zn(BPZNH_2), the two isomeric bis(amino)-tagged bipyrazolate MOFs **Zn(3,3'-L)** and **Zn(3,5-L)** exhibit exceptional performance in the conversion of the halogenated epoxides epichlorohydrin and epibromohydrin into their respective cyclic carbonates under solvent-free and co-catalyst-free conditions. This results in a doubling of the maximum conversion to 64% compared to the 32% achieved with Zn(BPZNH_2). Structural evidence of the activation of epoxides by the MOF structure is provided by the crystal structure of the [epibromohydrin@**Zn(3,3'-L)**] adduct, in which nonbonding Br···(H) – N interactions have been identified.

Bibliography

1. Yaghi, O. M., Kalmutzki, M. J. & Diercks, C. S. 'Introduction to reticular chemistry: Metal-organic frameworks and covalent organic frameworks'. (Wiley Blackwell, 2019).
2. Yaghi, O. M. 'Reticular Chemistry in All Dimensions'. *ACS Cent Sci*. 5, 1295–1300 (**2019**).
3. Stahl, G. 'Experimenta, observationes, animadversiones'. *chymicae et physicae*. 300, 281–283 (**1731**).
4. Werner, A. 'Beitrag zur Konstitution anorganischer Verbindungen'. *Zeitschrift für anorganische Chemie*. 3, 267–330 (**1893**).
5. Hofmann, K. A. & Küspert, F. 'Verbindungen von Kohlenwasserstoffen mit Metallsalzen'. *Zeitschrift für anorganische Chemie*. 15, 204–207 (**1897**).
6. Rayner, J. H. & Powell, H. M. 'Structure of molecular compounds. Part X. Crystal structure of the compound of benzene with an ammonia–nickel cyanide complex'. *J. Chem. Soc.* 319–328 (**1952**).
7. Kinoshita Y., Matsubara I. & Saito Y. 'The Crystal Structure of Bis(succinonitrilo)copper(I) Nitrate'. *Bulletin of the Chemical Society of Japan*. 32, 741–747 (**1959**).
8. Wells, A. F. 'The geometrical basis of crystal chemistry. Part 1'. *Acta Crystallogr*. 7, 535–544 (**1954**).
9. Ockwig, N. W., Delgado-Friedrichs, O., O'keeffe, M. & Yaghi, O. M. 'Reticular Chemistry: Occurrence and Taxonomy of Nets and Grammar for the Design of Frameworks'. *Acc. Chem. Res.* 38, 176–182 (**2005**).
10. Yaghi, O. M., Li, G. & Li, H. 'Selective binding and removal of guests in a microporous metal–organic framework'. *Nature* . 378, 703–706 (**1995**).
11. Li, H., Eddaoudi, M., Groy, T. L. & Yaghi, O. M. 'Establishing Microporosity in Open Metal−Organic Frameworks: Gas Sorption Isotherms for Zn(BDC) (BDC = 1,4-Benzenedicarboxylate)'. *J Am Chem Soc*. 120, 8571–8572 (**1998**).
12. Lionelle, J. E. & Staffa, J. A. 'Metal oxycarboxylates and method of making same'. (**1984**).

13. Li, H., Eddaoudi, M., O'Keeffe, M. & Yaghi, O. M. 'Design and synthesis of an exceptionally stable and highly porous metal-organic framework'. *Nature*. 402, 276–279 (**1999**).
14. Ghadiri, M. R. *et al.* 'Hydrothermal Synthesis of a Metal-Organic Framework Containing Large Rectangular Channels'. *Angew. Chem., Int. Ed. Engl* vol. 117 (1995).
15. Batten, S. R., Champness, N. R., Chen, X. M., Garcia-Martinez, J., Kitagawa, S., Öhrström, L., O'Keeffe, M., Suh, M. P. & Reedijk, J. 'Terminology of metal-organic frameworks and coordination polymers (IUPAC recommendations 2013)'. *Pure and Applied Chemistry*. 85, 1715–1724 (**2013**).
16. Janiak, C. 'Engineering coordination polymers towards applications'. *Dalton Trans.* 2781–2804 (**2003**).
17. Yaghi, O. M., O'Keeffe, M., Ockwig, N. W., Chae, H. K., Eddaoudi, M. & Kim, J. 'Reticular synthesis and the design of new materials'. *Nature*. 423, 705–714 (**2003**).
18. Farha, O. K., Eryazici, I., Jeong, N. C., Hauser, B. G., Wilmer, C. E., Sarjeant, A. A., Snurr, R. Q., Nguyen, S. T., Yazaydin, A. Ö. & Hupp, J. T. 'Metal-organic framework materials with ultrahigh surface areas: Is the sky the limit?'. *J Am Chem Soc*. 134, 15016–15021 (**2012**).
19. Schoedel, A., Ji, Z. & Yaghi, O. M. 'The role of metal–organic frameworks in a carbon-neutral energy cycle'. *Nature Energy* . 1, 1–13 (**2016**).
20. Chae, H. K., Siberio-Pérez, D. Y., Kim, J., Go, Y. B., Eddaoudi, M., Matzger, A. J., O'Keeffe, M. & Yaghi, O. M. 'A route to high surface area, porosity and inclusion of large molecules in crystals'. *Nature* . 427, 523–527 (**2004**).
21. Eddaoudi, M., Kim, J., Rosi, N., Vodak, D., Wachter, J., O'Keeffe, M. & Yaghi, O. M. 'Systematic design of pore size and functionality in isoreticular MOFs and their application in methane storage'. *Science*. 295, 469–472 (**2002**).
22. Mercuri, G., Moroni, M., Galli, S., Tuci, G., Giambastiani, G., Yan, T., Liu, D. & Rossin, A. 'Temperature-Dependent Nitrous Oxide/Carbon Dioxide Preferential Adsorption in a Thiazolium-Functionalized NU-1000 Metal-Organic Framework'. *ACS Appl Mater Interfaces*. 13, 58982–58993 (**2021**).
23. Nowacka, A., Vismara, R., Mercuri, G., Moroni, M., Palomino, M., Domasevitch, K. V., di Nicola, C., Pettinari, C., Giambastiani, G., Llabrés I Xamena, F. X., Galli, S. & Rossin, A. 'Cobalt(II) Bipyrazolate Metal-Organic Frameworks as Heterogeneous

Catalysts in Cumene Aerobic Oxidation: A Tag-Dependent Selectivity'. *Inorg Chem*. 59, 8161–8172 (**2020**).

24. Mercuri, G., Moroni, M., Domasevitch, K. V., di Nicola, C., Campitelli, P., Pettinari, C., Giambastiani, G., Galli, S. & Rossin, A. 'Carbon Dioxide Capture and Utilization with Isomeric Forms of Bis(amino)-Tagged Zinc Bipyrazolate Metal-Organic Frameworks'. *Chemistry*. 27, 4746–4754 (**2021**).
25. Mercuri, G., Giambastiani, G. & Rossin, A. 'Thiazole- and Thiadiazole-Based Metal–Organic Frameworks and Coordination Polymers for Luminescent Applications'. *Inorganics (Basel)*. 7, (**2019**).
26. Mercuri, G., Moroni, M., Galli, S., Piccirillo, C., Capodilupo, A. L., Tuci, G., Giambastiani, G. & Rossin, A. 'UiO-67-derived bithiophene and bithiazole MIXMOFs for luminescence sensing and removal of contaminants of emerging concern in wastewater'. *Inorg Chem Front*. 9, 90–102 (**2021**).
27. Horcajada, P., Serre, C., Vallet-Regí, M., Sebban, M., Taulelle, F. & Férey, G. 'Metal-organic frameworks as efficient materials for drug delivery.' *Angewandte Chemie*. 45, 5974–5978 (**2006**).
28. Wang, L. J., Deng, H., Furukawa, H., Gándara, F., Cordova, K. E., Peri, D. & Yaghi, O. M. 'Synthesis and characterization of metal-organic framework-74 containing 2, 4, 6, 8, and 10 different metals'. *Inorg Chem*. 53, 5881–5883 (**2014**).
29. Brozek, C. K. & Dincă, M. 'Ti(3+)-, V(2+/3+)-, Cr(2+/3+)-, Mn(2+)-, and Fe(2+)-substituted MOF-5 and redox reactivity in Cr- and Fe-MOF-5'. *J Am Chem Soc*. 135, 12886–12891 (**2013**).
30. Sun, D., Sun, F., Deng, X. & Li, Z. 'Mixed-Metal Strategy on Metal-Organic Frameworks (MOFs) for Functionalities Expansion: Co Substitution Induces Aerobic Oxidation of Cyclohexene over Inactive Ni-MOF-74'. *Inorg Chem*. 54, 8639–8643 (**2015**).
31. Zhai, Q. G., Bu, X., Mao, C., Zhao, X. & Feng, P. 'Systematic and Dramatic Tuning on Gas Sorption Performance in Heterometallic Metal-Organic Frameworks'. *J Am Chem Soc*. 138, 2524–2527 (**2016**).
32. Cui, Y., Xu, H., Yue, Y., Guo, Z., Yu, J., Chen, Z., Gao, J., Yang, Y., Qian, G. & Chen, B. 'A luminescent mixed-lanthanide metal-organic framework thermometer'. *J Am Chem Soc*. 134, 3979–3982 (**2012**).

33. Koh, K., Wong-Foy, A. G. & Matzger, A. J. 'A crystalline mesoporous coordination copolymer with high microporosity'. *Angew Chem Int Ed Engl*. 47, 677–680 (**2008**).
34. Deng, H., Doonan, C. J., Furukawa, H., Ferreira, R. B., Towne, J., Knobler, C. B., Wang, B. & Yaghi, O. M. 'Multiple functional groups of varying ratios in metal-organic frameworks'. *Science*. 327, 846–850 (**2010**).
35. Dutta, A., Wong-Foy, A. G. & Matzger, A. J. 'Coordination copolymerization of three carboxylate linkers into a pillared layer framework'. *Chem Sci*. 5, 3729–3734 (**2014**).
36. Zhang, Y. B., Furukawa, H., Ko, N., Nie, W., Park, H. J., Okajima, S., Cordova, K. E., Deng, H., Kim, J. & Yaghi, O. M. 'Introduction of functionality, selection of topology, and enhancement of gas adsorption in multivariate metal-organic framework-177'. *J Am Chem Soc*. 137, 2641–2650 (**2015**).
37. Deria, P., Mondloch, J. E., Karagiaridi, O., Bury, W., Hupp, J. T. & Farha, O. K. 'Beyond post-synthesis modification: evolution of metal-organic frameworks via building block replacement'. *Chem Soc Rev*. 43, 5896–5912 (**2014**).
38. Karagiaridi, O., Bury, W., Mondloch, J. E., Hupp, J. T. & Farha, O. K. 'Solvent-assisted linker exchange: an alternative to the de novo synthesis of unattainable metal-organic frameworks'. *Angew Chem Int Ed Engl*. 53, 4530–4540 (**2014**).
39. Kim, M., Cahill, J. F., Fei, H., Prather, K. A. & Cohen, S. M. 'Postsynthetic ligand and cation exchange in robust metal-organic frameworks'. *J Am Chem Soc*. 134, 18082–18088 (**2012**).
40. Karagiaridi, O., Bury, W., Tylianakis, E., Sarjeant, A. A., Hupp, J. T. & Farha, O. K. 'Opening metal-organic frameworks Vol. 2: Inserting longer pillars into pillared-paddlewheel structures through solvent-assisted linker exchange'. *Chemistry of Materials*. 25, 3499–3503 (**2013**).
41. Kim, M., Cahill, J. F., Su, Y., Prather, K. A. & Cohen, S. M. 'Postsynthetic ligand exchange as a route to functionalization of "inert" metal–organic frameworks'. *Chem Sci*. 3, 126–130 (**2011**).
42. Luconi, L., Mercuri, G., Islamoglu, T., Fermi, A., Bergamini, G., Giambastiani, G. & Rossin, A. 'Benzothiazolium-functionalized NU-1000: a versatile material for carbon dioxide adsorption and cyanide luminescence sensing'. *J Mater Chem C Mater*. 8, 7492–7500 (**2020**).

43. Deria, P., Bury, W., Hod, I., Kung, C. W., Karagiaridi, O., Hupp, J. T. & Farha, O. K. 'MOF functionalization via solvent-assisted ligand incorporation: Phosphonates vs carboxylates'. *Inorg Chem*. 54, 2185–2192 (**2015**).

44. Deria, P., Mondloch, J. E., Tylianakis, E., Ghosh, P., Bury, W., Snurr, R. Q., Hupp, J. T. & Farha, O. K. 'Perfluoroalkane functionalization of NU-1000 via solvent-assisted ligand incorporation: Synthesis and CO_2 adsorption studies'. *J Am Chem Soc*. 135, 16801–16804 (**2013**).

45. Yuan, S., Lu, W., Chen, Y. P., Zhang, Q., Liu, T. F., Feng, D., Wang, X., Qin, J. & Zhou, H. C. 'Sequential linker installation: Precise placement of functional groups in multivariate metal-organic frameworks'. *J Am Chem Soc*. 137, 3177–3180 (**2015**).

46. Friedel, G. 'Nouveaux essais sur les zéolithes'. *Bulletin de Minéralogie*. 19, 363–390 (**1896**).

47. Schaeffer, W. D., Dorsey, W. S., Skinner, D. A. & Christian, C. G. 'Separation of Xylenes, Cymenes, Methylnaphthalenes and Other Isomers by Clathration with Inorganic Complexes'. *American Chemical Society*. 79, 5870–5876 (**1957**).

48. A Allison, B. S., Barrer, R. M., Schaeffer, W. D., Dorsey, W. S. & Skinner, D. A. 'Sorption in the β-phases of transition metal(II) tetra-(4-methylpyridine) thiocyanates and related compounds'. *Journal of the Chemical Society A: Inorganic, Physical, Theoretical* . 79, 1717–1723 (**1969**).

49. McNaught, A. & Wilkinson, A. 'Compendium of chemical terminology. IUPAC recommendations'. *undefined* (1997).

50. James W & McBain M A. 'The mechanism of the adsorption ("sorption") of hydrogen by carbon'. *The London, Edinburgh, and Dublin Philosophical Magazine and Journal of Science*. 18, 916–935 (**1909**).

51. Thommes, M., Kaneko, K., Neimark, A. v., Olivier, J. P., Rodriguez-Reinoso, F., Rouquerol, J. & Sing, K. S. W. 'Physisorption of gases, with special reference to the evaluation of surface area and pore size distribution (IUPAC Technical Report)'. *Pure and Applied Chemistry*. 87, 1051–1069 (**2015**).

52. Sing, K. S. W. & Williams, R. T. 'Physisorption Hysteresis Loops and the Characterization of Nanoporous Materials'. *Adsorption Science & Technology*. 22, 773–782 (**2016**).

53. Langmuir, I. 'The adsorption of gases on plane surfaces of glass, mica and platinum'. *J Am Chem Soc*. 40, 1361–1403 (**1918**).
54. Everett, D. H. 'The thermodynamics of adsorption. Part II.—Thermodynamics of monolayers on solids'. *Transactions of the Faraday Society*. 46, 942–957 (**1950**).
55. Brunauer, S., Emmett, P. H. & Teller, E. 'Adsorption of Gases in Multimolecular Layers'. *J Am Chem Soc*. 60, 309–319 (**1938**).
56. Thommes, M., Kaneko, K., Neimark, A. v., Olivier, J. P., Rodriguez-Reinoso, F., Rouquerol, J. & Sing, K. S. W. 'Physisorption of gases, with special reference to the evaluation of surface area and pore size distribution (IUPAC Technical Report)'. *Pure and Applied Chemistry*. 87, 1051–1069 (**2015**).
57. Gómez-Gualdrón, D. A., Moghadam, P. Z., Hupp, J. T., Farha, O. K. & Snurr, R. Q. 'Application of Consistency Criteria To Calculate BET Areas of Micro- And Mesoporous Metal-Organic Frameworks.' *J Am Chem Soc*. 138, 215–224 (**2016**).
58. Sircar, S. & Cao, D. v. 'Heat of Adsorption'. *Chem Eng Technol*. 25, 945–948 (**2002**).
59. Du, Z., Nie, X., Deng, S., Zhao, L., Li, S., Zhang, Y. & Zhao, J. 'Comparative analysis of calculation method of adsorption isosteric heat: Case study of CO_2 capture using MOFs'. *Microporous and Mesoporous Materials*. 298, 110053 (**2020**).
60. Farrusseng, D., Daniel, C., Gaudillère, C., Ravon, U., Schuurman, Y., Mirodatos, C., Dubbeldam, D., Frost, H. & Snurr, R. Q. 'Heats of adsorption for seven gases in three metal - Organic frameworks: Systematic comparison of experiment and simulation'. *Langmuir*. 25, 7383–7388 (**2009**).
61. Cimino, R. T., Kowalczyk, P., Ravikovitch, P. I. & Neimark, A. v. 'Determination of Isosteric Heat of Adsorption by Quenched Solid Density Functional Theory'. *Langmuir*. 33, 1769–1779 (**2017**).
62. Sarkisov, L. & Harrison, A. 'Computational structure characterisation tools in application to ordered and disordered porous materials'. *Mol Simul*. 37, 1248–1257 (**2011**).
63. Sing, K. 'The use of nitrogen adsorption for the characterisation of porous materials'. *Colloids Surf A Physicochem Eng Asp*. 187–188, 3–9 (**2001**).
64. Barrett, E. P., Joyner, L. G. & Halenda, P. P. 'The Determination of Pore Volume and Area Distributions in Porous Substances. I. Computations from Nitrogen Isotherms'. *J Am Chem Soc*. 73, 373–380 (**1951**).

65. Dollimore, D. & Heal, G. R. ‘An improved method for the calculation of pore size distribution from adsorption data’. *Journal of Applied Chemistry*. 14, 109–114 (**1964**).

66. Ravikovitch, P. I., Vishnyakov, A. & Neimark, A. V. ‘Density functional theories and molecular simulations of adsorption and phase transitions in nanopores’. *Phys Rev E*. 64, 011602 (**2001**).

67. Landers, J., Gor, G. Y. & Neimark, A. V. ‘Density functional theory methods for characterization of porous materials’. *Colloids Surf A Physicochem Eng Asp*. 437, 3–32 (**2013**).

68. Rowsell, J. L. C., Spencer, E. C., Eckert, J., Howard, J. A. K. & Yaghi, O. M. ‘Gas adsorption sites in a large-pore metal-organic framework’. *Science*. 309, 1350–1354 (**2005**).

69. Furukawa, H., Ko, N., Go, Y. B., Aratani, N., Choi, S. B., Choi, E., Yazaydin, A. Ö., Snurr, R. Q., O’Keeffe, M., Kim, J. & Yaghi, O. M. ‘Ultrahigh porosity in metal-organic frameworks’. *Science*. 329, 424–428 (**2010**).

70. Zhang, X., Chen, Z., Liu, X., Hanna, S. L., Wang, X., Taheri-Ledari, R., Maleki, A., Li, P. & Farha, O. K. ‘A historical overview of the activation and porosity of metal-organic frameworks’. *Chem. Soc. Rev*. 49, 7406 (**2020**).

71. Yaghi, O. M., O’Keeffe, M., Ockwig, N. W., Chae, H. K., Eddaoudi, M. & Kim, J. ‘Reticular synthesis and the design of new materials’. *Nature*. 423, 705–714 (**2003**).

72. Kalmutzki, M. J., Hanikel, N. & Yaghi, O. M. ‘Secondary building units as the turning point in the development of the reticular chemistry of MOFs’. *Sci Adv*. 4, (**2018**).

73. Tranchemontagne, D. J., Tranchemontagne, J. L., O’keeffe, M. & Yaghi, O. M. ‘Secondary building units, nets and bonding in the chemistry of metal-organic frameworks.’ *Chem Soc Rev*. 38, 1257–1283 (**2009**).

74. Lu, W., Wei, Z., Gu, Z. Y., Liu, T. F., Park, J., Park, J., Tian, J., Zhang, M., Zhang, Q., Gentle, T., Bosch, M. & Zhou, H. C. ‘Tuning the structure and function of metal–organic frameworks via linker design’. *Chem Soc Rev*. 43, 5561–5593 (**2014**).

75. Wu, Y. P., Wu, X. Q., Wang, J. F., Zhao, J., Dong, W. W., Li, D. S. & Zhang, Q. C. ‘Assembly of Two Novel Cd_3/(Cd_3 + Cd_5)-Cluster-Based Metal-Organic Frameworks: Structures, Luminescence, and Photocatalytic Degradation of Organic Dyes’. *Cryst Growth Des*. 16, 2309–2316 (**2016**).

76. Nadin, A. 'The Chemistry of Heterocycles. Structures, Reactions, Synthesis, and Applications.' *Angewandte Chemie International Edition*. 43, 3876–3877 (**2004**).

77. Olguín, J. & Brooker, S. 'Spin crossover active iron(II) complexes of selected pyrazole-pyridine/pyrazine ligands'. *Coord Chem Rev*. 255, 203–240 (**2011**).

78. Park, K. S., Ni, Z., Côté, A. P., Choi, J. Y., Huang, R., Uribe-Romo, F. J., Chae, H. K., O'Keeffe, M. & Yaghi, O. M. 'Exceptional chemical and thermal stability of zeolitic imidazolate frameworks'. *Proc Natl Acad Sci U S A*. 103, 10186–10191 (**2006**).

79. Biemmi, E., Christian, S., Stock, N. & Bein, T. 'High-throughput screening of synthesis parameters in the formation of the metal-organic frameworks MOF-5 and HKUST-1'. *Microporous and Mesoporous Materials*. 1–2, 111–117 (**2009**).

80. Lee, Y. R., Kim, J. & Ahn, W. S. 'Synthesis of metal-organic frameworks: A mini review'. *Korean Journal of Chemical Engineering* . 30, 1667–1680 (**2013**).

81. Bauer, S., Serre, C., Devic, T., Horcajada, P., Marrot, J., Férey, G. & Stock, N. 'High-throughput assisted rationalization of the formation of metal organic frameworks in the Iron(III) aminoterephthalate solvothermal system'. *Inorg Chem*. 47, 7568–7576 (**2008**).

82. Biswas, S., Grzywa, M., Nayek, H. P., Dehnen, S., Senkovska, I., Kaskel, S. & Volkmer, D. 'A cubic coordination framework constructed from benzobistriazolate ligands and zinc ions having selective gas sorption properties'. *Dalton Transactions*. 6487–6495 (**2009**).

83. Schaate, A., Roy, P., Godt, A., Lippke, J., Waltz, F., Wiebcke, M. & Behrens, P. 'Modulated Synthesis of Zr-Based Metal–Organic Frameworks: From Nano to Single Crystals'. *Chemistry – A European Journal*. 17, 6643–6651 (**2011**).

84. Vermoortele, F., Bueken, B., le Bars, G., van de Voorde, B., Vandichel, M., Houthoofd, K., Vimont, A., Daturi, M., Waroquier, M., van Speybroeck, V., Kirschhock, C. & de Vos, D. E. 'Synthesis modulation as a tool to increase the catalytic activity of metal-organic frameworks: The unique case of UiO-66(Zr)'. *J Am Chem Soc*. 135, 11465–11468 (**2013**).

85. Shearer, G. C., Chavan, S., Ethiraj, J., Vitillo, J. G., Svelle, S., Olsbye, U., Lamberti, C., Bordiga, S. & Lillerud, K. P. 'Tuned to perfection: Ironing out the defects in metal-organic framework UiO-66'. *Chemistry of Materials*. 26, 4068–4071 (**2014**).

86. Cliffe, M. J., Wan, W., Zou, X., Chater, P. A., Kleppe, A. K., Tucker, M. G., Wilhelm, H., Funnell, N. P., Coudert, F. X. & Goodwin, A. L. 'Correlated defect nanoregions in a metal–organic framework'. *Nature Communications* . 5, 1–8 (**2014**).

87. Taddei, M. 'When defects turn into virtues: The curious case of zirconium-based metal-organic frameworks'. *Coord Chem Rev*. 343, 1–24 (**2017**).

88. Tranchemontagne, D. J., Hunt, J. R. & Yaghi, O. M. 'Room temperature synthesis of metal-organic frameworks: MOF-5, MOF-74, MOF-177, MOF-199, and IRMOF-0'. *Tetrahedron*. 64, 8553–8557 (**2008**).

89. Rabenau, A. 'The Role of Hydrothermal Synthesis in Preparative Chemistry'. *Angewandte Chemie International Edition in English*. 24, 1026–1040 (**1985**).

90. Bian, Y., Xiong, N. & Zhu, G. 'Technology for the Remediation of Water Pollution: A Review on the Fabrication of Metal Organic Frameworks'. *Processes*. 6, 122 (**2018**).

91. Li, P., Cheng, F. F., Xiong, W. W. & Zhang, Q. 'New synthetic strategies to prepare metal–organic frameworks'. *Inorg Chem Front*. 5, 2693–2708 (**2018**).

92. Jones, W. & Eddleston, M. D. 'Introductory Lecture: Mechanochemistry, a versatile synthesis strategy for new materials'. *Faraday Discuss*. 170, 9–34 (**2014**).

93. Garay, A. L., Pichon, A. & James, S. L. 'Solvent-free synthesis of metal complexes'. *Chem Soc Rev*. 36, 846–855 (**2007**).

94. Braga, D., Giaffreda, S. L., Grepioni, F., Pettersen, A., Maini, L., Curzi, M. & Polito, M. 'Mechanochemical preparation of molecular and supramolecular organometallic materials and coordination networks'. *Dalton Transactions*. 60, 1249–1263 (**2006**).

95. Klimakow, M., Klobes, P., Thünemann, A. F., Rademann, K. & Emmerling, F. 'Mechanochemical synthesis of metal-organic frameworks: A fast and facile approach toward quantitative yields and high specific surface areas'. *Chemistry of Materials*. 22, 5216–5221 (**2010**).

96. Luche, J.-L., Bianchi M, Chanon P, Cintas E & Claudia L. 'Synthetic organic sonochemistry'. *plenum press - New York and London*. (**1998**).

97. Aslani, A. & Morsali, A. 'Sonochemical synthesis of nano-sized metal-organic lead(II) polymer: A precursor for the preparation of nano-structured lead(II) iodide and lead(II) oxide'. *Inorganica Chim Acta*. 362, 5012–5016 (**2009**).

98. Son, W. J., Kim, J., Kim, J. & Ahn, W. S. 'Sonochemical synthesis of MOF-5'. *Chemical Communications*. 0, 6336–6338 (**2008**).

99. Li, Z. Q., Qiu, L. G., Xu, T., Wu, Y., Wang, W., Wu, Z. Y. & Jiang, X. 'Ultrasonic synthesis of the microporous metal–organic framework $Cu_3(BTC)_2$ at ambient temperature and pressure: An efficient and environmentally friendly method'. *Mater Lett*. 1, 78–80 (**2009**).

100. Kappe, C. O., Dallinger, D. & Murphree, S. S. 'Practical Microwave Synthesis for Organic Chemists Strategies, Instruments, and Protocols'. (2008).

101. Klinowski, J., Almeida Paz, F. A., Silva, P. & Rocha, J. 'Microwave-Assisted Synthesis of Metal–Organic Frameworks'. *Dalton Transactions*. 40, 321–330 (**2010**).

102. Liu, H., Zhao, Y., Zhou, C., Mu, B. & Chen, L. 'Microwave-assisted synthesis of Zr-based metal–organic framework (Zr-fum-fcu-MOF) for gas adsorption separation'. *Chem Phys Lett*. 780, 138906 (**2021**).

103. Ni, Z. & Masel, R. I. 'Rapid production of metal-organic frameworks via microwave-assisted solvothermal synthesis'. *J Am Chem Soc*. 128, 12394–12395 (**2006**).

104. Seo, Y. K., Hundal, G., Jang, I. T., Hwang, Y. K., Jun, C. H. & Chang, J. S. 'Microwave synthesis of hybrid inorganic-organic materials including porous $Cu_3(BTC)_2$ from Cu(II)-trimesate mixture'. *Microporous and Mesoporous Materials*. 119, 331–337 (**2009**).

105. Suh, M. P., Park, H. J., Prasad, T. K. & Lim, D.-W. 'Hydrogen Storage in Metal-Organic Frameworks'. *Chem. Rev*. 112, 782–835 (**2012**).

106. Daglar, H. & Keskin, S. 'Recent advances, opportunities, and challenges in high-throughput computational screening of MOFs for gas separations'. *Coord Chem Rev*. 422, 213470 (**2020**).

107. Cui, Y., Zhu, F., Chen, B. & Qian, G. 'Metal-organic frameworks for luminescence thermometry'. *Chem. Commun*. 51, 7420 (**2015**).

108. Lee, J., Farha, O. K., Roberts, J., Scheidt, K. A., Nguyen, S. T. & Hupp, J. T. 'Metal–organic framework materials as catalysts'. *Chem. Soc. Rev.* 38, 1450–1459 (**2009**).

109. Horcajada, P., Serre, C., Maurin, G., Ramsahye, N. A., Balas, F., Vallet-Regí, M., Sebban, M., Taulelle, F. & Férey, G. 'Flexible Porous Metal-Organic Frameworks for a Controlled Drug Delivery'. *J Am Chem Soc*. 130, 6774–6780 (**2008**).

110. Tahmasebi, E., Masoomi, M. Y., Yamini, Y. & Morsali, A. 'Application of Mechanosynthesized Azine-Decorated Zinc(II) Metal− Organic Frameworks for

Highly Efficient Removal and Extraction of Some Heavy-Metal Ions from Aqueous Samples: A Comparative Study'. *Inorg. Chem*. 54, 3 (**2015**).

111. Li, H., Wang, K., Sun, Y., Lollar, C. T., Li, J. & Zhou, H. C. 'Recent advances in gas storage and separation using metal–organic frameworks'. *Materials Today*. 21, 108–121 (**2018**).
112. He, Y., Zhou, W., Qian, G. & Chen, B. 'Methane storage in metal–organic frameworks'. *Chem. Soc. Rev.* 43, 5657–5678 (**2014**).
113. Edenhofer, O., Sokona, Y., Minx, J. C., Farahani, E., Kadner, S., Seyboth, K., Adler, A., Baum, I., Brunner, S., Kriemann, B., Savolainen Web Manager Steffen Schlömer, J., von Stechow, C. & Zwickel Senior Scientist, T. 'Climate Change 2014 Mitigation of Climate Change'. (**2014**).
114. Yu, C. H., Huang, C. H. & Tan, C. S. 'A Review of CO_2 Capture by Absorption and Adsorption'. *Aerosol Air Qual Res*. 12, 745–769 (**2012**).
115. Stuart, H. R. 'Carbon capture and storage: how green can black be?' *Science*. 325, 1647–1652 (**2009**).
116. Simmons, J. M., Wu, H., Zhou, W. & Yildirim, T. 'Carbon capture in metal–organic frameworks—a comparative study'. *Energy Environ. Sci.* 4, 2177–2185 (**2011**).
117. Britt, D., Furukawa, H., Wang, B., Glover, T. G. & Yaghi, O. M. 'Highly efficient separation of carbon dioxide by a metal-organic framework replete with open metal sites'. *Proc Natl Acad Sci U S A*. 106, 20637–20640 (**2009**).
118. Liao, P. Q., Chen, H., Zhou, D. D., Liu, S. Y., He, C. T., Rui, Z., Ji, H., Zhang, J. P. & Chen, X. M. 'Monodentate hydroxide as a super strong yet reversible active site for CO_2 capture from high-humidity flue gas'. *Energy Environ. Sci.* 8, 1011–1016 (**2015**).
119. Vaidhyanathan, R., Iremonger, S. S., Dawson, K. W. & Shimizu, G. K. H. 'An amine-functionalized metal organic framework for preferential CO_2 adsorption at low pressures'. *Chem. Commun.* 5230–5232 (**2009**) doi:10.1039/B911481E.
120. T Nguyen, N. T., Furukawa, H., Gμndara, F., Nguyen, H. T., Cordova, K. E., Yaghi, O. M., Furukawa, H., Gμndara, F., Cordova, K. E. & Yaghi, O. M. 'Selective CO_2 Capture in ZIFs Hot Paper Selective Capture of Carbon Dioxide under Humid Conditions by Hydrophobic Chabazite-Type Zeolitic Imidazolate Frameworks'. *Angew. Chem. Int. Ed*. 53, 10645–10648 (**2014**).

121. Merel, J., Clausse, M. & Meunier, F. 'Experimental Investigation on CO_2 Post−Combustion Capture by Indirect Thermal Swing Adsorption Using 13X and 5A Zeolites'. *Ind Eng Chem Res*. 47, 209–215 (**2008**).

122. Ye, S., Jiang, X., Ruan, L.-W., Liu, B., Wang, Y.-M., Zhu, J. & Qiu, L.-G. 'Post-combustion CO_2 capture with the HKUST-1 and MIL-101(Cr) metal–organic frameworks: Adsorption, separation and regeneration investigations'. *Microporous and Mesoporous Materials*. 179, 191–197 (**2013**).

123. Serra-Crespo, P., Wezendonk, T. A., Bach-Samario, C., Sundar, N., Verouden, K., Zweemer, M., Gascon, J., van den Berg, H. & Kapteijn, F. 'Preliminary Design of a Vacuum Pressure Swing Adsorption Process for Natural Gas Upgrading Based on Amino-Functionalized MIL-53'. *Chem Eng Technol*. 38, 1183–1194 (**2015**).

124. Frost, H. & Snurr, R. Q. 'Design Requirements for Metal-Organic Frameworks as Hydrogen Storage Materials'. *The Journal of Physical Chemistry C*. 111, 18794–18803 (**2007**).

125. Dincă, M. & Long, J. R. 'Hydrogen Storage in Microporous Metal–Organic Frameworks with Exposed Metal Sites'. *Angewandte Chemie International Edition*. 47, 6766–6779 (**2008**).

126. He, Y., Zhou, W., Qian, G. & Chen, B. 'Methane storage in metal–organic frameworks'. *Chem. Soc. Rev.* 43, 5657–5678 (**2014**).

127. He, Y., Zhou, W., Yildirim, T. & Chen, B. 'A series of metal–organic frameworks with high methane uptake and an empirical equation for predicting methane storage capacity'. *Energy Environ. Sci.* 6, 2735–2744 (**2013**).

128. Wilmer, C. E., Farha, O. K., Yildirim, T., Eryazici, I., Krungleviciute, V., Sarjeant, A. A., Snurr, R. Q. & Hupp, J. T. 'Gram-scale, high-yield synthesis of a robust metal–organic framework for storing methane and other gases'. *Energy Environ. Sci.* 6, 1158–1163 (**2013**).

129. Karger, B. L., Snyder, L. R. & Horváth, C. 'An introduction to separation science'. (Wiley, 1973).

130. Blasse, G. & Grabmaier, B. C. 'A General Introduction to Luminescent Materials'. *Luminescent Materials*. 1–9 (**1994**).

131. San Sebastian, E., Rodríguez-Diéguez, A., Seco, J. M. & Cepeda, J. 'Coordination Polymers with Intriguing Photoluminescence Behavior: The Promising Avenue for Greatest Long-Lasting Phosphors'. *Eur J Inorg Chem*. 2018, 2155–2174 (**2018**).

132. Binnemans, K. 'Lanthanide-based luminescent hybrid materials'. *Chem Rev*. 109, 4283–4374 (**2009**).

133. Bauer, C. A., Timofeeva, T. v, Settersten, T. B., Patterson, B. D., Liu, V. H., Simmons, B. A. & Allendorf, M. D. 'Influence of Connectivity and Porosity on Ligand-Based Luminescence in Zinc Metal-Organic Frameworks'. *J Am Chem Soc*. 129, 7136–7144 (**2007**).

134. Li, X., Wang, X. W. & Zhang, Y. H. 'Blue photoluminescent 3D Zn(II) metal-organic framework constructing from pyridine-2,4,6-tricarboxylate'. *Inorg Chem Commun*. 11, 832–834 (**2008**).

135. Wei, Y., Yu, N. & Wu, K. 'Highly stable five-coordinated Mn(II) polymer [Mn(Hbidc)]n (Hbidc=1H-benzimidazole-5,6-dicarboxylate): Crystal structure, antiferromegnetic property, and strong long-lived luminescence'. *Cryst Growth Des*. 8, 2087–2089 (**2008**).

136. Wang, G. H., Li, Z. G., Jia, H. Q., Hu, N. H. & Xu, J. W. 'Metal–organic frameworks based on the pyridine-2,3-dicarboxylate and a flexible bispyridyl ligand: syntheses, structures, and photoluminescence'. *CrystEngComm*. 11, 292–297 (**2009**).

137. An, J., Geib, S. J. & Rosi, N. L. 'Cation-Triggered Drug Release from a Porous Zinc-Adeninate Metal-Organic Framework'. *J Am Chem Soc*. 131, 8376–8377 (**2009**).

138. An, J., Shade, C. M., Chengelis-Czegan, D. A., Petoud, S. & Rosi, N. L. 'Zinc-Adeninate Metal−Organic Framework for Aqueous Encapsulation and Sensitization of Near-infrared and Visible Emitting Lanthanide Cations'. *J Am Chem Soc*. 133, 1220–1223 (**2011**).

139. Hanaoka, K., Kikuchi, K., Kojima, H., Urano, Y. & Nagano, T. 'Development of a Zinc Ion-Selective Luminescent Lanthanide Chemosensor for Biological Applications'. *J Am Chem Soc*. 126, 12470–12476 (**2004**).

140. Chen, B., Wang, L., Zapata, F., Qian, G. & Lobkovsky, E. B. 'A luminescent microporous metal-organic framework for the recognition and sensing of anions'. *J Am Chem Soc*. 130, 6718–6719 (**2008**).

141. Takashima, Y., Martínez, V. M., Furukawa, S., Kondo, M., Shimomura, S., Uehara, H., Nakahama, M., Sugimoto, K. & Kitagawa, S. 'Molecular decoding using luminescence from an entangled porous framework'. *Nature Communications* . 2, 1–8 (**2011**).

142. Lan, A., Li, K., Wu, H., Olson, D. H., Emge, T. J., Ki, W., Hong, M. & Li, J. 'A luminescent microporous metal-organic framework for the fast and reversible detection of high explosives'. *Angew Chem Int Ed Engl*. 48, 2334–2338 (**2009**).

143. Harbuzaru, B. V., Corma, A., Rey, F., Jordá, J. L., Ananias, D., Carlos, L. D. & Rocha, J. 'A Miniaturized Linear pH Sensor Based on a Highly Photoluminescent Self-Assembled Europium(III) Metal–Organic Framework'. *Angewandte Chemie International Edition*. 48, 6476–6479 (**2009**).

144. Kwan Park, Y. *et al.* 'Crystal Structure and Guest Uptake of a Mesoporous Metal–Organic Framework Containing Cages of 3.9 and 4.7 nm in Diameter'. *Angewandte Chemie International Edition*. 46, 8230–8233 (**2007**).

145. Guo, H., Zhu, Y., Qiu, S., Lercher, A. J. & Zhang, H. 'Coordination Modulation Induced Synthesis of Nanoscale Eu1-xTbx-Metal-Organic Frameworks for Luminescent Thin Films'. *Advanced Materials*. 22, 4190–4192 (**2010**).

146. Chen, B., Yang, Y., Zapata, F., Qian, G., Luo, Y., Zhang, J. & Lobkovsky, E. B. 'Enhanced near-infrared-luminescence in an erbium tetrafluoroterephthalate framework'. *Inorg Chem*. 45, 8882–8886 (**2006**).

147. Davis, M. E. 'New Vistas in Zeolite and Molecular Sieve Catalysis'. *Acc. Chem. Res*. 26, 111–115 (**1993**).

148. Cohen, S. M. 'The Postsynthetic Renaissance in Porous Solids'. *J Am Chem Soc*. 139, 2855–2863 (**2017**).

149. Pascanu, V., González Miera, G., Inge, A. K. & Martín-Matute, B. 'Metal–Organic Frameworks as Catalysts for Organic Synthesis: A Critical Perspective'. *J Am Chem Soc*. 141, 7223–7234 (**2019**).

150. Tarnowicz-Ligus, S., Augustyniak, A. & Trzeciak, A. M. 'Incorporation of $PdCl_2P_2$ Complexes in Ni-MOF for Catalyzing Heck Arylation of Functionalized Olefins'. *Eur J Inorg Chem*. 2019, 4282–4288 (**2019**).

151. Bai, C., Jian, S., Yao, X. & Li, Y. 'Carbonylative Sonogashira coupling of terminal alkynes with aryl iodides under atmospheric pressure of CO using Pd(II)@MOF as the catalyst'. *Catal Sci Technol*. 4, 3261–3267 (**2014**).

152. Zhao, M., Yuan, K., Wang, Y., Li, G., Guo, J., Gu, L., Hu, W., Zhao, H. & Tang, Z. 'Metal–organic frameworks as selectivity regulators for hydrogenation reactions'. *Nature*. 539, 76–80 (**2016**).

153. Zhang, H., Liu, X., Wu, Y., Guan, C., Cheetham, A. K. & Wang, J. 'MOF-derived nanohybrids for electrocatalysis and energy storage: current status and perspectives'. *Chemical Communications*. 54, 5268–5288 (**2018**).

154. Sun, M., Yan, S., Sun, Y., Yang, X., Guo, Z., Du, J., Chen, D., Chen, P. & Xing, H. 'Enhancement of visible-light-driven CO_2 reduction performance using an amine-functionalized zirconium metal–organic framework'. *Dalton Transactions*. 47, 909–915 (**2018**).

155. Aresta, M., Dibenedetto, A. & Angelini, A. 'Catalysis for the valorization of exhaust carbon: From CO_2 to chemicals, materials, and fuels. technological use of CO_2'. *Chem Rev*. 114, 1709–1742 (**2014**).

156. Tombesi, A. & Pettinari, C. 'Metal Organic Frameworks as Heterogeneous Catalysts in Olefin Epoxidation and Carbon Dioxide Cycloaddition'. *Inorganics (Basel)*. 9, (**2021**).

157. Pettinari, C. & Tombesi, A. 'Metal–organic frameworks for chemical conversion of carbon dioxide'. *MRS Energy & Sustainability*. 7, E31 (**2020**).

158. He, Y., Zhang, W., Guo, T., Zhang, G., Qin, W., Zhang, L., Wang, C., Zhu, W., Yang, M., Hu, X., Singh, V., Wu, L., Gref, R. & Zhang, J. 'Drug nanoclusters formed in confined nano-cages of CD-MOF: dramatic enhancement of solubility and bioavailability of azilsartan'. *Acta Pharm Sin B*. 9, 97–106 (**2019**).

159. Wang, Z., Hu, S., Yang, J., Liang, A., Li, Y., Zhuang, Q., Gu, J., Wang, Z., Yang, J., Li, Y. S., Zhuang, Q. X., Gu, L., Hu, S. & Liang, A. 'Nanoscale Zr-Based MOFs with Tailorable Size and Introduced Mesopore for Protein Delivery'. *Adv Funct Mater*. 28, 1707356 (**2018**).

160. Zheng, H., Zhang, Y., Liu, L., Wan, W., Guo, P., Nyström, A. M. & Zou, X. 'One-pot Synthesis of Metal–Organic Frameworks with Encapsulated Target Molecules and

Their Applications for Controlled Drug Delivery'. *J Am Chem Soc*. 138, 962–968 (**2016**).

161. Javanbakht, S., Nezhad-Mokhtari, P., Shaabani, A., Arsalani, N. & Ghorbani, M. 'Incorporating Cu-based metal-organic framework/drug nanohybrids into gelatin microsphere for ibuprofen oral delivery'. *Mater Sci Eng C Mater Biol Appl*. 96, 302–309 (**2019**).
162. Cunha, D., Gaudin, C., Colinet, I., Horcajada, P., Maurin, G. & Serre, C. 'Rationalization of the entrapping of bioactive molecules into a series of functionalized porous zirconium terephthalate MOFs'. *J Mater Chem B*. 1, 1101–1108 (**2013**).
163. Kritskiy, I., Volkova, T., Surov, A. & Terekhova, I. 'γ-Cyclodextrin-metal organic frameworks as efficient microcontainers for encapsulation of leflunomide and acceleration of its transformation into teriflunomide'. *Carbohydr Polym*. 216, 224–230 (**2019**).
164. Li, X., Guo, T., Lachmanski, L., Manoli, F., Menendez-Miranda, M., Manet, I., Guo, Z., Wu, L., Zhang, J. & Gref, R. 'Cyclodextrin-based metal-organic frameworks particles as efficient carriers for lansoprazole: Study of morphology and chemical composition of individual particles'. *Int J Pharm*. 531, 424–432 (**2017**).
165. Jiang, K., Zhang, L., Hu, Q., Zhao, D., Xia, T., Lin, W., Yang, Y., Cui, Y., Yang, Y. & Qian, G. 'Pressure controlled drug release in a Zr-cluster-based MOF'. *J Mater Chem B*. 4, 6398–6401 (**2016**).
166. Cai, W., Wang, J., Chu, C., Chen, W., Wu, C., Liu, G., Cai, W., Chen, W., Wu, C., Wang, J., Chu, C. & Liu, G. 'Metal–Organic Framework-Based Stimuli-Responsive Systems for Drug Delivery'. *Advanced Science*. 6, 1801526 (**2019**).
167. United Nations General Assembly. 'Transforming our World: The 2030 Agenda for Sustainable Development'. (2015).
168. Alrumman, S. A., El-kott, Attalla F. & Keshk, S. M. 'Water Pollution: Source & Treatment'. *Am J Environ Engineer*. 6, 88–98 (**2016**).
169. US EPA. 'Drinking Water Regulations'. (2015).
170. Tchounwou, P. B., Yedjou, C. G., Patlolla, A. K. & Sutton, D. J. 'Heavy metal toxicity and the environment'. *Exp Suppl*. 101, 133–164 (**2012**).

171. Galal-Gorchev, H. 'Dietary intake, levels in food and estimated intake of lead, cadmium, and mercury'. *Food Addit Contam*. 10, 115–128 (**2009**).
172. Suffet, I. H. & Malaiyandi, M. 'Organic pollutants in water : sampling, analysis, and toxicity testing'. (American Chemical Society, 1987).
173. Cotruvo, J. A. '2017 WHO Guidelines for Drinking Water Quality: First Addendum to the Fourth Edition'. *American Water Works Association*. 109, 44–51 (**2017**).
174. Bolisetty, S. & Mezzenga, R. 'Amyloid–carbon hybrid membranes for universal water purification'. *Nature Nanotechnology 2016 11:4*. 11, 365–371 (**2016**).
175. Yang, Y., Zheng, Z., Yang, M., Chen, J., Li, C., Zhang, C. & Zhang, X. 'In-situ fabrication of a spherical-shaped Zn-Al hydrotalcite with BiOCl and study on its enhanced photocatalytic mechanism for perfluorooctanoic acid removal performed with a response surface methodology'. *J Hazard Mater*. 399, 123070 (**2020**).
176. Rey, A., Mena, E., Chávez, A. M., Beltrán, F. J. & Medina, F. 'Influence of structural properties on the activity of WO_3 catalysts for visible light photocatalytic ozonation'. *Chem Eng Sci*. 126, 80–90 (**2015**).
177. Tolkou, A. K., Mitrakas, M., Katsoyiannis, I. A., Ernst, M. & Zouboulis, A. I. 'Fluoride removal from water by composite Al/Fe/Si/Mg pre-polymerized coagulants: Characterization and application'. *Chemosphere*. 231, 528–537 (**2019**).
178. Bailey, S. E., Olin, T. J., Bricka, R. M. & Adrian, D. D. 'A review of potentially low-cost sorbents for heavy metals'. *Water Res*. 33, 2469–2479 (**1999**).
179. Gupta, V. K. & Saleh, T. A. 'Sorption of pollutants by porous carbon, carbon nanotubes and fullerene- An overview'. *Environmental Science and Pollution Research*. 20, 2828–2843 (**2013**).
180. Burtch, N. C., Jasuja, H. & Walton, K. S. 'Water stability and adsorption in metal-organic frameworks'. *Chem Rev*. 114, 10575–10612 (**2014**).
181. Bosch, M., Zhang, M. & Zhou, H.-C. 'Increasing the Stability of Metal-Organic Frameworks'. *Advances in Chemistry*. 2014, 1–8 (**2014**).
182. Wang, L., Zhao, X., Zhang, J. & Xiong, Z. 'Selective adsorption of Pb (II) over the zinc-based MOFs in aqueous solution-kinetics, isotherms, and the ion exchange mechanism'. *Environmental Science and Pollution Research*. 24, 14198–14206 (**2017**).

183. Luo, F., Chen, J. L., Dang, L. L., Zhou, W. N., Lin, H. L., Li, J. Q., Liu, S. J. & Luo, M. B. 'High-performance Hg^{2+} removal from ultra-low-concentration aqueous solution using both acylamide- and hydroxyl-functionalized metal–organic framework'. *J Mater Chem A Mater*. 3, 9616–9620 (**2015**).

184. Zhang, H., Lan, X., Bai, P. & Guo, X. 'Adsorptive removal of acetic acid from water with metal-organic frameworks'. *Chemical Engineering Research and Design*. 111, 127–137 (**2016**).

185. Wang, C., Liu, X., Chen, J. P. & Li, K. 'Superior removal of arsenic from water with zirconium metal-organic framework UiO-66'. *Scientific Reports* . 5, 1–10 (**2015**).

186. Bai, Z. Q., Yuan, L. Y., Zhu, L., Liu, Z. R., Chu, S. Q., Zheng, L. R., Zhang, J., Chai, Z. F. & Shi, W. Q. 'Introduction of amino groups into acid-resistant MOFs for enhanced U(VI) sorption'. *J Mater Chem A Mater*. 3, 525–534 (**2014**).

187. Wang, B., Lv, X. L., Feng, D., Xie, L. H., Zhang, J., Li, M., Xie, Y., Li, J. R. & Zhou, H. C. 'Highly Stable Zr(IV)-Based Metal-Organic Frameworks for the Detection and Removal of Antibiotics and Organic Explosives in Water'. *J Am Chem Soc*. 138, 6204–6216 (**2016**).

188. Jung, B. K., Jun, J. W., Hasan, Z. & Jhung, S. H. 'Adsorptive removal of p-arsanilic acid from water using mesoporous zeolitic imidazolate framework-8'. *Chemical Engineering Journal*. 267, 9–15 (**2015**).

189. Seo, Y. S., Khan, N. A. & Jhung, S. H. 'Adsorptive removal of methylchlorophenoxypropionic acid from water with a metal-organic framework'. *Chemical Engineering Journal*. 270, 22–27 (**2015**).

190. Meng, A. N., Chaihu, L. X., Chen, H. H. & Gu, Z. Y. 'Ultrahigh adsorption and singlet-oxygen mediated degradation for efficient synergetic removal of bisphenol A by a stable zirconium-porphyrin metal-organic framework'. *Sci Rep*. 7, 1–9 (**2017**).

191. He, Y. C., Yang, J., Kan, W. Q., Zhang, H. M., Liu, Y. Y. & Ma, J. F. 'A new microporous anionic metal–organic framework as a platform for highly selective adsorption and separation of organic dyes'. *J Mater Chem A Mater*. 3, 1675–1681 (**2014**).

192. Cavka, J. H., Jakobsen, S., Olsbye, U., Guillou, N., Lamberti, C., Bordiga, S. & Lillerud, K. P. 'A new zirconium inorganic building brick forming metal organic frameworks with exceptional stability'. *J Am Chem Soc*. 130, 13850–13851 (**2008**).

193. Yuan, S., Qin, J. S., Lollar, C. T. & Zhou, H. C. 'Stable Metal-Organic Frameworks with Group 4 Metals: Current Status and Trends'. *ACS Cent Sci*. 4, 440–450 (**2018**).

194. Hua, C. & D'Alessandro, D. M. 'Systematic tuning of Zn(II) frameworks with furan, thiophene, and selenophene dipyridyl and dicarboxylate ligands'. *Cryst Growth Des*. 17, 6262–6272 (**2017**).

195. Alghamdi, A. A. B., Watters, D. C., Yi, H., Al-Faifi, S., Almeataq, M. S., Coles, D., Kingsley, J., Lidzey, D. G. & Iraqi, A. 'Selenophene vs. thiophene in benzothiadiazole-based low energy gap donor–acceptor polymers for photovoltaic applications'. *J Mater Chem A Mater*. 1, 5165–5171 (**2013**).

196. Yoon, M. & Moon, D. 'New Zr (IV) based metal-organic framework comprising a sulfur-containing ligand: Enhancement of CO_2 and H_2 storage capacity'. *Microporous and Mesoporous Materials*. 215, 116–122 (**2015**).

197. Müller, P., Bucior, B., Tuci, G., Luconi, L., Getzschmann, J., Kaskel, S., Snurr, R. Q., Giambastiani, G. & Rossin, A. 'Computational screening, synthesis and testing of metal–organic frameworks with a bithiazole linker for carbon dioxide capture and its green conversion into cyclic carbonates'. *Mol Syst Des Eng*. 4, 1000–1013 (**2019**).

198. Wu, H., Chua, Y. S., Krungleviciute, V., Tyagi, M., Chen, P., Yildirim, T. & Zhou, W. 'Unusual and highly tunable missing-linker defects in zirconium metal-organic framework UiO-66 and their important effects on gas adsorption'. *J Am Chem Soc*. 135, 10525–10532 (**2013**).

199. Arcoria, A., Maccarone, E. & Mamo, A. 'Nucleophilic substitution in the side chain of five-membered heterocycles. Part 4. Reaction kinetics of selenophen compounds'. *Journal of the Chemical Society, Perkin Transactions 2*. 1347–1352 (**1979**).

200. Masui, K., Ikegami, H. & Mori, A. 'Palladium-Catalyzed C-H Homocoupling of Thiophenes: Facile Construction of Bithiophene Structure'. *J Am Chem Soc*. 126, 5074–5075 (**2004**).

201. Islamoglu, T., Goswami, S., Li, Z., Howarth, A. J., Farha, O. K. & Hupp, J. T. 'Postsynthetic Tuning of Metal-Organic Frameworks for Targeted Applications'. *Acc Chem Res*. 50, 805–813 (**2017**).

202. Burla, M. C., Caliandro, R., Carrozzini, B., Cascarano, G. L., Cuocci, C., Giacovazzo, C., Mallamo, M., Mazzone, A. & Polidori, G. 'Crystal structure determination and refinement via SIR2014'. *J Appl Crystallogr*. 48, 306–309 (**2015**).

203. Sheldrick, G. M. 'SHELXT – Integrated space-group and crystal-structure determination'. *Acta Crystallographica Section A*. 71, 3–8 (**2015**).

204. Nardelli, M. 'PARST95 – an update to PARST: a system of Fortran routines for calculating molecular structure parameters from the results of crystal structure analyses'. *Journal of Applied Crystallography*. 28, 659–659 (**1995**).

205. Farrugia, L. J. 'ORTEP-3 for Windows - a version of ORTEP-III with a Graphical User Interface (GUI)'. *J Appl Crystallogr*. 30, 565–565 (**1997**).

206. Øien, S., Wragg, D., Reinsch, H., Svelle, S., Bordiga, S., Lamberti, C. & Lillerud, K. P. 'Detailed structure analysis of atomic positions and defects in zirconium metal-organic frameworks'. *Cryst Growth Des*. 14, 5370–5372 (**2014**).

207. Coelho, A. A. 'Whole-profile structure solution from powder diffraction data using simulated annealing'. *J Appl Crystallogr*. 33, 899–908 (**2000**).

208. Cheary, R. W. & Coelho, A. 'A fundamental parameters approach to X-ray line-profile fitting'. *J Appl Crystallogr*. 25, 109–121 (**1992**).

209. de Mello, J. C., Wittmann, H. F. & Friend, R. H. 'An improved experimental determination of external photoluminescence quantum efficiency'. *Advanced Materials*. 9, 230–232 (**1997**).

210. Taddei, M., van Bokhoven, J. A. & Ranocchiari, M. 'Influence of Water in the Synthesis of the Zirconium-Based Metal-Organic Framework UiO-66: Isolation and Reactivity of $[ZrCl(OH)_2(DMF)_2]Cl$'. *Inorg Chem*. 59, 7860–7868 (**2020**).

211. Mak, T. C. W. 'Refinement of the crystal structure of zirconyl chloride octahydrate'. *Can J Chem*. 46, 3491–3497 (**1968**).

212. Earl, L. D., Patrick, B. O. & Wolf, M. O. 'Synthesis, structure, and magnetic properties of bithiophene- and terthiophene-linked manganese metal-organic frameworks'. *Inorg Chem*. 52, 10021–10030 (**2013**).

213. Li, J., Yuan, S., Qin, J. S., Huang, L., Bose, R., Pang, J., Zhang, P., Xiao, Z., Tan, K., Malko, A. v., Cagin, T. & Zhou, H. C. 'Fluorescence Enhancement in the Solid State by Isolating Perylene Fluorophores in Metal-Organic Frameworks'. *ACS Appl Mater Interfaces*. 12, 26727–26732 (**2020**).

214. Cornelio, J., Zhou, T. Y., Alkaş, A. & Telfer, S. G. 'Systematic Tuning of the Luminescence Output of Multicomponent Metal-Organic Frameworks'. *J Am Chem Soc*. 140, 15470–15476 (**2018**).

215. Holmes, R. J., Forrest, S. R., Sajoto, T., Tamayo, A., Djurovich, P. I., Thompson, M. E., Brooks, J., Tung, Y. J., D'Andrade, B. W., Weaver, M. S., Kwong, R. C. & Brown, J. J. 'Saturated deep blue organic electrophosphorescence using a fluorine-free emitter'. *Appl Phys Lett*. 87, 243507 (**2005**).

216. Newsome, W. J., Ayad, S., Cordova, J., Reinheimer, E. W., Campiglia, A. D., Harper, J. K., Hanson, K. & Uribe-Romo, F. J. 'Solid state multicolor emission in substitutional solid solutions of metal-organic frameworks'. *J Am Chem Soc*. 141, 11298–11303 (**2019**).

217. Patel, M., Kumar, R., Kishor, K., Mlsna, T., Pittman, C. U. & Mohan, D. 'Pharmaceuticals of emerging concern in aquatic systems: Chemistry, occurrence, effects, and removal methods'. *Chem Rev*. 119, 3510–3673 (**2019**).

218. Ternes, T. A. 'Occurrence of drugs in German sewage treatment plants and rivers'. *Water Res*. 32, 3245–3260 (**1998**).

219. Kümmerer, K. 'Antibiotics in the aquatic environment-a review, part I'. *Chemosphere*. 75, 417–434 (**2009**).

220. Senta, I., Kostanjevecki, P., Krizman-Matasic, I., Terzic, S. & Ahel, M. 'Occurrence and Behavior of Macrolide Antibiotics in Municipal Wastewater Treatment: Possible Importance of Metabolites, Synthesis Byproducts, and Transformation Products'. *Environ Sci Technol*. 53, 7463–7472 (**2019**).

221. Rojas, S. & Horcajada, P. 'Metal-Organic Frameworks for the Removal of Emerging Organic Contaminants in Water'. *Chem Rev*. 120, 8378–8415 (**2020**).

222. Bhasin, H. & Mishra, D. 'Metal Organic Frameworks: A Versatile Class of Hybrid Compounds for Luminescent Detection and Adsorptive Removal of Enviromental Hazards'. *Comments on Inorganic Chemistry*. 41, 267–315 (**2021**).

223. Wu, R., Bi, C., Zhang, D., Fan, C., Wang, L., Zhu, B., Liu, W., Li, N., Zhang, X. & Fan, Y. 'Highly selective, sensitive and stable three-dimensional luminescent metal–organic framework for detecting and removing of the antibiotic in aqueous solution'. *Microchemical Journal*. 159, 105349 (**2020**).

224. Mercuri, G., Moroni, M., Fermi, A., Bergamini, G., Galli, S., Giambastiani, G. & Rossin, A. 'Zirconium metal−organic frameworks containing a biselenophene linker: Synthesis, characterization, and luminescent properties'. *Inorg Chem*. 59, 15832–15841 (**2020**).

225. Katz, M. J., Brown, Z. J., Colón, Y. J., Siu, P. W., Scheidt, K. A., Snurr, R. Q., Hupp, J. T. & Farha, O. K. 'A facile synthesis of UiO-66, UiO-67 and their derivatives'. *Chemical Communications*. 49, 9449–9451 (**2013**).

226. Bail, A. le. 'Whole powder pattern decomposition methods and applications: A retrospection'. *Powder Diffr*. 20, 316–326 (**2005**).

227. R. A. Young. 'The Rietveld Method'. (Oxford University Press, 1981).

228. Zhong, W. bin, Li, R. X., Lv, J., He, T., Xu, M. M., Wang, B., Xie, L. H. & Li, J. R. 'Two isomeric In(III)-MOFs: unexpected stability difference and selective fluorescence detection of fluoroquinolone antibiotics in water'. *Inorg Chem Front*. 7, 1161–1171 (**2020**).

229. Yang, Z., Gu, Y., Yuan, B., Tian, Y., Shang, J., Tsang, D. C. W., Liu, M., Gan, L., Mao, S. & Li, L. 'Thio-groups decorated covalent triazine frameworks for selective mercury removal'. *J Hazard Mater*. 403, 123702 (**2021**).

230. Spek, A. L. 'Structure validation in chemical crystallography'. *Acta Crystallographica Section D*. 65, 148–155 (**2009**).

231. Prakash, P., Sayyed-Ahmad, A., Zhou, Y., Volk, D. E., Gorenstein, D. G., Dial, E., Lichtenberger, L. M. & Gorfe, A. A. 'Aggregation behavior of ibuprofen, cholic acid and dodecylphosphocholine micelles'. *Biochim Biophys Acta*. 1818, 3040–3047 (**2012**).

232. Tudja, P., Khan, M. Z. I., Meštrović, E., Horvat, M. & Golja, P. 'Thermal behaviour of diclofenac sodium: decomposition and melting characteristics'. *Chem Pharm Bull (Tokyo)*. 49, 1245–1250 (**2001**).

233. Yoshikawa, T., Oki, J., Ichikawa, N., Yamashita, S. & Sugano, K. 'Small differences in acidic pH condition significantly affect dissolution equivalence between drug products of acidic drug salt'. *J Drug Deliv Sci Technol*. 63, 102546 (**2021**).

234. Zind, H., Mondamert, L., Remaury, Q., Cleon, A., Leitner, N. & Labanowski, J. 'Occurrence of carbamazepine, diclofenac, and their related metabolites and

transformation products in a French aquatic environment and preliminary risk assessment'. *Water Res*. 196, 117052 (**2021**).

235. Prasetya, N. & Li, K. 'MOF-808 and its hollow fibre adsorbents for efficient diclofenac removal'. *Chemical Engineering Journal*. 417, 129216 (**2021**).
236. Gil, A., Santamaría, L. & Korili, S. A. 'Removal of Caffeine and Diclofenac from Aqueous Solution by Adsorption on Multiwalled Carbon Nanotubes'. *Colloid Interface Sci Commun*. 22, 25–28 (**2018**).
237. Hasan, Z., Khan, N. A. & Jhung, S. H. 'Adsorptive removal of diclofenac sodium from water with Zr-based metal–organic frameworks'. *Chemical Engineering Journal*. 284, 1406–1413 (**2016**).
238. Tuci, G., Rossin, A., Xu, X., Ranocchiari, M., van Bokhoven, J. A., Luconi, L., Manet, I., Melucci, M. & Giambastiani, G. '"click" on MOFs: A versatile tool for the multimodal derivatization of N_3-decorated metal organic frameworks'. *Chemistry of Materials*. 25, 2297–2308 (**2013**).
239. Islamoglu, T., Otake, K. I., Li, P., Buru, C. T., Peters, A. W., Akpinar, I., Garibay, S. J. & Farha, O. K. 'Revisiting the structural homogeneity of NU-1000, a Zr-based metal–organic framework'. *CrystEngComm*. 20, 5913–5918 (**2018**).
240. Deria, P., Bury, W., Hupp, J. T. & Farha, O. K. 'Versatile functionalization of the NU-1000 platform by solvent-assisted ligand incorporation'. *Chemical Communications*. 50, 1965–1968 (**2014**).
241. Zhu, X., Tian, C., Veith, G. M., Abney, C. W., Dehaudt, J. & Dai, S. 'In Situ Doping Strategy for the Preparation of Conjugated Triazine Frameworks Displaying Efficient CO_2 Capture Performance'. *J Am Chem Soc*. 138, 11497–11500 (**2016**).
242. Yamaguchi, S., Yoshikawa, I., Mutai, T. & Araki, K. 'Solid-state luminescence of tetraphenylpyrene derivatives: mechano/vapochromic luminescence of 1,3,6,8-tetra(4'-carboxyphenyl)pyrene'. *J Mater Chem*. 22, 20065–20070 (**2012**).
243. Dolgopolova, E. A., Rice, A. M., Martin, C. R. & Shustova, N. B. 'Photochemistry and photophysics of MOFs: steps towards MOF-based sensing enhancements'. *Chem Soc Rev*. 47, 4710–4728 (**2018**).
244. Boughton, J. H. & Keller, R. N. 'Dissociation constants of hydropseudohalic acids'. *Journal of Inorganic and Nuclear Chemistry*. 28, 2851–2859 (**1966**).

245. Das, A. & Biswas, S. ‘A multi-responsive carbazole-functionalized Zr(IV)-based metal-organic framework for selective sensing of Fe(III), cyanide and p-nitrophenol’. *Sens Actuators B Chem*. 250, 121–131 (**2017**).

246. Karmakar, A., Kumar, N., Samanta, P., Desai, A. v. & Ghosh, S. K. ‘A Post-Synthetically Modified MOF for Selective and Sensitive Aqueous-Phase Detection of Highly Toxic Cyanide Ions’. *Chemistry – A European Journal*. 22, 864–868 (**2016**).

247. World Health Organization. ‘Guidelines for Drinking-water Quality ’. (1996).

248. Ravishankara, A. R., Daniel, J. S. & Portmann, R. W. ‘Nitrous Oxide (N_2O): The Dominant Ozone-Depleting Substance Emitted in the 21st Century’. *Science*. 326, 123–125 (**2009**).

249. Tian, H. *et al.* ‘A comprehensive quantification of global nitrous oxide sources and sinks’. *Nature*. 586, 248–256 (**2020**).

250. Gillman M.A. AND Lichtigfeld, F. J. ‘Nitrous oxide and carbon dioxide: Their similar and contrasting biological effects’. *S Afr J Sci*. 103, 104–106 (**2007**).

251. Nardelli, M. ‘Parst: A system of fortran routines for calculating molecular structure parameters from results of crystal structure analyses’. *Comput Chem*. 7, 95–98 (**1983**).

252. Coelho, A. A. ‘Indexing of powder diffraction patterns by iterative use of singular value decomposition’. *J Appl Crystallogr*. 36, 86–95 (**2003**).

253. Peters, A. W., Otake, K., Platero-Prats, A. E., Li, Z., Destefano, M. R., Chapman, K. W., Farha, O. K. & Hupp, J. T. ‘Site-Directed Synthesis of Cobalt Oxide Clusters in a Metal-Organic Framework’. *ACS Appl Mater Interfaces*. 10, 15073–15078 (**2018**).

254. Schell, J., Casas, N., Pini, R. & Mazzotti, M. ‘Pure and binary adsorption of CO_2, H_2, and N_2 on activated carbon’. *Adsorption*. 18, 49–65 (**2012**).

255. Das, P. & Mandal, S. K. ‘Unprecedented High Temperature CO_2 Selectivity and Effective Chemical Fixation by a Copper-Based Undulated Metal-Organic Framework’. *ACS Appl Mater Interfaces*. 12, 37137–37146 (**2020**).

256. Dubbeldam, D., Calero, S., Ellis, D. E. & Snurr, R. Q. ‘RASPA: molecular simulation software for adsorption and diffusion in flexible nanoporous materials’. *Mol Simul*. 42, 81–101 (**2015**).

257. Wells, B. A., de Bruin-Dickason, C. & Chaffee, A. L. 'Charge equilibration based on atomic ionization in metal-organic frameworks'. *Journal of Physical Chemistry C*. 119, 456–466 (**2015**).

258. Rappé, A. K., Casewit, C. J., Colwell, K. S., Goddard, W. A. & Skiff, W. M. 'UFF, a full periodic table force field for molecular mechanics and molecular dynamics simulations'. *J Am Chem Soc*. 114, 10024–10035 (**1992**).

259. Mayo, S. L., Olafson, B. D. & Goddard, W. A. 'DREIDING: A generic force field for molecular simulations'. *Journal of Physical Chemistry*. 94, 8897–8909 (**1990**).

260. Sladekova, K., Campbell, C., Grant, C., Fletcher, A. J., Gomes, J. R. B. & Jorge, M. 'The effect of atomic point charges on adsorption isotherms of CO_2 and water in metal organic frameworks'. *Adsorption*. 26, 663–685 (**2020**).

261. Harris, J. G. & Yung, K. H. 'Carbon Dioxide's Liquid-Vapor Coexistence Curve And Critical Properties as Predicted by a Simple Molecular Model'. *J Phys Chem*. 99, 12021–12024 (**1995**).

262. Chen, Q., Balaji, S. P., Ramdin, M., Gutiérrez-Sevillano, J. J., Bardow, A., Goetheer, E. & Vlugt, T. J. H. 'Validation of the CO_2/N_2O analogy using molecular simulation'. *Ind Eng Chem Res*. 53, 18081–18090 (**2014**).

263. Martyna, G. J., Tuckerman, M. E., Tobias, D. J. & Klein, M. L. 'Explicit reversible integrators for extended systems dynamics'. *Mol Phys*. 87, 1117–1157 (**2006**).

264. Zhang, C., Dai, H., Lu, P., Wu, L., Zhou, B. & Yu, C. 'Molecular Dynamics Simulation of Distribution and Diffusion Behaviour of Oil–Water Interfaces'. *Molecules 2019, Vol. 24, Page 1905*. 24, 1905 (**2019**).

265. Kempster, C. J. E. & Lipson, H. Iuc. 'A rapid method for assessing the number of molecules in the unit cell of an organic crystal'. *Acta Crystallographica Section B*. 28, 3674–3674 (**1972**).

266. Pang, J., Yuan, S., Qin, J. S., Lollar, C. T., Huang, N., Li, J., Wang, Q., Wu, M., Yuan, D., Hong, M. & Zhou, H. C. 'Tuning the Ionicity of Stable Metal-Organic Frameworks through Ionic Linker Installation'. *J Am Chem Soc*. 141, 3129–3136 (**2019**).

267. Denysenko, D., Jelic, J., Magdysyuk, O. v., Reuter, K. & Volkmer, D. 'Elucidating Lewis acidity of metal sites in MFU-4*l* metal-organic frameworks: N_2O and CO_2 adsorption in MFU-4*l*, CuI-MFU-4*l* and Li-MFU-4*l*'. *Microporous and Mesoporous Materials*. 216, 146–150 (**2015**).

268. Markewitz, P., Kuckshinrichs, W., Leitner, W., Linssen, J., Zapp, P., Bongartz, R., Schreiber, A. & Müller, T. E. 'Worldwide innovations in the development of carbon capture technologies and the utilization of CO_2'. *Energy Environ Sci*. 5, 7281–7305 (**2012**).

269. Aresta, M., Dibenedetto, A. & Angelini, A. 'Catalysis for the valorization of exhaust carbon: From CO_2 to chemicals, materials, and fuels. technological use of CO_2'. *Chem Rev*. 114, 1709–1742 (**2014**).

270. Chen, J., Shen, K. & Li, Y. 'Greening the Processes of Metal–Organic Framework Synthesis and their Use in Sustainable Catalysis'. *ChemSusChem*. 10, 3165–3187 (**2017**).

271. Vismara, R., di Nicola, C., Millán, R. G. S., Domasevich, K. v., Pettinari, C., Navarro, J. A. R. & Galli, S. 'Efficient hexane isomers separation in isoreticular bipyrazolate metal-organic frameworks: The role of pore functionalization'. *Nano Res*. 14, 532–540 (**2021**).

272. Vismara, R., Tuci, G., Mosca, N., Domasevitch, K. V., di Nicola, C., Pettinari, C., Giambastiani, G., Galli, S. & Rossin, A. 'Amino-decorated bis(pyrazolate) metal–organic frameworks for carbon dioxide capture and green conversion into cyclic carbonates'. *Inorg Chem Front*. 6, 533–545 (**2019**).

273. Zhou, Y., Hu, S., Ma, X., Liang, S., Jiang, T. & Han, B. 'Synthesis of cyclic carbonates from carbon dioxide and epoxides over betaine-based catalysts'. *J Mol Catal A Chem*. 284, 52–57 (**2008**).

274. Kielland, N., Whiteoak, C. J. & Kleija, A. W. 'Stereoselective Synthesis with Carbon Dioxide'. *Adv Synth Catal*. 355, 2115–2138 (**2013**).

275. Domasevitch, K. V., Gospodinov, I., Krautscheid, H., Klapötke, T. M. & Stierstorfer, J. 'Facile and selective polynitrations at the 4-pyrazolyl dual backbone: straightforward access to a series of high-density energetic materials'. *New Journal of Chemistry*. 43, 1305–1312 (**2019**).

276. Gospodinov, I., Domasevitch, K. V., Unger, C. C., Klapötke, T. M. & Stierstorfer, J. 'Midway between Energetic Molecular Crystals and High-Density Energetic Salts: Crystal Engineering with Hydrogen Bonded Chains of Polynitro Bipyrazoles'. *Cryst Growth Des*. 20, 755–764 (**2020**).

277. Mosca, N., Vismara, R., Fernandes, J. A., Tuci, G., di Nicola, C., Domasevitch, K. V., Giacobbe, C., Giambastiani, G., Pettinari, C., Aragones-Anglada, M., Moghadam, P. Z., Fairen-Jimenez, D., Rossin, A. & Galli, S. 'Nitro-Functionalized Bis(pyrazolate) Metal–Organic Frameworks as Carbon Dioxide Capture Materials under Ambient Conditions'. *Chemistry – A European Journal*. 24, 13170–13180 (**2018**).

278. Vismara, R., Tuci, G., Tombesi, A., Domasevitch, K. V., di Nicola, C., Giambastiani, G., Chierotti, M. R., Bordignon, S., Gobetto, R., Pettinari, C., Rossin, A. & Galli, S. 'Tuning Carbon Dioxide Adsorption Affinity of Zinc(II) MOFs by Mixing Bis(pyrazolate) Ligands with N-Containing Tags'. *ACS Appl Mater Interfaces*. 11, 26956–26969 (**2019**).

279. Tuci, G., Filippi, J., Ba, H., Rossin, A., Luconi, L., Pham-Huu, C., Vizza, F. & Giambastiani, G. 'How to teach an old dog new (electrochemical) tricks: aziridine-functionalized CNTs as efficient electrocatalysts for the selective CO_2 reduction to CO'. *J Mater Chem A Mater*. 6, 16382–16389 (**2018**).

280. Mousavi, B., Chaemchuen, S., Moosavi, B., Zhou, K., Yusubov, M. & Verpoort, F. 'CO_2 Cycloaddition to Epoxides by using M-DABCO Metal–Organic Frameworks and the Influence of the Synthetic Method on Catalytic Reactivity'. *ChemistryOpen*. 6, 674–680 (**2017**).

281. Dick, B. L., Patel, A. & Cohen, S. M. 'Effect of heterocycle content on metal binding isostere coordination'. *Chem Sci*. 11, 6907–6914 (**2020**).

282. Beck, A., Weibert, B. & Burzlaff, N. 'Monoanionic N,N,O-Scorpionate Ligands and their Iron(II) and Zinc(II) Complexes: Models for Mononuclear Active Sites of Non-Heme Iron Oxidases and Zinc Enzymes'. *Eur J Inorg Chem*. 2001, 521–527 (**2001**).